Absolute Energy Calibration of the Pierre Auger Observatory using Radio Emission of Extensive Air Showers

Absolute Energiekalibration des Pierre Auger Observatoriums durch die Messung von Radiosignalen ausgedehnter Luftschauer

Von der Fakultät für Mathematik, Informatik und Naturwissenschaften
der RWTH Aachen University zur Erlangung des akademischen Grades
eines Doktors der Naturwissenschaften genehmigte Dissertation

vorgelegt von
Jens Christian Glaser, M.Sc.
aus Moers

Berichter:

Universitätsprofessor Herr Prof. Dr.rer.nat Martin Erdmann
Universitätsprofessor Herr Prof. Dr.rer.nat Christopher Wiebusch

Tag der mündlichen Prüfung: 10.3.2017

Contents

Introduction

1

Cosmic rays are the most energetic particles observed in the universe. With energies of more than 10^{20} eV ($\approx$ 16 Joules) concentrated in a single particle, their energy is seven orders of magnitude larger than the energy achievable in the largest particle accelerators on Earth such as the large hadron collider (LHC) at CERN [1]. Observation of these ultra-high-energy cosmic rays (UHECRs) enables the study of the most violent phenomena in the universe such as active galactic nuclei or gamma ray bursts which are probable sources of UHECRs.

The Earth is constantly bombarded by cosmic rays that create huge cascades of secondary particles in the atmosphere due to collisions with air molecules, so-called air showers. However, cosmic rays at the highest energies are very rare. Less than one particle with an energy above 10^{20} eV hits the Earth per square kilometer and century which requires observatories of enormous size. The world's largest detector – the Pierre Auger Observatory [2] – covers an area of more than $3000\,\mathrm{km}^2$ in western Argentina and thus allows for a measurement of cosmic rays at the highest energies.

Although cosmic rays are known for more than hundred years [3] they are still a mystery, e.g., their sources are still not unambiguously identified and their exact chemical composition is unknown. This is partly because UHECRs are difficult to measure as they can only be detected indirectly by the measurement of air showers. Thereby, the complete atmosphere acts as a detector medium comparable to a giant calorimeter. The state of the atmosphere is far from being a controlled laboratory environment. It changes with changing weather conditions which complicates an accurate measurement of the properties of cosmic rays such as their energy and mass.

Traditionally, cosmic rays are measured by detecting the particles of the air shower that reach the ground, by telescopes that observe the isotropic fluorescence light emitted by molecules which have been excited by the shower particles [2, 4] or by air-Cherenkov telescopes that measure the incoherent Cherenkov light produced by the shower particles [5]. In this thesis, a complementary method is explored: The measurement of cosmic rays by the detection of short radio pulses in the MHz regime. This method was already probed in the 1960s [6] but, after a proof of concept, abandoned in the mid 1970s mostly due to the lack of digital signal processing and the success of the fluorescence technique. With the development of powerful digitizing hardware this technology experienced a revival in the early 2000s. The experiments LOPES and CODALEMA located in Karlsruhe, Germany and Nançay, France [7, 8] demonstrated that the radio technique is sensitive to all main air-shower observables: the incoming direction, energy and mass [9, 10]. As a next step, the Auger Engineering Radio Array (AERA) [11] – the radio detector of the Pierre Auger Observatory – was designed. AERA is an array of more than 150 autonomous radio detector stations covering an area of $\sim$17 km^2. By measuring air showers in coincidence with the surface and fluorescence detectors, AERA enables benchmarking the radio technique in comparison to the well understood reconstruction of air showers of the Pierre Auger Observatory.

AERA contributed significantly to the understanding of radio emission processes in air showers.

AERA identified and measured the strength of the charge-excess emission process relative to the dominant geomagnetic emission process [12]. Further, detailed insights of the emission processes and the spacial and temporal shape of the radio signal were obtained with the high precision measurements of LOFAR, a radio telescope located in the Netherlands that samples the radio footprint with hundreds of antennas [13–15]. Additionally, the sensitivity to the cosmic-ray mass was demonstrated by AERA [16], LOFAR [17–19], and Tunka-Rex, the radio detector of the Tunka air-Cherenkov experiment located in Siberia [20, 21]. See [22] and [23] for a recent review of theoretical and experimental results.

This thesis, however, goes one step further. After the proof of concept and the understanding of the mechanisms of radio emission, this new technology is used to improve the state-of-the-art technique of measuring UHECRs. We develop a new method to reconstruct the energy of cosmic rays and apply it to AERA data which allows for a direct comparison between the radio technique and the hybrid detector of the Pierre Auger Observatory. We find that a precision well compatible with surface detectors is reached. Furthermore, we demonstrate that this new technology is capable to determine the cosmic-ray energy with unprecedented accuracy of less than 10%. This is achieved by using two of the main advantages of radio emission, namely that the atmosphere is transparent to radio waves and that the radio emission can be calculated from first principles via classical electrodynamics. These advantages result in less sources of uncertainties compared to the currently used fluorescence technology, as changing atmospheric conditions have only negligible influence on the radio emission.

These new developments contribute to one of the central tasks of the Pierre Auger Observatory: the accurate determination of the cosmic-ray energy scale. The energy scale has direct impact on many results of the Pierre Auger Observatory: The interpretation of features of the energy spectrum such as the ankle and the cutoff build on their exact location. In addition, the test of hadronic interaction models at energies beyond the reach of LHC as well as correcting deflections in Galactic magnetic fields depend strongly on the accuracy of the energy scale.

This thesis is structured as follows. We start with an introduction to cosmic rays and air showers. Next, we discuss the emission of radio signals from air showers in detail and determine the radiation energy, i.e., the amount of energy transferred from the primary cosmic ray into radio emission during the air-shower development, by first-principles calculations. Then, we describe the Pierre Auger Observatory and its Engineering Radio Array and explain the reconstruction of air showers from radio detector data. After that, we develop a new method to reconstruct the cosmic-ray energy. We present a measurement of the radiation energy using AERA and compare it with the cosmic-ray energy reconstructed by the surface detector of the Pierre Auger Observatory. Finally, we combine the measurement with the first-principle prediction of the radiation energy to set the cosmic-ray energy scale and discuss its impact on recent results of the Pierre Auger Observatory.

Cosmic rays

Cosmic rays are charged energetic particles that travel through outer space. Some of them find their way to Earth so that the Earth is constantly hit by cosmic rays. Among other things, cosmic rays produce about the half of the ionizing radiation observed at the Earth's surface [3]. The energy of cosmic rays ranges up to energies exceeding 10^{20} eV which is seven orders of magnitude higher than the single-beam energy that can be reached in the largest particle accelerator on Earth, the large hadron collider [1]. With increasing energy the flux of cosmic rays drops rapidly. More precisely, per decade of energy the flux drops approximately by a factor of thousand. Below energies of 10^{12} eV more than one cosmic ray hits the Earth per second and square meter. Above an energy of 10^{16} eV only a few cosmic rays hit the Earth per square meter and year and the flux for energies larger than 10^{20} eV is less than one cosmic ray per square kilometer and century.

Due to the large energy range of cosmic rays, different techniques are necessary to measure cosmic rays. A direct detection of cosmic rays is only possible outside of the Earth's atmosphere, i.e., before the cosmic ray interacts with air molecules. Cosmic rays with energies up to $\sim 10^{14}$ eV can be measured directly with balloon experiments at the top of the atmosphere [24–27] or with spaceborn detectors such as satellites [28, 29] or detectors at the international space station (ISS) [30, 31]. A direct detection allows for a precise determination of the energy and the particle type. One prominent example is the energy spectrum, i.e., the flux of cosmic rays as a function of their energy. The energy spectrum of cosmic rays is presented in Fig. 2.1. The data is shown for different particle species. Roughly 79% of the cosmic rays are protons followed by helium nuclei which make up about 70% of the remaining nuclei. Except for small energies per nucleon, the spectrum can be described with a simple power law. The flux decreases proportionally to $E_n^{-\gamma}$ with $\gamma = 2.7$ and E_n being the energy per nucleon. The ratio between different particle species remains nearly constant over the presented energy range [32].

Cosmic rays with energies larger than $\sim 10^{14}$ eV can not be measured directly anymore because of two reasons. First, the detector size of balloons or spaceborn experiments is limited and the flux of cosmic rays decreases with increasing energy such that not enough statistics can be obtained. Second, even if a cosmic ray hits the detector, the energy would be so large that the cosmic ray would just go through the detector so that a measurement of its energy or momentum would not be possible. Cosmic rays at large energies can only be measured indirectly with large ground based detectors [2, 4, 46, 47]. When such a cosmic ray hits the Earth's atmosphere it interacts with air molecules and creates an *air shower* – a shower of secondary particles – that can be observed from the ground. One can think of the atmosphere as a giant calorimeter that is read out from the ground. Due to the indirect detection, the measurement is less precise. Whereas the arrival direction of the cosmic ray can still be determined precisely at the level of $1°$, and its energy can be measured at a level of $\mathcal{O}(>10\%)$ while the uncertainties on the particle mass on an event-by-event basis are larger by far owing to the sizable overlap of the longitudinal air-shower shape originating from the different nuclei.
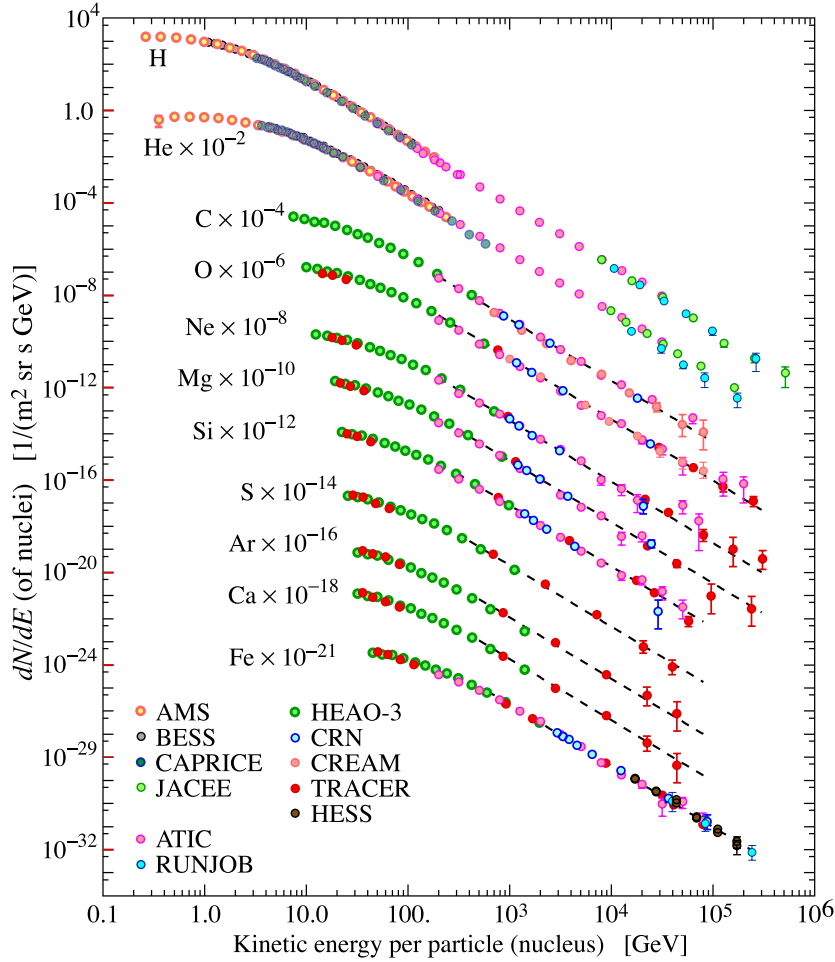
Figure 2.1: Cosmic-ray energy spectrum of primary nuclei obtained from direct measurements. Data from [33–45]. Figure from [32].

Measurements of the all-particle flux from different experiments are presented in Fig. 2.2. The spectrum shows again a remarkably simple structure although is does not continue with $E^{-2.7}$ towards the highest energies but exhibits a few breaks in the spectral index. The energy E refers to the energy per particle. To display these features the differential flux was multiplied by $E^{2.6}$. The spectrum steepens to a spectral index of $\gamma \approx 3.1$ (e.g. [48]) at the so-called *knee* which is between 10^{15} eV and 10^{16} eV. At the *ankle* at around 5×10^{18} eV the spectrum flattens again to $\gamma = 2.6$ [49]. The Kascade-Grande experiment also reported a *second knee* near 8×10^{16} eV where a second steepening of the spectrum to $\gamma \approx 3.24$ occurs [50].

The energy spectrum is generally interpreted by assuming that cosmic rays below 10^{18} eV = 1 EeV are of galactic origin. Then, the steepening of the spectrum at the knee reflects the fact that most galactic accelerators have reached their maximum energy for protons. As the maximum achievable energy scales with the charge number Z of the cosmic-ray nucleus, a transition from light to heavier cosmic-ray nuclei takes place between the first and second knee and the second steepening reflects the maximum achievable energy for iron nuclei [50]. The ankle then marks the transition from galactic to extragalactic origin of the cosmic rays.
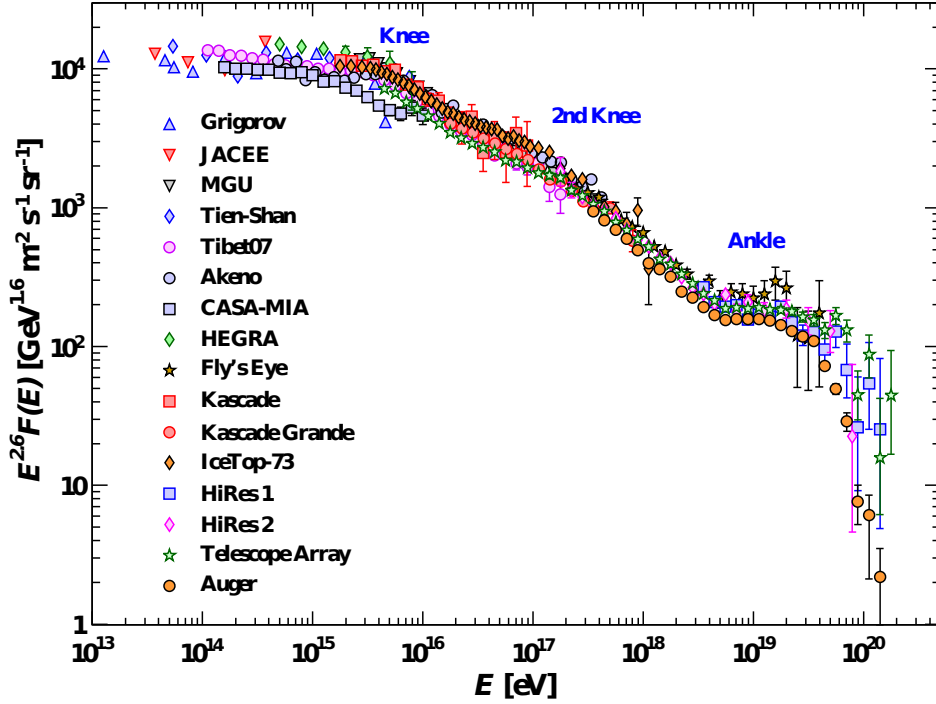
Figure 2.2: Energy spectrum of cosmic rays obtained from indirect measurements of air showers. Data from [48–66]. Figure from [32].

As visible in Fig. 2.2, the cosmic-ray flux reported by different experiments differs by as much as a factor of two in the knee region. The plot shows statistical uncertainties only. At higher energies the differences become smaller but are still sizable and most probably attributed to systematic uncertainties in the determination of the cosmic-ray energy, indicating the importance of the systematic uncertainties on the energy scale for the interpretation of the spectrum. This becomes especially evident when looking at the high precision data from the Telescope Array (TA) and Pierre Auger collaborations at the highest energies which is shown in Fig. 2.3. Both experiments see a cutoff at the highest energies. Whereas the two measurements are in good agreement below 2×10^{19} eV with a difference in the flux of about 20%[1], the discrepancy in the cutoff region is significant [67]. The position of the ankle (TA: (5.2 ± 0.2) EeV, Auger: (4.8 ± 0.1) EeV) is in good agreement, but the position of the cutoff $E_{1/2}$, which is defined as the position at which the flux drops to half of what would be expected with no cutoff [68], is significantly different with $E_{1/2} = 60 \pm 7$(stat) EeV reported by TA and 24.7 ± 0.1(stat) $^{+8.2}_{-3.4}$(syst) EeV reported by Auger. The reason for the cutoff is under debate. One explanation is that the cutoff is due to energy losses of cosmic rays with photons from the cosmic microwave background (CMB), the so-called GZK effect which is discussed in more detail in Sec. 2.3. The other explanation is that the cosmic-ray accelerators have reached their maximum energy. Further insights to distinguish the two scenarios can be gained by the chemical composition. If only protons are observed at the highest energies, the GZK cutoff would be favorable. If instead the composition shows a transition towards heavier elements, a cutoff due to a limited maximum energy of the accelerators would be more likely as the maximum energy of a source typically scales with the charge number Z of the nucleus.

---

[1]The Telescope Array and the Pierre Auger collaborations report a systematic uncertainty of 21% and 14%, respectively.
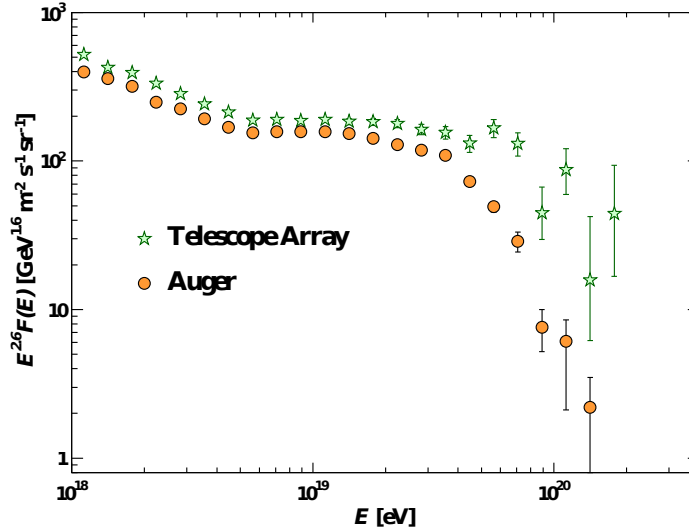
Figure 2.3: Cosmic-ray energy spectrum at the highest energies as measured by the Telescope Array [66] and Pierre Auger Observatory [49]. Figure from [32].

2.1   Composition

A robust estimator of the particle mass is given by the position of the air-shower maximum X_{max}. The average X_{max} per energy bin as measurement by the TA and Auger experiments are presented in Fig. 2.4 together with the prediction of the two extremes of cosmic rays being protons or iron nuclei for different hadronic interaction models. The data can not be directly compared to each other because in case of TA data, detector effects are folded into the model predictions whereas the Auger collaboration first unfolds detector effects from the X_{max} measurement and then compares it to the models. A combined analysis of the two collaborations showed that the two measurements are compatible within their systematic uncertainties [69]. However, the interpretation of the data differs. The measurement of TA is compatible with a relatively pure, light composition whereas Auger sees a transition towards heavier nuclei above the ankle.

Another estimator of the cosmic-ray composition is the standard deviation of the X_{max} distribution which is presented by the Pierre Auger collaboration and shown in Fig. 2.5 left. The heavier the cosmic-ray nucleus, the less fluctuations are expected. If the composition is not pure, the spread of the distribution increases due to the superposition of distributions with different mean, e.g., for a continuous transition from proton to iron nuclei, a spread larger than the spread for a pure proton composition is expected. Hence, also the measurement of the X_{max} fluctuations by Auger supports the transition towards heavier elements. Under the assumption of a specific hadronic interaction model, the average mass number A of the cosmic rays was determined using the information from the X_{max} distributions [70–73] which is shown in Fig. 2.5 right. From $10^{17}\,\text{eV}$ to $2 \times 10^{18}\,\text{eV}$ the cosmic-ray compositions shows a transition towards lighter particles. At larger energies the trend reverses and the composition gets heavier again. A more refined analysis fits the X_{max} distributions with predictions of hadronic interaction models for different particle species [74]. The data can not be described consistently with a mix of only protons and iron nuclei. Only if cosmic rays of intermediate mass are included, the fit gives acceptable results. A model of three (protons, nitrogen and iron nuclei)
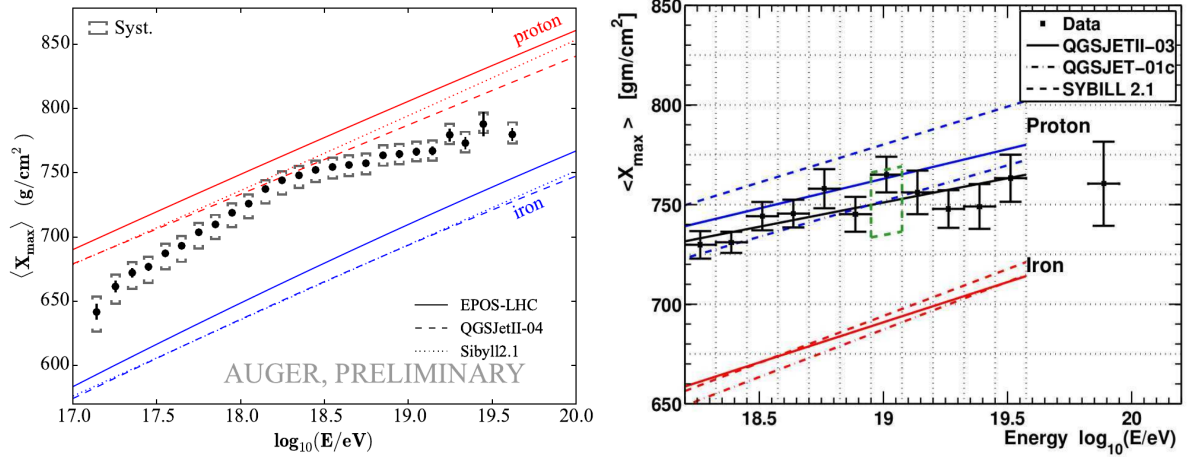
Figure 2.4: Measurement of the average depth of the shower maximum X_{max} measured by the Pierre Auger Observatory [73] and the Telescope Array [75].
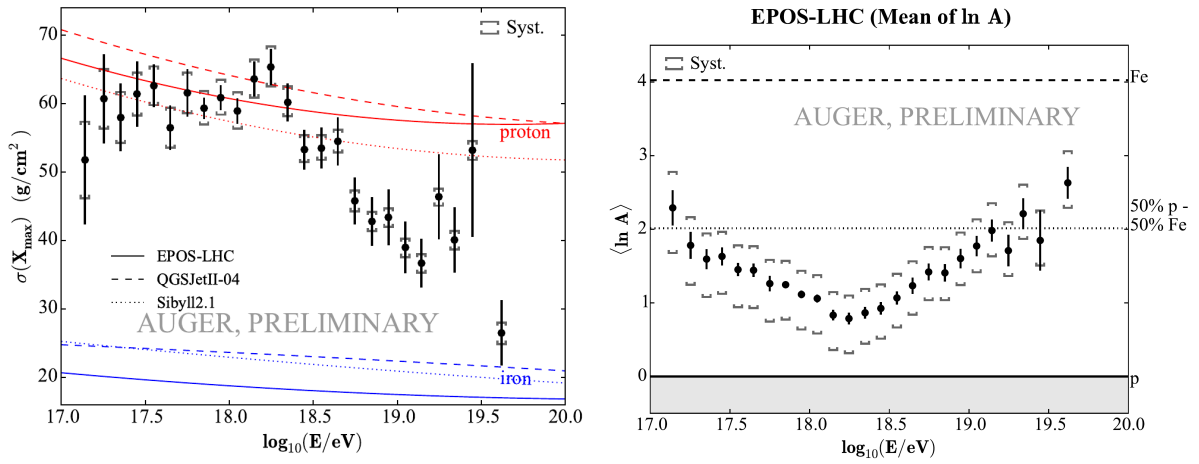
Figure 2.5: (left) Measurement of the standard deviation of the X_{max} distributions by the Pierre Auger Observatory. (right) Average logarithm of the mass number A obtained from the X_{max} distributions using EPOS-LHC [76] as hadronic interaction model. Figures from [73].

and four (protons, helium, nitrogen and iron nuclei) particle species was used to describe the data. The proton fraction shows an energy dependency and decreases towards higher energies. Iron nuclei do not contribute significantly to the cosmic-ray composition over the studied energy range of $10^{17.8}$ eV to 10^{20} eV. In case of the four parameter model, the fraction of the cosmic rays with intermediate masses (helium and nitrogen nuclei) show a strong dependence on the choice of hadronic interaction model.

Another and completely independent estimator of the cosmic-ray mass is the average number of muons produced in the interactions of cosmic rays within our atmosphere [77]. The muon number is estimated by a parameter $\langle R_\mu \rangle$ which is the average number of muons with energies larger than 0.3 GeV relative to the number of muons of a 10^{19} eV proton shower simulated with the hadronic interaction model QGSJetII-03 [78]. The value $R_\mu = 1$ corresponds to 2.146×10^7 muons above 0.3 GeV at an altitude of 1425 m a.s.l. which is the average altitude of the Pierre Auger Observatory for an air shower with an inclination of $60°$. The measurement of R_μ is presented in Fig. 2.6. The mea-
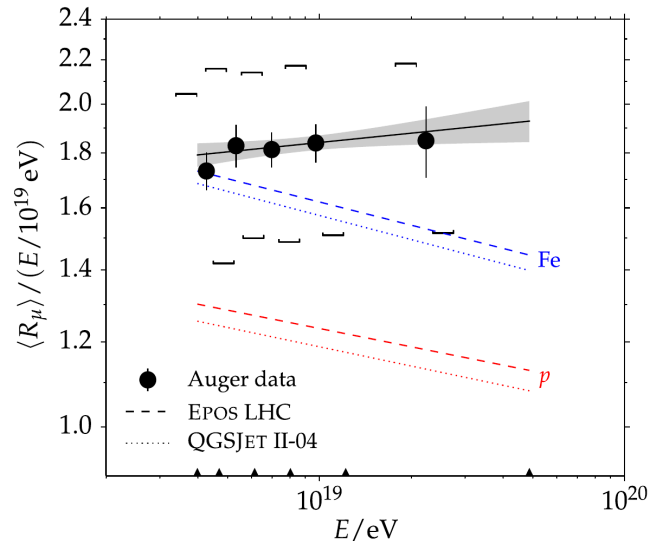
Figure 2.6: Relative average number of muons on ground $\langle R_\mu \rangle$ as a function of cosmic-ray energy (black filled circles). The square brackets denote the systematic uncertainty primarily due to the uncertainty of the energy scale. Also shown are the predictions from hadronic interaction models for proton and iron induced air showers. Figure from [77].

surement shows a large abundance of muons with respect to all modern hadronic interaction models. To a large extend, this discrepancy can be resolved by a shift of the energy scale within its systematic uncertainty of 14%. As indicated by the open brackets in Fig. 2.6, a shift of the cosmic-ray energies by one standard deviation towards higher energies brings the data in agreement with the model predictions. This result again stresses the importance of an accurate energy scale for the interpretation of the data.

2.2 Origin

Although high-energy cosmic rays are known for more than hundred years, their origin remains unknown. This is because cosmic rays are charged particles that get deflected during their propagation in galactic and extragalactic magnetic fields. As the deflections reduce with increasing energy, cosmic rays at the highest energies are especially interesting because they presumably point back to their sources.

Cosmic rays are generally believed to be accelerated by stochastic processes in magnetized plasma. The acceleration continues as long as the cosmic rays remain confined by magnetic fields in the source region. Such a stochastic acceleration process results in the observed power-law energy spectrum and the spectral index depends on the specific properties of the acceleration [79]. The exact acceleration mechanism is unclear. A possible mechanism was proposed by Enrico Fermi [80] where cosmic rays collide with magnetic clouds that move at random relativistic velocities. In each collision the cosmic ray gains energy proportional to β^2, the speed of the cloud measured in units of the speed of light. This mechanism is known as the *second-order Fermi acceleration*. A more efficient mechanism is the acceleration by diffuse scattering in supersonic shocks that spread out in the source region. As the cosmic rays are bound by magnetic fields, they collide with the shock several times and acquire more
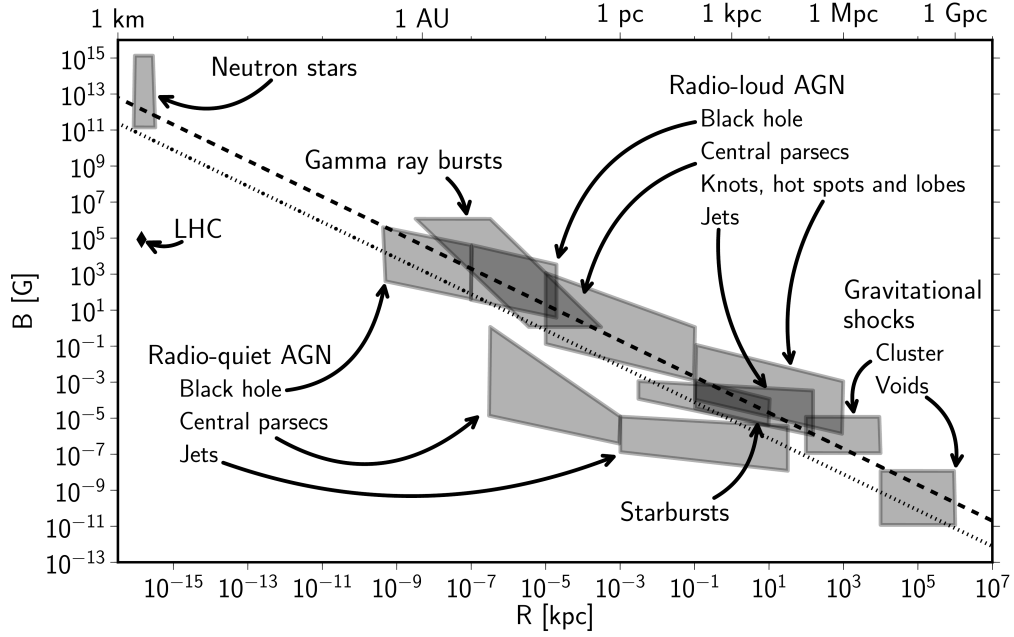
Figure 2.7: Hillas diagram. The magnetic-field strength and size of possible UHECR sources is shown including their uncertainties. Above the dashed (dotted) line protons (iron nuclei) can be confined up to energies of $10^{20}\,\mathrm{eV}$ (for $\beta = 1$). Figure from [82].

energy in each crossing. This mechanism is known as the *first-order Fermi acceleration* as the energy gain is directly proportional to β [81].

Then, the maximum energy achievable is only determined by the time the cosmic ray remains in the source which depends on the source's size R and magnetic-field strength B and is given by

$$\left(\frac{E_{\mathrm{max}}}{1\,\mathrm{EeV}}\right) \approx 2.16\, Z\, \beta \left(\frac{B}{1\,\mu\mathrm{G}}\right) \left(\frac{R}{1\,\mathrm{kpc}}\right), \tag{2.1}$$

where Z is the charge of the cosmic ray [82]. This equation is known as the Hillas criterion [83] and potential sources can be grouped in the so-called Hillas diagram where the magnetic field is plotted versus the size of the source candidate and is shown in Fig. 2.7. The size and magnetic-field strength necessary to accelerate particles to the highest energies of $\geqslant 10^{20}\,\mathrm{eV}$ are much larger than our galaxy, implying an extragalactic origin of the sources of ultra-high-energy cosmic rays (UHECRs). This equation also shows that heavier nuclei, if present at the source, can be accelerated to Z times higher energies. Plausible sources of UHECRs are accretion shocks in large-scale structures, active galactic nuclei (AGN), gamma ray bursts (GRBs) and neutron stars or magnetars [84].

2.3 Propagation

Cosmic rays do not propagate unimpeded through the universe but are deflected in magnetic fields or interact with photon fields, in particular with the cosmic microwave background (CMB). The knowledge of the extragalactic magnetic field (EGMF) is poor. The magnetic-field strength in the core of clusters of galaxies is estimated by Faraday rotation measurements and is in the order of $\sim (1\text{–}40)\,\mu\mathrm{G}$
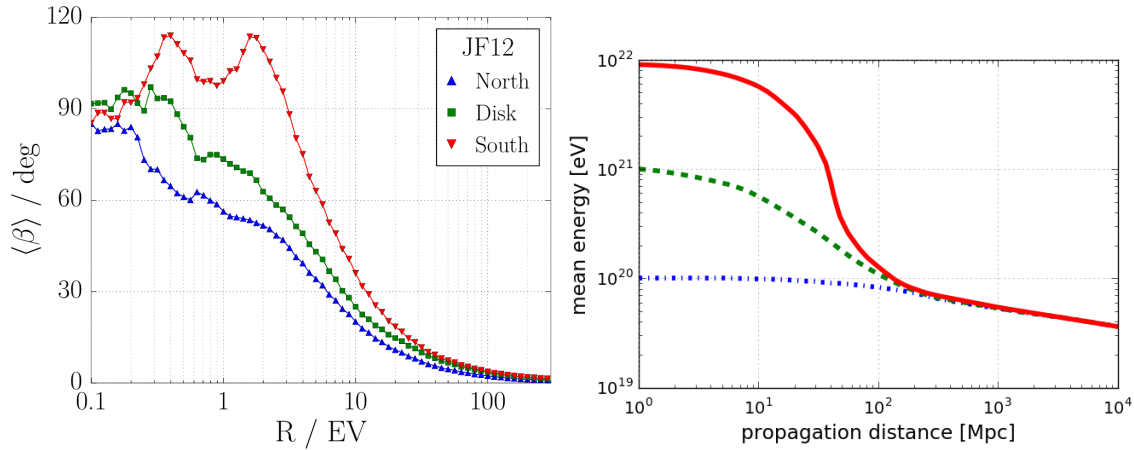
Figure 2.8: (left) Average deflections in the galactic magnetic field as a function of rigidity (i.e. the energy of the cosmic ray divided by its charge) according to the JF12 model for three regions in the galaxy. Figure from [92]. (right) Proton energy as function of propagation distance. Protons loose energy through interactions with the cosmic microwave background. Figure adapted from [93].

[84]. The magnetic field in filaments and voids is less well known. In voids it can range from 10^{-17} G to 10^{-9} G constrained by γ-ray observations [85]. An estimate of the EGMF properties can be obtained from magnetohydrodynamical large-scale structure simulations. Different models all reproduce the measured magnetic-field strength in galaxy clusters but differ in the predicted field strengths in filaments ranging from $1\,\mu G$ to $1\,nG$ and below ([82] and references therein). The field strength in voids is roughly two orders of magnitude smaller. Besides the magnitude of the magnetic field also the coherence length is relevant for the resulting deflections. The EGMF models also predict the coherence lengths such that the resulting deflections of cosmic rays can be estimated. The results obtained with the different models vary significantly [86] but it is likely that the EGMF has less influence than the galactic magnetic field and that light cosmic rays, i.e., particles with a small charge number, at the highest energies still point back to their sources when they enter our galaxy [87].

The galactic magnetic field (GMF) is better known than the EGMF as it can be constrained using Faraday rotation measures of mostly extragalactic sources, which are sensitive to the parallel component of the magnetic field [86, 88], and measurements of the total and polarized synchrotron emission by galactic relativistic electrons, which are sensitive to the magnetic field perpendicular to the line of sight. The most sophisticated GMF model is the so-called JF12 field [89–91] that models the GMF with a large-scale regular field which follows the spiral arms, an extended halo field and two additional small-scale random components. The magnetic-field strengths are at the order of μG. The resulting deflections of cosmic rays during the propagation through the Milky Way to Earth are shown in Fig. 2.8 as a function of rigidity, i.e., the ratio of the energy of the cosmic ray and its charge. The average deflection is roughly described with $\langle\beta\rangle \approx 5° \times Z \times 60\,\text{EeV}/E$ [86]. The relatively precise knowledge of the GMF allows in principle for a correction of the deflections if the charge and the energy of the cosmic ray is known [92].

In future, even further improvements of the GMF models are expected with new data from the PLANCK satellite [94] and with future ground based optical (e.g. the Atacama Large Millimeter Array ALMA) and radio telescopes (e.g. the Square Kilometer Array SKA) [88].

Relevant photon fields for the propagation of cosmic rays through the intergalactic space are the cosmic radio background (CRB), the extragalactic background light (EBL) and the cosmic microwave background (CMB). The CMB is the most important one and will be discussed in the following. An overview of the impact of the other photon fields can be found, e.g., in [86] and [84]. The CMB has an almost perfect blackbody spectrum of temperature T = 2.726 K corresponding to meV photon energies [32]. With roughly 400 photons per cm^3 it is the most intense extragalactic radiation field. For energies above $E \approx 5 \times 10^{19}$ eV, the cross section of the interaction of protons with the CMB photons rises dramatically and protons loose energy mainly by photo-pion production via the delta resonance:

$$p + \gamma_{\mathrm{CMB}} \rightarrow \Delta^+ \rightarrow p + \pi^0$$
$$\hookrightarrow \gamma + \gamma$$
$$\rightarrow n + \pi^+$$
$$\hookrightarrow \mu^+ + \nu_\mu$$
$$\hookrightarrow e^+ + \nu_e + \bar{\nu}_\mu$$
$$\hookrightarrow p + e^- + \bar{\nu}_e$$
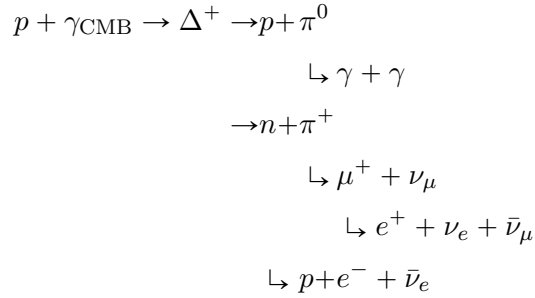
This is the well known GZK effect that was independently predicted by Greisen [95] and Zatsepin and Kuzmin [96]. The resulting decrease of the cosmic-ray energy with increasing propagation distance is shown in Fig. 2.8 right. Independent of the initial cosmic-ray energy, after a propagation length of $\sim$100 Mpc, the proton energy is below 10^{20} eV. Cosmic-ray nuclei show a similar energy loss behavior, although the underlying process is different. Nuclei loose energy primarily via photo-disintegration

$$X_A^Z + \gamma \rightarrow X_{A-1}^{Z-1} + p$$
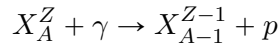
and the energy threshold depends on the energy per nucleon E/A. The energy loss length, i.e., the propagation distance after the cosmic ray has lost $1/e$ of its energy, is shown in Fig. 2.9 for protons and carbon-12 nuclei.

The implication of these energy losses is that cosmic rays with energies above $\sim 5 \times 10^{19}$ eV must originate from within $\sim$100 Mpc. This local universe is not isotropic but exhibits significant structure. Therefore, anisotropies in the arrival directions of cosmic rays are expected.

Another implication of the interaction of cosmic rays with the intergalactic photon fields is the production of high energy neutrinos and photons which are referred to as GZK or cosmogenic neutrinos/photons. The number of neutrinos and photons expected from cosmic-ray interactions depends strongly on the chemical composition as the production from heavier nuclei is suppressed as it is only due to succeeding decays and accordingly significantly smaller than the number of neutrinos and photons from photo-pion production of protons. A measurement or non-measurement of cosmogenic neutrinos and photons gives important constrains on the origin and sources of cosmic rays. However, current experiments are not yet sensitive enough to do so.
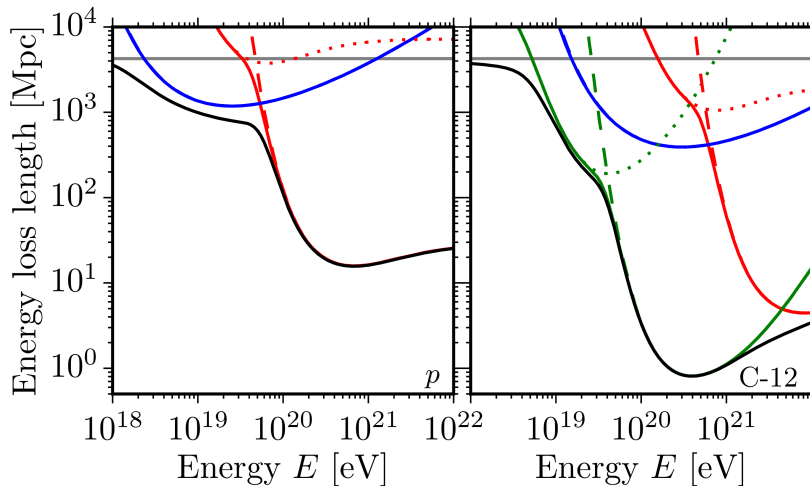
Figure 2.9: Propagation distance after the cosmic ray has lost $1/e$ of its energy for protons (left) and carbon-12 (right). The black line shows the total energy loss length. The contributions from the different processes are also shown. Red curves show energy losses due to photo-pion production, green curves photo disintegration and blue curves the subdominant pair production. Dashed curves represent interactions with the CMB and dotted curves interactions with the EBL. Figure from [86].

2.4   Arrival directions

Due to the large-scale structure of the universe and the limited (GZK) horizon of high-energy cosmic rays of $\lesssim 100\,\mathrm{Mpc}$, anisotropies in the arrival directions of cosmic rays are in-principle expected. However, even the arrival directions of cosmic rays at high energies ($E > 10^{19}\,\mathrm{eV}$) are largely isotropic with no clear correlation with source candidates.

Different search strategies have been exploited to find sources of cosmic rays. The first type searches for localized excesses in the arrival directions which would be an imprint of a bright nearby source if deflections in magnetic fields are at a moderate level. The Pierre Auger collaboration reported an excess into the direction of Centaurus A which is the closest radio-loud AGN at $4\,\mathrm{Mpc}$ distance and the Centaurus cluster containing a large number of galaxies that lies at $50\,\mathrm{Mpc}$ distance into the same direction [97]. For a search window of $15°$, 14 events above $5.8 \times 10^{19}\,\mathrm{eV}$ are observed whereas 4.5 are expected from isotropy. This corresponds to a local significance of $3\,\sigma$ with a post-trial significance of $2.5\,\sigma$. Also the Telescope Array collaboration reported a hotspot of $20°$ radius at $\alpha = 148.4°$ and $\delta = 44.5°$ in equatorial coordinates for cosmic rays exceeding $E = 5.7 \times 10^{19}\,\mathrm{eV}$ with a post-trial significance of $3.4\,\sigma$ [98, 99]. Other search strategies such as two-point angular correlations or a scan for local excesses have been performed as well but are all compatible with isotropy [100].

The next type of searches considers multiple point sources where the signal from each single source is too faint to be detected individually. The Pierre Auger collaboration compared the arrival directions of the highest energetic cosmic rays ($E > 5.7 \times 10^{19}\,\mathrm{eV}$) with the positions of nearby AGNs ($< 75\,\mathrm{Mpc}$) from the VCV catalog [101] and found a correlation fraction of $28.1^{+3.8}_{-3.6}\%$ [100] which is only $2\,\sigma$ above the isotropic expectation of 21%[2]. Also other cross-correlation analyses with

---

[2]In the first publication of this analysis in 2006 [102], the correlation fraction was 61% corresponding to a significance of more than $3\,\sigma$. With more statistics the fraction of cosmic rays correlating with the AGN catalog decreased to the value reported here.
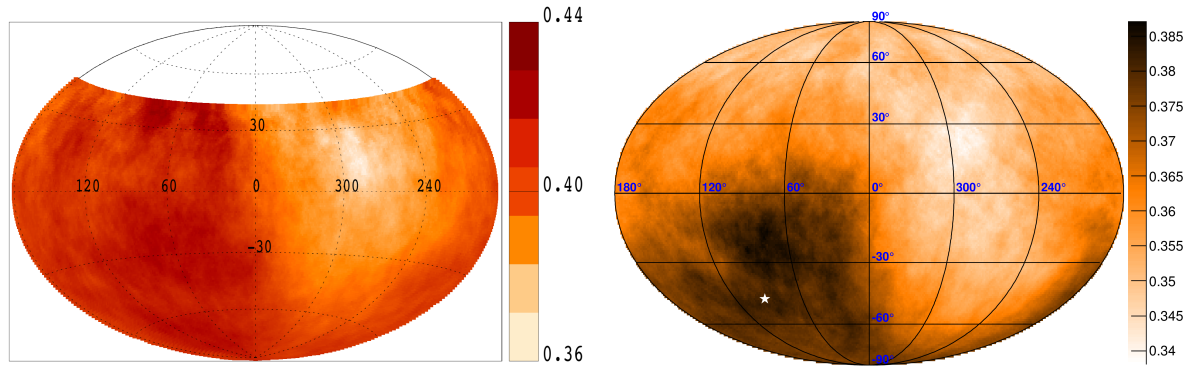
Figure 2.10: Sky maps in equatorial coordinates of the flux of cosmic rays in units of $\mathrm{km}^{-2}\mathrm{yr}^{-1}\mathrm{sr}^{-1}$. (left) Measurement by the Pierre Auger Observatory. The flux of cosmic rays with energies above $8 \times 10^{18}\,\mathrm{eV}$ is smoothed with an angular window of $45°$ radius. Figure from [104]. (right) Combined data of the Pierre Auger and Telescope Array experiments. Shown is the flux for energies above $10^{19}\,\mathrm{eV}$ and a smoothing of $60°$ radius was applied. The star indicates the position of the dipole. Figure from [107].

different astrophysical objects have been performed. None of the analyses presented so far shows a significant evidence for anisotropy [103].

The third type of searches focuses on large-scale anisotropies at large angular scales. This is achieved by harmonic analyses where the distribution of arrival directions is decomposed into multipole moments. Recently, the Pierre Auger collaboration reported a dipole signature in the arrival directions of cosmic rays with energies larger than $8 \times 10^{18}\,\mathrm{eV}$ with a significance of $4\,\sigma$. The dipole points into $\alpha = (95 \pm 13)°$ and $\delta = (-39 \pm 13)°$ in equatorial coordinates and has an amplitude of $(7.3 \pm 1.5)\,\%$ [104, 105]. A sky map showing this large-scale anisotropy is shown in Fig. 2.10 left. The arrival directions of cosmic rays with smaller energies are compatible with isotropy. This analysis is complicated by the fact that a single cosmic-ray observatory does not cover the whole sky. Therefore, data of the Pierre Auger Observatory has been combined with data from the Telescope Array yielding a full sky coverage [106]. The resulting sky map of the cosmic-ray flux for energies above $10^{19}\,\mathrm{eV}$ is presented in Fig. 2.10 right. A harmonic analysis of the combined data set finds a compatible dipole structure with an amplitude of $(6.5 \pm 1.9)\,\%$ into a direction of $\alpha = (93 \pm 24)°$ and $\delta = (-46 \pm 18)°$ with a significance of $2.8\,\sigma$ [107].

Air showers
and their radiation energy release

Ultra-high-energy cosmic rays (UHECRs) produce extensive air showers when they interact in the Earth's atmosphere. These are huge particle cascades with billions of secondary particles traversing the atmosphere. In the following, we will first give a general overview of air showers and their development. Then, we will describe the radio emission produced by air showers. We continue with a section on Monte-Carlo simulations of air showers and explain how the radio emission can be calculated from first principles before we discuss the radiation energy release in air showers which is one essential ingredient in the determination of the cosmic-ray energy scale with a radio detector.

The first interaction of the cosmic ray with an air nucleus (mainly nitrogen, oxygen and argon) typically happens at a height between $15\,\mathrm{km}$ and $35\,\mathrm{km}$ [110]. The particles produced in the interaction will interact again or decay and are forming an air shower (see Fig. 3.1 left for an illustration). Air showers can be subdivided into three components. The first is the hadronic shower component mainly composed of long-lived secondary hadrons (baryons, charged pions and kaons). The second component is composed of electromagnetic sub showers (electrons, positrons and photons) and the third component consists of muons and neutrinos that are produced along with the muons. The neutrinos are irrelevant for the shower development and for the observation of air showers due to their low interaction cross section. However, they carry a significant part of the initial cosmic-ray energy and are thus essential to consider to estimate the cosmic-ray energy correctly. The evolution of the particle numbers of the different shower components is shown in Fig. 3.1 right.

Most of the particles that are produced in the high-energy hadronic interactions are pions followed by kaons. Neutral pions ($c\tau = 26\,\mathrm{nm}$) directly decay into two photons and give rise to the electromagnetic cascade. Charged pions ($c\tau = 7.8\,\mathrm{m}$) and kaons ($c\tau = 3.7\,\mathrm{m}$) live long enough to interact before they decay as long as their energy is large enough[1]. For pions, this critical energy where a

---

[1] Due to the relativistic speed of the particles, the lifetime τ is increased by the gamma factor γ.
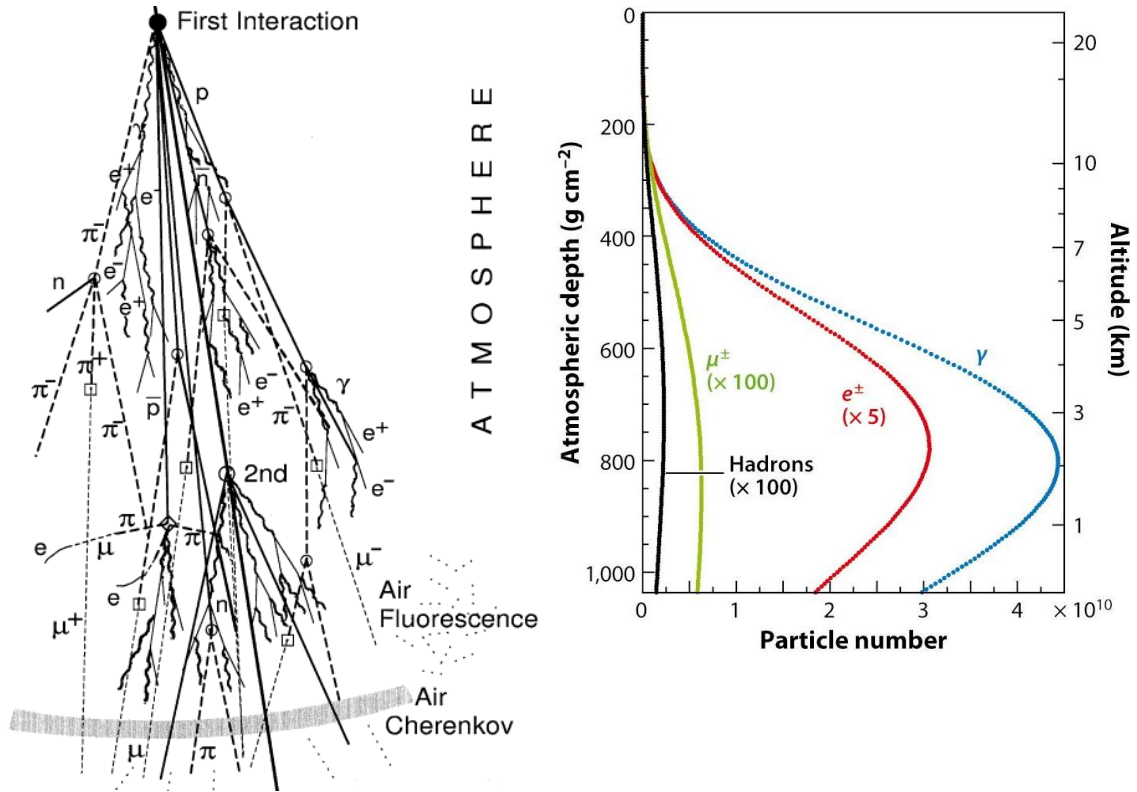
Figure 3.1: (left) Schematic view of an extensive air shower. Figure adapted from [111]. (right) Evolution of the particle numbers of the different shower components. Figure from [110].

decay becomes more likely than an interaction is typically $\xi_c^\pi = 20\,\text{GeV}$ [112]. Kaons already start to decay at higher energies and decay into pions, muons and muon neutrinos. Charged pions decay almost exclusively into muons and the corresponding neutrino ($\pi^+ \rightarrow \mu^+ + \nu_\mu$, $\pi^- \rightarrow \mu^- + \bar{\nu}_\mu$).

Electromagnetic sub showers develop by bremsstrahlung of electrons (and positrons) and pair production of photons. A qualitative understanding can be acquired in the simplified model of Heitler [113, 114]. Interactions take place after a fixed interaction length λ_e. Electrons and positrons radiate one photon in each interaction and photons convert into an electron-positron pair. Thereby, the energy of the mother particle is equally distributed onto the two daughter particles. An illustration of this model of succeeding two-body splittings is presented in Fig. 3.2 left. Hence, after n splittings, 2^n particles are present and the interactions continue until the electrons (positrons) reach a critical energy ξ_c^e where the collisional energy losses exceed the radiative energy losses. This is at approximately 86 MeV in air. As the initial energy E_0 is distributed equally over all particles, the maximum number of particles N_max is given by E_0/ξ_c^e and the atmospheric depth where the maximum is reached – referred to as X_max in the following – is proportional to the logarithm of E_0. Despite the simplifications of this model, it correctly predicts these proportionalities. However, N_max is underestimated by roughly one order of magnitude and the number of photons is actually higher then the number of electrons as often multiple photons are radiated during bremsstrahlung [112].

Similar to the simplified description of electromagnetic showers, we can use an extension of the Heitler model to hadronic interactions [112] to also gain insights into the hadronic shower development. First, we consider only protons as initial cosmic rays. Later, we will generalize the model to
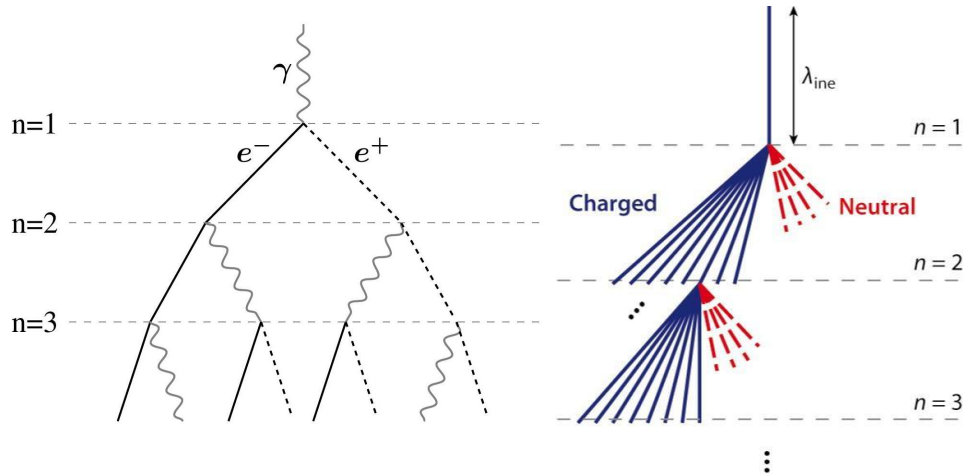
Figure 3.2: (left) Heitler model of an electromagnetic shower. (right) Heitler-Matthews model of an hadronic shower. Dashed lines represent neutral particles (π^0), and solid lines represent charged particles ($\pi^\pm$). Only one charged hadron interaction is shown for each generation. Figures and captions adapted from [110, 115].

heavier nuclei. Again, interactions take place after a fixed interaction length of λ_π which is about $120 \, \mathrm{g/cm^2}$ in air [116] and only pions are considered which make up the majority of hadrons. In each interaction, n_tot new particles with the same energy are created ($n_\mathrm{tot} \approx 15$). One third of them are neutral pions that directly decay into photon pairs and thus transfer $1/3$ of the energy to the electro-magnetic shower component in each step. The rest of the new particles ($n_\mathrm{ch} = 2/3 \, n_\mathrm{tot}$) are charged pions that interact further and produce a new generation of pions until their energy is below their critical energy. An illustration of this model is presented in Fig. 3.2 right. Hence, after n interaction lengths, the energy in the hadronic shower component is reduced by $E_\mathrm{had} = \left(\frac{2}{3}\right)^n E_0$ and the energy in the electromagnetic shower component is increased by $E_\mathrm{EM} = \left[1 - \left(\frac{2}{3}\right)^n\right] E_0$. After six interaction lengths roughly 90% of the initial energy is transferred into the electromagnetic shower component. The larger the initial energy, the more splittings n take place until the critical energy is reached. Therefore the amount of energy transferred to the electromagnetic shower component increases with increasing initial energy.

Muons are produced mostly by the decay of charged pions and to a smaller extend by kaons (roughly ten times less frequent) [117]. Muons do not interact in the atmosphere or deposit only a small fraction of their energy in the atmosphere. In the extended Heitler model, the number of muons is given by the number of charged pions $N_\mu = n_\mathrm{ch}^n$. Hence, the initial cosmic-ray energy E_0 is given by

$$E_0 = \xi_c^e N_\mathrm{max} + \xi_c^\pi N_\mu \, . \tag{3.1}$$

This formula is still valid in a more realistic modeling of air showers if the critical energy ξ_c^π is interpreted as an effective critical energy that also takes into account the production of muons in other interactions. This formula shows that the cosmic-ray energy can be determined by a measurement of the electromagnetic as well as the muonic shower component. The energy carried away by neutrinos is already taken into account as it is proportional to the number of muons.

Different cosmic-ray nuclei can be described in the superposition model. As the binding energy is only $\sim 5 \, \mathrm{MeV}$ per nucleon [110] and therewith much smaller than the energy of the first interaction,
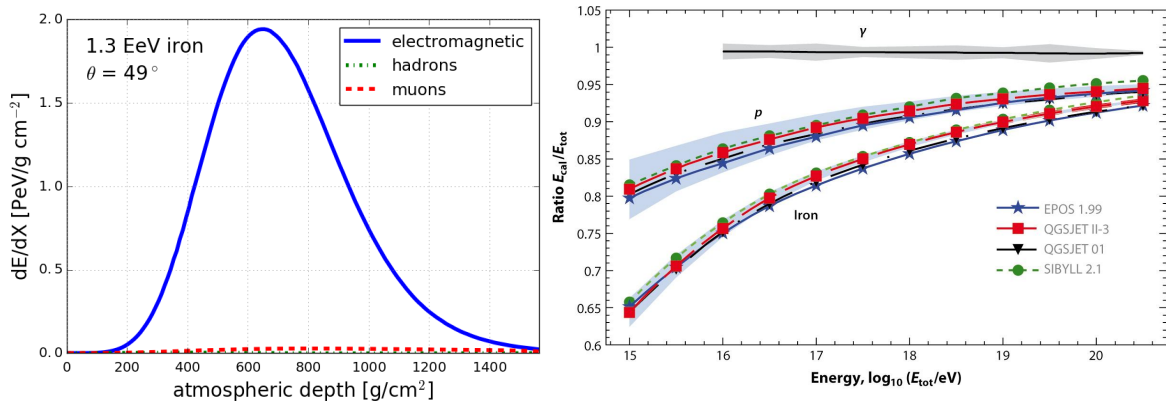
Figure 3.3: (left) Longitudinal profile of the energy deposit dE/dX as a function (slant) atmospheric depth. (right) Fraction of calorimetric energy as a function of the cosmic-ray energy. Figure from [110].

a nucleus with mass number A can be modeled as A independent nucleons with energy $E = E_0/A$. Then it follows from the extended Heitler model that the shower maximum is reached earlier and corresponds to the value of a proton shower with energy E_0/A. Also the energy ending up in the electromagnetic shower component is reduced for heavier nuclei because the fraction of energy in the electromagnetic component decreases with decreasing energy and each nucleus has a reduced energy of E_0/A. Correspondingly, the number of muons is increased for heavier nuclei.

Although these simplified models cannot be used for a quantitative prediction of air showers, the qualitative understanding gained from these models is reproduced in full Monte-Carlo simulations of extensive air showers. Also, these simplified models only describe the average shower development correctly. In nature however, the shower development is subject to stochastic variations. The air-shower development for exactly the same cosmic ray can vary significantly, e.g., the position of the shower maximum for a proton and an iron shower of same energy can happen to be the same. The exact properties of the cosmic rays can therefore not be determined on an event-by-event basis. For this reason the masses or the particle types of the cosmic rays are often referred to as the (chemical) composition of the cosmic rays to stress that the mass of a single cosmic ray cannot be fully determined.

Traditionally, extensive air showers are measured by detecting the particles of the air shower that reach the ground or by observation of interactions of the air-shower particles in the atmosphere. This is done by telescopes that observe the isotropic fluorescence light emitted by molecules that have been excited by the shower particles [2, 4] or by non-imagining air-Cherenkov telescopes that measure the incoherent Cherenkov light produced by the shower particles [5]. The fluorescence method gives a direct measurement of the shower development in the atmosphere as the fluorescence light is proportional to the energy deposit dE/dX of the air shower. A typical longitudinal shower profile is presented in Fig. 3.3 left. Compared to the energy deposit of the electromagnetic shower component, the contributions from the muonic and hadronic components are negligible. Hence, the integral over the dE/dX profile gives the energy in the electromagnetic shower component and can be measured directly with the fluorescence technique. In the literature this energy is also referred to as the *calorimetric* energy whereas the other part of the cosmic-ray energy – carried away by neutrinos and muons – is referred to as the *invisible* energy. The dependence of the calorimetric energy fraction on
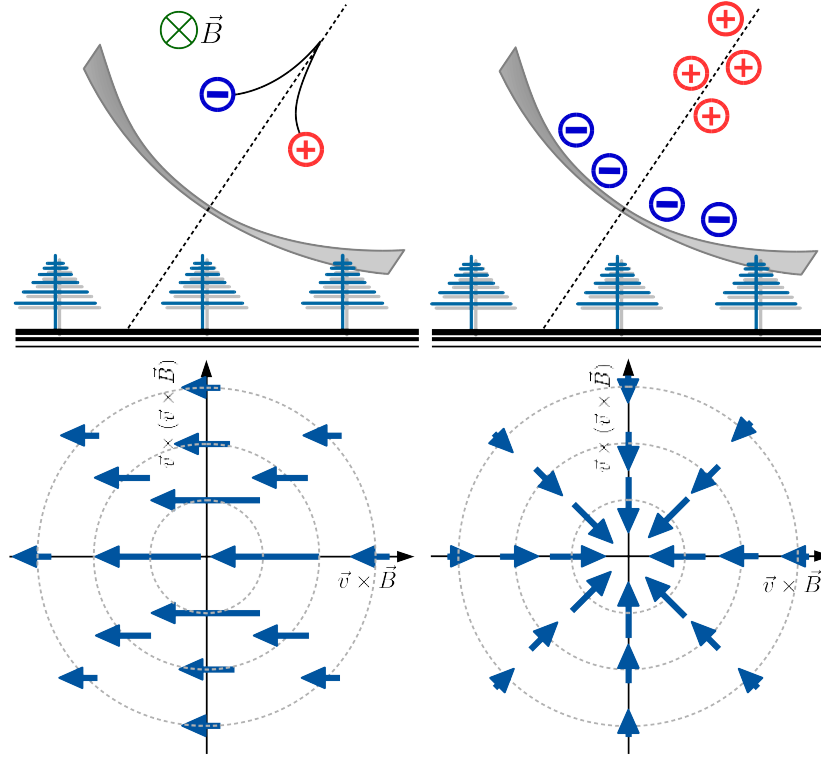
Figure 3.4: Sketch of the two mechanisms of radio emission from air showers. (left) The dominant geomagnetic emission and (right) the sub-dominant charge-excess emission. The lower plot shows the polarization of the radio pulses originating from the two processes. The polarization is shown in a coordinate system in the shower plane where one axis is aligned in the $\vec{v} \times \vec{B}$ direction and the other axis perpendicular to it.

the cosmic-ray energy is shown in Fig. 3.3 right. Muons and neutrinos carry a significant part of the cosmic-ray energy but do not deposit their energy in the atmosphere and reach the ground basically unimpeded.

3.1 Radio emission from extensive air showers

Another independent method to observe air showers is the detection of broadband megahertz (MHz) radio emission which has become an active field of research in recent years [7, 8, 20, 22, 118, 119]. Two emission processes have been identified. The dominant geomagnetic emission arises from the deflection of electrons and positrons in the shower front at the Earth's magnetic field and is polarized along the direction of the Lorentz force ($\propto \vec{v} \times \vec{B}$) that is acting on the charged particles [7, 10, 120, 121]. The field strength of the emission scales with the absolute value of the geomagnetic field $\vec{B}$ and the sine of the angle α between the shower direction $\vec{v}$ and the geomagnetic field. Muons are also deflected in principle, but due to their much lower charge/mass ratio they do not contribute significantly to the radio emission [22].

The second, subdominant emission arises from a time-varying negative charge-excess in the shower front which is polarized radially with respect to the axis of the air shower and is referred to as the *charge-excess* or *Askaryan* effect [12, 122–125]. An illustration of the two emission mechanisms is given in Fig. 3.4.
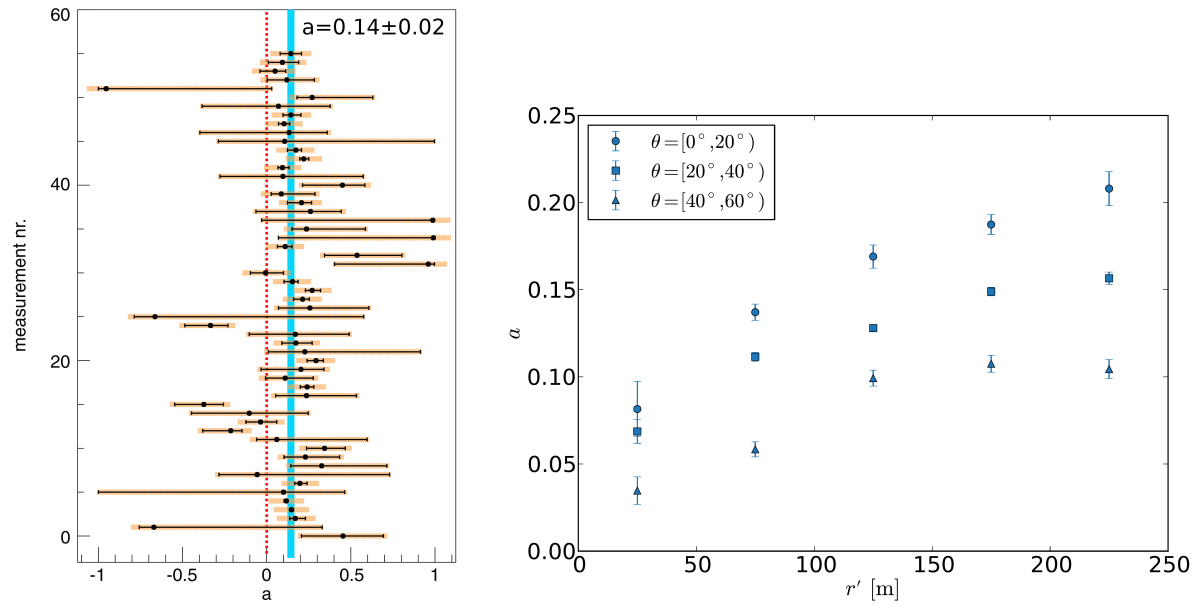
Figure 3.5: Relative strength of the charge-excess fraction a. (left) Measurement at the Pierre Auger Observatory. Multiple measurements at individual radio detector stations are combined to an overall average (blue band). Figure from [12]. (right) Measurement of a at LOFAR. A dependence of a on the zenith angle θ of the incoming air-shower direction and the distance from the observer to the shower axis r' was found. Figure from [125].

In addition to the two emission processes, the refractive index of air has a significant impact on the radio emission. As the refractive index of air is larger than unity, signals emitted at different stages of the shower development arrive at the same time at observers that see the shower under a specific angle, the so-called *Cherenkov angle*. This leads to an increased signal strength on a ring around the shower axis, the *Cherenkov ring*, and leads to coherent emission up to GHz frequencies. As the refractivity is not constant but scales with the air density towards higher altitudes, the ring is smeared out.

Due to coherence effects, the radio emission is strongest below $100\,\mathrm{MHz}$ [126]. At larger frequencies the emission is less coherent resulting in smaller signal strengths. At frequencies well beyond $100\,\mathrm{MHz}$ the emission can be detected only in very specific geometries where observers are at the Cherenkov angle [127].

The relative strength of the charge-excess emission with respect to the geomagnetic emission, normalized to air showers arriving perpendicularly to the geomagnetic field, is defined as

$$a = \sin\alpha\,\frac{|\vec{E}_{\mathrm{ce}}|}{|\vec{E}_{\mathrm{geo}}|}\,, \tag{3.2}$$

where $\vec{E}_{\mathrm{geo}}$ and $\vec{E}_{\mathrm{ce}}$ are the electric-field amplitudes of the geomagnetic and charge-excess emission. The relative charge-excess strength a varies with the absolute value of the geomagnetic field, the incoming direction of the air shower and the distance from an observer to the shower axis and can take values ranging from a few percent up to almost 50% (cf. Sec. 3.3.3). The charge-excess strength can be measured with the polarization of the signal pulse. At the site of the Pierre Auger Observatory, a has been measured to be 0.14 ± 0.02 on average (cf. Fig. 3.5 left and [12]). A more detailed measurement
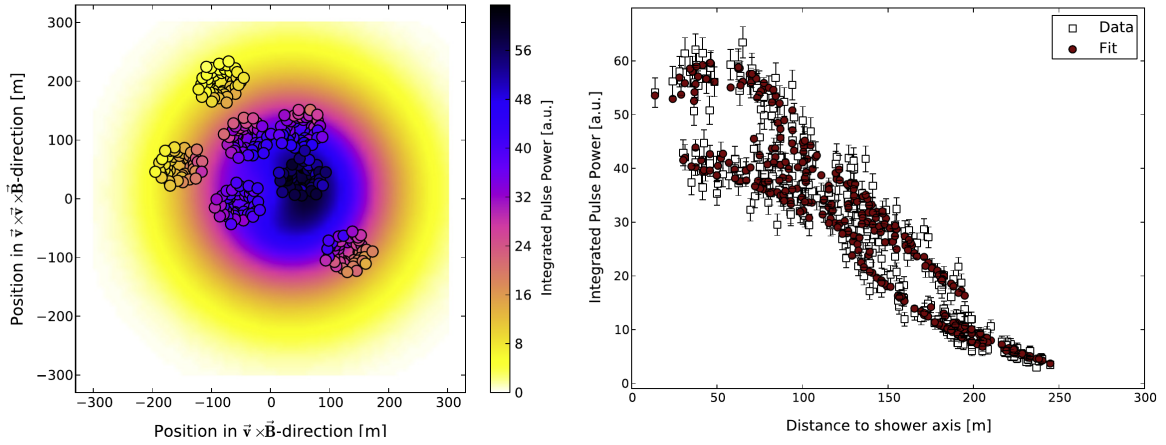
Figure 3.6: Distribution of the radio signal on ground as measured by LOFAR. (left) Two dimensional representation. The color code indicates the signal strength. Each filled colored circle represents the measurement of one antenna of the LOFAR array. The background color map shows the values of the analytic function that is fitted to the data. (right) One dimensional projection of the same data. For the position of each data point (open squares) also the value of the LDF function is shown (filled circles). Figure from [14].

by LOFAR showed that a has a dependence on the zenith angle of the incoming air-shower direction and the distance from the observer to the shower axis (cf. Fig. 3.5 right and [125]). The geomagnetic field strength at LOFAR is roughly two times larger as at the Pierre Auger Observatory. Hence, the geomagnetic emission is expected to be two times stronger and accordingly the charge-excess fraction a is expected to be two times smaller.

As a consequence of the superposition of the two emission mechanisms, the lateral distribution function (LDF) of the electric-field strength has been found to have a radial asymmetry [14, 128–130]. The two-dimensional shape of the LDF is best understood in a coordinate system with one axis perpendicular to the shower direction $\vec{v}$ and Earth's magnetic field $\vec{B}$ (along the Lorentz force $\sim \vec{v} \times \vec{B}$), and the perpendicular axis $\vec{v} \times (\vec{v} \times \vec{B})$. In this coordinate system, as visible from the sketch of Fig. 3.4, the two emission mechanisms interfere destructively left from the shower axis and interfere constructively right from the shower axis. An example of this asymmetric signal distribution is shown in Fig. 3.6. This peanut-like shape can be modeled analytically with an empirical function consisting of two two-dimensional Gaussians [14]. The function has nine free parameters. However, five of them can be fixed using predictions from Monte-Carlo simulations which results in a large practical usability of this parametrization [19, 126], e.g., the amplitude or the integral of the function can be used to determine the cosmic-ray energy and the width of the function depends on the distance to the shower maximum X_{max}.

The shape of the wavefront of the radio pulse is not plane but a hyperbola, i.e., near the shower axis the wavefront has a spherical form and further away from the shower axis it has a conical form [15, 131]. This shape can be understood in a toy model where the signal is emitted at a certain time from a point source that moves at the speed of light in air $c' = c/n$ (n is the refractive index) along the shower axis. The exact shape of the hyperbola depends on the geometry of the air shower. If the emission region is far away, i.e., if the extend of the emission region is small compared to its distance to the observer, the observer sees it basically as a single point and the wavefront takes the simplified form of
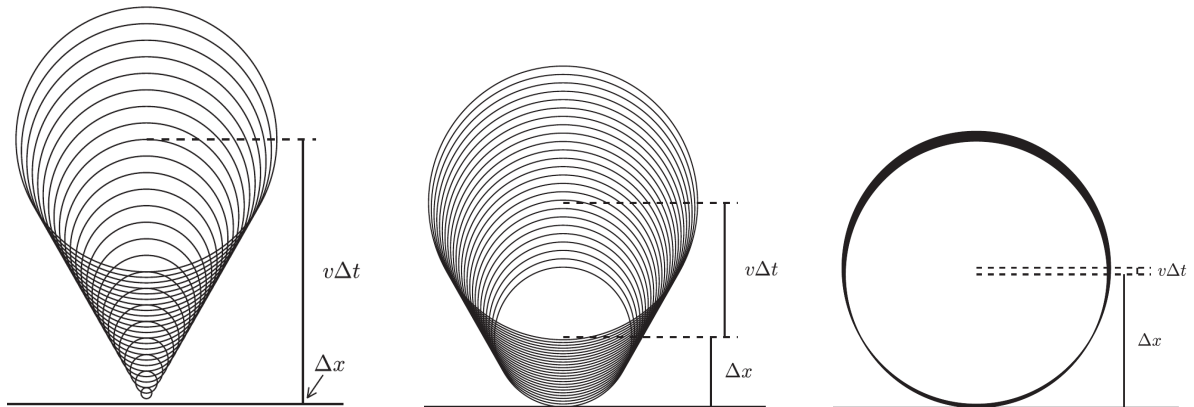
Figure 3.7: Toy model motivating a hyperbolic wavefront shape. Depending on the length of the emission region $v\Delta t$ with respect to the closest distance to the observer Δx, the shape of the wavefront changes from a conical wavefront (left) to a hyperbolic wavefront (center) to a spherical wavefront (right). Figure adapted from [15].

a spherical wave. If, in contrast, the observer is very close to the emission region, the superposition of the spherical waves emitted by the point source that moves with the speed of light leads to a conical wavefront (similar to a supersonic cone). If the observer has an intermediate distance to the emission region, the wavefront takes the form a hyperbola. This behavior is illustrated in Fig. 3.7.

A comparison between different wavefronts with respect to a plane wave is presented in Fig. 3.8. The deviations of the signal arrival times with respect to a plane wave are small and in the order of a few nano seconds. Hence, a corresponding time resolution is mandatory to be able to resolve the wavefront in a measurement. Often a plane wave is sufficient to reconstruct the arrival direction of the air shower. However, detailed measurements showed that the wavefront of the radio pulse is indeed a hyperbola [15, 131]. In addition it was shown that the opening angle of the cone is sensitive to the position of the shower maximum [131] and can thus be used to determine the mass of the primary cosmic ray.

3.2   Simulation of air showers

A simulation of air showers requires modeling of hadronic and electromagnetic interactions as well as a description of the atmosphere (the target material). Detailed models of the atmosphere that are based on measurements exist ([132, 133] and cf. Appendix D). Also electromagnetic showers are well understood and can be modeled, e.g., using the well-tested EGS4 code [134]. The difficult part to model are high-energy hadronic interactions. In principle, hadronic interactions are described by the theory of quantum chromodynamics (QCD). However, it is currently not possible to calculate the bulk of particle productions, as e.g., perturbative methods can only describe processes with large momentum transfer which are of minor importance in air showers [110]. Also cosmic-ray interactions take place at much higher energies (up to 10^{20} eV corresponding to a center-of-mass energy of $\sqrt{s} = 4 \times 10^{14}$ eV) than accessible in accelerators and most of the relevant interactions are in the forward direction which are of minor importance in accelerator experiments [135]. Hence, hadronic interactions are described by phenomenological models which are tuned to accelerator data and are then extrapolated to higher
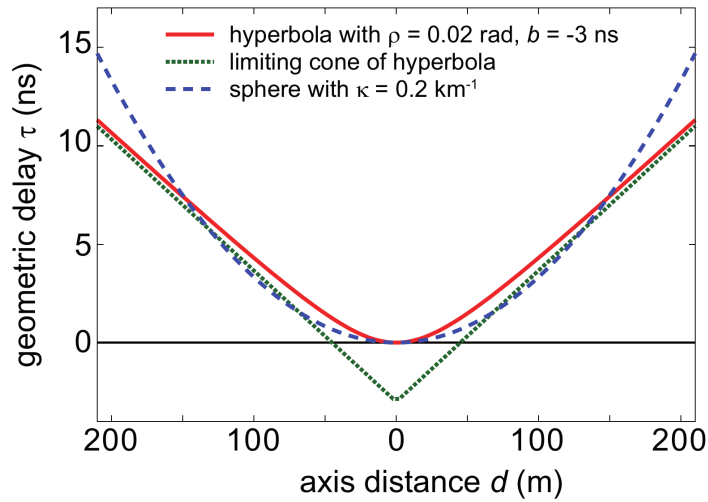
Figure 3.8: Comparison of a spherical, conical and hyperbolic wavefront with respect to a plane wavefront for typical parameters. Figure from [131].

energies.

Several models for high-energy hadronic interactions are available. The most common models used in air-shower simulations are QGSJetII, EPOS and SIBYLL. The newest versions of all three models (QGSJetII-04 [136], EPOS-LHC [76] and SYBILL 2.3 [137]) were already tuned to $7\,\text{TeV}$ LHC data (also $8\,\text{TeV}$ data in case of SIBYLL 2.3). In air-shower simulations these high-energy hadronic interaction models are combined with low-energy models that treat interactions below $\sim 200\,\text{GeV}$. Commonly used models are FLUKA [138] and UrQMD [139].

Air showers are simulated using the Monte-Carlo technique to properly take into account the stochastic nature of the underlying physics. Two full Monte-Carlo simulation codes are available: CORSIKA [140] and AIRES [141]. In these codes, in principle all shower particles are tracked through the atmosphere and their interactions and decays are simulated. As the number of particles is proportional to the initial cosmic-ray energy and for an $10^{20}\,\text{eV}$ proton shower the number of shower particles exceeds 10^{11}, the tracking of each individual particle is computationally not feasible. Therefore, a thinning technique is implemented that combines several particles with same properties to one particle with a higher weight. The exact implementation of the thinning technique differs in the two codes. AIRES uses an extension of the original thinning algorithm introduced by Hillas [142] to reduce statistical weight fluctuations [141] whereas CORSIKA uses a thinning with optimized weight limitation [143]. Currently, the CORSIKA code is better maintained and offers more flexibility. It is constantly improved, features parallel computing through MPI and can interface all hadronic interaction models presented above. Nevertheless, it is a strong advantage that two completely independent Monte-Carlo codes exist as, e.g., a correct implementation can be cross-checked.

3.2.1 Simulation of radio emission from air showers

Two approaches exist to simulate the radio emission from extensive air showers. The first category are macroscopic models. The advantages of these models are that they provide direct insights into the underlying physics, are mostly analytic and require only small computational effort. In the past,

macroscopic models have significantly contributed to the understanding of the radio emission from air shower [144–146]. From the air-shower simulations, macroscopic quantities such as electrical currents in the atmosphere are calculated. These quantities then correspond to a certain emission mechanism. E.g., transverse drift currents are modeled that result from an acceleration in the geomagnetic field and deceleration due to interactions with air molecules. These currents vary in time with the air shower evolution and the radio emission results from the time derivative of the transverse currents. Also the time-varying charge excess is modeled and the resulting radiation is calculated. The disadvantage of macroscopic models is that every physical process needs to be modeled explicitly. However, it is not always possible to clearly separate the different effects under realistic conditions which might result in double counting as well as some processes might be neglected in the modeling. The model has also free parameters (e.g. the transverse drift velocity) that need to be tuned and have significant impact on the resulting electric-field amplitudes. The most widely known code is MGMR [144] and its successor EVA [147, 148]. A more comprehensive description of macroscopic models can be found in [22].

The other category are microscopic models. Here, each air-shower particle is tracked and its radiation is calculated from first-principles following the outcome of classical electrodynamics that radiation comes from accelerated charges [149]. Then, the radiation from all shower particles is superimposed and results in the macroscopically observed radio pulse. The starting point for the microscopic calculation are the Liénard-Wiechert potentials that follow directly from Maxwell's equations

$$\phi(\vec{x}, t) = \left[\frac{e}{(1 - n\vec{\beta} \cdot \hat{r})R} \right]_{\text{ret}}, \quad \vec{A}(\vec{x}, t) = \left[\frac{e\vec{\beta}}{(1 - n\vec{\beta} \cdot \hat{r})R} \right]_{\text{ret}}, \qquad (3.3)$$

where R is the distance from the point of emission to an observer, $\hat{r}$ is the unit vector into the direction of the observer, $\vec{\beta}$ is the velocity of the particle in units of the speed of light c and n is the refractive index of the medium [150]. The subscript "ret" denotes that the equation needs to be evaluated at the retarded time $t' = t - nR/c$. Two different formalisms exist to calculate the resulting electric field from the particle motion: the ZHS [151, 152] and the endpoint [150] formalism. It was shown that the two formalisms are mathematically equivalent [153, 154].

In the ZHS formalism the particle motion is subdivided into straight track segments described by their start and stop time, velocity and starting point. Then with Eq. (3.3), the scalar and vector potentials ϕ and $\vec{A}$ arising from the distribution of charges can be calculated and from this the resulting electric field. This formalism was implemented directly into the AIRES air-shower simulation code and is know as ZHAireS [130]. The ZHS formalism was originally developed for calculating the radiation from showers in ice and uses the Fraunhofer approximation, where the track length needs to be small with respect to both the wavelength and the distance from the track to the observer. In dense media (such as ice) this condition is automatically fulfilled but in air showers, the shower size is similar to the distance to the observer. Hence, the typical track lengths used in the air-shower simulation are too large and the tracks need to be subdivided further [130, 155].

In the endpoint formalism, the radiation arising from the motion of each charge is calculated directly from the Liénard-Wiechert potentials. From Eq. (3.3) follows that the electric field of a single

charge q is given by [150]

$$\vec{E}(\vec{x}, t) = q \left[\frac{\hat{r} - n\vec{\beta}}{\gamma^2 (1 - n\vec{\beta} \cdot \hat{r})^3 R^2} \right]_{\text{ret}} + \frac{q}{c} \left[\frac{\hat{r} \times [(\hat{r} - n\vec{\beta}) \times \dot{\vec{\beta}}]}{(1 - n\vec{\beta} \cdot \hat{r})^3 R} \right]_{\text{ret}}, \qquad (3.4)$$

where $\dot{\vec{\beta}}$ is the time derivative of $\vec{\beta}$ and γ the relativistic gamma factor. The first term is the near-field term as it decreases with $1/R^2$. It gives only a minor correction to the radiation term (the second term) and is neglected in this formalism. The particle motion is subdivided into straight track segments and the radiation is calculated from the instantaneous acceleration of a charge at the beginning and the end of each track. The radiation coming from the track is thus the superposition of the radiation originating from the creation and the destruction of the charge. The radiation from a moving charge is then given by the sum of the radiation from each "endpoint" and the radio pulse at a specific observer location is given by the superposition of the radiation from all tracks. This formalism is directly implemented into the CORSIKA code and known as CoREAS [156]. A downside of the endpoint formalism is that it breaks down for an observer near the Cherenkov cone and a fallback to a ZHS-like calculation becomes necessary. On the other hand, no approximation is made that requires particular small track segments so that the tracks defined by CORSIKA can be directly used which gives a potential improvement in computation speed compared to ZHAireS.

As shown in [150], the endpoint formalism correctly reproduces classical radiating systems such as synchrotron, Cherenkov or transition radiation which demonstrates that the origin of the radiation is indeed the acceleration of charges. In contrast, the classical named radiation processes are not fundamental mechanisms but correspond to specific types of particle acceleration.

The microscopic calculation of the radio emission is computationally expensive. For each observer position the calculation needs to be performed separately (the Liénard-Wiechert potentials depend on the vector $\hat{r}$ between observer and the moving charge). Under realistic conditions the computing time that is needed to calculate the radio emission at $\sim$20 observer positions is already as large as the time needed to simulate the complete air shower.

The advantage of a microscopic calculation is that the calculation does not have any free parameters. It is purely based on classical electrodynamics. Uncertainties in the simulation of the radio emission arises only from approximations made in the simulation to speed up the computation or from the simulation of the air shower itself (mainly uncertainties in hadronic interactions) or the modeling of the atmosphere. Hence, we can use the microscopic models for an quantitative prediction of the radio emission from extensive air showers.

Experimental validation of radio-emission simulation codes

The first and only experiment so far that probes the calculation of radio emission used in air-shower simulations in a controlled laboratory environment is the SLAC T-510 experiment [157]. It was performed at the Stanford linear collider. Two bunches of electrons with energies of $\sim$4.5 GeV are shot onto a plastic target generating compact showers with an energy that correspond to a $\sim$4 × 10^{18} eV cosmic ray (see Fig. 3.9 for a sketch of the experiment). The plastic target is exposed to a homogeneous magnetic field of 1000 G oriented perpendicular to the electron beam direction. The strength
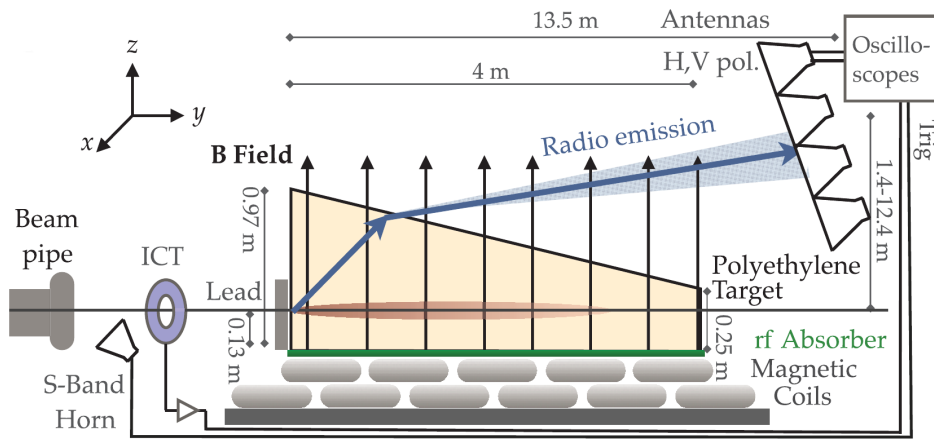
Figure 3.9: Sketch of the SLAC T-510 experiment. Not to scale. Figure from [157].
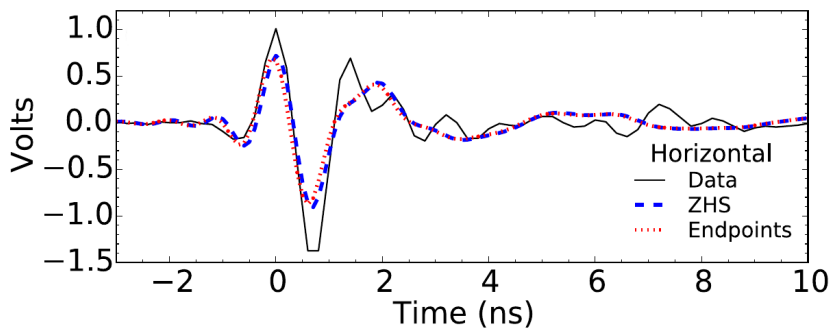
Figure 3.10: Simulated and measured voltage trace of the horizontally polarized channel of the antenna in the SLAC T-510 experiment. Figure from [157].

of the magnetic field is adjusted to the density of the plastic target to have the same proportion as in air showers. Hence, the dimensions of an extensive air shower are basically scaled down to fit into a controlled laboratory environment.

As in the case of air showers, radio emission is generated by the interaction of the shower with the magnetic field and a time-varying negative charge excess in the shower front. Due to the smaller dimensions, the frequencies of coherent emission are shifted upwards. Four dual-polarized horn antennas that are sensitive between 200 - 1200 MHz and used in the ANITA experiment [158] record the radio emission. This bandwidth translates to approximately 10 - 60 MHz in air showers.

The measured radio emission is compared to the predicted radiation from the simulation codes. The showers are simulated using Geant4 and include a detailed modeling of the target material and the magnetic field. The radio emission is then calculated from the shower particles using both the ZHS and endpoint formalism. One of the measured radio pulses together with the predictions from the two models is shown in Fig. 3.10. The two predictions agree to high precision and are compatible to the measurement within the systematic uncertainties of ∼35% of the experiment. This measurement is the first direct experimental evidence for the accuracy in the prediction of the radio emission by microscopic models, although the systematic uncertainty of the experiment is too large to draw strict constrains on the accuracy of the models.

3.3 Simulation of radiation energy release

As air showers are traditionally measured using fluorescence telescopes, the shower development and the energy deposit resulting in the emission of fluorescence light have been studied extensively [159]. This is not true for the radio emission from air showers. Although processes producing radio emission are well understood by now, a detailed study of how much radiation is emitted at which stage of the shower development has not been presented yet. This longitudinal shower development with respect to the radio emission will be studied in this section.

The total amount of radio emission emitted by an air shower can be quantified using the concept of radiation energy [126, 160, 161], which is the energy emitted by the air shower in the form of radio waves. In most experimental setups, the "golden" frequency band between 30 - 80 MHz is used [126]. Below 30 MHz atmospheric noise and short-wave band transmitters make measurements unfeasible and above 80 MHz the FM band interferes. Also, owing to coherence effects, the radio emission from air showers is strongest below 100 MHz. Hence, in our analysis we will concentrate on this frequency band.

In an experiment, the radiation energy can be determined by interpolating and integrating the measured energy fluence on the ground (cf. Chap. 6 or [126, 160, 161]). As soon as the air shower has emitted all radio emission at the end of the shower development, the radiation energy measured at increasing atmospheric depths remains constant because the atmosphere is essentially transparent for radio emission. In particular, the radiation energy is independent of the signal distribution on the ground that changes drastically with incoming direction of the air shower or the altitude of the observation.

In the first part of this section we will determine the "longitudinal profile of the radiation energy release", i.e., how much radiation energy is emitted at what stage of the shower development. In the second part we will determine the fundamental relation between the radiation energy and the energy in the electromagnetic part of the air shower and study second order dependencies.

3.3.1 Model

In this section we develop a mathematical model to extract the radiation energy from air-shower simulations in an efficient manner and describe the setup of the simulations.

The three-dimensional electric-field vector $\vec{E}$ of the cosmic-ray-induced radio signal can be reduced to two dimensions, because the component in the direction of propagation can be assumed to be zero with great accuracy, as an electromagnetic wave is only polarized in the plane perpendicular to its direction of propagation. This plane is usually referred to as the shower plane. An advantageous choice to align the axes in the shower plane is to align one axis with the $\vec{v} \times \vec{B}$ direction, i.e., the direction perpendicular to the shower axis $\vec{v}$ and the geomagnetic field $\vec{B}$. The other axis is then aligned with the $\vec{v} \times (\vec{v} \times \vec{B})$ direction to get an orthogonal coordinate system.

The energy fluence f, i.e., the energy deposit per area, is the time-integral over the Poynting flux of the radio pulse and is calculated using the formula

$$f = f_{\vec{v} \times \vec{B}} + f_{\vec{v} \times (\vec{v} \times \vec{B})} \tag{3.5}$$

with the two components

$$f_{\vec{v}\times\vec{B}}(\vec{r}) = \varepsilon_0 c \Delta t \sum_i E^2_{\vec{v}\times\vec{B}}(\vec{r}, t_i) \tag{3.6}$$

$$f_{\vec{v}\times(\vec{v}\times\vec{B})}(\vec{r}) = \varepsilon_0 c \Delta t \sum_i E^2_{\vec{v}\times(\vec{v}\times\vec{B})}(\vec{r}, t_i)\,, \tag{3.7}$$

where ε_0 is the vacuum permittivity, c is the speed of light in vacuum and Δt is the sampling interval of the electric field $\vec{E}(\vec{r}, t)$ which depends on the position $\vec{r}$ and time t and is broken down into its components $E_{\vec{v}\times\vec{B}}$ and $E_{\vec{v}\times(\vec{v}\times\vec{B})}$.

The components $f_{\vec{v}\times\vec{B}}$ and $f_{\vec{v}\times(\vec{v}\times\vec{B})}$ can be further divided into a part originating from the geomagnetic and a part originating from the charge-excess emission processes. The geomagnetic component is polarized in the direction of the Lorentz force that is acting on the shower particles, i.e., in the $\vec{v} \times \vec{B}$ direction, and is thus only present in the $E_{\vec{v}\times\vec{B}}$ component of the electric field [144]. The contribution of the charge-excess emission to the electric field is radially polarized towards the shower axis. Therefore, its contribution to $E_{\vec{v}\times\vec{B}}$ and $E_{\vec{v}\times(\vec{v}\times\vec{B})}$ depends on the detector position relative to the shower axis [162] which can be expressed by the angle ϕ as defined in Fig. 3.11. The electric-field components can hence be written as

$$E_{\vec{v}\times\vec{B}}(\vec{r}, t) = E_{\mathrm{geo}}(\vec{r}, t) + \cos\phi\, E_{\mathrm{ce}}(\vec{r}, t) \tag{3.8}$$

$$E_{\vec{v}\times(\vec{v}\times\vec{B})}(\vec{r}, t) = \sin\phi\, E_{\mathrm{ce}}(\vec{r}, t)\,, \tag{3.9}$$

where E_{geo} (E_{ce}) is the modulus of the electric field resulting from the geomagnetic (charge-excess) emission.

We define f_{geo} and f_{ce} as the energy fluence calculated from E_{geo} and E_{ce}. From the definition of the energy fluence (Eq. (3.6)+(3.7)) it follows that

$$f_{\vec{v}\times(\vec{v}\times\vec{B})}(\vec{r}) = \sin^2\phi\, f_{\mathrm{ce}}(\vec{r}) \tag{3.10}$$

and after some lines of calculations it follows that

$$f_{\vec{v}\times\vec{B}}(\vec{r}) = \left(\sqrt{f_{\mathrm{geo}}(\vec{r})} + \cos\phi\,\sqrt{f_{\mathrm{ce}}(\vec{r})}\right)^2 \tag{3.11}$$

if the geomagnetic and charge-excess components are "in phase", i.e., $E_{\mathrm{geo}}(\vec{r}, t) = k(\vec{r})\, E_{\mathrm{ce}}(\vec{r}, t)$ for some $k \in \mathbb{R}$. Within the precision necessary for this work, this assumption is indeed valid. This approximation results in bias of 1% resulting in an overestimation of $f_{\vec{v}\times\vec{B}}(\vec{r})$ of 1%, and is discussed in Appendix A.1.

Calculation of radiation energy

The energy fluence f changes with the position in the shower plane which we denote in polar coordinates (r, ϕ) relative to the shower axis. The radiation energy, i.e., the complete energy contained in

the radio signal at a given height above ground, is calculated with the formula

$$E_{\text{rad}} = \int\limits_0^{2\pi} \mathrm{d}\phi \int\limits_0^{\infty} \mathrm{d}r\, r\, f(r, \phi)\,. \tag{3.12}$$

Exploiting the radial symmetry of the geomagnetic and charge-excess lateral distribution functions (LDFs), Eq. (3.12) can be rewritten as

$$E_{\text{rad}} = \int\limits_0^{2\pi} \mathrm{d}\phi \int\limits_0^{\infty} \mathrm{d}r\, r\, \left[\left(\sqrt{f_{\text{geo}}(r)} + \cos\phi\, \sqrt{f_{\text{ce}}(r)} \right)^2 + \sin^2\phi\, f_{\text{ce}}(r) \right] \tag{3.13}$$

$$= \int\limits_0^{2\pi} \mathrm{d}\phi \int\limits_0^{\infty} \mathrm{d}r\, r\, \left(f_{\text{geo}}(r) + f_{\text{ce}}(r) + 2\cos\phi \sqrt{f_{\text{geo}}(r)\, f_{\text{ce}}(r)} \right) \tag{3.14}$$

$$= 2\pi \int\limits_0^{\infty} \mathrm{d}r\, r\, \left(f_{\text{geo}}(r) + f_{\text{ce}}(r) \right) \tag{3.15}$$

$$= 2\pi \int\limits_0^{\infty} \mathrm{d}r\, r\, \left(f_{\vec{v} \times \vec{B}}(r, \phi = 90°) + f_{\vec{v} \times (\vec{v} \times \vec{B})}(r, \phi = 90°) \right) \tag{3.16}$$

$$= 2\pi \int\limits_0^{\infty} \mathrm{d}r\, r\, f(r, \phi = 90°) \tag{3.17}$$

The validity of assuming radial symmetry of the geomagnetic and charge-excess LDFs is shown in Appendix A.2 and additional effects of the air refractivity on the symmetry of the footprint are discussed in Sec. 3.3.2.

This result has a direct impact on how the radiation energy can be determined in Monte Carlo simulations of extensive air showers and their radio emission. Instead of simulating the radio emission at numerous positions to sample the full two-dimensional emission pattern, it is sufficient to simulate the radio signal at positions along the positive $\vec{v} \times (\vec{v} \times \vec{B})$ axis, i.e., for $\phi = 90°$. This significantly reduces the simulation time compared to the star-shaped pattern [17] (cf. Fig. 3.11).

We note that the component of the electric field parallel to the shower direction is not exactly zero as the radio shower front shows a slight deviation from a plane wave [15, 131]. Hence, also $f_{\vec{v}}$ is not exactly zero but is significantly smaller than $f_{\vec{v} \times \vec{B}}$ and $f_{\vec{v} \times (\vec{v} \times \vec{B})}$. However, to exclude any potential additional uncertainty we determine f of Eq. (3.17) as $f = f_{\vec{v} \times \vec{B}} + f_{\vec{v} \times (\vec{v} \times \vec{B})} + f_{\vec{v}}$.

Another benefit of this method is that along the $\vec{v} \times (\vec{v} \times \vec{B})$ axis the geomagnetic and charge-excess contributions to the energy fluence separate ($f_{\vec{v} \times \vec{B}} = f_{\text{geo}}$ and $f_{\vec{v} \times (\vec{v} \times \vec{B})} = f_{\text{ce}}$) and can consequently be analyzed separately. In addition, the energy fluence at any position in the shower plane can be calculated from the geomagnetic and charge-excess LDFs according to Eq. (3.10) and (3.11). This approximation is similar to the approach presented in [163], but does away with the necessity of simulating the air shower a second time without a geomagnetic field to disentangle the geomagnetic and charge-excess components.
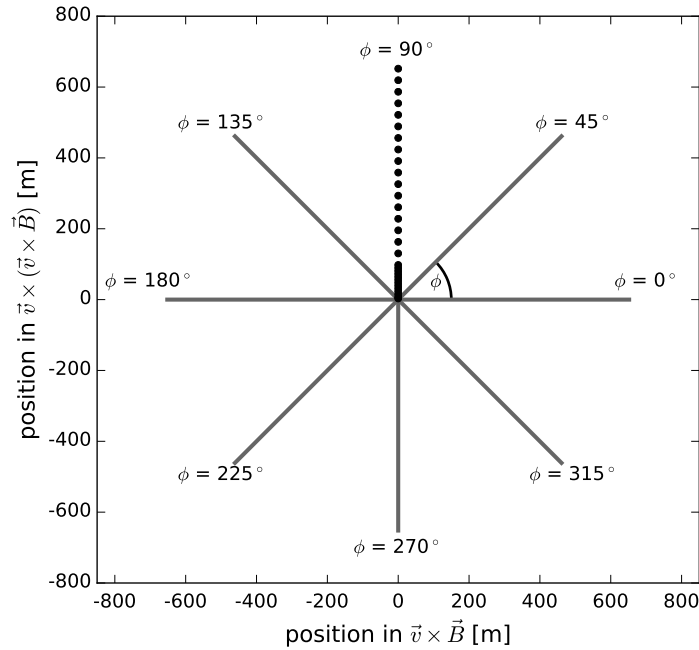
Figure 3.11: Sketch of the simulated observer positions. Each circle represents a simulated observer position. The observer spacing is denser near the shower axis to correctly sample the larger variations in signal strength near the shower axis.

Simulation setup

We use the CORSIKA 7.4005 code [140] to simulate extensive air showers with hadronic interaction models QGSJetII.04 [136] and FLUKA 2011.2c [138], and the CoREAS [156] extension to calculate the radio emission. Thinning is applied at a level of 10^{-6} with optimized weight limitation [143].

We use the model of the US standard atmosphere and set the geomagnetic field to an inclination of -35.7° with an absolute field strength of 0.243 Gauss. This corresponds to the geomagnetic field at the AERA detector [118] of the Pierre Auger Observatory [2]. The influence of a different geomagnetic field as present at the LOFAR [119] or the Tunka [20] detector will be discussed in Sec. 3.3.4. The refractivity of the atmosphere is set to $n - 1 = 2.92 \times 10^{-4}$ at sea level and is scaled proportionally to higher altitudes by means of air density.

We simulate the radio emission at 30 observer positions along the positive $\vec{v} \times (\vec{v} \times \vec{B})$ axis. The observer spacing is denser near the shower axis to improve sampling in this region with larger variations in signal strength (see Fig. 3.11)[2]. According to Eq. (3.17) we calculate the radiation energy by numerical integration of the energy fluence using the composite trapezoidal rule. Using a toy Monte Carlo we checked that the uncertainty due to the numerical integration is well below 1%.

As the footprint of the radio emission becomes larger with increasing distance to the emission region we dynamically adjust the maximum distance of a simulated observer position to the shower axis[3]. All observers are placed in the shower plane, i.e., depending on the incoming direction of the air

---

[2]The first station is placed at 0.5% of the maximum distance d_{max}, the next 12 stations are placed equidistantly until 15% of d_{max} and the remaining 17 stations are again placed equidistantly until d_{max}.

[3]The maximum distance of an antenna to the shower axis range from $100\,m$ at an observation height that corresponds to a slant depth of $100\,g/cm^2$ to almost $3\,km$ at an observation height that corresponds to a slant depth of $5800\,g/cm^2$.

shower and their distance from the shower axis, the observer positions have a different height above ground. In the following, we refer to the height of the observer at the shower axis as the height above ground h or, alternatively, by specifying the atmospheric depth X.

Simulated data set

The simulated data set comprises 592 air showers. The primary energy is distributed randomly between 10^{17} eV and 10^{19} eV according to a uniform distribution of the logarithm of the energy. The zenith angle θ is distributed uniformly between $0°$ and $80°$ and the azimuth angle is distributed uniformly between $0°$ and $360°$. For each combination of primary energy and shower direction, one simulation with a proton primary and one simulation with an iron primary is performed.

In air-shower experiments, the zenith angle distribution typically follows a $\sin\theta\cos\theta$ distribution. The term $\sin\theta$ arises from the increasing solid angle for larger zenith angles and $\cos\theta$ arises because the projected area becomes smaller and radio detectors are typically triggered by particle detectors. We therefore reweight our data set in all fits and histograms to match such a zenith angle distribution.

An important quantity for the analysis presented in the following sections is the sine of the angle α between the shower axis and the magnetic-field axis. For the geomagnetic field at the Pierre-Auger site and a zenith angle distribution following $\sin\theta\cos\theta$, the $\sin\alpha$ distribution peaks at large values of $\sin\alpha$. A fraction of 45% of the events has a value of $\sin\alpha$ larger than 0.9 and more than 97% of the events have a value of $\sin\alpha$ larger than 0.2. Also for other configurations of the geomagnetic field, the number of events with low values of $\sin\alpha$ is small. If we set the geomagnetic field to the configuration at the LOFAR [119] or the Tunka [20] detector, still 96% of the events have a value of $\sin\alpha$ larger than 0.2. In addition, the radiation energy of the dominant geomagnetic emission component is proportional to $\sin^2\alpha$. Therefore, the number of events with a small value of $\sin\alpha$ that can be measured in an experiment is even smaller than the above estimation, which is based solely on geometry. Hence, the practical relevance of air showers with small $\sin\alpha$ is generally small.

3.3.2 Longitudinal profile of radiation energy release

In this section it is determined how much radiation energy is released at what stage of the shower development. In contrast to the energy deposit of shower particles, the radiation energy cannot be accessed for different atmospheric depths in the standard output of the CoREAS simulation. As the radio pulse observed at a specific point in space is the result of constructive and destructive interference of all charged shower particles it is different at each position. Hence, it needs to be calculated separately for each observer position so that the computing time scales linearly with the number of observers.

To obtain the radiation energy, we simulate an air shower with observers at different atmospheric depths. Fig. 3.12 shows the lateral distribution of the energy fluence f on the positive $\vec{v}\times(\vec{v}\times\vec{B})$ axis for six different atmospheric depths. The second simulated height at $X = 700$ g/cm^2 (Fig. 3.12b) is very close to the shower maximum $X_{\max}$ of 715 g/cm^2. (Throughout the paper we use $X_{\max}$ to refer to the maximum of the longitudinal profile of the energy deposit $\mathrm{d}E/\mathrm{d}X$ of the electromagnetic part of the air shower.) At the beginning of the shower development, the energy fluence is concentrated around the shower axis and becomes broader for observers at lower altitudes. The largest energy fluence is seen by an observer at the height of the shower maximum $X_{\max}$. From this height onwards,

the total radiation energy continues to increase, but is distributed over a larger area resulting in smaller values of the energy fluence.

From an atmospheric depth of $X = 1000\,\text{g/cm}^2$ onwards, the radiation energy basically remains the same whereas the signal distribution becomes increasingly broader. It even occurs that the energy fluence f first increases with an increasing distance from the shower axis before it decreases again. This behavior can be explained by Cherenkov-like effects. The refractivity of the atmosphere is not unity, but has a typical value of $n - 1 = 2.92 \times 10^{-4}$ at sea level and scales proportionally with air density. For an observer at the Cherenkov angle, all radiation emitted along the shower axis arrives simultaneously at the observer. This leads to additional coherence effects which results in a larger energy fluence at this specific distance from the shower axis.

To demonstrate the strength of this effect, we resimulated the air shower shown in Fig. 3.12 with a constant refractive index of $n = 1$ in the complete atmosphere and show the resulting energy fluence as a dashed line in Fig. 3.12. The shower development is exactly the same as in the case of realistic modeling of the refractivity. Without Cherenkov-like effects, the energy fluence falls off monotonically with increasing distance to the shower axis and also the resulting radiation energy is significantly lower (cf. Fig. 3.12).

Using this approach we can investigate the radiation energy and its development with increasing atmospheric depth which is shown in Fig. 3.13. The lower part of the figure shows the total radiation energy at a given atmospheric depth, whereas the upper plot shows the radiation energy release per atmospheric depth which is calculated via

$$\frac{\text{d}E_{\text{rad}}}{\text{d}X}\left(\frac{X_i + X_{i+i}}{2}\right) = \frac{E_{\text{rad}}(X_{i+1}) - E_{\text{rad}}(X_i)}{X_{i+1} - X_i}, \tag{3.18}$$

where X_i is the ith simulated height of the observer. In this example the uncertainty of the radiation energy release per atmospheric depth is relatively large, because the difference in radiation energy between two succeeding simulated atmospheric depths is small compared to the uncertainty of E_{rad}. Therefore, we show the running average of $\frac{\text{d}E_{\text{rad}}}{\text{d}X}$ of five surrounding atmospheric depth bins as black diamonds and the unsmoothed values as gray diamonds.

In the upper figure we compare the radiation energy release per atmospheric depth, which we will hereafter refer to as the "longitudinal profile of the radiation energy release", with the longitudinal profile of the energy deposit of the electromagnetic cascade of the air shower. The profile of the radiation energy release starts with a delay, but reaches its maximum before the maximum of the energy deposit. Thereafter it decreases faster than the energy deposit by the particle shower.

We note that the radiation energy release $\text{d}E_{\text{rad}}/\text{d}X$ is conceptually different from the energy deposit of the electromagnetic shower component $\text{d}E/\text{d}X$. The shower particles are absorbed by the atmosphere and deposit their energy in the atmosphere. In contrast, the radiation energy is released in the atmosphere and propagates freely as the atmosphere is transparent for radio emission.
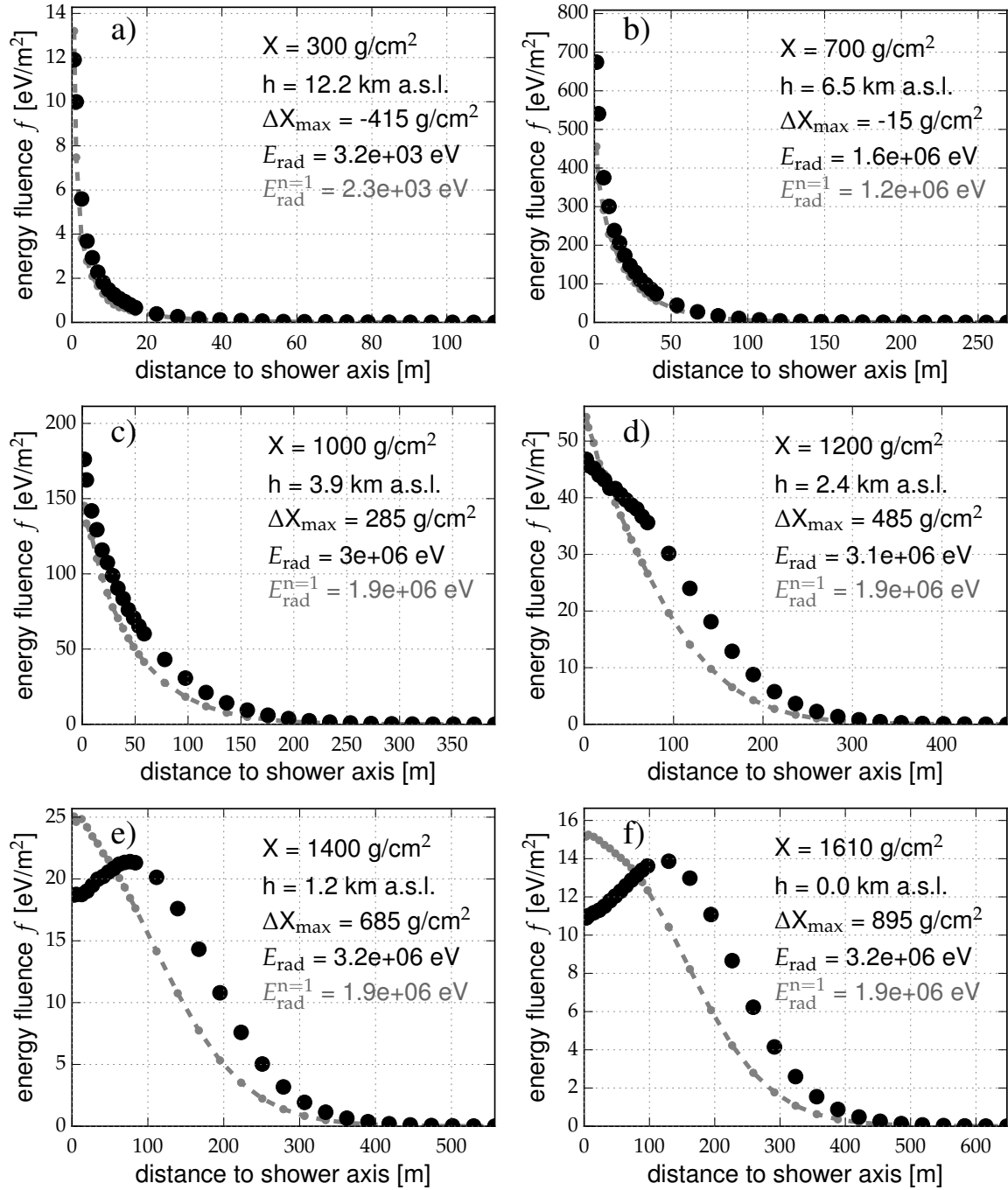
Figure 3.12: The black circles show the energy fluence in the 30 - 80 MHz band along the positive $\vec{v} \times (\vec{v} \times \vec{B})$ axis at different atmospheric depths X for a proton-induced air shower with an energy of 0.5 EeV and a zenith angle of 50° which is coming from the south. The dashed gray line shows the energy fluence in case of constant refractivity in the complete atmosphere for the exact same air shower. Please note the different horizontal and vertical axis scales.
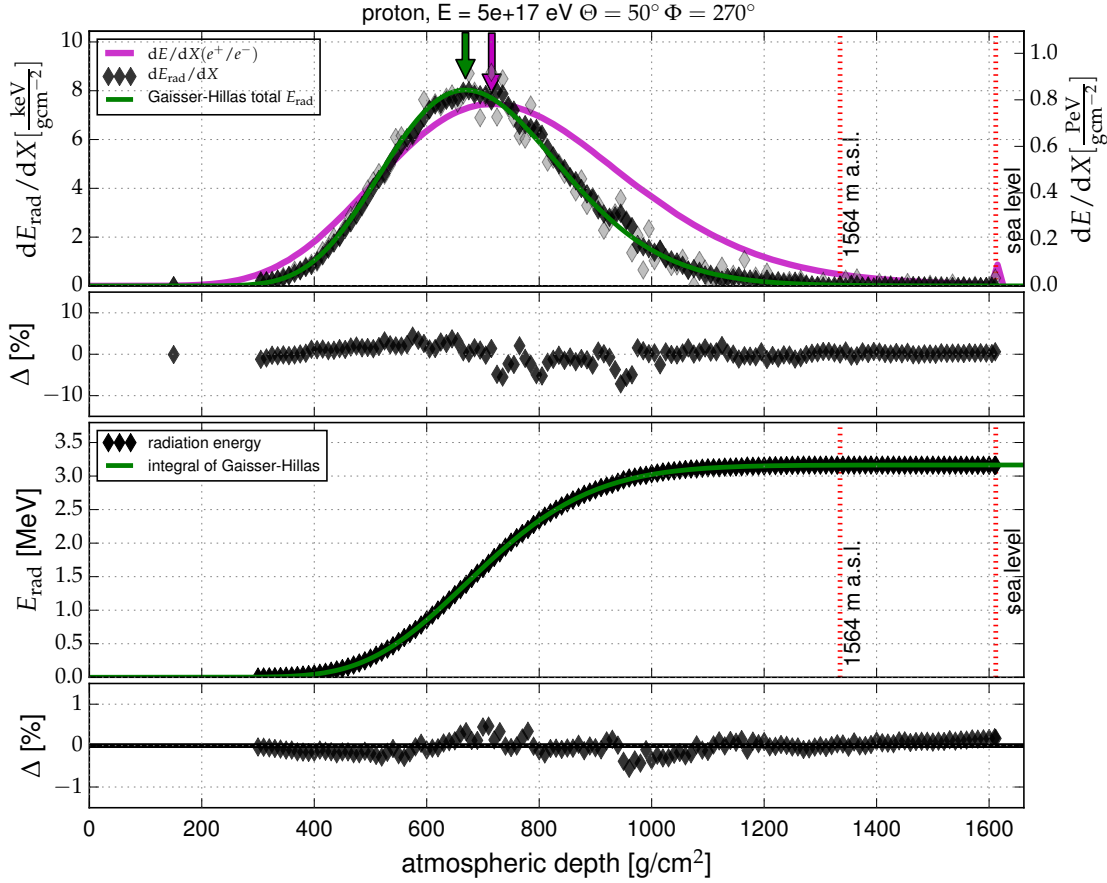
Figure 3.13: Longitudinal profile of the radiation energy release of the same air shower as shown in Fig. 3.12. The lower diagram plots the total radiation energy measured at a given atmospheric depth. The green line demonstrates a fit of the integral of a Gaisser-Hillas function to the radiation energy. The residuals are also shown. The upper diagram plots the same data and fit, but as radiation energy release at a given atmospheric depth. Also shown is the energy deposit of the electromagnetic shower particles as a purple line that needs to be read on the right vertical axis. The bump at ∼1600 g/cm² comes from shower particles that deposit their energy in the ground. The vertical lines indicate the atmospheric depth that corresponds to the height of the radio detector of the Pierre Auger Observatory and sea level (height of the LOFAR detector) for the simulated geometry. The arrows indicate the position of the shower maximum. See text for details.

Fit of Gaisser-Hillas function

The longitudinal profile of the radiation energy release can be described well with a Gaisser-Hillas function [164] in the version with three parameters.

$$\frac{\mathrm{d}E_{\mathrm{rad}}}{\mathrm{d}X}(X) = A \left(\frac{X}{X_{\max}^{\mathrm{rad}}} \right)^{\frac{X_{\max}^{\mathrm{rad}}}{\lambda}} \exp\left(\frac{X_{\max}^{\mathrm{rad}} - X}{\lambda} \right), \tag{3.19}$$

where A, $X_{\max}^{\mathrm{rad}}$, and λ are the free parameters. The integral of Eq. (3.19) over X gives the total radiation energy, which is the primary objective of this paper. Therefore, we fit the integral of the Gaisser-Hillas function to the total radiation energy measured at a given atmospheric depth (lower panel of Fig. 3.13), which we found to result in a more precise determination of the radiation energy.

With this approach we can even determine the full radiation energy in cases where the air shower hits the ground before all radiation energy has been emitted. We note that no analytic form of the integral of the Gaisser-Hillas function exists. The integration is therefore performed numerically.

Except for the example shown in Fig. 3.13, we simulate 5 - 7 different observation heights per air shower which is sufficient to constrain the Gaisser-Hillas function. We distribute the observation heights around the shower maximum and simulate additional observation heights for air showers that traverse more atmosphere, i.e., air showers that have a large zenith angle[4].

For all simulated air showers, we compare the parameters of the Gaisser-Hillas function of the radiation energy release with the parameters that describe the energy deposit of the electromagnetic air-shower particles. We find that X_{max}^{rad} is on average 48 g/cm^2 before the X_{max} of the energy deposit by the electromagnetic part of the air shower with a scatter of +6.2/-7.5 g/cm^2. The difference in the λ-parameter is -32 g/cm^2 with a scatter of 4 g/cm^2. These shifts show no dependence on the shower energy but exhibit a small zenith angle dependence. The difference $X_{max}^{rad} - X_{max}$ shows a constant offset of -49 g/cm^2 until $60°$ zenith angle and rises for higher zenith angles to -37 g/cm^2. The difference in the λ parameter increases from -34 g/cm^2 at $0°$ zenith angle to -28 g/cm^2 at $80°$ zenith angle. This zenith dependence is difficult to interpret as it is also influenced by the mixing of geomagnetic and charge-excess radiation that have a different longitudinal profile of the radiation energy release (see Sec. 3.3.3).

Uncertainties of the total radiation energy

The dominant uncertainty of the radiation energy originates from the approximation of calculating the radiation energy only from the energy fluence on the positive $\vec{v} \times (\vec{v} \times \vec{B})$ axis instead of a full 2D integration of the radio footprint. We estimated the resulting uncertainty by simulating the energy fluence in the entire shower plane for a representative set of shower geometries consisting of 150 air showers. We compared the radiation energy calculated from the energy fluence on the positive $\vec{v} \times (\vec{v} \times \vec{B})$ axis with the radiation energy determined via a full two-dimensional integration of the energy fluence. We find a scatter of 3% with a bias of 3% towards higher radiation energies, i.e., in our approach we overestimate the radiation energy by 3% on average.

The reason for the observed asymmetry that results in the bias is well understood and can be attributed to two effects. As discussed before, we overestimate the radiation energy by $\sim 1\%$ by the approximation that the geomagnetic and charge-excess components of the electric field are in-phase. In addition, the Cherenkov-like effects that lead to additional coherence and thereby larger energy fluences are not radially symmetric around the shower axis. Except for exactly vertical showers, the observer positions in the shower plane have different heights above ground. Therefore, observer positions with the same distance to the shower axis see different effective refractivities on their line of sight to the emission region. The average refractive index between a position below the shower axis and the emission region is larger than for a position above the shower axis with the same distance to the shower axis. And as already visible from Fig. 3.12, larger refractivities generally result in more radiation energy. Hence, depending on the orientation of the positive $\vec{v} \times (\vec{v} \times \vec{B})$ axis in ground

---

[4]The first 4 observation heights are distributed symmetrically around the position of the shower maximum X_{max} at $X_{max} \pm 300$ g/cm^2 and $X_{max} \pm 50$ g/cm^2 and the 5th observation height is at sea level. If the traversed atmosphere is large enough also an observation level at $X_{max} + 500$ g/cm^2 and $X_{max} + 1000$ g/cm^2 is added.

coordinates, we over or underestimate the radiation energy. The orientation of the positive $\vec{v} \times (\vec{v} \times \vec{B})$ axis depends on the incoming direction of the air shower and therefore the bias in the determination of the radiation energy exhibits directional dependence. For the distribution of incoming directions in our simulated data set, the positive $\vec{v} \times (\vec{v} \times \vec{B})$ axis is mostly below the shower axis, resulting in an additional overestimation of the radiation energy of 2% on average. The scatter of 3% results from the dependence on the shower geometry. However, this result is not critical for the desired accuracy of this analysis. In the following, we will correct the radiation energy by 3% and use the 3% scatter as uncertainty of the radiation energy.

An additional source of uncertainty arises from the determination of the radiation energy on the positive $\vec{v} \times (\vec{v} \times \vec{B})$ axis itself. We use the tiny scatter of the radiation energy around the integral of the Gaisser-Hillas function (cf. Fig. 3.13 bottom) to estimate this uncertainty. The scatter can have two reasons: either the Gaisser-Hillas function in the version with three parameters does not describe the longitudinal profile of the radiation energy release in all detail, or the scatter is due to statistical uncertainties which originate from the determination of the simulated radiation energy and/or from fluctuations in the simulation itself. We use this scatter to estimate the precision of the radiation energy determination. Inserting an uncertainty of 0.5%, the distribution of the χ^2 probability of the fit of the integral of the Gaisser-Hillas function of all simulated air showers is distributed uniformly. For a slightly larger uncertainty (0.7%) the χ^2 probability distribution indicates an overestimation of the errors. Furthermore, we observe that the Gaisser-Hillas function fits slightly better for air showers with proton primaries than for air showers with iron primaries.

Using this upper limit of 0.5% as an estimate for the statistical uncertainty of the radiation energy that has been released up to a specific observation height, we determine the uncertainty of the total radiation energy, i.e., the integral over the fitted Gaisser-Hillas function, in a dedicated toy Monte Carlo. If the radiation energy is released fully in the atmosphere, the uncertainty is 0.3%. As long as more than 90% of the radiation energy is released in the atmosphere, the uncertainty is less than 1%, and even if only 70% of the radiation energy is released in the atmosphere, the uncertainty is still below 2% without any bias.

3.3.3   Decomposition of the radiation processes

Our method to extract the radiation energy from the air shower simulations allows a decomposition into the part originating from the geomagnetic emission $E_{\mathrm{rad}}^{\mathrm{geo}}$ and the part originating from the charge-excess emission $E_{\mathrm{rad}}^{\mathrm{ce}}$. Fig. 3.14 shows the lateral distribution of the energy fluence of the geomagnetic and the charge-excess component at three different atmospheric depths. The shape of the lateral signal distribution of the two components is different. The geomagnetic LDF has the same shape as the LDF of the total energy fluence (cf. Fig. 3.12), because the geomagnetic emission is the dominant mechanism in this example.

The energy fluence of the charge-excess component is zero at the shower axis, then increases with increasing distance before it decreases again. The further away the observer is from the shower maximum, the more prominent this effect is. This behavior is expected, as the charge-excess emission is polarized radially towards the shower axis. This implies that the polarization of the charge-excess emission turns by $180°$ when going from one side of the shower to the other, which can only be a
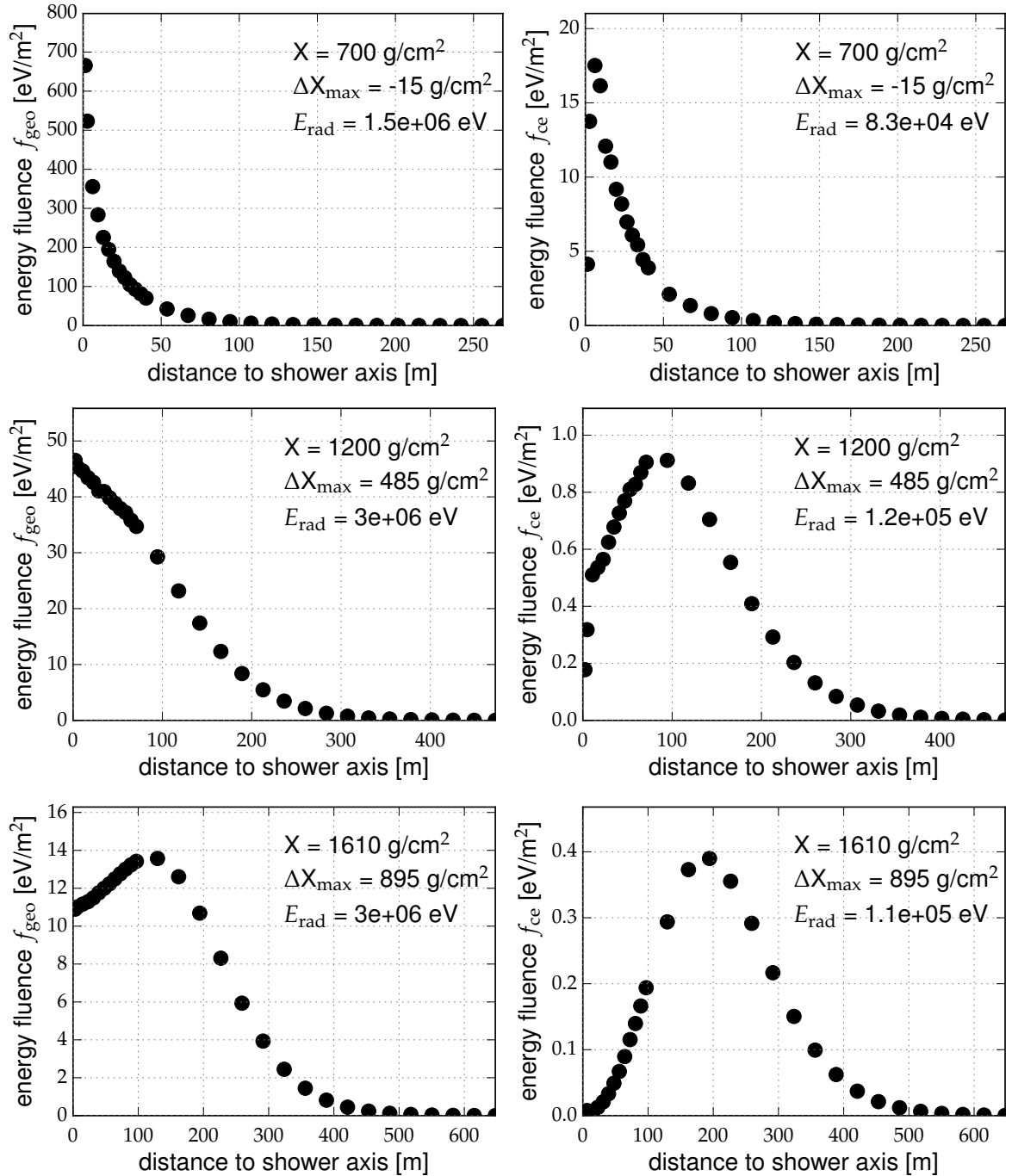
Figure 3.14: Distribution of the energy fluence in the 30 - 80 MHz band along the positive $\vec{v} \times (\vec{v} \times \vec{B})$ axis at different atmospheric depths for the same air shower as shown in Fig. 3.12. Here, the total energy fluence is split into the part that originates from the geomagnetic emission (plots on the left side) and the part that originates from the charge-excess emission (plots on the right side). Please note the different vertical axis scales.

continuous transition if the amplitude crosses zero as well.

From the geomagnetic and charge-excess LDFs we calculate the radiation energies at different atmospheric depths to obtain the longitudinal profiles of the radiation energy release of the two emission mechanisms (see Fig. 3.15). The longitudinal profile of the geomagnetic radiation energy release fol-
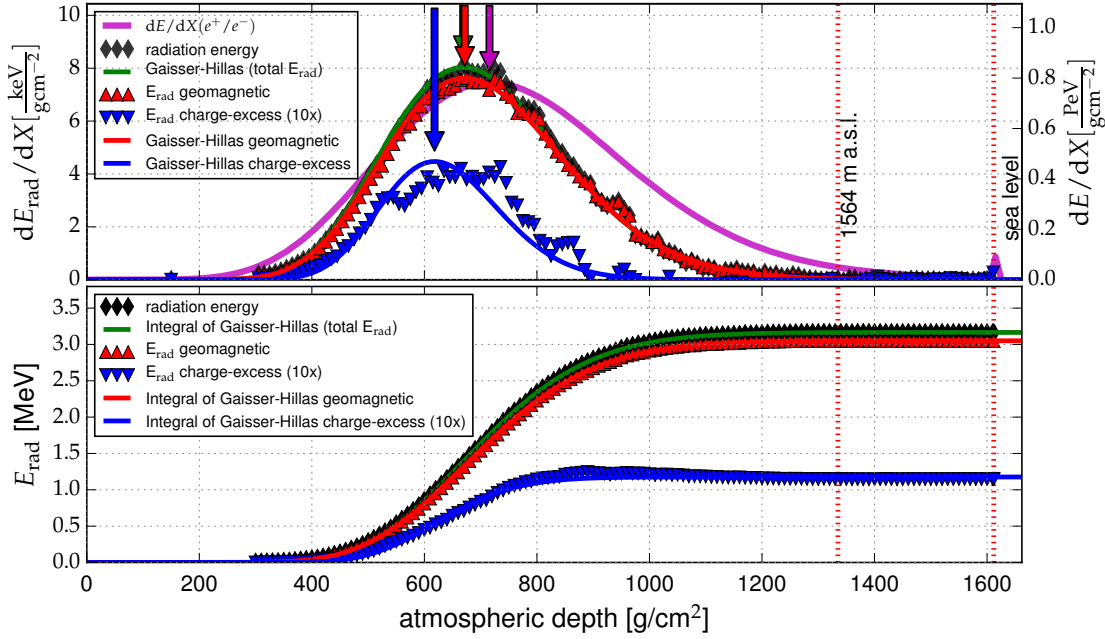
Figure 3.15: Longitudinal profile of the radiation energy release for the same data as shown in Fig. 3.13. Here also the parts of the radiation energy release with geomagnetic and charge-excess origin are shown. The charge-excess radiation energy is multiplied by a factor of 10.

lows the profile of the total radiation energy release as the amount of charge-excess radiation energy is small for this air shower.

The total charge-excess radiation energy exhibits some unexpected features. After the radiation energy has reached its maximum at $\sim 900\,\mathrm{g/cm^2}$, it decreases slightly with increasing atmospheric depths and then remains constant. A plausible explanation is given by the fact that the orientation of the radial electric-field vectors associated with charge-excess radiation reverses when the total net charge excess reaches its maximum and thus turns from a growing net charge to a diminishing net charge. The radiation of the late stages of the air shower evolution thus interferes destructively with that of the early stages, leading to a decrease of the total, integrated radiation energy. The decrease in radiation energy means that energy has to be absorbed by some mechanism. This could, for example, happen by absorption of the electromagnetic radiation by charged particles in the shower cascade. As the total amount of energy that needs to be absorbed is more than ten orders of magnitude smaller than the shower energy it is irrelevant for the shower development and is therefore not implemented in the simulation. Another possible explanation is that the polarization changes slightly during the shower development, so that a part of the geomagnetic radiation is also visible in the $\vec{v} \times (\vec{v} \times \vec{B})$ polarization or vice versa. In addition, the longitudinal profile of the charge-excess radiation energy release deviates from a Gaisser-Hillas function. Therefore, the results on $X_{\max}^{\mathrm{rad}}$ obtained from the Gaisser-Hillas fit must be interpreted with caution; however, as the integral of the Gaisser-Hillas function is fitted to the cumulative energy distribution, the radiation energy is still estimated correctly.

For all simulated air showers, we fit the integral of a Gaisser-Hillas function separately to the geomagnetic and charge-excess radiation energy at a given atmospheric depth and compare the corresponding Gaisser-Hillas function (cf. Eq. (3.19)) to the longitudinal profile of the electromagnetic

part of the air shower. For the geomagnetic radiation energy we find $X_{\text{max}}^{\text{rad}} - X_{\text{max}} = -47^{+6}_{-8}\,\text{g/cm}^2$ and $\Delta\lambda = (-32 \pm 4)\,\text{g/cm}^2$. For the charge-excess radiation energy we find a significantly different behavior, with $X_{\text{max}}^{\text{rad}} - X_{\text{max}} = -87^{+13}_{-10}\,\text{g/cm}^2$ and $\Delta\lambda = (-48^{+6}_{-7})\,\text{g/cm}^2$ under the assumption that the longitudinal profile of the radiation energy release with charge-excess origin can be described with a Gaisser Hillas function.

With the separate determination of $E_{\text{rad}}^{\text{geo}}$ and $E_{\text{rad}}^{\text{ce}}$ we are able to generalize previous work regarding the relative charge-excess strength a [12, 21, 125, 146], where a was defined as the ratio of the electric-field amplitudes of the charge-excess and geomagnetic components for maximum geomagnetic emission ($\sin\alpha = 1$). In [12], an average value of $a = 14\%$ was measured at the Auger site. Using LOFAR [125], additional dependencies of a on the distance to the shower axis and zenith angle were found. The dependence of a on the distance from the shower axis can be explained by the different shapes of the geomagnetic and charge-excess LDFs (cf. Fig. 3.14).

In the following we generalize the definition of the charge-excess fraction using the radiation energy, i.e., the integral of the LDF, and define

$$a = \sin\alpha \sqrt{\frac{E_{\text{rad}}^{\text{ce}}}{E_{\text{rad}}^{\text{geo}}}}\,, \tag{3.20}$$

where $E_{\text{rad}}^{\text{geo}}$ and $E_{\text{rad}}^{\text{ce}}$ are the radiation energies after the shower has fully developed, which corresponds to the integrals of the respective Gaisser-Hillas functions. We do not study the development of the charge-excess fraction during the shower development. We take the square root of the ratio of radiation energies to be consistent with the previous work [12, 125], because the radiation energy scales quadratically with the electric-field amplitude.

We find that the value of a depends on where in the atmosphere the radiation is generated. More precisely, a depends on the density in the part of the atmosphere in which the radiation is generated. As most of the radiation energy is released near the shower maximum X_{max}, we use the atmospheric density $\rho_{X_{\text{max}}}$ at the position of the shower maximum to parametrize this dependence. The density $\rho_{X_{\text{max}}}$ depends on the zenith angle θ and X_{max} of the air shower and can be calculated from the atmospheric density profile. We use the model of the US standard atmosphere as it is also used in the air-shower simulations.

Fig. 3.16 shows the dependence of a on the atmospheric density at the shower maximum. We observe that a increases with increasing $\rho_{X_{\text{max}}}$ which is consistent with the result of [125] who reported an increase of a with decreasing zenith angle. We do not observe any difference between air showers induced by protons or iron nuclei. We describe the dependence with an exponential function with the following parameters:

$$a(\rho_{X_{\text{max}}}) = 0.43\left(e^{1.11\,\text{m}^3/\text{kg}\,(\rho_{X_{\text{max}}} - \langle\rho\rangle)}\right) - 0.24\,, \tag{3.21}$$

where $\langle\rho\rangle = 0.65\,\text{kg/m}^3$ is the atmospheric density at the shower maximum for an average zenith angle of $45°$ and an average $\langle X_{\text{max}}\rangle = 669\,\text{g/cm}^2$ as predicted for a shower energy of $1\,\text{EeV}$ for a 50% proton/50% iron composition using QGSJetII-04 [165]. The color code of Fig. 3.16 shows that only air showers with small values of $\sin\alpha$ exhibit some deviation from the parametrization.

Using Eq. (3.21) together with the geometry of the air shower and a description of the atmosphere,
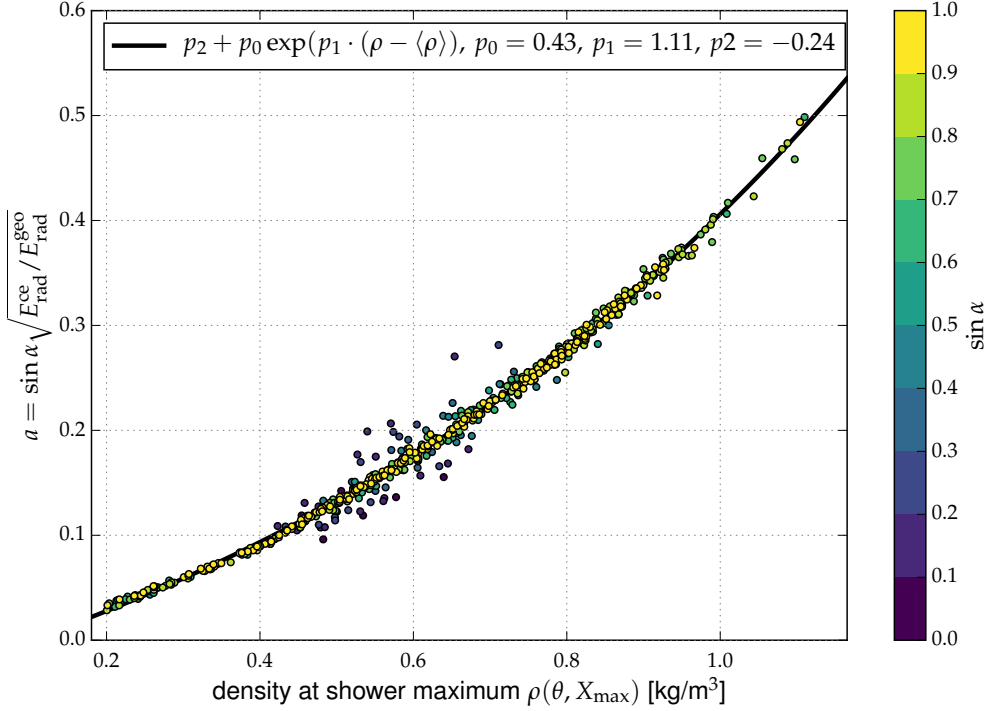
Figure 3.16: Dependence of charge-excess fraction a on the atmospheric density at the position of the shower maximum. The dashed line represents an exponential fit to the data.

the ratio of $E_{\rm rad}^{\rm ce}/E_{\rm rad}^{\rm geo}$ can be converted to the position of the shower maximum. Therefore in a measurement, a separate determination of the geomagnetic and charge-excess radiation energies, e.g., through a combined fit of the geomagnetic and charge-excess LDFs according to Eq. (3.10) and (3.11), can be used to estimate the position of the shower maximum $X_{\rm max}$ which is an estimator of the mass of the cosmic ray.

3.3.4   Properties of the radiation energy

Dependence on shower energy

The radiation energy originates from the radiation generated by the electromagnetic part of the air shower. Hence, the radiation energy correlates best with the energy of the electromagnetic cascade and not with the complete shower energy, which includes energy carried by neutrinos and high-energy muons that are not relevant for radio emission. This is not necessarily a disadvantage but a benefit for several analyses. Other detection techniques are also only sensitive to the electromagnetic shower energy, such as fluorescence or air-Cherenkov telescopes, which allows for a direct cross-calibration. Also the measurement of the electromagnetic shower energy can be combined with a separate measurement of the muonic shower component (e.g. via buried scintillators) to obtain a sensitivity on the particle species of the primary cosmic-ray particle. If, however, the goal is to measure the cosmic-ray energy, an additional scatter arises from the varying fraction of cosmic-ray energy entering the electromagnetic cascades for different particle species. For a cosmic-ray energy of $1\,{\rm EeV}$ the difference in electromagnetic shower energy is $\sim$4.5% for the two extreme cases of cosmic-rays being protons or

iron nuclei and decreases to 3% at $10\,\mathrm{EeV}$ [110]. The average fraction of the electromagnetic shower energy can be inferred from hadronic interaction models assuming a specific cosmic-ray composition or using a direct measurement as presented in [117].

Before correlating the radiation energy with the energy of the electromagnetic cascade, the geomagnetic radiation energy needs to be corrected for geometry. The radiation energy of the geomagnetic contribution depends on the magnitude of the geomagnetic field B_{Earth} and the angle α between the shower direction and the geomagnetic field and scales with $\sin^2\alpha$. We first study only the dependence on $\sin^2\alpha$ as all simulations were performed using the same geomagnetic field strength. We investigate the scaling with the geomagnetic field in the next section. In contrast, the radiation energy of the charge-excess component does not depend on the geomagnetic field. From Eq. (3.15) it follows that the radiation energy is the sum of the radiation energy of the geomagnetic emission and the radiation energy of the charge-excess emission [21]. We therefore correct the radiation energy by

$$S_{\mathrm{RD}} = \frac{E_{\mathrm{rad}}}{a(\rho_{X_{\mathrm{max}}})^2 + (1 - a(\rho_{X_{\mathrm{max}}})^2)\sin^2\alpha}\,, \tag{3.22}$$

where $a(\rho_{X_{\mathrm{max}}})$ is the parametrization of the charge-excess fraction from Eq. (3.21). We fit a power law of the form

$$S_{\mathrm{RD}} = A \times 10^7\,\mathrm{eV}\,(E_{\mathrm{em}}/10^{18}\,\mathrm{eV})^B \tag{3.23}$$

and find that S_{RD} scales quadratically with the energy of the electromagnetic cascade E_{em} as expected for coherent emission. The scatter around the calibration curve is less than 10%.

In addition to this $\sin\alpha$ correction we expect a second-order dependence. The air shower develops according to the slant depth, whereas the amount of radiation increases with the geometric path length of the shower development. In a region of low atmospheric density, the ratio of the geometric path length and propagation length measured in atmospheric depth is larger than in high-density regions. Therefore, a shower that develops early in the atmosphere has a slightly larger radiation energy than a shower with the same energy that develops deeper in the atmosphere, as the air density increases with increasing atmospheric depth. This depends primarily on the zenith angle of the incoming direction of the air shower and secondarily on the position of the shower maximum. We again use the atmospheric density at the position of the shower maximum $\rho_{X_{\mathrm{max}}}$ to parametrize this second-order dependence.

The residuals of the relation between the corrected radiation energy S_{RD} as defined in Eq. (3.22) and the energy in the electromagnetic part of the air shower indeed show a dependence on $\rho_{X_{\mathrm{max}}}$ and are shown in Fig. 3.17. For air showers with the same electromagnetic shower energy, the radiation energy increases with decreasing atmospheric density $\rho_{X_{\mathrm{max}}}$. We incorporate this dependence of the radiation energy by applying a second correction term to S_{RD}:

$$S_{\mathrm{RD}}^{\rho} = \frac{E_{\mathrm{rad}}}{a(\rho_{X_{\mathrm{max}}})^2 + (1 - a(\rho_{X_{\mathrm{max}}})^2)\sin^2\alpha}\,\frac{1}{(1 - p_0 + p_0\,\exp[p_1(\rho_{X_{\mathrm{max}}} - \langle\rho\rangle)])^2}\,. \tag{3.24}$$

As in Eq. (3.21) we normalize the correction to an average $\langle\rho\rangle = 0.65\,\mathrm{kg/m^3}$.

The correlation between the corrected radiation energy S_{RD}^{ρ} and the energy in the electromagnetic part of the air shower is shown in Fig. 3.18. We determine the calibration constants A and B of
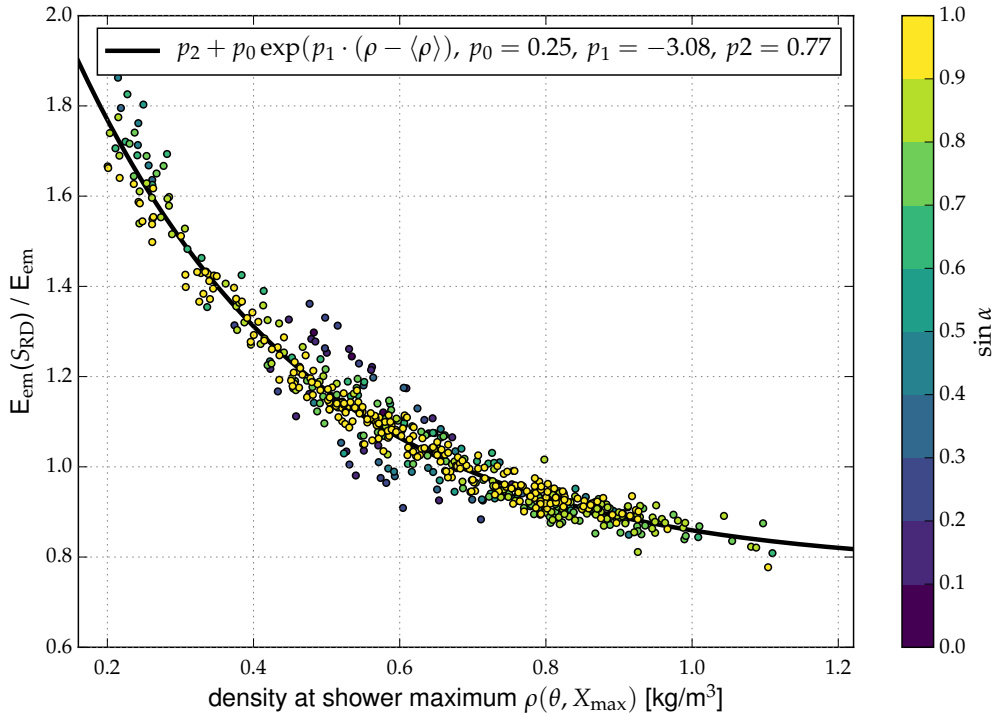
Figure 3.17: Residuals of the correlation between S_{RD} and the energy in the electromagnetic part of the air shower plotted as a function of the density at the shower maximum. An exponential function is adapted to the data.

Eq. (3.23) and the parameter p_0 and p_1 in a combined chi-square fit and present the results in Tab. 3.1.

Table 3.1: Best-fit parameters for an energy estimator with density at shower maximum correction as defined in Eq. (3.24).

A	1.683 ± 0.004
B	2.006 ± 0.001
p_0	0.251 ± 0.006
p_1	$-2.95 \pm 0.06 \, \mathrm{m^3/kg}$

The reduced chi-squared is 1.4, which may indicate an even higher-order dependence of the radiation energy not taken into account in Eq. (3.24). Hence, the uncertainties of the fit parameters are also slightly underestimated. The parameters p_0 and p_1 exhibit a strong correlation which is, however, not critical as the parameters are always used mutually in the $\rho_{X_{\mathrm{max}}}$ correction and are never inspected separately. In addition, parameter A also shows some correlation with p_0 and p_1 as A depends on the absolute normalization of the $\rho_{X_{\mathrm{max}}}$ correction. To estimate a possible bias we fixed the parameters p_0 and p_1 to the values obtained in the separate fit of Fig. 3.17 and find a value of A that is well compatible with the result of the combined chi-square fit within the uncertainties.

The inset of Fig. 3.18 shows a histogram of the scatter around the calibration curve. The standard deviation as computed from the data amounts to 3.5% owing to tails of the distribution which are related to data points with small values of $\sin \alpha$ that exhibit larger fluctuations. If we fit a Gaussian distribution to the binned data we obtain an uncertainty of 2.7%. The color code of the data points in
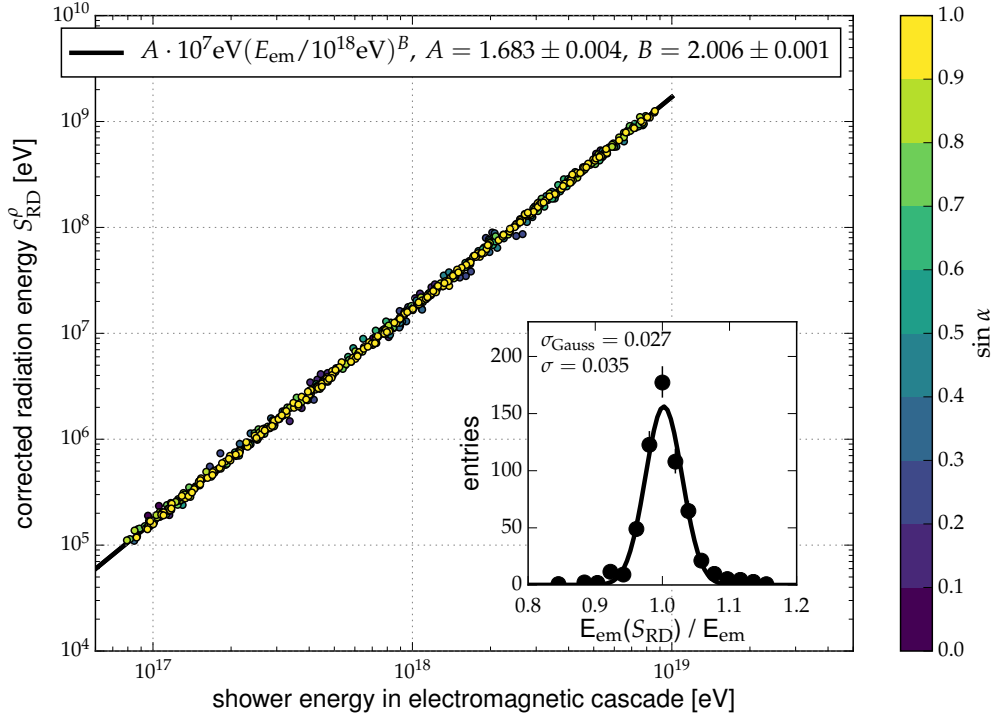
Figure 3.18: Correlation between the energy in the electromagnetic part of the air shower and the radiation energy corrected for $\sin \alpha$ as well as the atmospheric density at the shower maximum (cf. Eq. (3.24)). The black line shows a power-law fit to the data. The inset figure shows the scatter around the calibration curve. The color scale shows the value of $\sin \alpha$.

Fig. 3.18 shows that the fluctuations are not biased to a certain direction, e.g., towards smaller radiation energies, but are instead centered around the calibration curve. Hence, we conclude that our method works for all incoming directions with slightly larger uncertainties for showers with small values of $\sin \alpha$.

Furthermore, we investigated possible differences between air showers with proton and iron primaries after we applied the corrections. The difference in the fraction of cosmic-ray energy that enters the electromagnetic cascade is irrelevant as we correlate S_{RD}^{ρ} directly with the electromagnetic energy. As we also correct for the density at the shower maximum, our analysis is insensitive to the difference in the average X_{max} between different particle species. However, if we analyze only air showers induced by protons (induced by iron nuclei), we find a 2% larger (2% smaller) calibration constant A, i.e., proton-induced air showers have a larger corrected radiation energy S_{RD}^{ρ} than iron-induced air showers. As the radiation energy scales quadratically with the electromagnetic shower energy, the $\pm 2\%$ shift in radiation energy corresponds to a $\pm 1\%$ shift in the electromagnetic shower energy, which is well below current experimental uncertainties. Hence, the slight dependence of the corrected radiation energy on the cosmic-ray mass is irrelevant for practical purposes.

Scaling with the geomagnetic field

The amount of radiation energy that is released by an air shower depends on the geomagnetic field. More precisely, the contribution of the geomagnetic emission process to the radiation energy scales

with the magnitude of the geomagnetic field B_{Earth}. Naively, one would assume that the amplitude of the electric-field pulse scales proportionally with the magnitude of the Lorentz force which is proportional to the magnitude of the geomagnetic field. The radiation energy of the geomagnetic contribution would thus be proportional to the magnitude of the geomagnetic field squared. However, we investigated the scaling with the geomagnetic field in the air-shower simulations and found that the radiation energy of the geomagnetic component deviates significantly from a quadratic scaling with B_{Earth} and scales approximately with $(B_{\mathrm{Earth}})^{1.8}$.

We obtained this number by simulating air showers with different magnitudes of the geomagnetic field. For each air shower we calculated the corrected radiation energy according to Eq. (3.24) and corrected the geomagnetic part not only by $\sin^2 \alpha$, but also by $(B_{\mathrm{Earth}}/0.243\,\mathrm{G})^k$ and determined the scaling factor k that best fits the simulations. The value of $0.243\,\mathrm{G}$ is the geomagnetic field strength at the location of the Pierre Auger Observatory and is used as a reference in this analysis. We simulated air showers with geomagnetic field magnitudes ranging from the reference field strength to three times the reference field strength which covers the complete range of variations in the geomagnetic field strength occurring on Earth.

A plausible explanation for the deviation from the naively expected quadratic scaling is that the electrons and positrons do not propagate unimpeded but interact continuously with air molecules. The geomagnetic emission should therefore not be confused with synchrotron emission. The shower particles move chaotically within the shower front, they collide with other particles, get accelerated and decelerated and they drift only on average into the direction of the Lorentz force. The drift velocity is thereby much smaller than the average velocity of the particles inside the shower front [144]. With stronger acceleration by a larger geomagnetic field also the number of collisions with other particles increases resulting in a slightly smaller effective acceleration.

Within the variations of the geomagnetic field strength occurring on Earth and the desired accuracy of this analysis, the scaling with the geomagnetic field can be described effectively with $(B_{\mathrm{Earth}})^{1.8}$. However, we note that we observe a small second order dependence. The gain in radiation energy, if the geomagnetic field is increased from $B = B_{\mathrm{Auger}}$ to $B = 1.5 \times B_{\mathrm{Auger}}$, is slightly larger than the gain in radiation energy, if the geomagnetic field is increased from $B = 2 \times B_{\mathrm{Auger}}$ to $B = 1.5 \times 2 \times B_{\mathrm{Auger}} = 3 \times B_{\mathrm{Auger}}$.

For the same reason, this saturation effect sets in later for air showers with smaller values of $\sin \alpha$ as the Lorentz force is proportional to $\sin \alpha \times B_{\mathrm{Earth}}$. Hence, at locations with strong geomagnetic field strengths also a deviation from a quadratic scaling with $\sin \alpha$ is expected. For $B = B_{\mathrm{Auger}}$ we do not observe any deviation from a quadratic scaling with $\sin \alpha$. In addition, we observe that the saturation effect is stronger pronounced for larger zenith angles where the air shower develops in a part of the atmosphere with smaller density and traverses more geometrical distance during the shower development. Hence, the shower particles are longer, and therefore also stronger, accelerated by the geomagnetic field which results in an earlier onset of saturation effects. All this higher order dependencies support the explanation presented above where a saturation effect is expected.

A recent analysis of the impact of thunderstorm electric fields on the radio emission strength [166] also reported that the radio emission does not scale proportional to the atmospheric electric-field component that is oriented into the direction of the Lorentz force. At larger field strengths they also observed a saturation effect that was explained by the change in coherence length scales. Due to the

larger transverse velocity, electrons and positrons trail further than the coherence length behind the shower front. This behavior might also or partly explain the saturation effects that we observe.

However, within the variations of the geomagnetic field strength occurring on Earth and the desired accuracy of this analysis, this second order dependence can be neglected. Hence, we extend Eq. (3.24) by the geomagnetic field dependence to

$$S_{\mathrm{RD}}^{\rho} = \frac{E_{\mathrm{rad}}}{a'(\rho_{X_{\mathrm{max}}})^2 + (1 - a'(\rho_{X_{\mathrm{max}}})^2) \sin^2 \alpha \left(\frac{B_{\mathrm{Earth}}}{0.243\,\mathrm{G}}\right)^{1.8}} \frac{1}{(1 - p_0 + p_0 \exp[p_1(\rho_{X_{\mathrm{max}}} - \langle\rho\rangle)])^2}$$

(3.25)

with

$$a'(\rho_{X_{\mathrm{max}}}) = a(\rho_{X_{\mathrm{max}}})/(B_{\mathrm{Earth}}/0.243\,\mathrm{G})^{0.9} \qquad (3.26)$$

as the relative strength of the charge-excess component a also changes with changing geomagnetic field. This formula is then applicable to any location on Earth.

Suitable energy estimator for a measurement

In a measurement, X_{max} is not always accessible or may have large experimental uncertainties. As most of the variation in $\rho_{X_{\mathrm{max}}}$ is due to the zenith angle of the shower direction, we implement a correction that takes only the zenith angle into account. For all air showers we assume the same average $\langle X_{\mathrm{max}}\rangle$ of $669\,\mathrm{g/cm^2}$ to calculate the density at the position of the shower maximum $\rho_\theta = \rho(\theta, \langle X_{\mathrm{max}}\rangle)$. We first parametrize the variation of the charge-excess fraction using the zenith angle and find

$$a(\rho_\theta) = 0.45 \left(\exp[1.14\,\mathrm{m^3/kg}\,(\rho_\theta - \langle\rho\rangle)]\right) - 0.24\,, \qquad (3.27)$$

and then define the energy estimator as

$$S_{\mathrm{RD}}^{\rho_\theta} = \frac{E_{\mathrm{rad}}}{a'(\rho_\theta)^2 + (1 - a'(\rho_\theta)^2) \sin^2 \alpha \left(\frac{B_{\mathrm{Earth}}}{0.243\,\mathrm{G}}\right)^{1.8}} \frac{1}{(1 - p_0 + p_0 \exp[p_1(\rho_\theta - \langle\rho\rangle)])^2} \qquad (3.28)$$

with

$$a'(\rho_\theta) = a(\rho_\theta)/(B_{\mathrm{Earth}}/0.243\,\mathrm{G})^{0.9}\,. \qquad (3.29)$$

Again, we perform a chi-square fit and find the parameters listed in Tab. 3.2. We determine the energy resolution by fitting a Gaussian function to the scatter around the calibration curve and find a standard deviation of 4%.

Table 3.2: Best-fit parameters for an energy estimator with zenith angle correction as defined in Eq. (3.28).

A	1.629 ± 0.003
B	1.980 ± 0.001
p_0	0.239 ± 0.007
p_1	$-3.13 \pm 0.07\,\mathrm{m^3/kg}$

The slope parameter B shows a deviation from 2 that is significantly larger than the uncertainties. This is because the average X_{max} increases linearly with the logarithm of the cosmic-ray energy [73].
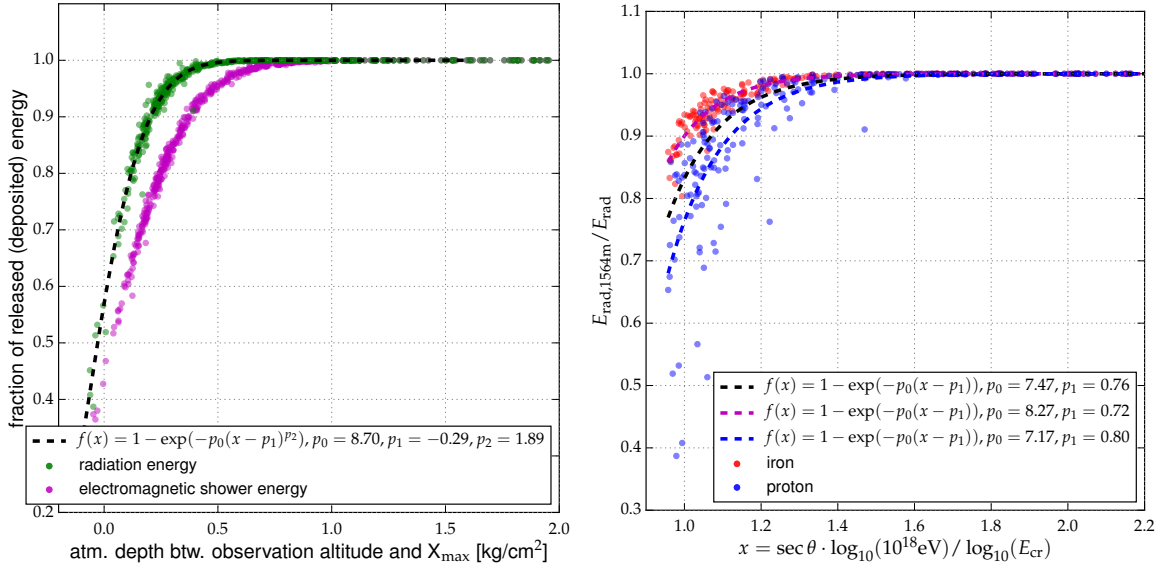
Figure 3.19: (left) The green circles show the fraction of radiation energy that is released in the atmosphere as a function of the atmospheric depth between the observation height and shower maximum. The dashed line shows a parametrization of this dependence. The magenta circles show the fraction of the deposited energy of the electromagnetic part of the air shower in the atmosphere. (right) Fraction of radiation energy that is released until a height of 1564 m a.s.l. as a function of the zenith angle and cosmic-ray energy. Red circles represent iron-induced air showers and blue circles show proton-induced air showers. The dashed lines show parametrizations of the dependence for all data points (black), proton showers (blue) and iron showers (magenta).

Hence, for the same zenith angle, more energetic showers develop deeper in the atmosphere, i.e., in a region of higher atmospheric density, and consequently have a smaller radiation energy. As we do not correct for an X_{max} dependence, the effect appears with a value slightly smaller than 2 in the slope parameter B. However, the energy resolution achieved using only a zenith angle correction is still only 4%, which is small compared to current experimental uncertainties [126].

Clipping

If the radiation energy is detected by an observer at a height h above sea level, the air shower may not have released all its radiation energy. The shower might not be fully developed when it reaches the ground, i.e., some part of the shower that would have contributed to the radiation energy is clipped. The strength of the clipping depends on the atmospheric depth between the observer and the shower maximum X_{max} and is defined as

$$D_{\mathrm{X_{max}}} = \int\limits_{h_0}^{\infty} \frac{\rho(h)}{\cos\theta}\, \mathrm{d}h - X_{\mathrm{max}} = \int\limits_{h_0}^{h(X_{\mathrm{max}})} \frac{\rho(h)}{\cos\theta}\, dh, \tag{3.30}$$

where h_0 is the altitude of the observer, θ is the zenith angle and $\rho(h)$ the atmospheric density at height h above sea level.

Fig. 3.19 shows the fraction of radiation energy released in the atmosphere as a function of $D_{\mathrm{X_{max}}}$. This dependence is independent of observation altitude, as we directly calculate the atmospheric depth

Table 3.3: Parametrization of the clipping effect using the zenith angle θ and the cosmic ray energy E_{cr} for different heights above sea level with the function $f(x) = 1 - \exp(-p_0(x - p_1))$ with $x = \sec\theta \cdot \log_{10}(10^{18} \text{ eV})/\log_{10}(E_{cr})$.

composition	p_0	p_1
1564 m a.s.l. (Auger)		
pure proton	7.17	0.8
pure iron	8.27	0.72
50% proton, 50% iron	7.46	0.76
675 m a.s.l. (Tunka-Rex)		
pure proton	9.57	0.77
pure iron	10.22	0.68
50% proton, 50% iron	9.73	0.74
0 m a.s.l. (LOFAR)		
pure proton	11.93	0.76
pure iron	11.85	0.66
50% proton, 50% iron	11.9	0.72

between the observation altitude and X_{max}. An observer at higher altitude observes smaller "distances to X_{max}" and is influenced more strongly by clipping. We parametrize the dependence using the following function

$$\frac{E_{rad}(D_{X_{max}})}{E_{rad}} = 1 - \exp\left(-8.7 \,\text{cm}^2/\text{kg} \,(D_{X_{max}} + 0.29 \,\text{kg/cm}^2)^{1.89}\right) . \tag{3.31}$$

The clipping of the electromagnetic part of the air shower is significantly stronger, which is also shown in Fig. 3.19 on the left. This is in agreement with the previous finding that the longitudinal profile of the radiation energy release is shifted towards smaller atmospheric depths compared to the energy deposit of the electromagnetic part of the air shower (cf. Fig. 3.13). At the point where only 75% of the electromagnetic part of the air shower has deposited its energy in the atmosphere, 90% of the radiation energy has already been released.

This effect is of prime importance in an experiment, as the radiation energy needs to be corrected for clipping to correctly estimate the cosmic-ray energy. As X_{max} is not always accessible or may have large experimental uncertainties, we present an alternative parametrization of the clipping effect for different observation heights using the zenith angle and the cosmic-ray energy. The atmospheric depth between the observer and shower maximum is proportional to the secant of the zenith angle with a second-order dependence on the cosmic-ray energy as the average X_{max} increases proportionally to the logarithm of the energy (cf. Eq. (3.30)). Fig. 3.19 on the right shows this parametrization for an observation height of 1564 m a.s.l., which corresponds to the altitude of the radio detector of the Pierre Auger Observatory [118]. A significant difference between air showers induced by protons or iron nuclei is visible, as iron showers have a smaller average X_{max} than proton showers. We again parametrize the dependence with an exponential function and provide the best-fit values for a mixed, a pure proton and a pure iron composition in the legend of the figure and in Tab. 3.3.

We repeated the analysis for an observation height of 675 m asl which corresponds to the location of the Tunka-Rex experiment [20] and for an observation height of 0 m a.s.l. which corresponds to the
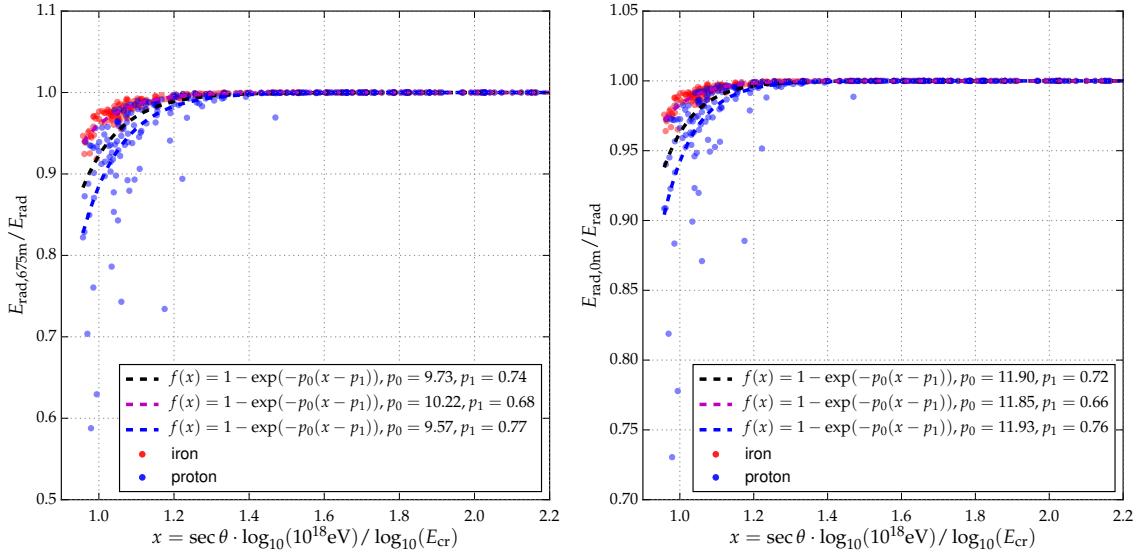
Figure 3.20: Fraction of the radiation energy that is generated up to a height of 675 m a.s.l. (left) and 0 m a.s.l. (right) as a function of the zenith angle and cosmic-ray energy. Red circles represent iron-induced air showers and blue circles show proton-induced air showers. The dashed lines show parameterizations of the dependence for all data points (black), proton showers (blue) and iron showers (magenta).

location of the LOFAR experiment [119] in Fig. 3.20 and Tab. 3.3.

Alternatively, the parametrization of Eq. (3.31) together with the parametrization of the average $X_{\max}$ as a function of cosmic-ray energy and mass using different interaction models [165] can be used to calculate the clipping effect for any observation altitude and assumption of the average $X_{\max}$.

3.3.5 Influence of settings of the air-shower simulation

In this section, we study the influence of different settings of the air-shower simulation on the radiation energy in the 30-80 MHz frequency band. In each cross-check we follow the same procedure. For the different settings of the simulation, we simulate several air showers with fixed geometry and energy. The incoming direction of the air shower is fixed to $50°$ zenith angle coming from the south and we use only iron primaries to minimize $X_{\max}$ fluctuations. We simulate an observer at sea level so that we can exclude any clipping effect for this geometry. Unless otherwise stated, the same simulation setup as described in Sec. 3.3.1 is used.

We correct the resulting radiation energy for its $\sin \alpha$ and $X_{\max}$ dependence according to Eq. (3.24) and normalize S_{RD}^{ρ} to the mean electromagnetic shower energy of the set of simulated air showers by multiplying S_{RD}^{ρ} with $(\langle E_{\mathrm{em}} \rangle / E_{\mathrm{em}})^2$, as the amount of cosmic-ray energy that ends up in the electromagnetic shower energy is slightly different for each shower. Thereby, we correct for all known dependencies and are most sensitive to the influence of different settings in the simulation. However, the effect of different settings is mostly smaller than the random fluctuations in the radiation energy. Hence, we simulate at least 20 air showers for each setting of the simulation and compare the mean of the normalized radiation energies.

Table 3.4: The table shows the normalized radiation energies for different cosmic-ray energies and thinning levels. The geometry of the air showers is fixed to a zenith angle of 50° coming from the south. Each cell shows the mean of at least 20 air showers simulated with the same settings, but different random seeds. The uncertainties shown are the uncertainty of the mean, and the standard deviations are shown in brackets.

thinning level	cosmic-ray energy		
	1 EeV	10 EeV	100 EeV
10^{-3}	11.7 ± 0.1 (1) MeV	1285 ± 14 (100) MeV	139 ± 2 (12) GeV
10^{-4}	11.10 ± 0.05 (0.34) MeV	1234 ± 6 (42) MeV	131.7 ± 0.5 (3.3) GeV
10^{-5}	10.91 ± 0.03 (0.22) MeV	1214 ± 4 (19) MeV	129.7 ± 0.5 (2.1) GeV
10^{-6}	10.97 ± 0.03 (0.21) MeV	1216 ± 3 (13) MeV	129.8 ± 0.4 (1.6) GeV
10^{-7}	10.96 ± 0.04 (0.19) MeV	1216 ± 4 (19) MeV	129.8 ± 0.3 (1.2) GeV

Impact of hadronic interaction models

We investigated the impact of the choice of the high-energy hadronic interaction model on the radiation energy by simulating 39 air showers for each of the two post-LHC models QGSJeII-04 [136] and EPOS-LHC [76]. We use the settings described above and fix the cosmic-ray energy to 1 EeV. For both interaction models we obtain consistent normalized radiation energies of 10.97 ± 0.03 MeV (QGSJetII-04) and 10.99 ± 0.02 MeV (EPOS-LHC). The quoted uncertainty is the uncertainty of the mean. We conclude that the effects of the high-energy hadronic interaction models are negligible for the prediction of the radiation energy.

We also checked for the influence of the low-energy hadronic interaction models and compared the two models FLUKA [138] and UrQMD [139]. We used the same settings as above, allow QGSJetII-04 to treat the high-energy hadronic interactions and obtain a mean normalized radiation energy of 10.97 ± 0.03 MeV using FLUKA and 10.95 ± 0.04 MeV using UrQMD. We conclude that the choice of low-energy hadronic interaction model also has a negligible influence on the radiation energy.

Impact of approximations in the air-shower simulation

As a full simulation of all shower particles is not feasible at high cosmic-ray energies due to the large number of shower particles, only a representative sub-sample of particles is tracked. This approach is known as "thinning". In this analysis we apply thinning at a level of 10^{-6} with optimized weight limitation [143]. To test the impact of the thinning level on radiation energy, we simulate air showers with thinning levels of 10^{-3}, 10^{-4}, 10^{-5}, 10^{-6} and 10^{-7} and cosmic-ray energies of 1 EeV, 10 EeV and 100 EeV and calculate the normalized radiation energy. In other words, we calculate the corrected radiation energy S_{RD}^{ρ} and for each set of showers with the same cosmic-ray energy we normalize S_{RD}^{ρ} to the average electromagnetic shower energy of this set. The results are presented in Tab. 3.4.

Regardless of the air-shower energy we obtain consistent results for thinning levels of 10^{-5}, 10^{-6} and 10^{-7}. For lower thinning levels we obtain larger radiation energies and observe an increased spread. On average, simulations with a thinning level of 10^{-4} produce ~1% more radiation energy and simulations with a thinning level of 10^{-3} produce ~6% more radiation energy. We conclude that thinning at a level of 10^{-6} does not introduce any bias in the simulation of the radiation energy.

The runtime of the simulation depends strongly on the thinning level. Relative to the runtime of

Table 3.5: The table shows the normalized radiation energies for different cosmic-ray energies and lower energy cuts for the electromagnetic shower particles. The geometry of the air showers is fixed to a zenith angle of $50°$ coming from south. Each cell shows the mean of at least 20 air showers simulated with the same settings but different random seeds. The uncertainties shown are the uncertainty of the mean, and the standard deviations are shown in brackets. The percentage values denote the relative deviations to the reference refractivity.

	cosmic-ray energy	
energy cut	1 EeV	10 EeV
250 keV	$10.97 \pm 0.03\,(0.21)\,\text{MeV}$	$1217 \pm 3\,(13)\,\text{MeV}$
150 keV	$10.91 \pm 0.04\,(0.19)\,\text{MeV}$	$1205 \pm 3\,(14)\,\text{MeV}$
80 keV	$10.84 \pm 0.03\,(0.15)\,\text{MeV}$	$1197 \pm 3\,(12)\,\text{MeV}$

a simulation with a thinning level of 10^{-6}, a simulation with a thinning level of 10^{-3} (10^{-4}, 10^{-5}) needs only 1% (6%, 20%) of the runtime, whereas a simulation with a thinning level of 10^{-7} needs six times more computing time. Hence, even a stronger thinning at a level of 10^{-5} could be used in future to further speed up the simulations.

Another approximation in the simulation is that each shower particle is only followed until it reaches a minimum energy. The threshold energy is different for different particle species. In this analysis, we use a minimum energy of 100 MeV for hadrons, 50 MeV for muons and 250 keV for the electromagnetic shower particles (electrons, positrons and photons). We check for the impact of the energy threshold of the electromagnetic particles that are relevant for the generation of radio emission by simulating iron-induced air showers with a fixed geometry and cosmic-ray energy, but different energy thresholds of 250 keV, 150 keV and 80 keV. We use the same settings as in the previous cross-checks and simulate air showers with cosmic-ray energies of 1 EeV and 10 EeV and calculate the normalized radiation energy as in the thinning cross-check. The results are presented in Tab. 3.5. We observe a slight trend towards smaller average radiation energies for lower energy thresholds. This is not a violation of energy conversation as in the endpoint formalism [129, 150] of CoREAS the radiation from stopping the particle is already considered and simulating the movement of a particle up to small energies results in less radiation than an instantaneous stop. Also lowering the photon energy threshold leads to the consideration of low energetic Bremsstrahlungs photons resulting in a less straight movement of electrons and consequently less coherent radiation. However, for a 1 EeV air shower, the shift in the average radiation energy is only 1%, which would correspond to a shift of 0.5% in the cosmic-ray energy. Hence, for the desired accuracy of the analysis this effect is negligible.

Again, the runtime depends strongly on the energy threshold. A simulation with a lower energy cut of 150 keV (80 keV) runs 1.4 times (3 times) longer than a simulation with the default energy cut of 250 keV.

3.3.6 Influence of atmosphere

As already visible from Fig. 3.12, the refractive index of the atmosphere has an influence on the radiation energy. In the simulation, we specify the refractivity at sea level which is then scaled proportionally to higher altitudes with the air density. To estimate the influence of the air refractivity on the radiation energy we vary the value of $n - 1$. We again simulate at least 20 air showers induced by

Table 3.6: The table shows the normalized radiation energies for different refractivities of the atmosphere. The geometry of the air showers is fixed to a zenith angle of $50°$ coming from south. Each cell shows the mean of at least 20 air showers simulated with the same settings but different random seeds. The uncertainties shown are the uncertainty of the mean, and the standard deviation is shown in brackets.

refractivity at sea level	normalized radiation energy
2.04×10^{-4} (-30%)	9.84 ± 0.04 (0.17) MeV (-10.3%)
2.63×10^{-4} (-10%)	10.63 ± 0.04 (0.18) MeV (-3.1%)
2.77×10^{-4} (-5%)	10.79 ± 0.05 (0.20) MeV (-1.6%)
2.92×10^{-4}	10.97 ± 0.03 (0.21) MeV
3.07×10^{-4} (+5%)	11.12 ± 0.05 (0.21) MeV (+1.4%)
3.21×10^{-4} (+10%)	11.29 ± 0.04 (0.19) MeV (+2.9%)
3.80×10^{-4} (+30%)	11.82 ± 0.05 (0.21) MeV (+7.7%)

iron nuclei for each choice of refractivity for a cosmic-ray energy of $1\,\text{EeV}$ and a fixed geometry as in the previous cross-checks and calculate the normalized radiation energy. The results are presented in Tab. 3.6. A change in the refractivity of +10% (-10%) results in a 3% larger (3% smaller) radiation energy and a change of $\pm 5\%$ in refractivity results in a shift of $\pm 1.5\%$ in radiation energy. We note again that the $\pm 3\%$ ($\pm 1.5\%$) shift in radiation energy would correspond to a $\pm 1.5\%$ ($\pm 0.8\%$) shift in the electromagnetic shower energy, as the radiation energy scales quadratically with the electromagnetic shower energy.

We determine the variations in refractivity using data from the Global Data Assimilation System (GDAS). This system combines several meteorological measurements with numerical weather predictions and provides the main state variables of the atmosphere on a $1° \times 1°$ latitude longitude grid every three hours. Among other things the temperature, pressure and humidity at the surface is provided from which we calculate the refractivity. The yearly fluctuations of the air refractivity at the site of the Pierre Auger Observatory are 7%, and are only 4% and 3% at the LOFAR and Tunka sites, respectively. Hence, this environmental dependence is small compared to current experimental uncertainties. We also calculated the average refractivity at sea level by rescaling the average refractivity at the surface to its value at sea level using the model of the US standard atmosphere. We find a refractivity at sea level of 3.12×10^{-4} for the Pierre Auger and Tunka site and 3.2×10^{-4} for the LOFAR site.

For the site of the Pierre Auger Observatory we also studied the influence of changing atmospheric density profiles. Monthly-averaged density profiles were derived from weather balloon measurements and GDAS data (cf. Chap. 4.3 and [133, 167–169]) and implemented in CORSIKA. For each monthly density profile we simulated at least 20 proton and iron induced air showers with an energy of $1\,\text{EeV}$ and the same fixed geometry as before. We also determined the average refractivity at ground level for each month from the GDAS data, shown in Fig. 3.21 left, and rescaled it to sea level which is the required input of the simulation code. The resulting radiation energies for the different months are presented in Fig. 3.21 right. The yearly scatter in the radiation energy due to changing atmospheric conditions at the Pierre Auger Observatory is 2.5%. This translates to an influence of changing atmospheric conditions onto the cosmic-ray energy of only 1.25%. We can also use this result to correct for this minor dependence on the conditions of the atmosphere.

What is not taken into account in this cross-check is that the refractivity might not scale exactly
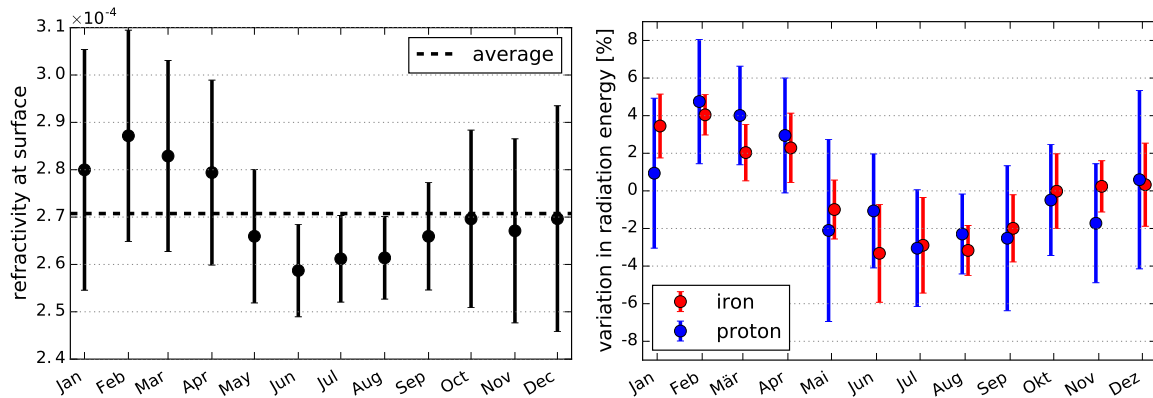
Figure 3.21: (left) Monthly-averaged refractivity at the surface at the Pierre Auger Observatory. The errorbars represent the spread. (right) Variation of radiation energy due to changing atmospheric conditions. Shown is the radiation energy obtained with CoREAS simulations using the monthly density profiles and the corresponding refractivity. The errorbars represent the spread.

with the density to higher altitudes. The height dependence of the refractivity can also be extracted from GDAS data that provide the atmospheric state variables at several heights above ground. However, it is currently not possible to specify a separate refractivity profile in CoREAS as it is expected to have only minor influence on the radio emission.

3.3.7   Independent cross-check with ZHAireS

To cross-check a correct implementation of the underlying physics in the simulation code, the analysis presented above was partly repeated using the ZHAireS simulation code in [170]. In particular, we can verify a correct implementation of

- the shower development using the hadronic and electromagnetic interaction models.
- the modeling of the atmospheric density profiles and the impact of the refractive index.
- the calculation of the radio emission from the particle movement from classical electrodynamics. (CoREAS uses the endpoint formalism [150] whereas ZHAireS uses the ZHS formalism [151].)

The only available hadronic interaction model in ZHAireS is SIBYLL 2.1 [171]. SIBYLL 2.1 is outdated and has been superseded by SIBYLL 2.3 [137]. The former model predicts slightly more radiation energy as the longitudinal shower profile comes out more narrow, so we cannot use this model for an accurate quantitative prediction of the radiation energy. However, we can nevertheless use this model in both CoREAS and ZHAireS to compare the two simulation codes.

In ZHAireS, the variation of the refractivity is not scaled with the air density to higher altitudes but a simplified description is used which models the scaling of the air refractivity with increasing height with a single exponential function. Therefore, we modified the CoREAS code to also use this simplified description.

Another free parameter in the simulation is the thinning level. The implementation of the thinning mechanism is different in the two codes and can therefore not be set to the same value. To exclude the influence of thinning, in [170] a similar study as in Sec. 3.3.5 was performed, where the thinning
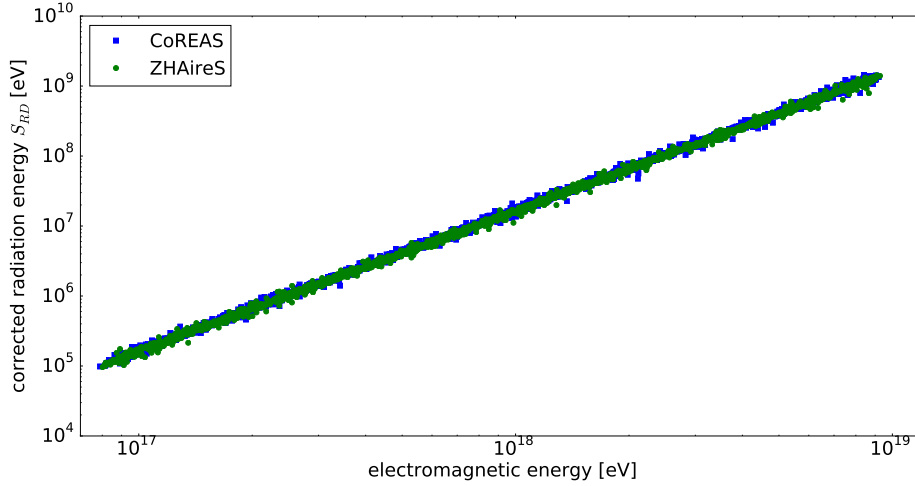
Figure 3.22: Comparison between CoREAS and ZHAireS simulations. The corrected radiation energy is shown as a function of electromagnetic shower energy. Blue dots represent CoREAS simulation and green dots ZHAireS simulations. Figure from [170].

settings were determined such that thinning has only negligible influence on the simulated radiation energy.

With these modifications all free parameters of the simulation can be set to the same value or have been found to have negligible influence on the radiation energy. Hence, we can directly compare the predictions of the radiation energy from CoREAS and ZHAireS. Details of this analysis can be found in [170]. We only highlight the final result which is presented in Fig. 3.22. The dependence of the radiation energy on the incoming direction and position of the shower maximum is corrected according to Eq. (3.24). Then, the corrected radiation energy is plotted versus the electromagnetic shower energy and the parameters A and B of the calibration function (Eq. (3.23)) are determined. The difference in the parameter A obtained from CoREAS and from ZHAireS is the difference in the prediction of the radiation energy. The radiation energies computed by the two independent simulation codes have a difference of only 3.3%. As the radiation energy scales quadratically with the electromagnetic shower energy this corresponds to a difference of only 1.7% with regard to the cosmic-ray energy scale. This difference is much smaller than typical experimental systematic uncertainties in the measurement of the radiation energy of $\mathcal{O}(10\%)$ [126].

3.3.8 Discussion

As soon as the air shower has emitted all its radiation energy, the total radiation energy, i.e., the integral over the signal distribution on the ground, remains constant. In particular, it does not depend on the signal distribution on the ground or on the observation altitude and is thus directly comparable between different experiments.

The radiation energy is well suited to determine the cosmic-ray energy. The radiation energy – corrected for the dependence on the geomagnetic field – correlates best with the energy in the electromagnetic part of the air shower and exhibits quadratic scaling with the electromagnetic shower energy, as is expected for coherent emission. The electromagnetic shower energy can be converted to the pri-

mary cosmic-ray energy using predictions from hadronic interaction models or a direct measurement of the invisible energy fraction.

The radiation energy has a second-order dependence on the air density of the emission region. After correcting this effect, the corrected radiation energy and the electromagnetic shower energy have a scatter of less than 3%. In addition, we developed a more practical parametrization of the dependence between radiation energy and electromagnetic shower energy using only the geometry of the air shower, i.e., without using X_{max} information, and obtain a resolution of 4%. This scatter of 4% is well below current experimental uncertainties.

If the radiation energy is detected at a particular observation height, the air shower may not have released all its radiation energy. The strength of this effect depends on the atmospheric depth between observation height and shower maximum. We presented a parametrization of this effect that can be used in experiments to correctly determine the full radiation energy and thereby estimate the cosmic-ray energy. The radiation energy is influenced less by clipping than the electromagnetic part of the air shower as the radiation energy is released earlier in the shower development.

We studied the effects of specific settings of the air-shower simulation on the radiation energy. We found that the choice of hadronic interaction model has a negligible influence on the radiation energy as well as our choice of thinning level and lower energy thresholds in the simulation. We also checked for the impact of changing atmospheric conditions, i.e., a change in the density profile and the refractivity, and found a scatter of the radiation energy of merely $\sigma = 2.5\%$ within the course of the year.

We conclude that the radiation energy released by extensive air showers is well understood and with the methods and parametrizations developed here, the radiation energy can be used to precisely determine the cosmic-ray energy as well as to cross-calibrate different experiments.

<div style="text-align:right">*4*</div>

Pierre Auger Observatory and its Engineering Radio Array

Parts of this chapter have been published in:

C. Glaser for the Pierre Auger Collaboration
„Results and Perspectives of the Auger Engineering Radio Array"
Proc. of ARENA 2016, Groningen, The Netherlands (2016), arXiv:1609.01513

The Pierre Auger Observatory is the world's largest detector for high energy cosmic rays covering an area of $3000\,\mathrm{km}^2$ [2]. It is located on a vast, high plain in western Argentina known as the Pampa Amarilla (yellow prairie) East of the Andes near the town Malargüe. The area is generally flat with an average height of 1400 m a.s.l. that corresponds to an atmospheric overburden of $875\,\mathrm{g/cm}^2$.

The observatory is designed as a hybrid detector with two baseline components, a large surface detector array (SD) and a fluorescence detector (FD). The SD comprises 1660 water Cherenkov particle-detector stations distributed on a hexagonal grid with a spacing of 1500 m which is overlooked by 24 air fluorescence telescopes positioned at four different sites around the SD array. A map of the array is shown in Fig. 4.1. The SD has a duty cycle of 100% whereas the detection of fluorescence light is restricted to moonless nights with good weather conditions resulting in a duty cycle of 12% at early years [172] that has been increased to ∼15% at the present time [2].

This hybrid design is extended by three high elevation fluorescence telescopes (HEAT) [173] that overlook an infill array consisting of 61 stations with a smaller spacing of 750 m covering an area of $23.5\,\mathrm{km}^2$ in the western part of the array. This extension lowers the full efficiency threshold of the surface detector from 3 EeV (=$10^{18.5}$ eV) [174] by one order of magnitude to 0.3 EeV (=$10^{17.5}$ eV) [175]. Furthermore, the observatory is equipped with a large number of monitoring systems to track the state of the atmosphere above the array. With this information the production as well as the scattering and absorption of fluorescence light can be corrected for environmental influences to precisely reconstruct air showers.

In addition to the extension to lower the energy threshold, several new technologies to detect ultra high energy cosmic rays are explored within the Pierre Auger Observatory. Buried scintillators are installed in the infill region to measure muons separately from electromagnetic shower particles [176]. Several efforts have been undertaken to measure molecular Bremsstrahlung at the Pierre Auger Observatory [177], a predicted isotropic radiation in the GHz regime [178] that is generated in the plasma behind the air-shower front which would allow a measurement of the longitudinal shower profile similar to the fluorescence measurement but with a 100% duty cycle. However, recent measurements
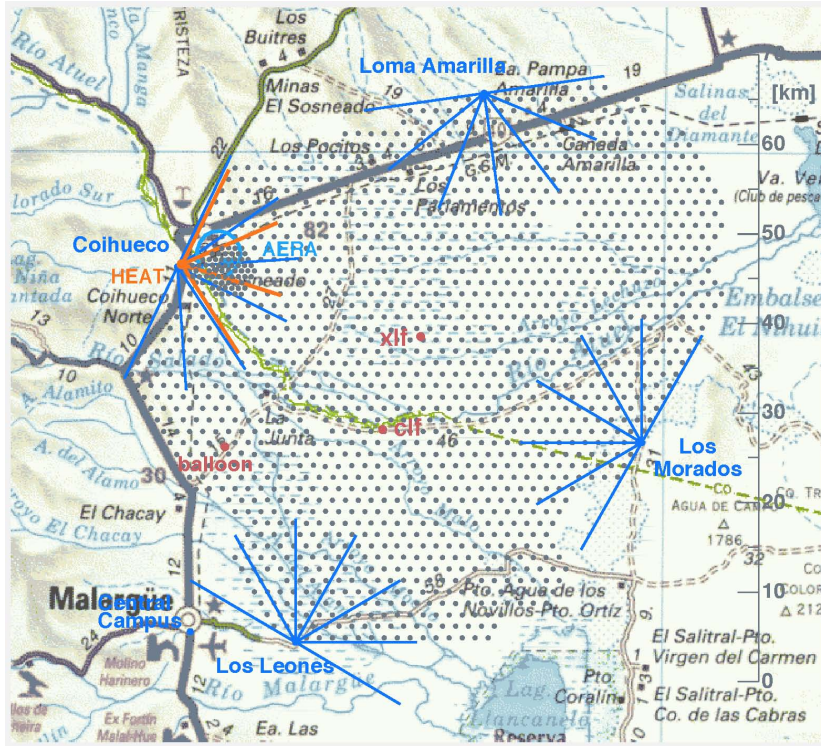
Figure 4.1: Map of the Pierre Auger Observatory. Each dot corresponds to a surface detector station. The field-of-view of the 27 fluorescence telescopes at the fife different sites Los Leones, Los Morados, Loma Amarilla, Coihueco and HEAT are marked with blue lines (yellow lines in case of HEAT).

and calculations show that the intensity of molecular Bremsstrahlung is significantly smaller than than expected [179–181] reducing the feasibility of this approach to measure air showers.

The largest and most successful extension of the observatory is the Auger Engineering Radio Array (AERA) that measures the radio emission from air showers in the 30 - 80 MHz regime [11, 118]. AERA is located in the western part of the array within the infill array of the surface detector and covers an area of $17 \, km^2$ with 153 autonomous radio detector stations. It will be presented in detail in Sec. 4.4.

The Observatory takes data since 2004 and was completed in 2008. Since then it is in successful operation and has recorded data with an exposure exceeding $40{,}000 \, km^2$ sr yr. A complete and comprehensive description of the Pierre Auger Observatory can be found in [2].

In the following we will describe the different detector components in more detail. In case of the fluorescence and surface detector we will also describe briefly how air showers are reconstructed from measured data. The reconstruction of air showers using radio detector data (AERA) will be described in detail in Chap. 5.

4.1 Fluorescence detector

At each of the four sites Los Leones, Los Morados, Loma Amarilla and Coihueco, six air fluorescence telescopes are contained in a clean and climate-controlled building. Each telescope has a field of view of $30° \times 30°$ in azimuth and elevation with a minimum elevation of $1.5°$. The six telescopes have a

combined coverage of $180°$ in azimuth and are oriented towards the interior of the surface detector array.

A sketch of the design of the telescope can be found in Fig. 4.2 left and an actual picture of the interior of the telescope in Fig. 4.2 right. The telescope is build using a Schmidt optic to reduce coma aberration. The ultra-violet (UV) fluorescence light enters through a circular diaphragm with a 1.1 m radius which is covered with a UV filter glass. The transmission of the filter in the relevant UV range from 310 to 390 nm is above 50%. The filter reduces background light of other wavelength and thus improves the signal-to-noise ratio. On the other hand the glass protects the interior of the telescope and keeps the building clean and climate controlled. In addition, the aperture is protected by a shutter that is closed when the telescope is not in operation and by a fail safe curtain to protect the camera from daylight in case of a failure in the telescope control system or a malfunction of the shutter. The aperture is supplemented with a segmented corrector ring with an inner and outer radii of 850 mm and 1100 mm to correct spherical aberration and to eliminate coma aberration [182, 183].

The light is reflected by a $\sim 13\,\text{m}^2$ large segmented spherical mirror onto the camera. The average reflectivity is above 90% for a wavelength of 370 nm. However, the reflectivity decreases by up to 5% due to dust deposit especially on the lower mirror segments that are tilted slightly upwards [2]. Hence, a continuous maintenance is required. The camera comprises 440 pixels arranged in 22 rows and 20 columns. The PMTs have a hexagonal shape that are extended with a simplified Winston cone to minimize the dead area between the pixels. The PMTs have a distance of 45.6 mm from side to side and a corresponding field of view of $1.5°$. The design of the optics is such that a distant point source falling on the camera is well below the size of one pixel which is important to enable the identification of the tracks of fluorescence light created by an air shower.

A multi-stage trigger is implemented to trigger air showers. The first stage is a single pixel trigger where the threshold is dynamically adjusted to a trigger rate of 100 Hz. The second stage searches for tracks of at least five pixels which results in a varying trigger rate of 0.1 - 10 Hz. The third stage is a software algorithm which cleans the hardware triggers from noise events resulting in a trigger rate of 0.012 Hz per FD building. For these triggers also a hybrid trigger for the surface detector is generated.

An end-to-end calibration of the telescopes, i.e., the conversion factors of ADC counts to light flux for each pixel, is performed with a so-called drum calibration [184]. A drum-shaped, pulsed light source that covers the complete aperture is used. The light source provides a uniform illumination of each pixel over the full acceptance of the telescope and its light intensity is calibrated to a precision of better than 4% [185]. The known pulsed photon flux of the drum can then be compared to the ADC pulse integrals to obtain the calibration factors which are approximately 4.5 photons/ADC count. The systematic uncertainty of the absolute FD calibration is 9.9%[1] [186].

Recently, a new calibration method was developed and performed that uses a well-calibrated isotropic light source which is carried by a drone (a octocopter was used in this measurement) into the field-of-view of the FD telescope [187]. So far, one eye of the Los Leones telescope was calibrated in two calibration campaigns in 2014 and 2015. Both campaigns consistently found smaller calibration constants of only $86.8\% \pm 3.8\%$ of the calibration constants obtained with the drum calibration. Such a change in the calibration constants would result in a shift of the reconstructed cosmic-ray energies

---

[1]As the number of photons is proportional to the energy deposit of the air shower, this uncertainty directly propagates into the systematic uncertainty of the cosmic-ray energy measurement.
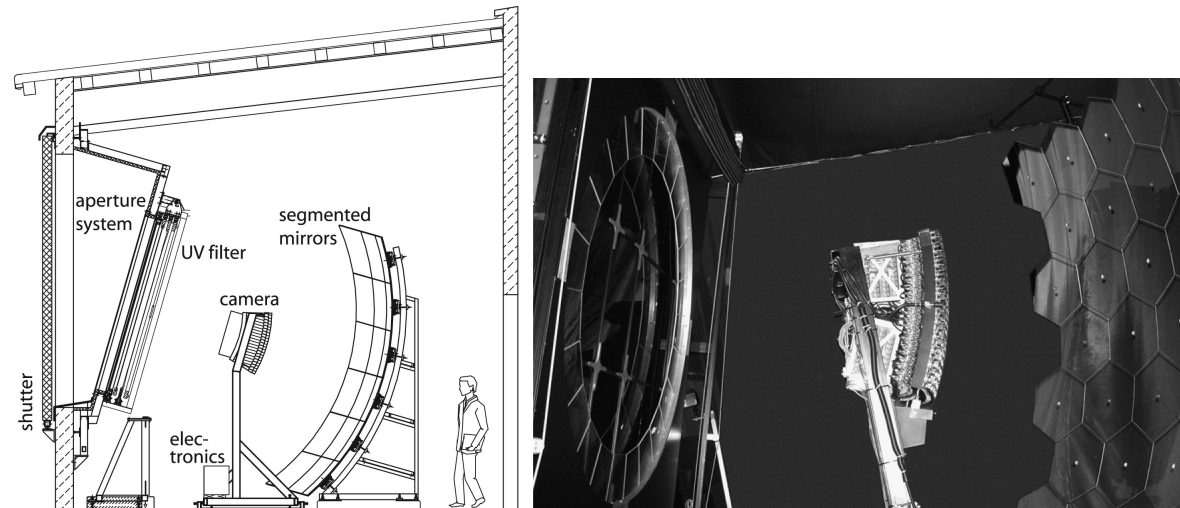
Figure 4.2: (left) Schematic view of a fluorescence telescope with a description of its main components. (right) Photo of a fluorescence telescope at Coihueco. Figures and captions from [2].

of +13.2%.

There is evidence that these new calibration constants describe the response of the FD telescopes to air-shower signals more precisely as this method has several advantages over the drum calibration. On the one hand, a smaller systematic uncertainty of better than 4.6% could be achieved. On the other hand, this measurement realistically resembles the conditions of an air-shower measurement as the light source is seen as a distant point source by the telescope. Qualitative differences between the two calibration methods are, e.g., that the light reflected from the outer UV filter glass can not be scattered back into the telescope as it is the case in the drum calibration. This can result in a significant difference as a dust layer on the filter can easily attenuate 11% of the incoming light. Another difference is that only a single pixel of the camera is illuminated whereas the drum calibration illuminates all pixels isotropically. Thereby, the octocopter calibration is sensitive to the fraction of light that is deflected away from the target pixel into neighboring pixels, i.e., it is sensitive to the point-spread function, which is relevant for air-shower measurements as only signals from a small region around the target pixel are integrated. Hence, scattered light is mostly not taken into account.

To be more comparable to the drum calibration, not only the signal of the pixel of the camera that is illuminated by the octocopter light source is used but also the signals of the surrounding pixels are taken into account. However, this still leads to calibration constants of only $92.5\% \pm 4\%$ of the calibration constants obtained with the drum calibration. The size of the light source as seen by the telescope corresponds to the size of a distant shower, i.e., to high-energy air showers. For less energetic showers (E $\sim 10^{18}$ eV), the showers have smaller distances to the telescope and their relative size is accordingly larger which might lead to different scattering of the light not measured by the octocopter calibration. Hence, high-energy showers would have 13.5% more energy whereas the energy shift for low-energy showers might be less but at least 7.5%. At the time of writing these new results are being discussed within the collaboration but not yet taken into account in the reconstruction.

In addition, three light sources are installed in each telescope for relative calibration [184], e.g., the light from a xenon flash lamp is directed to a Teflon diffuser at the sides of of the camera and
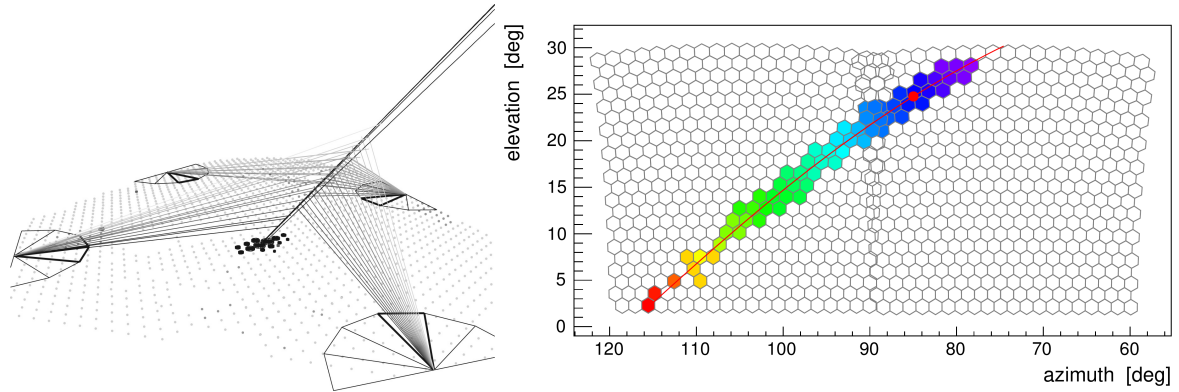
Figure 4.3: (left) Geometry reconstruction of an event observed by four telescopes and the surface detector. Figure and caption from [2]. (right) Combined camera image of an air shower detected by two of the Coihueco fluorescence telescopes. The color indicates the time distribution of the pulses in the shown pixels (purple = early, red = late). The line indicates the reconstructed plane spanned by the shower axis and the fluorescence telescopes. Figure and caption from [115].

directed towards the mirror. From these measurements, the long-term time variations of the calibration constants can be monitored.

The first step to reconstruct an air shower is to subtract the noise from the recorded ADC traces of each pixel. Then the ADC counts are converted to the number of photons at the aperture using the calibration constants obtained via the drum and relative calibration. From the signal times in the different pixels (cf. Fig. 4.3 right for an example) the geometry of the air shower is reconstructed. First, the shower detector plane, i.e., the plane containing the telescope and the air-shower axis is determined. Then, the shower axis is reconstructed using the signal times and the pointing direction of the pixels of the shower track measured in the camera and an additional time information of the surface-detector station with the highest signal to increase the lever arm. A hybrid-event display of an air shower observed from all four FD sites and the surface detector is shown in Fig. 4.3 left.

Then, the detected light as a function of time is determined. To do so, the signals of all pixels within a certain angle that maximizes the SNR (typically $\sim 1.3°$) around the vector from the telescope to the shower center at time i are summed up. The resulting light-at-aperture profile is presented in Fig. 4.4 left. All contributing light sources other than the fluorescence light [188] including Cherenkov light [189, 190] and multiple scattered light [191–193] are determined and subtracted. The remaining fluorescence light is corrected for the attenuation in the atmosphere and converted into the energy deposit of the air shower using the measured fluorescence yield[2] [194–196]. An example of the resulting dE/dX profile of an air shower as a function of slant depth is shown in Fig. 4.4 right. A precise knowledge of the atmospheric conditions at the time of the event is crucial, as the light attenuation in the atmosphere as well as the fluorescence yield depends on the current state of the atmosphere. Therefore the observatory is equipped with a large number of atmospheric monitoring systems that are presented in Sec. 4.3.

---

[2]The fluorescence yield is the conversion factor from energy deposit in the atmosphere to emitted fluorescence light.
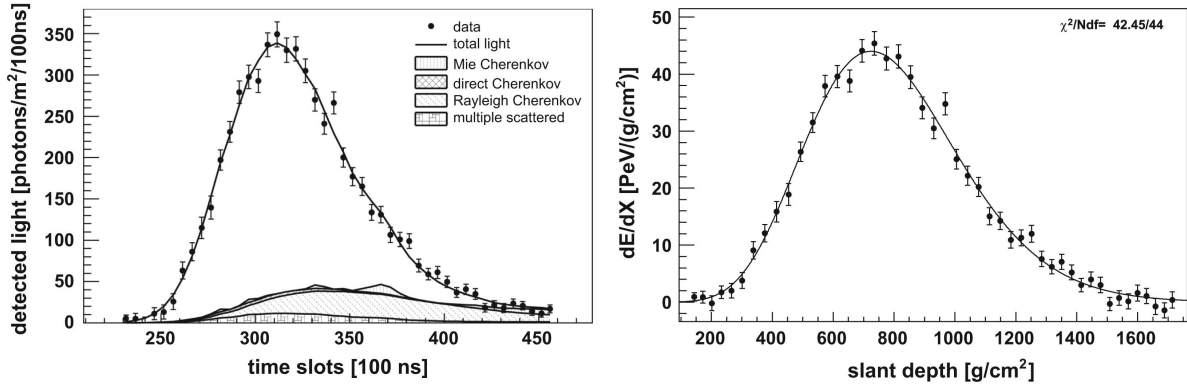
Figure 4.4: Example of a reconstructed shower profile. (left) Light at aperture. (right) Energy deposit. Figures and captions from [2].

A Gaisser-Hillas function [164]

$$f_{\mathrm{GH}}(X) = \left(\frac{\mathrm{d}E}{\mathrm{d}X}\right)_{\max} \left(\frac{X - X_0}{X_{\max} - X_0}\right)^{(X_{\max} - X_0)/\lambda} e^{(X_{\max} - X)/\lambda} \tag{4.1}$$

is fitted to the shower profile. Depending on the quality of the measured profile, the shape parameters X_0 and λ can be fixed to their mean values to allow a transition from a 2 to 4 parameter fit. The parameter $X_{\max}$ denotes the maximum of the longitudinal shower profile. The integral of f_{GH} over X gives the calorimetric shower energy, i.e., the complete shower energy except for the energy carried away by neutrinos and high-energy muons. This *invisible energy* was measured experimentally [117] so that the calorimetric energy can be converted to the energy of the primary cosmic ray in a model-independent way with a systematic uncertainty of 3% at 3 EeV decreasing to 1.5% at higher energies. The total systematic uncertainty on the cosmic-ray energy measurement is 14% at energies above 1 EeV [186] and increases to 16% at 0.3 EeV.

Auger High Elevation Telescopes   In addition to the 24 regular FD telescopes, three *Auger High Elevation Telescopes* (HEAT) [173] are installed 120 m in front of the Coihueco telescopes and form an independent fifth site (see Fig. 4.1). The three HEAT telescopes are situated in three tiltable buildings and cover an elevation of $30°$ to $58°$ if operated in tilted mode, thereby extending the field-of-view of the Coihueco telescopes by almost $30°$ in elevation. A photo of the three buildings in tilted mode can be found in Fig. 4.5 left. The design to tilt the whole building instead of directly building a telescope with a different elevation range has several advantages. Basically the same design as the regular FD telescopes can be used and the non-tilted operation mode can be used for calibration as then the field-of-view of HEAT and the regular Coihueco telescopes overlap.

The main objective of HEAT is to lower the energy threshold of FD by observing nearby low-energy showers that develop earlier in the atmosphere. HEAT overlooks the 750 m SD array so that a large number of hybrid events can be obtained. In the data analysis, the HEAT telescopes can be combined with the Coihueco telescopes if the shower was visible in both telescopes. An example of such an event is presented in Fig. 4.5 right.
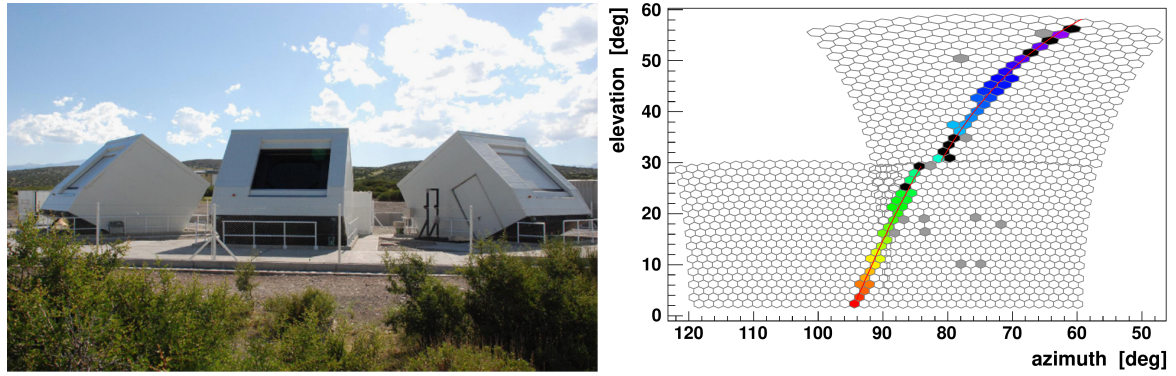
Figure 4.5: (left) Photo of the three HEAT telescopes in tilted mode. Figure and caption adapted from [2]. (right) Example of a low-energy event recorded in coincidence with HEAT and two Coihueco telescopes. The plot shows the camera image of the recorded signal. The arrival time of the light is color-coded (blue early, late red). Figures and captions adapted from [173].

4.2 Surface detector

The water Cherenkov particle-detector stations of the surface detector have a diameter of 3.5 m and a height of 1.2 m. A photo of such a SD station is shown in Fig. 4.6 left. The water tank contains a sealed liner with a reflective surface that is filled with 12,000 l of ultra-pure water. The air-shower particles on ground are measured by Cherenkov light that is generated in the water as the shower particles move faster than the speed of light in water through the water. The height of 1.2 m results in a good sensitivity also to inclined showers which is a significant advantage compared to flat scintillators. The extend in height makes the detector also sensitive to photons as they can convert in the water volume to an electron positron pair.

Each detector station is equipped with three 9 inch diameter photo multiplier tubes (PMTs). Each PMT has a high and a low gain channel and the analog signal is digitized with 40 MHz. Each station operates autonomously. The stations are powered with a solar system that delivers 10 W on average. Accurate time synchronization is obtained with a GPS receiver and communication is handled by a custom Wireless Large Area Network (WLAN) operating in the 902 to 928 MHz ISM band.

Apart from calibration and monitoring triggers, two different air-shower triggers are implemented on station level. A single-bin threshold trigger is efficient for stations that are near the impact point of an air shower but is also contaminated by small showers. Currently, a signal of $2 \times I_{\text{VEM}}$ (the signal that corresponds to two vertical equivalent muon (VEM)) in two high gain channels is required which results in a trigger rate of 100 Hz. In addition, a time-over-threshold (ToT) trigger is implemented that selects a sequences of small signals spread in time and is thus efficient to showers incident far away from the station and has a rate of a few Hz. This trigger requires a single bin exceeding $0.2\,I_{\text{VEM}}$ in at least 12 samples in a sliding window of 3 μs length (120 samples) in two of the three PMTs.

The local station triggers are combined by the central data acquisition system (CDAS). The main air-shower trigger requires a time and spacial coincidence of multiple SD stations. First, a preliminary time coincidence of ± 25 μs of at least three station triggers are required. Stations that pass this cut are checked for spacial coincidence. To determine spacial coincidences, concentric hexagons centered in each station are defined. Two different modes to check for spacial coincidences are used. The
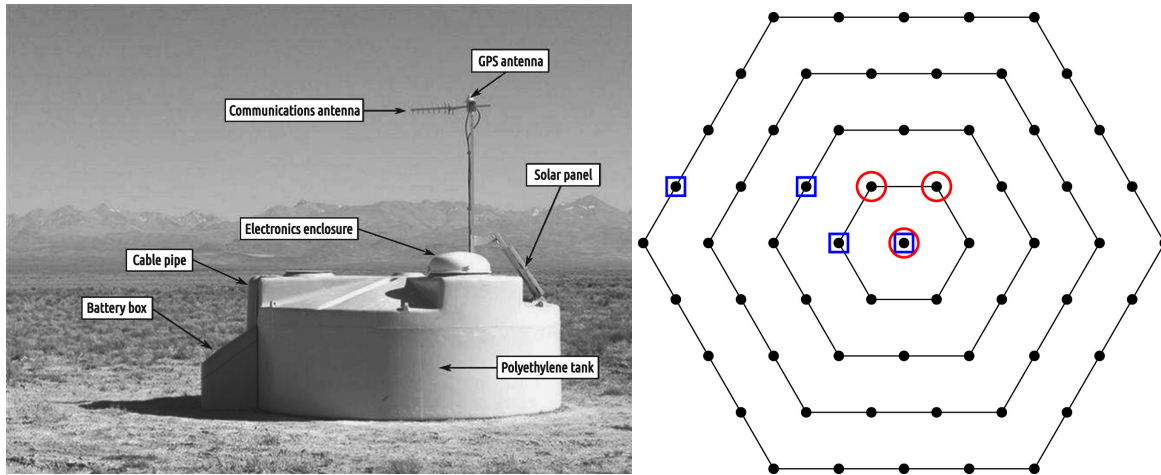
Figure 4.6: (left) A schematic view of a surface detector station in the field, showing its main components. (right) Sketch of the spatial trigger requirements. Four hexagons around a central surface station are depicted. Two examples of the topology of triggers are shown: a 4-fold coincidence in which the triggered stations are identified by open blue squares, and a 3-fold coincidence identified by open red circles. Figures and captions adapted from [2].

first requirement are three ToT (3ToT) triggers with minimum compactness, i.e., one of the triggered station must have one of the other stations in the first hexagon of neighbors and the other station within the second hexagon. See Fig. 4.6 right for an illustration of the required geometry. The second requirement is more permissive and requires four local station triggers with moderate compactness. One of the triggered stations is allowed to be within the 4th hexagon if one station is withing the 2nd and another is in the 1st hexagon around the remaining station. If a spacial coincidence has been found, a more stringent timing criteria is applied. All station triggers must be within $(6 + 5n)\,\mu$s of the central station where n is the number of the hexagon. If also this trigger condition applies, the measured FADC trace of $30\,\mu$s length is requested from all participating stations and sent via WLAN. The trigger rate is 0.1 Hz resulting in 3 million SD events per year. In addition, also a trigger from the FD can be received. The trigger delay is ~ 1 s and a roughly estimated geometry of the air shower is already available. With this information, the SD stations that are near the shower impact point are determined and a corresponding event is formed. The resulting trigger efficiency depends on the energy of the air shower and is shown in Fig. 4.7 right. The 1500 m spaced SD array is fully efficient above 3×10^{18} eV and the 750 m spaced SD array is full efficient above 3×10^{17} eV [175] for air showers with incoming directions of less than $60°$ and $55°$ zenith angle, respectively. A reconstruction algorithm for horizontal showers have been implemented only for the 1500 m spaced array so far. The full-efficiency threshold of horizontal air showers is 4×10^{18} eV [197].

The reconstruction of air showers from surface-detector data is based on the size and the time of the signals in multiple detector stations. The information of all three PMTs is combined to determine the signal size in VEM and the signal arrival time. Two additional triggers are applied offline before reconstruction. A trigger based on time coincidences deselects stations with incompatible timings that are mainly caused by hits from unrelated muons. The cut is optimized such that 99% of the stations containing a signal from the air shower are kept [2]. The second trigger selects only events having an impact point of the shower (the shower core) within the array. The so-called 6T5 trigger requires the
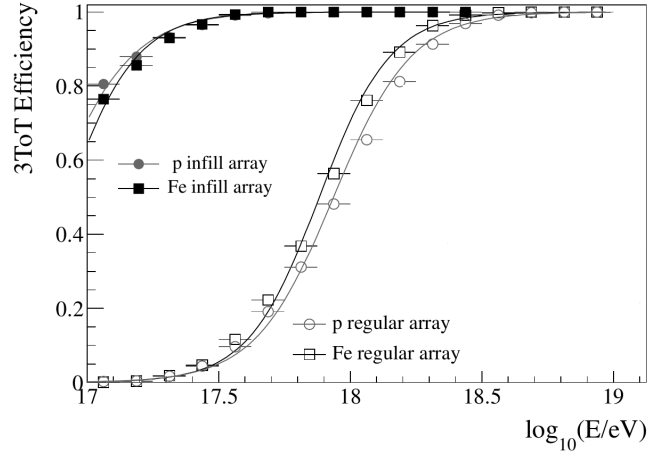
Figure 4.7: 3ToT trigger efficiency for vertical showers of the infill ($\theta < 55°$) and regular ($\theta < 60°$) array obtained from simulations of iron and proton primaries. For inclined air showers ($\theta > 60°$) the $1500\,\text{m}$ spaced SD array is full efficient above $4 \times 10^{18}\,\text{eV}$ [197]. Figure and caption adapted from [175].
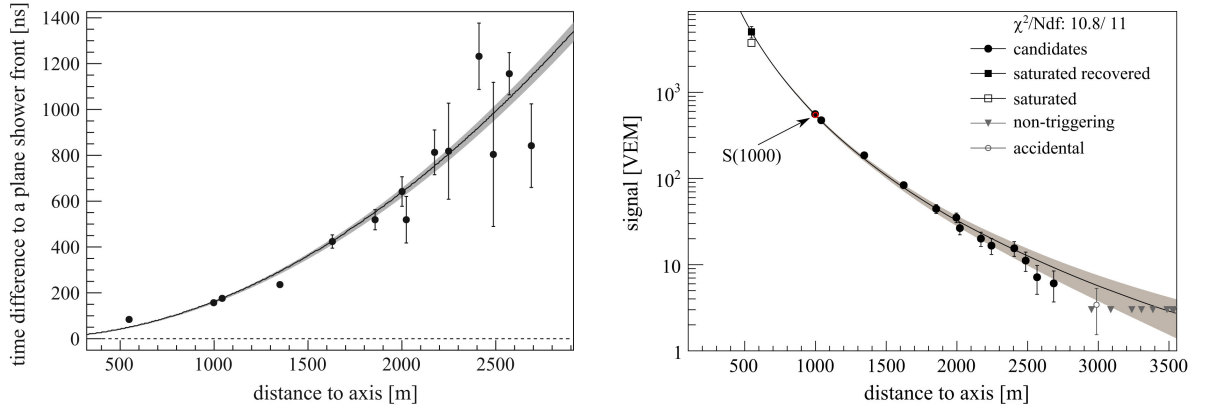
Figure 4.8: Reconstruction of shower geometry. (left) Dependence of signal start times (relative to the timing of a plane shower front) on perpendicular distance to the shower axis. The shaded line is the resulting fit of the evolution model and its uncertainty. (right) Signal size as a function of distance to shower axis. Figures and captions from [2].

station with the largest signal to be surrounded by a hexagon of active (currently working) stations. This cut allows for an accurate reconstruction of the shower core and enables a simple calculation of the exposure [174] which is, e.g., required is the determination of the energy spectrum [198].

The incoming direction of the air shower is reconstructed by triangulation using the signal times in multiple detector stations. First, a plane wavefront is assumed and in case of enough triggered stations a spherical wavefront is fitted to the signal times. The measured signal times of one air shower is shown in Fig. 4.8. The angular resolution of the incoming direction is $1.6°$ for events with at least three stations and reduces to $0.9°$ for events with more than 5 stations [199]. In case of the infill array with smaller detector spacing of $750\,\text{m}$ the angular resolution varies between $1.3°$ and $0.7°$ depending on the cosmic-ray energy and zenith angle [175].

The reconstruction of the core position and the energy of the cosmic ray is different for vertical and horizontal showers. The amount of atmosphere traversed by the air shower gets larger with in-

creasing zenith angle θ and scales approximately with $1/\cos\theta$ (cf. Appendix D). Therefore, the signal of inclined showers is mostly due to high-energy muons as the bulk of the electromagnetic part of the air showers is already absorbed in the atmosphere. In addition, the footprint is asymmetric as the muons travel long distances and get deflected in the geomagnetic field which requires a different analysis strategy than for vertical showers [197]. The zenith angle threshold is $60°$ for the 1500 m array and $55°$ for the 750 m array. We will first discuss the reconstruction of vertical showers and discuss horizontal showers at the end of this section.

In case of vertical air showers, the core position and the energy of the cosmic ray is determined from the signal distribution (cf. Fig. 4.7 left). A modified Nishimura-Kamata-Greisen (NKG) function [200, 201] of the form

$$S(r) = S_{r_{\text{opt}}} \left(\frac{r}{r_{\text{opt}}} \right)^{\beta} \left(\frac{r + r_1}{r_{\text{opt}} + r_1} \right)^{\beta + \gamma} \tag{4.2}$$

is used as the lateral distribution function (LDF) with $r_1 = 700$ m. The distance r_{opt} is the optimal distance that depends on the geometry of the detector. In case of the SD array with 1500 m spacing the optimal distance is $r_{\text{opt}} = 1000$ m [202]. For the infill array with smaller detector spacing of 750 m the optimal distance reduces to $r_{\text{opt}} = 450$ m [175]. The parameters β and γ determine the shape of the LDF. The parameter $S_{r_{\text{opt}}}$ is an estimator of the showersize. At the optimal distance r_{opt} it has the smallest dependence on the shower geometry and development and can be used as an estimator for the cosmic-ray energy.

For a fixed shower energy, the showersize parameters S_{1000} and S_{450} depend on the zenith angle of the air shower as for larger zenith angles the shower traverses more atmosphere and is therefore stronger attenuated. This effect is partly reduced by the fact that muons traverse the water Cherenkov detector more horizontally with larger zenith angle and will therefore emit a stronger signal because the signal of a muon is roughly proportional to the length of water crossed. The dependence of the showersize on the zenith angle is determined experimentally using the constant intensity cut (CIC) method [203]. In this method an isotropic cosmic-ray flux at the top of the atmosphere is assumed. Then the number of events exceeding a certain showersize should be the same in each zenith angle bin if normalized to the corresponding solid angle. The minimum showersize is chosen such that the detector is fully efficient over the considered zenith angle range. In this way the attenuation can be determined directly from the measured data. In case of a changing chemical composition of the cosmic rays with energy, the CIC method is not independent of the cosmic-ray energy and thus only an approximation that, however, works well in the energy range of interest [204].

The showersize S_{1000} (S_{450}) that depends on the energy E and zenith angle θ of the shower is normalized to an average zenith angle of $38°$ ($35°$) using the attenuation function $f_{\text{CIC}}(\theta)$

$$S_{38}(E) = S_{1000}(E, \theta)/f_{\text{CIC},1000}(\theta) \tag{4.3}$$

$$S_{35}(E) = S_{450}(E, \theta)/f_{\text{CIC},450}(\theta). \tag{4.4}$$

The attenuation curve is described best with a third order polynomial in $x = \cos^2\theta - \cos^2 38°$ ($x =$
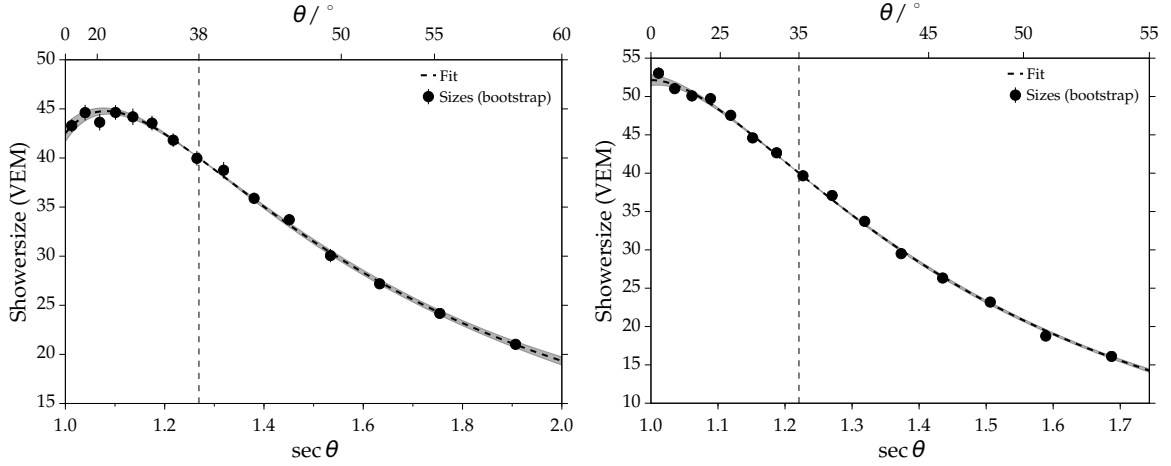
Figure 4.9: Dependence of showersize $S(r_{\mathrm{opt}})$ on the zenith angle obtained with the constant intensity cut method as used for the energy spectrum presented in [49]. (left) CIC curve for the 1500 m SD array. (right) CIC curve for the 750 m SD infill array.

$\cos^2\theta - \cos^2 35°$). The result for the 1500 m (750 m) array is shown in Fig. 4.9 and reads

$$f_{\mathrm{CIC},1000}(\theta) = 1 + (0.956 \pm 0.044)x + (-1.625 \pm 0.086)x^2 + (-1.21 \pm 0.47)x^3 \tag{4.5}$$

$$f_{\mathrm{CIC},450}(\theta) = 1 + (1.621 \pm 0.035)x + (-1.455 \pm 0.089)x^2 + (-2.03 \pm 0.47)x^3. \tag{4.6}$$

The energy estimators S_{38} and S_{35} are then calibrated using a sample of high-quality hybrid events that have been measured both in the surface and fluorescence detector. Only events above the full-efficiency thresholds are considered. The resulting calibration curves are presented in Fig. 4.10. The relation between the energy estimators and the cosmic-ray energy is described with a power law of the form $E_{\mathrm{FD}} = A \times S_{38,35}^{B}$ that is fitted to the data using a tailored maximum-likelihood method [205] that takes into account all measurement uncertainties and the expected event distribution due to the steeply falling energy spectrum.

The core position and energy of the air shower of inclined events ($\theta > 60°$) is obtained by fitting reference 2D muon distributions on ground to the recorded signals [197]. A scaling parameter N_{19} is introduced that scales the measured signals to the reference distribution for a given incoming shower direction and corresponds to the average muon number of a proton shower with an energy of 10^{19} eV. The reference muon distributions have been obtained from air-shower simulations using QGSJetII-03. The full efficiency threshold of the 1500 m array for inclined shower is 4 EeV. A modification of this reconstruction technique for the 750 m array has not yet been performed.

As the parameter N_{19} is by construction independent of the zenith angle, it can be directly used as cosmic-ray energy estimator and calibrated using the energy measurement of the FD. The corresponding calibration curve is presented in Fig. 4.10 and the same method as for vertical events is used to fit the calibration curve. The cross-calibration showed that the simulations have a deficit of muons at the ground compared to the measured data [197].

An analysis especially interesting for an accurate determination of the absolute energy scale is the measurement of the invisible energy fraction, i.e., the amount of shower energy going into neu-
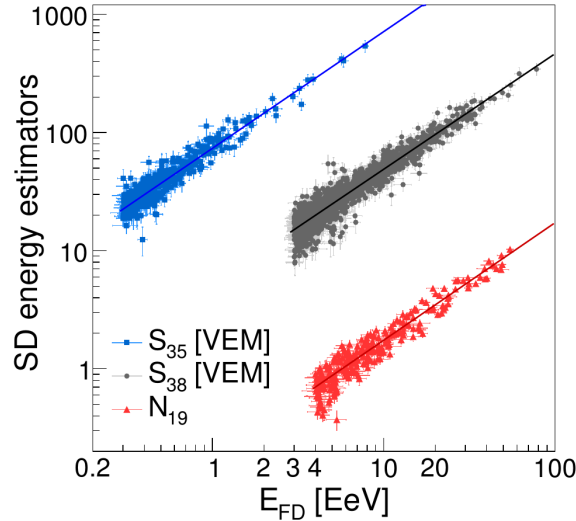
Figure 4.10: Correlation between the energy estimators (see text) and the FD energy. S_{38} and S_{35} are given in units of Vertical Equivalent Muon or VEM, corresponding to the signal produced by a vertical muon traversing the detector through its center. Since N_{19} is a scaling factor it is dimensionless. Figure and caption from [49].

trinos and high-energy muons which is accordingly not visible in the FD. A hybrid measurement of inclined showers using FD and SD can be used to determine the invisible energy experimentally. The FD measures only the electromagnetic part of the air shower whereas the N_{19} parameter is a direct measurement of the number of high-energy muons. Most of the muons originate from charged-pion decays ($\pi \rightarrow \mu + \nu_\mu$) (and to a 10 times smaller extend from kaon decays) and are therefore directly correlated with the number of neutrinos. Exploiting these two independent measurements, the invisible energy as a function of calorimetric shower energy can be obtained with a systematic uncertainty of 3% at 3 EeV decreasing to 1.5% at higher energies [117].

4.3 Atmospheric monitoring

A precise and continuous monitoring of the atmospheric conditions above the Pierre Auger Observatory is crucial for a correct reconstruction of measured air showers as the atmosphere is used as a giant calorimeter [133, 167, 168, 206]. The state of the atmosphere affects primarily the measured fluorescence light but also the surface detector is influenced by changing atmospheric conditions as the air density near the ground alters the lateral signal distribution of the electromagnetic component of the shower [207]. Although the site of the observatory has generally good viewing conditions, an extensive program to monitor the atmosphere is required to achieve an accurate reconstruction of air showers. It is especially important for an accurate calibration of the absolute energy scale of cosmic rays and will therefore be presented in some detail in this thesis. Later we will see that most of the atmospheric monitoring efforts are not necessary for radio detection of air showers as the radiation energy emitted by the air shower is basically independent of changing atmospheric conditions and requires only very basic monitoring.

The FD measurement depends in several ways on the properties of the atmosphere. On the one hand, the fluorescence yield itself, i.e., the conversion between deposited shower energy in the atmo-

sphere to emitted fluorescence light, depends on the state of the atmosphere [188, 208–210], as well as the longitudinal development of the air shower [133, 208]. On the other hand, the scattering and absorption of the emitted fluorescence light depends on the atmospheric state variables, the amount and properties of aerosols and the cloud coverage. A large number of different monitoring system have been installed at the observatory to measure different properties of the atmosphere and are briefly summarized in the following. A more detailed description can be found in [2] or in the references given in the following paragraphs.

In Fig. 4.11 an overview of the different monitoring systems and their position in the Auger array is shown. Ground-based weather stations are installed at each FD building and at the central laser facility (CLF) and provide pressure, temperature, humidity and wind information at ground level. More important than a measurement of the atmospheric state variables at ground are the atmospheric profiles of temperature, pressure and humidity up to 20 - 25 km a.s.l. from which the relevant quantities such as air density or atmospheric depth can be calculated. During 2004 and 2010 more than 300 profiles were measured using meteorological radiosondes attached to weather balloons [167]. The upper limit of the profile was typically at 23 km, determined by the height of the burst of the balloon. From these measurements monthly atmospheric profiles were derived [167, 168] and also implemented into the air-shower simulation software CORSIKA [140]. Later, the time and cost expensive balloon launching program was superseded by the usage of data from the Global Data Assimilation System (GDAS) which is an atmospheric model that combines several meteorological measurements with numerical weather predictions and provides the main state variables of the atmosphere on a $1° \times 1°$ latitude longitude grid every three hours [133]. The validity of GDAS data was verified with the data obtained from the balloon program.

The measurement of aerosols and clouds are the most dynamic monitoring challenge. These measurements are needed to determine the optical transmission properties across the Auger array which is then used in the reconstruction to relate the light measured at the telescope to the light generated along the shower axis [168, 206]. The aerosol optical depth profiles are measured hourly by the central laser facility (CLF) [211] and eXtreme Laser Facility (XLF) [212]. Both facilities comprise a Q-switched frequency tripled YAG laser with a wavelength of 355 nm which corresponds to the center of the nitrogen UV spectrum. The energy per pulse is 7 mJ which corresponds roughly to a 100 EeV air shower in light intensity in the atmosphere. During FD data taking, every 15 minutes a set of 50 vertical laser shots is fired into the atmosphere and observed by the four FD sites. The aerosol vertical optical depth, which is the integral of the aerosol extinction from the ground to a point at a given altitude, observed at a given elevation angle, is then determined by a comparison of the 50-shot averages to the average situation at clear conditions or to simulations [212]. In addition, the heights of clouds directly above the CLF and XLF can be determined from this measurement.

Furthermore, the scattering of fluorescence and Cherenkov light occurs over a large range of scattering angles and the angular distribution (phase function) can only be estimated analytically for the atmospheric molecular component but must be measured for the aerosol component [206]. Therefore, a collimated xenon flash lamp with a wavelength between 350 and 390 nm is used to direct light horizontally through the field of view of the Coihueco and Los Morados telescopes. The FD measures then the light as a function of scattering angle. The data taken over several years was used to parametrize the phase function analytically in a version for nights with Mie scattering and version for clear nights
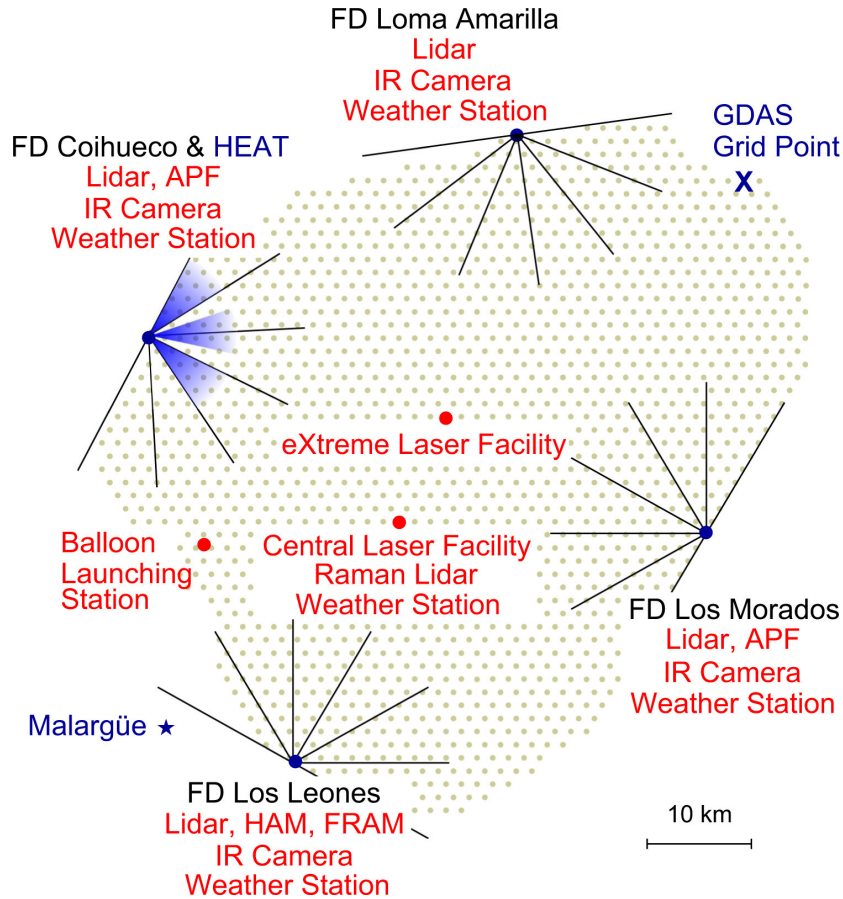
Figure 4.11: Schematic overview of the atmospheric monitoring devices installed at the Pierre Auger Observatory. At each FD site, there is a lidar station, a ground-based weather station, and an infrared camera for cloud cover detection. In addition, there are devices for measuring the Aerosol Phase Function (APF) at FD Coihueco and Los Morados and a Horizontal Attenuation Monitor (HAM) at FD Los Leones. A steerable backscatter elastic lidar system is installed at each of the 4 FD sites to measure aerosols and the positions of clouds near each site. At central positions within the surface detector array, two laser facilities are installed (CLF and XLF). These instruments, together with the FD, are used to measure aerosol optical depth in the line of sight of each FD telescope 4 times per hour. Near the western boundary of the array, the Balloon Launching Station (BLS) was assembled. From this launch station, the weather balloons were typically carried across the entire array by westerly winds. Figure and caption adapted from [2].

[213].

The aerosol attenuation also depends on the wavelength and is modeled by a falling exponential with an exponential parameter γ that is typically 4 for clean air. This parameter is measured at the observatory by a so-called Horizontal Attenuation Monitor (HAM). The HAM is a system of a high intensity discharge lamp installed close to the FD site at Coihueco and a CCD camera at Los Leones to measure the light about 45 km away. An average value of $\gamma \approx 0.7$ was obtained which corresponds to desert-like conditions [206].

The presence of clouds within the field-of-view of the FD has two opposite effects. On the one hand, clouds generally attenuate the fluorescence light but they also enhance the scattering of intense Cherenkov light which can, depending on the geometry, lead to an increase in the detected light [214]. At each FD building an infrared camera is installed which measures clouds by their temper-

ature which is warmer than the surrounding atmosphere. This method serves for creating a binary image (cloudy/clear) of the sky which is mapped on the pixels of the FD camera to indicate the presence or absence of clouds in each pixel. In addition, also data from the Geostationary Operational Environmental Satellites (GOES) is analyzed [215]. GOES data is available every 30 minutes and provides radiance data in several frequency (visible and infrared) bands that can be used to create cloud coverage probability maps with a grid of 2.4 km by 5.5 km pixel size.

At each FD site an elastic lidar is installed to measure cloud cover, cloud height and aerosols [216, 217]. Each lidar is continuously operated during FD data taking by one of the two "shifters" (personnel that is operating the FD during data taking) and hence requires significant man-power. A lidar (=light detection and ranging) is similar to a radar (=radio detection and ranging) but uses laser light instead of radio waves. Each lidar is equipped with a Nd:YLF laser that produces 0.1 mJ pulses at a wavelength of 351 nm with a repetition rate of 333 Hz. The backscattered light is detected with a mirror optic on a PMT. The system is steerable and normally points outside the FD field to not interfere with the FD data taking, except for horizontal shots to determine the horizontal aerosol attenuation and shots fired into the direction of interesting cosmic-ray candidates to probe the detector-shower plane.

4.4　Auger Engineering Radio Array

The Auger Engineering Radio Array (AERA) is the radio extension of the Pierre Auger Observatory, located in its western part within the $750\,\mathrm{m}$ spaced surface detector array and in the field of view of the Coihueco and HEAT fluorescence telescopes (cf. Fig. 4.1). In its current stage of expansion it covers an area of $17\,\mathrm{km^2}$ and consists of more than 150 autonomously operating radio detector stations (RDS) sensitive to the frequency range of 30 to $80\,\mathrm{MHz}$. A map of AERA is presented in Fig. 4.12. AERA measures air showers with energies above $10^{17}\,\mathrm{eV}$ which coincides with the energy thresholds of SD and HEAT and thus allows for a coincident detection of air showers.

As AERA is an engineering array, different detector types have been designed, tested and installed in the field. Therefore, AERA contributes to many different engineering and scientific aspects which are discussed in detail in Sec. 4.4.6. To cope with the diversity of the array and the corresponding inhomogeneities and increased complexity in data handling and analysis, a flexible and robust reconstruction software was developed (cf. Chap. 5 and [218, 219]) that can cope with different detector responses and data formats of the individual RDS as well as with a time-varying detector layout.

AERA was deployed in three stages of expansion. During the austral summer 2011, the first 24 stations were installed on a $144\,\mathrm{m}$ triangular grid covering an area of $0.4\,\mathrm{km^2}$ (AERA24). In the austral spring 2013, 100 additional RDS were installed on a $250\,\mathrm{m}$ and $375\,\mathrm{m}$ triangular grid now covering $6\,\mathrm{km^2}$ (AERA124) and two years later in 2015 again 29 additional RDS were installed on a $750\,\mathrm{m}$ triangular grid increasing the total instrumented area to $17\,\mathrm{km^2}$ (AERA153).

4.4.1　Antenna designs

Each RDS consists of two antennas integrated in one mechanical structure. The antennas are horizontally polarized and perpendicularly aligned to each other. One antenna is aligned into the magnetic north-south direction and the other into the east-west direction with a precision of better than $1°$ [220]. A measurement of the radio signal in two polarizations is necessary to reconstruct the incident electric-field pulse from an air shower (cf. Sec. 5.3). The most obvious difference in the RDS design is a change of the antenna between the first and the succeeding expansion stages. The first 24 RDS use a log-periodic dipole antenna (LPDA) whereas the rest of the RDS use a so-called butterfly antenna.

A photo and technical drawing of the LPDA is shown in Fig. 4.13. The LPDA consists of nine dipoles with different lengths to achieve a broadband sensitivity in the 30 - $80\,\mathrm{MHz}$ interval. The different dipoles are mounted at different heights to a pole in the middle of the dipoles and are connected to a waveguide inside the pole. The largest dipole arm is located at the bottom and has a length of $2125\,\mathrm{mm}$ to each side which coincides to half the wavelength that corresponds to $35.3\,\mathrm{MHz}$ whereas the smallest dipole at the top has a length of $735\,\mathrm{mm}$ to both sides which corresponds to half the wavelength of $102\,\mathrm{MHz}$. The height differences of the dipoles are adjusted such that the signals interfere constructively at the so-called footpoint which is a position on the waveguide at the top of the antenna. A detailed documentation of the design criteria of the LPDA can be found in [220, 221].

The largest dipole is integrated in an aluminum support rod. The rest of the dipole arms are implemented as wires that are stretched between the main pole and a rope that is spanned from the upper to the lower aluminum support rod. Enough tension of the wires is guaranteed by springs between the wire and the rope. This design was chosen to sustain the strong winds occurring in the
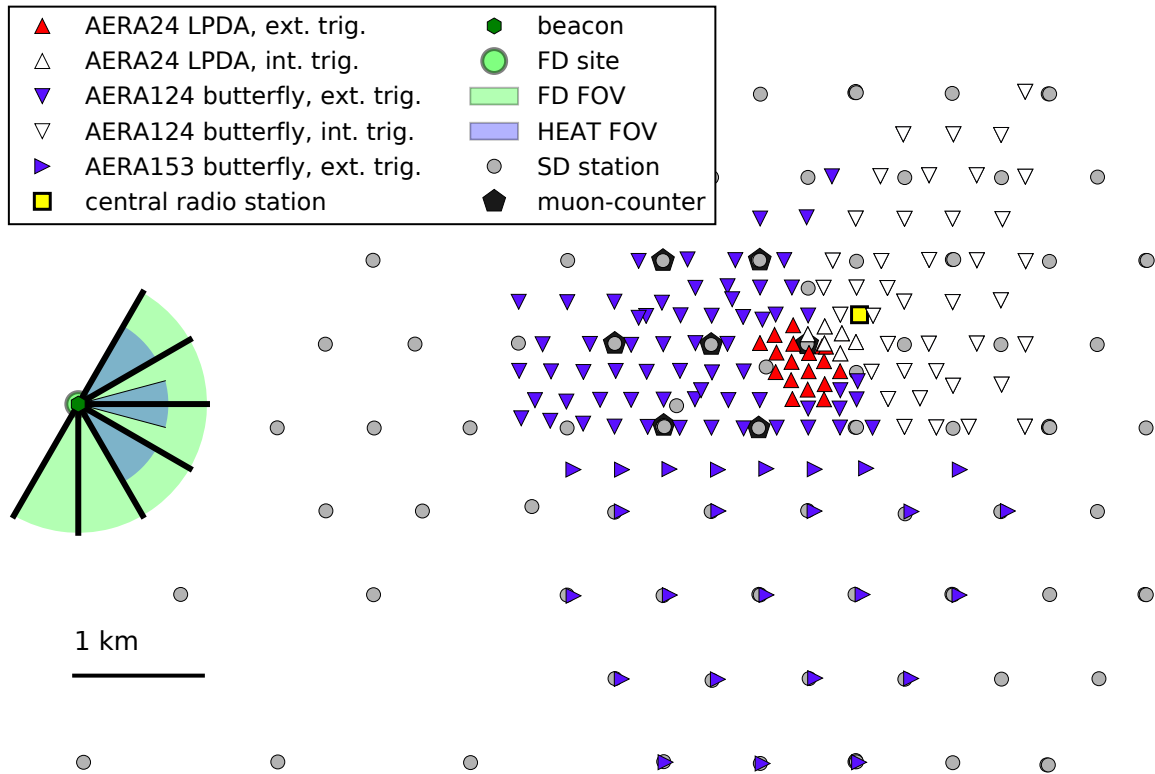
Figure 4.12: Map of AERA within the Pierre Auger Observatory. The radio detector stations (triangles) equipped with different antennas and digitizing hardware are surrounded by surface detector stations (gray filled circles) and underground muon counters (black pentagons). AERA is in the field of view of the Coihueco and HEAT fluorescence telescopes. The orientation of the triangles indicate the three stages of expansion, upturned triangles the first (AERA24), down-turned triangles the second (AERA124) and right-turned triangles the third stage of expansion (AERA153). The color of the triangles indicate the version of the electronics. Figure adapted from [118].

Argentinian Pampa. If the dipole arms had been implemented as solid rods, they would start to swing in the wind and break [222]. In contrast, the design developed for AERA was proven to be very robust and sustains well the extreme climate conditions at the AERA site. The LPDA itself has a total height of $3.6\,\mathrm{m}$ and is mounted at a height of $\sim 1.5\,\mathrm{m}$. Despite its large outer dimensions, the antenna can be transported easily due to its folding mechanism. Once the lower four tensioning ropes are loosened, the aluminum support rods can be folded upwards.

The optimal place for the low-noise amplifier (LNA) is the footpoint of the antenna as faint signals should be amplified as soon as possible. However, due to practical reasons and as the footpoint of the LPDA is at $\sim 5\,\mathrm{m}$ height above ground, the signal is guided through a coaxial cable to the bottom of the LPDA. The LNA is then placed in a small housing at the bottom of the LPDA (cf. Fig. 4.13 right) and is thus covered from environmental influences and easily accessible for maintenance. This is necessary as lightning strikes that hit the antenna or a region nearby can damage the LNA.

For the LPDA a dedicated LNA was developed [223] which matches the characteristics of the LPDA. Hence, an individual inspection of the LPDA and LNA response is not meaningful and the antenna and the LNA is treated as one combined part. If we refer to the antenna response in the following we mean the combined response of antenna and LNA.
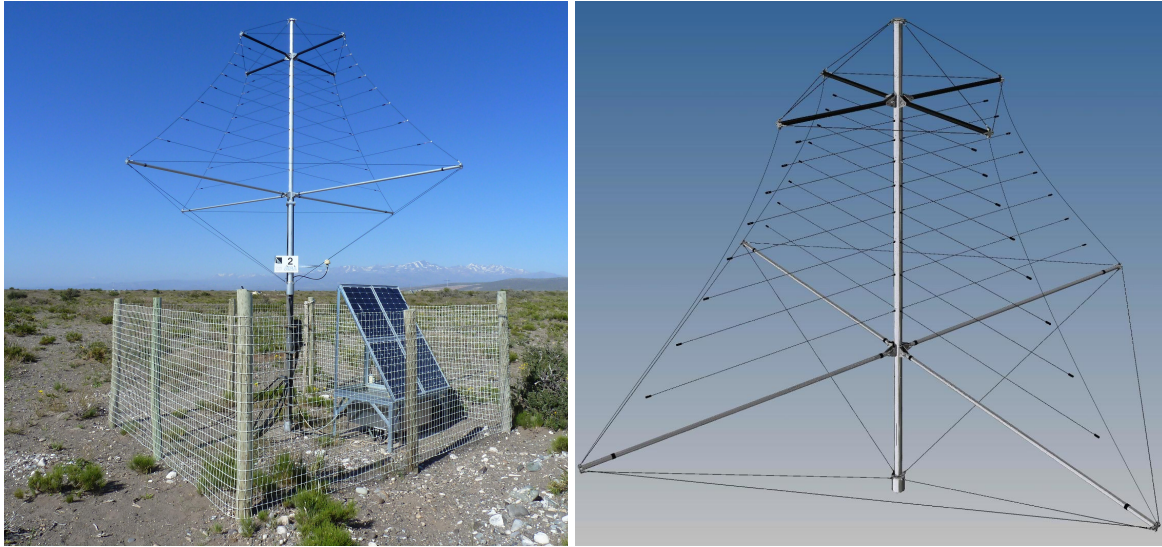
Figure 4.13: The log-periodic dipole antenna (LPDA) of the Auger Engineering Radio Array. (left) Photo of one of the LPDA stations installed in Argentina. (right) Technical drawing of the antenna design. Figure from [221].

At the rest of the AERA stations, the so-called butterfly antenna is used which is presented in Fig. 4.14. It is a broad-band dipole antenna of the family of bow-tie antennas. Its radiator are two triangular arms of $1139\,\mathrm{mm}$ length and a height of $754\,\mathrm{mm}$. The butterfly antenna is an active antenna, i.e., its broadband sensitivity is achieved by an interplay of antenna and LNA. The impedance and amplification of the LNA changes in frequency such that the antenna + LNA response is approximately constant in frequency [224]. In particular, the butterfly antenna is sensitive in the frequency range from 30 - 80 MHz.

The dipole arms are attached to a central nut (a black cylinder made of plastic, cf. Fig. 4.14 right). Inside the nut, the dipole arms are connected via short cables to the LNA. The LNA output is accessible from below the nut and transmitted via coax cables through the main pole into a triangular electronics box. The antenna was originally developed for the CODALEMA experiment situated in France [8] and adapted for the use at AERA [221]. The main change was an additional support structure for the dipole arms to sustain the strong winds at the AERA site. Additional fiber tubes hold the dipole arms in place.

Comparison of the two antennas   One advantage of the LPDA is the robust and flexible mechanical structure. Due to its folding mechanism the transportation and deployment is very convenient. Also the LNAs can be accessed and connected easily. An additional advantage is a low sensitivity to signals reflected from the ground and entering the antenna from below. Therefore, the antenna is mostly insensitive to changing ground conditions (e.g. a wet surface after rain). This is especially relevant for obtaining a small uncertainty on the absolute level of the antenna response which is a crucial ingredient for the determination of the cosmic-ray energy scale as presented in Chap. 7.

The advantages of the butterfly antenna are its relatively small mechanical complexity and corresponding low manufacturing costs. In addition, the butterfly has a small group delay, i.e., a small signal dispersion, and correspondingly a higher signal-to-noise ratio.
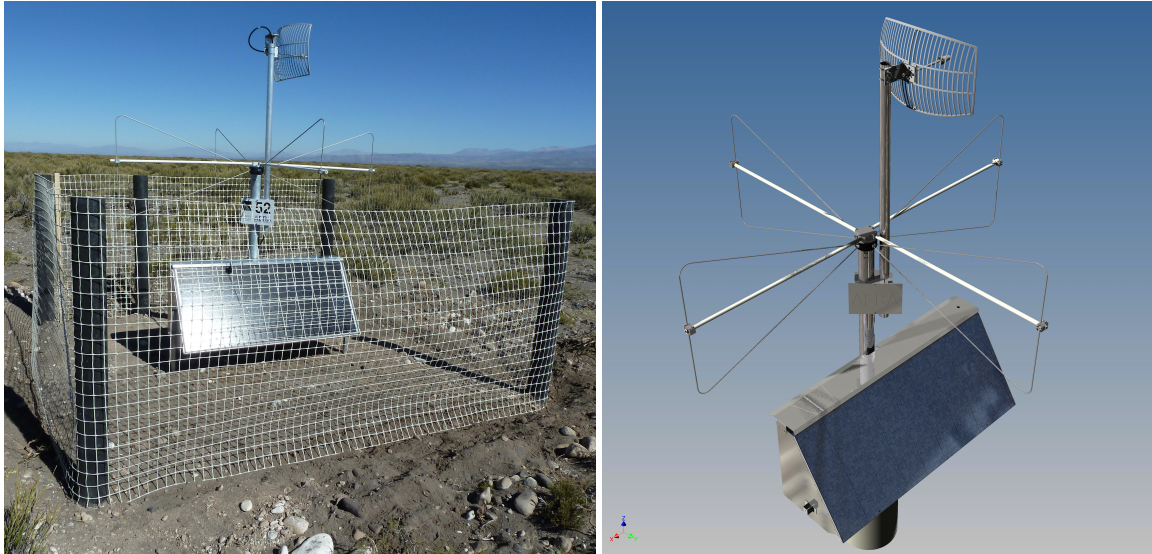
Figure 4.14: The butterfly antenna of the Auger Engineering Radio Array. (left) Photo of one of the butterfly stations installed in Argentina. (right) Three dimensional CAD model of the antenna and station design. Figure from [221].

Most of the advantages of the butterfly antenna are drawbacks of the LPDA and vice-versa. Disadvantages of the LPDA are relatively large manufacturing costs and a larger group delay compared to the butterfly antenna. Also the sensitivity of the LPDA in terms of signal-to-noise ratio is slightly smaller than that of the butterfly antenna.

The downsides of the butterfly antenna are that the access to the LNA is difficult due to the additional support structure and that the fully assembled antenna can not be transported easily as no folding mechanism exists. Therefore, the antenna was shipped in its individual components to Argentina. Due to the difficult environmental conditions in the AERA field (high winds, very hot, dusty) the antennas were not assembled in the field but in the workshop of the Pierre Auger Observatory. Then, the antennas are transported to the field with a trailer especially build for this purpose.

A significant part of the sensitivity of the butterfly antenna comes from the signals that are reflected from the ground and enter the antenna from below. This has the advantage of a better sensitivity but also the disadvantage that the antenna response depends on ground conditions and to conducting parts below the antenna such as the electronic box. Therefore, the antenna response is not rotationally symmetric as in case of the LDPA. Also the modeling of parts below the antenna imposes additional uncertainties in the simulation of the antenna response. Additional details of the two antennas can be found in [221, 225].

4.4.2 Station electronics

The signals coming out of the LNAs are fed into a filter-amplifier and get digitized with flash analog-to-digital converters (FADCs). The station electronics feature a field programmable gate array (FPGA) which allows for fast real-time data processing, e.g., narrowband noise sources can be filtered out and different trigger schemes can be implemented [226]. Then the data is passed to a CPU which optionally applies additional trigger conditions and time-stamps the trigger using the GPS receivers.

Two main types of digitizing hardware are used at AERA. The first type of electronics features a $4\,$GB ring buffer which can hold the data from two channels for $\sim 7\,$s which is sufficiently long to receive an external trigger from the surface and fluorescence detector of the Observatory. The second type of electronics is designed for self-triggering and does not feature a large buffer.

The digitizers that are suited for external triggering sample the signals at $180\,$MHz with 12-bit FADCs. To increase the dynamic range the signal is split up into a low-gain and a high-gain channel. Hence, each digiziter has four channels, two for each polarization direction of the antenna. In case of the LPDA stations (AERA24), the LNA has a gain of $+18.8\,$dB [223] and the low-gain channel is amplified by additional $10\,$dB whereas the high-gain channel is amplified by additional $30\,$dB. In case of the AERA124 stations, the LNA has a higher gain of $+26\,$dB [224]. To achieve the same overall amplification, the low-gain channel has a gain of $+0\,$dB and the high-gain channel has a gain of $+20\,$dB [227]. The digitizers manufactured for the AERA153 stations only feature high-gain channels as it turned out that the low-gain channels remained mostly unused partly due to the larger complexity in the FPGA programming, the increased data rates and because the buffer size is reduced to $3.5\,$s if all four channels are stored which is too little to receive all external SD and FD triggers. Instead, these stations already have a third high-gain channel that can be used for a future extension of the stations with a third vertically polarized antenna to directly measure all three components of the electric-field pulse.

The digitizers not equipped with a ring buffer sample the data with $200\,$MHz. In case of the AERA24 stations, the same filter-amplifier as described above is used and also 12-bit FADCs are used to digitize the two low- and two high-gain channels. In case of the butterfly stations, the dynamic range of the FADCs were increased to 14-bits which makes the split into a low- and high-gain channel superfluous. Also the filter-amplifier was replaced by a passive filter, i.e., without any amplification [228]. The two remaining channels are then used for an additional internal trigger. Two (or one) small plastic scintillators ($457\,$mm $\times$ $172\,$mm $\times$ $24\,$mm) are placed below and above the battery in the electronic box and are read out by the two remaining channels. The trigger efficiency of the scintillators is above 90% for cosmic-ray energies above $10^{17.6}\,$eV and zenith angles below $60°$ [115].

4.4.3   Station designs

The RDS are designed to operate autonomously. Each station is solar powered and equipped with a battery to run $24\,$h each day. The station electronics are placed inside an RFI shielded water- and dust-proof metallic box. In case of a LPDA station, the box is placed underneath the support structure of the solar panel. In case of a butterfly station, a triangular box is mounted on the main pole which also serves as a mounting for the solar panel. Each station is equipped with GPS receivers for accurate timing and a fence is put around each station to protect it from animals living in the Argentinian Pampa.

The 24 LPDA stations are connected via optical fibers to the central radio station (CRS) [229]. For the second and third stage of expansion a wired connection was no longer feasible due to the large number of stations and the larger spacing between the stations. Instead a commercial wireless communication system manufactured by Ubiquity operating in the $5\,$GHz band was used. Each RDS connects to one of four access points, two installed at the CRS and two at Coihueco. The system is

Figure 4.15: The central radio station (CRS).

complemented by two point-to-point links between the CRS and Coihueco. A typical data rate is about $40\,\mathrm{kbps}$ per station and up to $2.5\,\mathrm{Mbps}$ at the access points. The system is capable to transmit even larger data rates so that a limited data rate is not a limiting factor for the triggering. More information on the wireless communication system can be found in [115].

The CRS is a modified shipping container placed next to the LPDA stations in the AERA field (cf. Fig. 4.15). It is supplied with power using solar panels and an array of batteries. In the first two years of runtime of AERA, the data acquisition (DAQ) was situated in the CRS. When the second stage of expansion was build, the DAQ was gradually moved to the building of the Coihueco telescopes and a fast wireless link between the CRS and Coihueco was installed. However, the CRS still serves as a relay station and as a base in the field from which all RDS can be accessed and is often the starting point for maintenance work as it also features a small workshop.

4.4.4 Detector calibration

The most challenging part of the detector calibration is the absolute calibration of the antenna response to cosmic-ray radio signals. To be unaffected by near-field effects, a calibrated signal source needs to be placed at least $\sim 20\,\mathrm{m}$ away from the antenna at any place around the antenna. Several calibration campaigns were performed and the measurement setup was continuously improved. The first campaign used a weather balloon to lift the calibrated signal source and measured the horizontal component of antenna response with an accuracy of 12.5% [126, 225]. The directional antenna response is characterized using the vector effective length (VEL) and a result of this calibration campaign is presented in Fig. 4.16 left. The measurement was set up as a transmission measurement, i.e., the network analyzer generates and measures the signal. The signal is transmitted via cable to a calibrated biconical antenna that is mounted underneath the balloon. The signal is then received by the LPDA antenna (the antenna under test (AUT)), amplified by the LNA and fed back into the spectrum network analyzer. The position and orientation of the transmitting antenna is adjusted using a rope construction. The advantages of this setup is that a transmission measurement is performed which - in principle - can reach smaller systematic uncertainties as the signal is generated and received by the
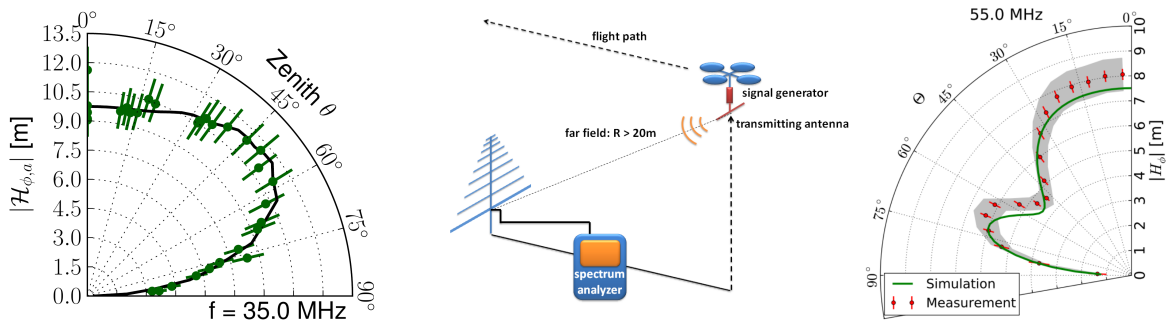
Figure 4.16: Measurement of the antenna response. (left) Vector effective length (VEL) as a function of zenith angle for a frequency of $35\,\mathrm{MHz}$ as measured with the balloon setup [225]. Green filled circles represent the measurement and the solid black line is the antenna response obtained by a simulation. (center) Sketch of improved setup using a flying drone to carry the calibration source [235]. (right) VEL as a function of zenith angle for a frequency of $55\,\mathrm{MHz}$ as measured with the drone setup. Shown is the average VEL per zenith angle bin obtained with several flights (filled circles and errorbars). The gray band shows the systematic uncertainties [231].

same device. Also, the antenna response can be measured at all frequencies simultaneously as well as the group delay. However, the cable that transmits the signal to the transmitting antenna works as an antenna itself and can disturb the measurement if not sufficiently shielded. This is especially relevant for positions where the transmitting antenna is directly above the AUT and the cable hangs near the AUT [221]. A proper shielding results in a relatively thick and heavy cable which puts a large payload on the lifting device. Also from the measurement itself it can not be determined if the cable had negligible influence. Other disadvantages of this method are the high costs of each balloon and gas filling and the need for a windless environment. Hence, this setup is not well suited for the windy environment at the AERA site.

Therefore, a new method that uses a remotely piloted drone to lift the signal source was developed [221, 230, 231]. This setup is much less dependent on wind but also has a more limited payload. Hence, the signal is not transmitted via cable from the ground to the transmitting antenna but generated using a battery-powered frequency generator [232] that is mounted directly underneath the drone and generates a frequency spectrum with signals every $5\,\mathrm{MHz}$. This gives high flexibility and allows for repeated measurements to reduce the statistical uncertainty. A sketch of the setup is shown in the middle of Fig. 4.16. This setup was completed with an optical camera system to accurately determine the position of the signal source during the flight [233]. Two standard digital cameras are placed at to orthogonal axes at $\sim100\,\mathrm{m}$ distance from the antenna. From the photos taken every few seconds, the position of the signal source can be reconstructed. This information is combined with the position information from the GPS and the barometer of the drone to achieve a small statistical as well as systematic uncertainty in the position of the signal source. One result of this calibration campaign is presented in Fig. 4.16 right. Using this new method an accuracy of below 10% for most incoming signal directions was achieved for the LPDA antenna [234]. The disadvantages of this method are that the antenna response is only measured at discrete frequencies (every $5\,\mathrm{MHz}$) and that the group delay can not be measured.

Also the rest of the signal chain was measured for each station individually. In case of the LPDA

stations this measurement was performed directly in the field and has a systematic uncertainty of 6%.

Another part of the detector calibration concerns the relative timing of the RDS. The GPS units installed at AERA do not achieve the timing resolution claimed by the manufacturer of $5\,\text{ns}$ but exhibit drifts on the order of tens of ns. To nevertheless achieve a timing precision of $\sim 1\,\text{ns}$, a method was develop to calibrate the relative timing of the radio stations. This is achieved by a beacon reference transmitter installed at Coihueco that emits sine waves at four different frequencies at $58.887\,\text{MHz}$, $61.523\,\text{MHz}$, $68.555\,\text{MHz}$ and $71.191\,\text{MHz}$. The frequencies were chosen such that timing differences of up to $80\,\text{ns}$ can be corrected for and such that they match exactly one bin of the Fourier transform of the time traces recorded by AERA. From an analysis of the phase differences of the four beacon frequencies that are measured by each RDS, the relative timing of the RDS can be corrected for the drifts in the GPS receivers.

This method was crosschecked by a second independent method that uses the fact that commercial airplanes emit short radio pulses in the frequency range of AERA. Airplanes also transmit their position in real time via digital ADS-B messages such that the expected pulse arrival times at the RDS can be calculated and compared to the measured times. This analysis showed that both methods have a combined precision of $2\,\text{ns}$. From this it can be concluded that the beacon system alone achieves a timing precision of better than $2\,\text{ns}$. A detailed description of the beacon system and the crosscheck using airplanes can be found in [236].

4.4.5 Data acquisition and triggering

As AERA is an engineering array different triggers have been implemented. The trigger settings evolved with time or have been changed completely after hardware changes or extensions of the array. The different triggers can be grouped in two main categories. The first category are triggers to measure air showers and contains a self trigger, an external trigger and an internal particle trigger. The second category are triggers that are meant for monitoring or calibration purposes and contains periodic triggers, random triggers and an air-plane trigger used for timing calibration purposes.

Self trigger

The performance of a self trigger depends strongly on the noise conditions. A definitive limit is set by the diffuse radio emission from the galactic plane. This noise floor scales exponentially with frequency and is largest at low frequencies. It also changes in time as the galactic center moves over the sky with a periodicity of one sidereal day. In addition, anthropogenic noise contributes to the noise floor and its strength varies during the course of the day and correlates with human activity. Hence, a simple signal-over-threshold trigger is not sufficient but the threshold needs to be adjusted to the current noise situation at AERA. All AERA stations are equipped with an FPGA to implement advanced trigger algorithms and basic signal cleaning. E.g., narrowband transmitters are filtered out using infinite-impulse response notch filters in the time domain or median filters in the frequency domain [226].

The main limitation of the self trigger is, however, pulsed broadband noise. Although AERA is located in a remote and rural area, the single station trigger rate is above $100\,\text{Hz}$ for a 5σ adapted signal-over-threshold trigger [237] that, e.g., also takes the number of crossings of an additional threshold

into account to reject long pulses that can not originate from an air shower [226]. Most of the triggered pulses must originate from noise sources as the signal rate from cosmic rays is significantly lower. This is aggravated by the fact that cosmic-ray pulses and noise pulses can not be distinguished by their pulse form as the pulse form is mainly determined by the limited bandwidth of the detector. Hence, a trigger logic on a single station is not sufficient to filter out noise pulses.

If multiple stations send a trigger in coincidence, a level 3 trigger (L3) is formed. The exact requirement for a L3 trigger was subject to several changes and depends on the hardware of the local stations. In most cases, a threefold time and spacial coincidence is required. For the stations equipped with an internal particle detector, in addition at least two internally triggered stations need to participate in an event, except for tenfold or larger coincidences. When the L3 trigger is formed, enough information is available to reconstruct the direction. The direction of most self-triggered events point back to the horizon indicating a man-made origin and can thus be rejected. However, also noise pulses from above the horizon are visible in AERA either from actual sources in the sky (airplanes etc.) or because of falsely reconstructed directions due to timing uncertainties or a mutual detection of noise pulses from multiple sources. Even if all pulsed broadband noise could be rejected by an advanced trigger algorithm, it imposes a principle problem because of the resulting dead time and thus reduced efficiency of the detector.

Several strategies to suppress man-made noise pulses have been exploited and refined during the runtime of the detector. A certain class of noise pulses show a periodicity of $100\,\text{Hz}$ which is twice the power grid frequency of Argentina and can accordingly be removed. Another noise rejection strategy uses the reconstructed direction. The only requirement is that the reconstruction is fast enough to keep up with the event rate. A simple algorithm uses only the time differences of two stations which is constant for a stationary anthropic source at the horizon [226, 238]. However, also a plane wave fit is sufficiently fast, so that the full directional information can be used to veto noise sources. In addition to the vetoing of events originating from the horizon a cone algorithm is implemented [220, 239]. Here, events that arrive from a certain region (within a cone of certain opening angle) within a given time window are rejected. Typical settings are a cone angle of $5°$ and a time window of $10\,\text{min}$ [238] which reject anthropic noise sources efficiently. Cosmic rays are mostly unaffected by this algorithm as they do not cluster on this time and angular scales.

External trigger

The radio detector stations that are equipped with a ring buffer also receive an external trigger from the surface and the fluorescence detector of the Pierre Auger Observatory. The advantage of this trigger is that only air showers are triggered, although the radio signal might be so low that it can not be detected in any radio detector station. The delay of an SD trigger is typically $3\,\text{s}$ and $7\,\text{s}$ for a trigger from FD. From the external trigger information the position of the radio pulse in the buffered trace can only be estimated roughly which requires the read out and storage of a long trace (Currently $57\,\mu\text{s}$ long traces are saved which is much longer than needed for analysis as the width of a cosmic-ray pulse is only about $20\,\text{ns}$ long.). In addition, all stations are read out, as it is difficult to estimate from the external trigger information which stations should be able to see a signal. This leads, together with the long trace length, to large data volumes of $\mathcal{O}(10\,\text{GB})$ per month.

Internal particle trigger

Most of the radio detector stations that do not have a large ring buffer to receive an external trigger, are equipped with scintillation counters that are integrated in the radio detector station. Such a design is especially interesting for possible future stand-alone radio detector arrays. Similar to the self trigger, an event is formed if several scintillators detect a particle in time and spacial coincidence. Hence, an air shower is directly associated with radio detector stations allowing for clear identification of radio pulses. An additional advantage of the particle detection at each radio station is that the trigger time is very close to the time of the radio pulse. Hence, the signal search window can be constrained and the required signal-to-noise ratio can be lowered accordingly. However, the disadvantage of the scintillator trigger, and especially of the particular scintillators used in AERA, is the small detection efficiency for inclined showers [115] where a radio detector has an increased sensitivity. This trigger is further improved by a combination with the self-trigger.

Monitoring and calibration triggers

A continuous monitoring of the detector performance and the environmental conditions are crucial for the analysis of cosmic-ray data. Therefore, several triggers to monitor AERA are implemented. A periodic trigger reads out a trace from the complete detector every 100 seconds (every 10 seconds before July 2014). This data provides useful information on the detector uptime, the current noise situation or the probability to detect noise pulses (cf. Sec. 5.7). The measure of the noise floor can be used for a relative calibration of the radio detector stations or even for an absolute calibration using a prediction of the Galactic radio emission as it dominates the received noise [240–243]. The recorded traces are also useful for simulation studies, where they can be added to simulated cosmic-ray pulses as a realistic noise background.

In addition, a random trigger is implemented that records every 40,000th level 1 trigger in case of the internally triggered stations and every 999th level 1 trigger in case of the stations equipped with a ring buffer.

A successful way to calibrate the timing of the RDS is to record radio pules emitted by commercial airplanes (cf. Sec. 4.4.4) [236]. However, the continuously emitted pules are rejected by the cone algorithm discussed above. Therefore, the cone algorithm is deactivated within a $5°$ window around the airplane position that is inferred from the ADS-B information broadcasted by the airplane [244].

4.4.6 Scientific potential

The different antenna and electronic designs implemented in AERA and the location of AERA next to additional detectors of the Pierre Auger Observatory where air showers are measured with three independent detection techniques create a large engineering and scientific potential.

AERA can be used to explore the optimal setup to measure cosmic rays. Two different antenna designs are tested in the harsh environment of the Argentinian Pampa. The different detector spacings allow the determination of the optimal layout for different energy regimes, e.g., the $750\,\text{m}$ spaced stations are located directly next to SD stations to test the potential of a large-scale extension of a surface particle detector with radio antennas. The different types of station hardware allow the

implementation of different trigger schemes such as self-triggering directly on the radio signal using advanced signal processing in an FPGA, external triggering or an internal particle trigger using the small scintillators integrated into the station design. The latter setup is especially interesting for a possible future stand-alone radio array.

The Auger surface detector, which is calibrated with the fluorescence detector, provides an accurate measurement of the cosmic-ray energy and is used to develop and cross-calibrate the energy measurement with AERA (see Sec. 6 or [126, 160, 161]). Furthermore, the position of the shower maximum X_{max}, which is an estimator of the primary-particle type of the cosmic ray, is directly measured with the fluorescence telescopes. Coincident measurements of AERA with FD are thus used to evaluate the performance of the different techniques used at AERA to reconstruct the cosmic-ray particle type. Different methods are developed at present to derive the cosmic-ray composition from the radio measurements [16].

In addition to a reconstruction of X_{max} using solely radio data, the AERA measurement can be combined with the other detectors. The radio signal measures the electromagnetic component of the air shower. Hence, a coincident measurement of the muonic shower component using underground particle detectors is sensitive to the cosmic-ray particle type. In case of horizontal air showers, the electromagnetic part of the air shower is completely absorbed in the atmosphere so that the SD measures only the muonic shower component whereas AERA still measures the electromagnetic part of the shower as the atmosphere is transparent to radio waves. Hence, a combined radio and particle measurement of horizontal air showers is sensitive to the cosmic-ray particle type [245].

Reconstruction of air showers from radio detector data

In this chapter, we give an overview of all relevant steps to reconstruct air showers from radio-detector data and present the corresponding software that has been used and partly developed within this thesis.

5.1 The software framework Offline

$\overline{\text{Off}}\underline{\text{line}}$ is the modular software framework of the Pierre Auger Observatory. It is written in C++ and originally developed to reconstruct air showers from the data of the surface and fluorescence detectors [218]. While the Auger Observatory was extended by additional detector components such as the radio detector AERA or the additional muon detectors AMIGA, also $\overline{\text{Off}}\underline{\text{line}}$ was extended accordingly [219].

This became possible due to the flexible structure of the software. Fig. 5.1 shows a sketch of the three principal parts of the $\overline{\text{Off}}\underline{\text{line}}$ framework. The first part is a detector description which provides access to the configuration and performance data of the different detectors of the Observatory. The second part is a collection of processing modules that interact with the event data, which is the third part and stores all detected, simulated and reconstructed event information. The modules have no direct interface to each other but exchange data through the event structure. Due to this design, algorithms and data are clearly separated and all data processing and reconstruction steps are modularized. Hence, a reconstruction pipeline can be extended easily by adding additional modules or different reconstruction techniques can be tested by exchanging individual modules.

Due to the clear separation of the event structure and data processing modules, different data sources can be accessed. $\overline{\text{Off}}\underline{\text{line}}$ provides input modules for the different detector data (SD, FD, radio, etc.) as well as for different air-shower simulation programs such as CORSIKA/CoREAS, AireS/ZHAireS, SELFAS, etc., so that $\overline{\text{Off}}\underline{\text{line}}$ can not only be used to reconstruct measured cosmic-ray data but also to perform a complete detector simulation using simulated air showers as input.
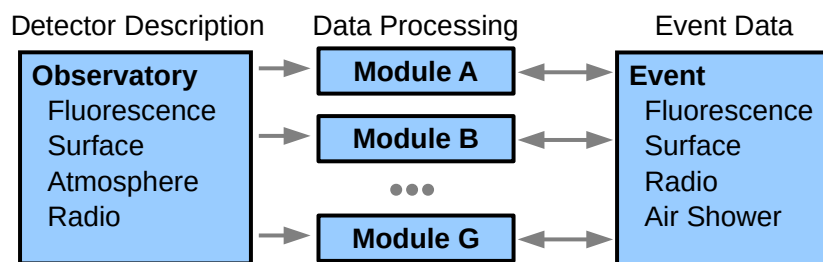

Figure 5.1: The three principal parts of the Offline framework. Adapted from [246].
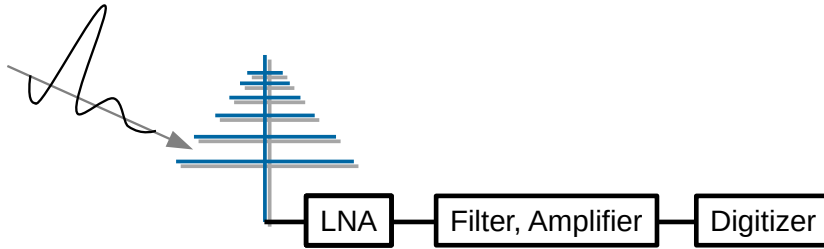
Figure 5.2: Sketch of the signal chain of an AERA radio station.

These three principal parts are complemented by a collection of utility classes. A geometry class handles all coordinate transformations internally so that the user needs to specify a coordinate system only in the definition of a new geometrical object. All further calculations can be performed independently of a choice of coordinate system. Also a default system of units is defined, so that only at the declaration of a quantity its unit needs to be specified. Especially useful for radio data, $\overline{\text{Off}}\underline{\text{line}}$ provides a class to store time series such as the electric-field traces of a cosmic-ray radio pulse. As some reconstruction steps are performed in the time domain and some in the frequency domain an interface is provided to directly obtain one of the two. A corresponding Fourier transformation is performed automatically if necessary. Furthermore, a class providing the geomagnetic field configuration at any time and location according to the *International Geomagnetic Reference Field* (IGRF) [247] exists. This is needed in the reconstruction of radio data as the amplitude and polarization of the electric-field pulse depends strongly on the geomagnetic field.

An interface to access environmental data such as temperature and atmospheric conditions from different databases is provided. Also the time-dependent detector configuration is described in a database that can be accessed from within $\overline{\text{Off}}\underline{\text{line}}$. Thus, the reconstruction automatically takes any hardware changes into account, such as the replacement of a low-noise amplifier after a lightning strike. Hence, the detector remains in a well-calibrated state. Also a connection to a "bad period database" has been implemented, in which time periods of hardware or software problems or mechanical damage of the detector stations are flagged. Bad periods can be reported through a web interface and are filled into the database. After review by an expert, this information is directly available in the reconstruction.

5.2   Hardware incorporation and RFI suppression

The first step in the reconstruction pipeline is the incorporation of the radio-detector response. The signal chain is depicted in Fig. 5.2. An electric-field pulse induces a voltage in the antenna which is amplified and filtered in two stages and then digitized. First, the measured ADC counts are converted into their voltage equivalent. Second, the voltage trace is corrected for the frequency-dependent response of the analog signal chain, consisting of filters, cables and two amplification stages, to obtain the voltage at the footpoint of the antenna, i.e., the voltage that has been induced in the antenna by the electric-field pulse. An overview of the impact of the different reconstruction steps are presented in Fig. 5.3.

The next step is the correction of the GPS clocks using a reference beacon signal (cf. Sec. 4.4.4)
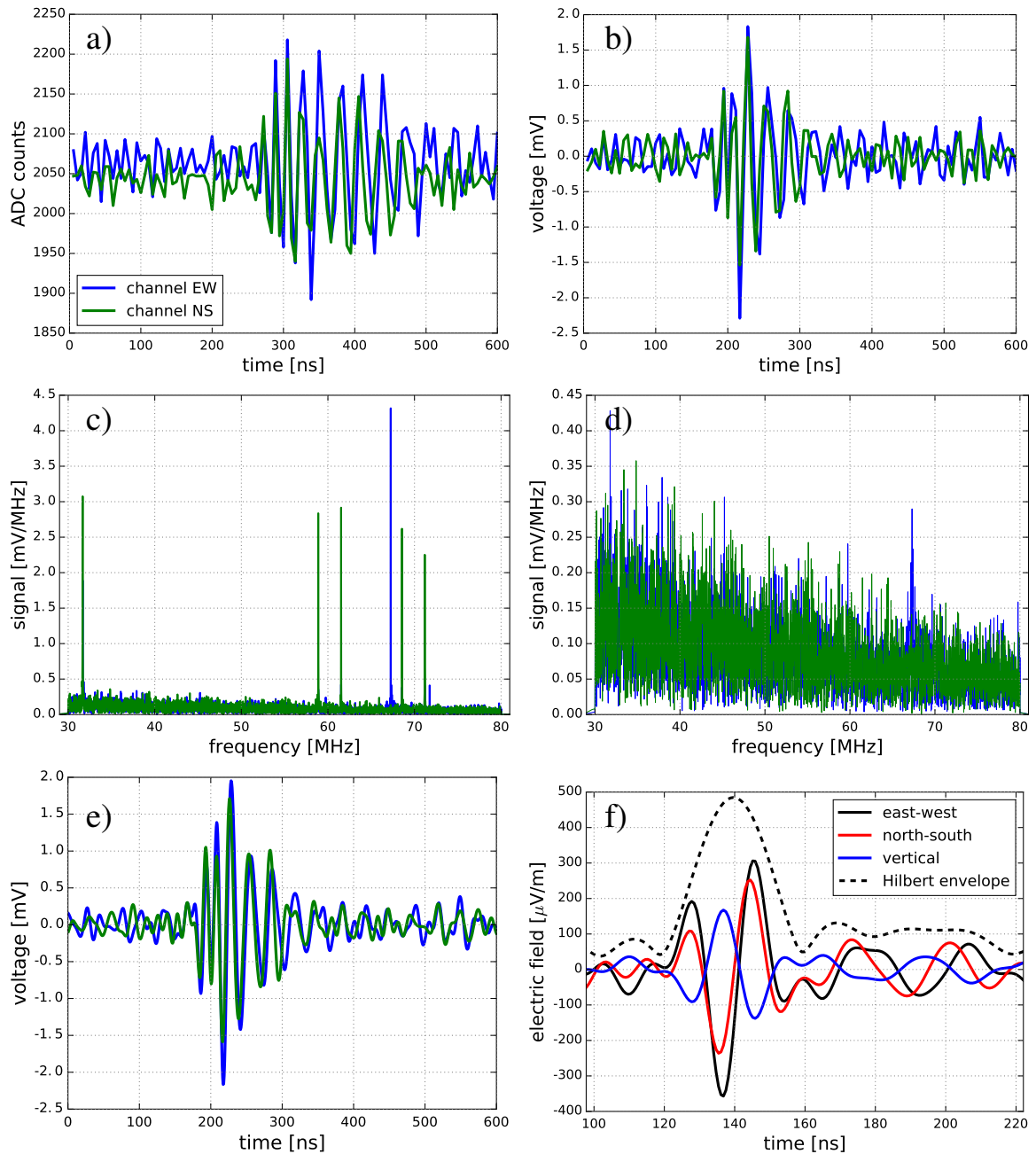
Figure 5.3: Impact of the different reconstruction steps. Shown is the radio signal from an air shower measured on the afternoon of the 6th September 2015. The air shower has an energy of $1.14\,\mathrm{EeV}$ and was incident at a zenith angle of $30°$ and $14°$ south of east. Shown is data from the LPDA station number 14. a) Raw ADC time traces of the East-West (blue) and North-South (green) channels. b) Voltage trace after unfolding of the detector response. c) Frequency spectrum of b). The four beacon lines are clearly visible in the NS channel. In addition, narrowband noise sources at $32\,\mathrm{MHz}$ and $\sim 67\,\mathrm{MHz}$ are present. d) Frequency spectrum after noise filtering using the sine-wave suppression in the time domain. e) Voltage trace after noise filtering and upsampling by a factor of 8. f) Three-dimensional electric-field trace obtained by unfolding the antenna response. Note the changed x-axis range.

[236]. It has been found that the GPS clocks in different radio detector stations have offsets that can be as large as several 10 ns which is significantly larger than the accuracy of 5 ns claimed by the manufacturer. This time offset is also not constant but drifts systematically on time scales of several hours. Fortunately, the GPS-clock drifts can be corrected for in the offline analysis using the reference beacon signal to an accuracy of better than 2 ns.

After the beacon correction has been performed, the four bins in the frequency spectrum that contain the beacon signal are removed or rather set to zero which is already the first step of RFI suppression. The four frequencies of the beacon signal are chosen such that each frequency occupies only one bin in the frequency spectrum given the sampling rate of 180 MHz or 200 MHz of the detector and a trace length of at least 2048 bins. Although AERA is located in a rural and remote area, several transmitters are visible in the frequency spectrum and make certain frequency bins unusable. The easiest way to suppress these RFI sources is to apply a bandstop filter and set the corresponding frequency bins to zero. However, this method has the disadvantage that a certain amount of signal strength is removed from the cosmic-ray radio pulse as well.

The situation is even more challenging as the RFI is not stable in time or frequency. One way that is provided in $\overline{\text{Off}}\underline{\text{line}}$ is to dynamically search for excesses in the frequency spectrum and remove the corresponding bins. This would result in clean radio pulses, so that the pulse arrival time can be determined with high precision and used in the directional reconstruction, but the pulse power would depend on the bandwidth that has been cut away and would thus be different from station to station and event to event. We therefore use this method only to remove the beacon frequencies and a strong and constant noise source between 66.4 and 68 MHz that is visible in the east-west polarized antenna.

Instead, a more sophisticated method to suppress mono-frequent RFI is used [243, 248]. In the time-domain, sine waves are fitted to the time trace, thereby determining the amplitude, frequency and phase of the RFI source. Then, only this specific RFI source can be removed from the data without altering the power of the radio pulse, although the radio pulse contains also the frequency of the noise source. This is because the length of the radio pulse is only several tens of nanoseconds whereas the total trace length is typically several micro seconds. The fit of the sine wave can therefore be performed using the complete trace except for the small part containing the signal. The disadvantage of this method is that it is computationally expensive. A common approach is therefore to first reconstruct all data using the online bandstop filter and then reconstruct only the interesting events again using the RFI filtering in the time domain.

The sampling rate of 180 MHz or 200 MHz of the detector corresponds to a size of one time bin of $5.\bar{5}$ ns and 5 ns respectively. To achieve a better precision, e.g., in the determination of the signal time, the measured traces are upsampled to smaller time binnings. This is possible because the sampling frequency is more than two time larger than the maximum frequency of 80 MHz contained in the the measured trace. Then, according to the Nyquist-Shannon theorem, the sampled signal contains all information of the original signal [249–251]. Hence, from the measured samples, the signal at any time between the measured samples can be determined. In most analyses an upsampling by a factor of 5 is applied to reduce the size of one time bin to $\sim$1 ns.
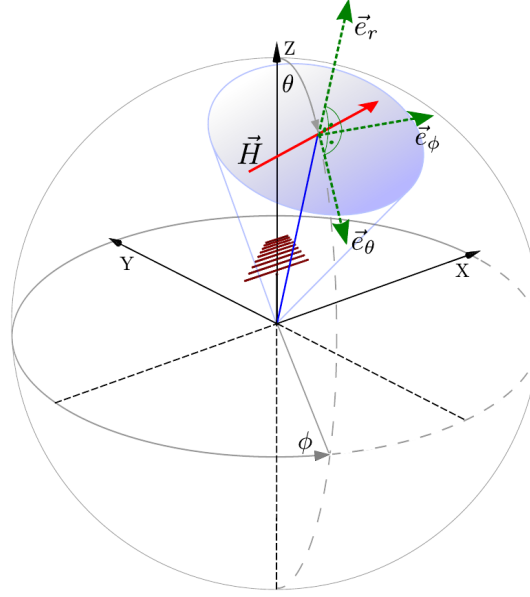
Figure 5.4: The spherical coordinate system with the antenna structure in the center. The origin of coordinate system is located in the XY-plane below the antenna which takes the placement of the antenna above a ground plane into account. Depicted is a logarithmic periodic antenna structure. The zenith angle θ is counted from the top, the azimuth angle ϕ counterclockwise from the x-axis of the coordinate system. A specific direction (θ, ϕ) is considered as the incoming direction of a signal. The vector of the *vector effective length* $\mathcal{H}$ for the specified direction is given. $\mathcal{H}$ as well as the vector of the electric field (not depicted) are contained in the plane spanned by the unity vectors e_θ and e_ϕ. Plot and caption adapted from [225].

5.3 Reconstruction of the electric field

The electric-field pulse generated by the air shower is a major quantity of interest and independent of the experimental setup. To obtain the electric-field trace from the measured voltage trace, the antenna response needs to be unfolded. The antenna response is described via the *vector effective length* (VEL) $\mathcal{H}$ that depends on the frequency f and the incoming direction of the electric field, described via its zenith and azimuth angle θ and ϕ. Then the relation

$$\mathcal{V}(f) = \vec{\mathcal{H}}(f, \theta, \phi) \cdot \vec{\mathcal{E}}(f) \tag{5.1}$$

holds in Fourier space, where $\mathcal{V}$ and $\mathcal{E}$ are the Fourier transforms of the voltage trace and electric-field trace respectively. The electric field is a three-dimensional quantity but it can be reduced to two dimensions as it has no component in the direction of propagation if the far field approximation applies. Using spherical coordinates, the electric field can be decomposed into

$$\vec{E}(t) = E_\theta(t) \, \vec{e}_\theta + E_\phi(t) \, \vec{e}_\phi \,, \tag{5.2}$$

where $\vec{e}_\theta$ and $\vec{e}_\phi$ are the unit vectors of the spherical coordinate system. In the same way, also $\vec{\mathcal{H}}$ can be decomposed. This choice of coordinate system is depicted in Fig. 5.4.

The electric field is obtained by solving Eq. (5.1). Obviously, a measurement of the voltage in just

one antenna is not sufficient to reconstruct the two components of the electric field. Therefore, the same electric field is measured in two orthogonal-polarized antennas at the same position simultaneously. This leads to the following system of equations

$$\mathcal{V}_1(f) = \vec{\mathcal{H}}_1(f, \theta, \phi) \cdot \vec{\mathcal{E}}(f) \tag{5.3}$$
$$= \mathcal{H}_{1,\theta}(f, \theta, \phi)\, \mathcal{E}_\theta(f) + \mathcal{H}_{1,\phi}(f, \theta, \phi)\, \mathcal{E}_\phi(f) \tag{5.4}$$
$$\mathcal{V}_2(f) = \vec{\mathcal{H}}_2(f, \theta, \phi) \cdot \vec{\mathcal{E}}(f) \tag{5.5}$$
$$= \mathcal{H}_{2,\theta}(f, \theta, \phi)\, \mathcal{E}_\theta(f) + \mathcal{H}_{2,\phi}(f, \theta, \phi)\, \mathcal{E}_\phi(f), \tag{5.6}$$

that can be solved for $\vec{\mathcal{E}}$. The indices 1 and 2 denote the two orthogonal-polarized antennas.

As the VEL depends on the incoming direction of the radio pulse, the air-shower direction needs to be known before the electric-field reconstruction. This imposes a principle problem if the air shower is reconstructed from radio data alone. The air-shower direction is reconstructed via triangulation of the pulse arrival times in multiple radio detector stations but the unfolding of the antenna response changes the pulse arrival times. This is because the frequency spectrum of the radio pulse is not the same in each radio detector station and the group delay of the antenna changes with frequency. Therefore, the electric field is determined in an iterative procedure. First, the incoming direction is estimated using the pulse arrival times determined on the voltage trace. Then, the electric field is reconstructed using this estimate of the air-shower direction. Next, the pulse arrival times are determined on the electric-field trace and are used to re-reconstruct the incoming direction of the air shower. With this improved directional information the electric field is reconstructed again. This procedure is repeated several times until the change in reconstructed direction is below some threshold value. However, most analyses use only air showers that have been measured in coincidence with the surface detector so that the directional information from the SD reconstruction can be used directly.

5.4   The antenna response pattern

A good description of the antenna response is a crucial ingredient for the reconstruction of the three-dimensional electric field. We use the software Nec2 [253] to simulate the antenna response pattern of the LPDAs as well as the butterfly antennas. The simulation includes not only the antenna but models all parts of the radio-detector station that have an influence on the antenna response, e.g., the communication antenna and the triangular box are taken into account in case of a butterfly antenna station. The complete model of butterfly antenna as used in the Nec2 simulations is shown in Fig. 5.5.
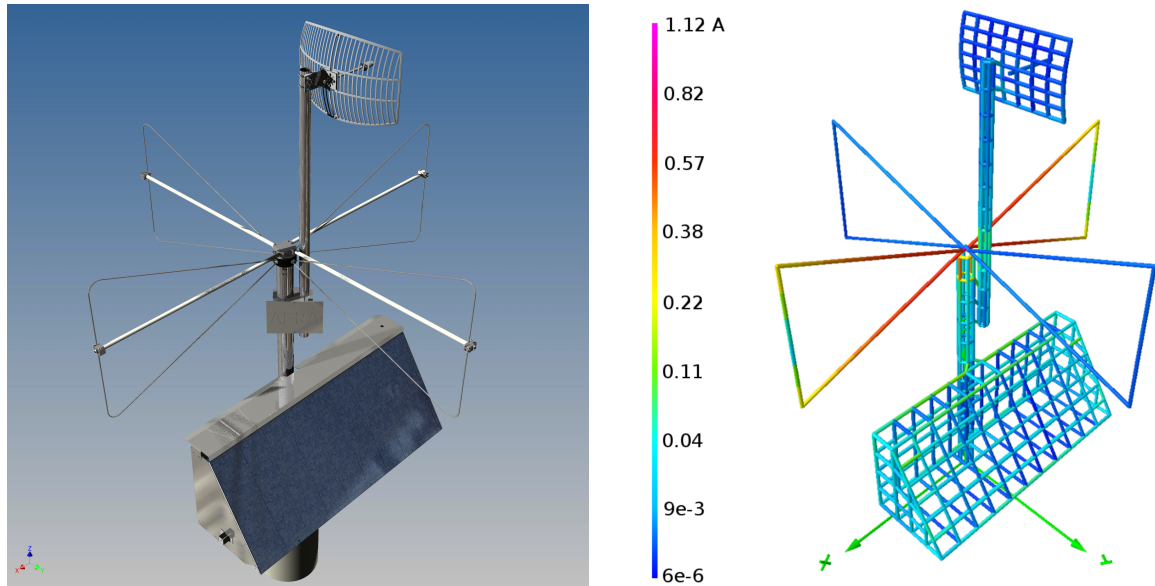
Figure 5.5: CAD model (left) of the Butterfly antenna station in comparison the model in the antenna simulation software (right). The color scale indicates the magnitude of the currents simulated at a frequency of 55 MHz. Figure and caption from [221].

The VEL which depends on the zenith and azimuth angle and the frequency is a pair of complex numbers, one complex number for the ϕ and one complex number for the θ polarization of the antenna response pattern. A complex number can be visualized either in the Euler representation, i.e., in magnitude and phase, or decomposed into its real and imaginary part.

The antenna response pattern of the butterfly antenna station is shown in Fig. 5.6 using the Euler representation and in Fig. 5.7 using the complex representation. One observes that the phase shows several phase jumps at specific zenith and azimuth angles whereas the representation in real and imaginary part is totally smooth. The reason for the phase jumps are partly due to the confinement of phases to the $[-\pi, +\pi]$ interval and partly due to a real physical effect of the antenna. Please note that the magnitude is zero at the points where a physical phase jump occurs.

5.4.1 Linear interpolation of the antenna response pattern

The antenna response can only be simulated for discrete values of the frequency, the zenith and the azimuth angle. Hence, it is necessary to interpolate between the discrete data points to get the correct antenna response for arbitrary frequencies, zenith and azimuth angles.

Two options are available to interpolate linearly between two complex numbers. First, the Euler representation of a complex number can be used, i.e., the magnitude and the phase are interpolated separately. Second, the complex number is used directly which corresponds to a separate interpolation of the real and imaginary part. An arbitrary value y at position x between two points (x_0, y_0) and (x_1, y_1) can be calculated using a linear interpolation as

$$y = y_0 + (y_1 - y_0) \cdot \frac{x - x_0}{x_1 - x_0}, \tag{5.7}$$

where y, y_0 or y_1 can be either real or complex.

Figure 5.6: *Vector effective length* of the butterfly antenna station for 40 MHz in Euler representation.

Figure 5.7: *Vector effective length* of the butterfly antenna station for 40 MHz in complex representation.

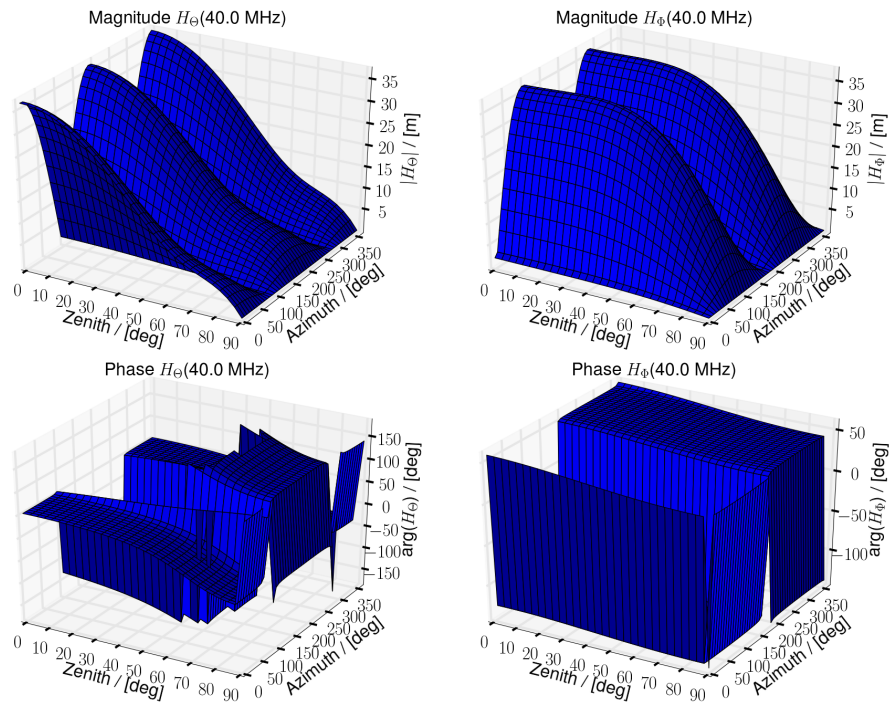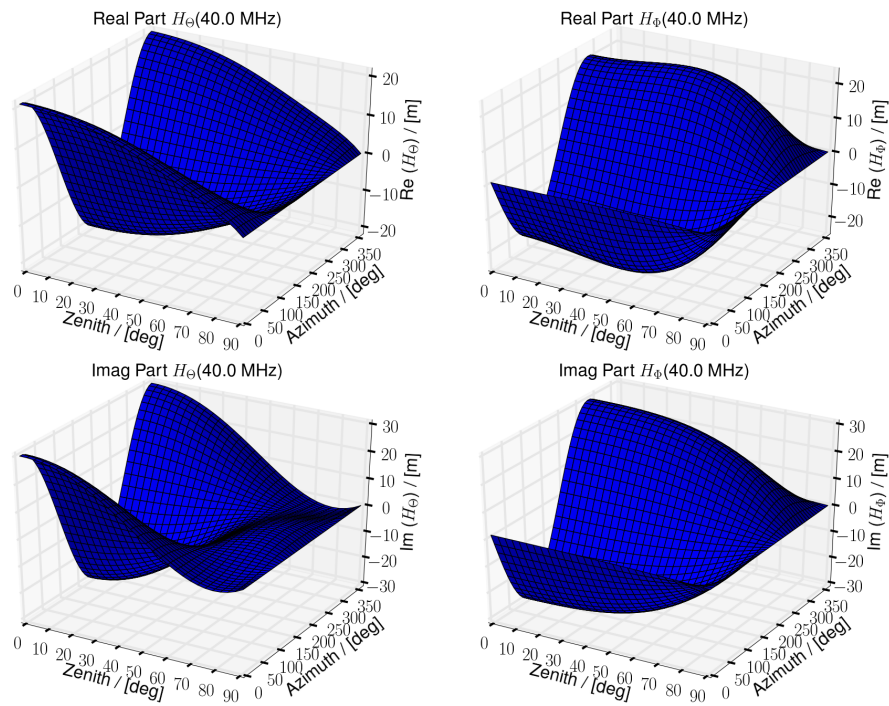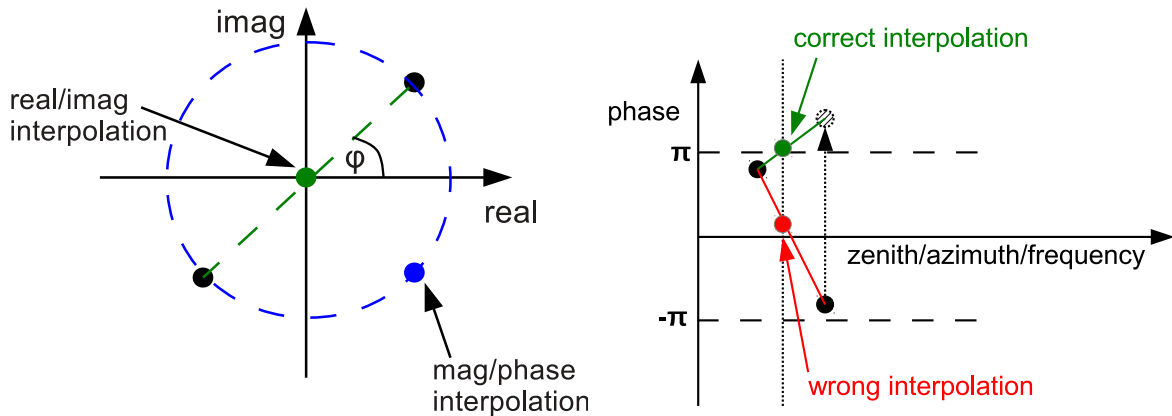**Figure 5.8:** (left) Illustration of the difference of a linear interpolation in Euler and complex representation. The black dots are the two data points and ϕ is the phase. (right) Illustration of phase interpolation error due to wrapped phases.

However, as Fig. 5.8 left illustrates, a linear interpolation in Euler and complex representation do not lead to the same result. In case of the Euler representation, an error occurs in the linear interpolation of the phase. The phase of a complex number has a periodicity of 2π and our simulation tool Nec2 [253] delivers the phases in a wrapped form, i.e., all phases are constrained to the interval $[-\pi, +\pi]$. As illustrated in Fig. 5.8 right, it can lead to completely wrong results of a linear interpolation near the edges of the $[-\pi, +\pi]$ interval.

One way to avoid this problem is to have an unwrapped antenna pattern, i.e., the phase is not constrained to the $[-\pi, +\pi]$ interval but is continuous so that no phase jumps due to the 2π periodicity occur anymore. In addition, at the positions where the magnitude is zero, a sampling point must be provided as otherwise the interpolation in the magnitude will lead to wrong results.

Technically, such a modification is difficult to be performed in an automated way. In one dimension a simple algorithm to unwrap the phases exists. If the difference between two sample points is greater than π, one of the points is shifted by $\pm 2\pi$. However, for the phases of our antenna response pattern this algorithm is not always correct because there are real phase jumps by π for specific zenith and azimuth angles, which makes it impossible to unwrap the phases in an automated way. Furthermore, the phases need to be unwrapped in three dimensions (zenith-, azimuth-angle, frequency) which makes the problem quite complex. This problem does not occur with an interpolation in complex representation.

Originally, the Euler representation was used in $\overline{\text{Off}\underline{\text{line}}}$ to interpolate the *vector effective length*. In the following, we compare the interpolation of the VEL using the two representations of the complex VEL to determine the uncertainty resulting from the simulation and to determine which complex representation leads to more accurate results.

5.4.2 Comparison of complex representations

To evaluate which representation of the complex *vector effective length* leads to better results in the linear interpolation, we test both methods with a very finely simulated antenna response pattern. Usually, a sampling of the azimuth angle of $7.5°$ and a sampling of $3°$ for the zenith angle is used. For
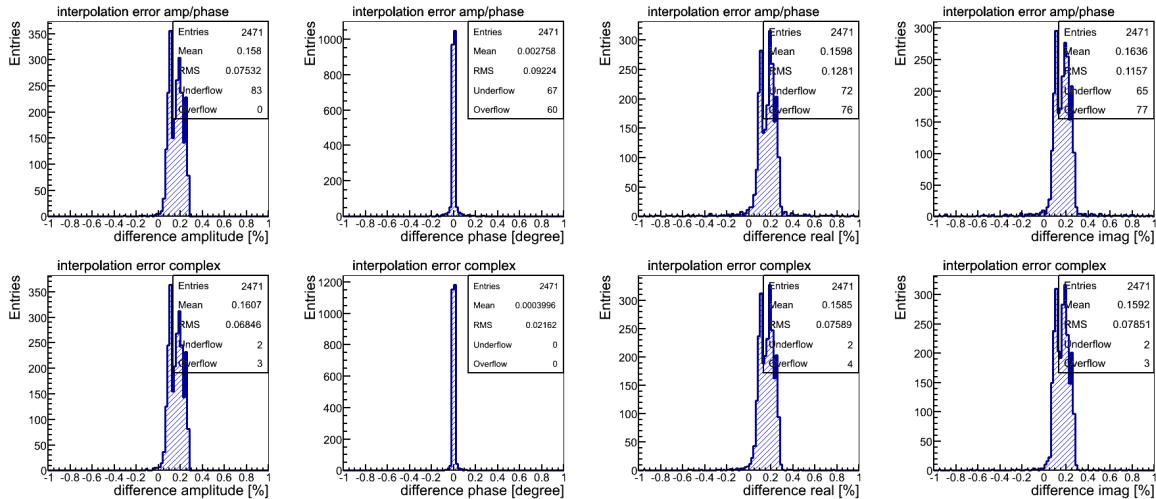
Figure 5.9: Difference between true and interpolated VEL along the azimuth angle. The results of an interpolation in the Euler representation are shown in the upper plots and the results of an interpolation directly with the complex numbers are shown in the lower plots.

this evaluation we use an antenna response pattern with a $1°$ sampling for both azimuth and zenith angle. As most of the critical structure is present in the azimuthal direction, we discuss the azimuth interpolation in some detail and mention the test of the zenith angle and frequency interpolation only briefly. All details of this analysis can be found in [252].

Azimuth interpolation   We interpolate linearly between the data points ϕ_0 and $\phi_1 = \phi_0 + 8°$. An interval of $8°$ is chosen because it corresponds best to the current sampling of $7.5°$ in azimuth. Then, seven simulated data points lie inside this interval which we can compare with the result of the linear interpolation. This comparison is performed for all values of $\phi_0 \in [0°, 360° - 8°]$ resulting in $353 \cdot 7 = 2471$ values to compare. This comparison can be done for all zenith angles and frequencies.

The result of this comparison for a zenith angle of $47°$ and a frequency of 40 MHz is summarized in Fig. 5.9. The upper four plots correspond to a linear interpolation in Euler representation and the lower four plots to a complex linear interpolation.

One observes that in case of the linear interpolation in Euler representation several under- and overflow bins are present. This means that the interpolated values differ largely (over 1% or $1°$ respectively) from the true value. A detailed look into these events reveal that the large deviations occur at data points where the phase jumps by π and the interpolation results in wrong results. The reason for this is illustrated in Fig. 5.10. If the phase jumps by π between two data points, the magnitude goes through zero. A complex linear interpolation resembles this fact whereas a linear interpolation in Euler representation will be inherently wrong. This is a strong argument to not use the Euler representation. The small number of under-/overflow bins in case of a complex linear interpolation is due to the fact that the true magnitude (real or imaginary part respectively) is close to zero. Therefore, a small absolute difference is divided by "zero" resulting in large relative deviation[1].

Neglecting the under and overflow bins, both methods lead to good results. The error due to the

---

[1]The relative deviation is defined as $\frac{y_{\text{true}} - y_{\text{interpolated}}}{y_{\text{true}}}$.
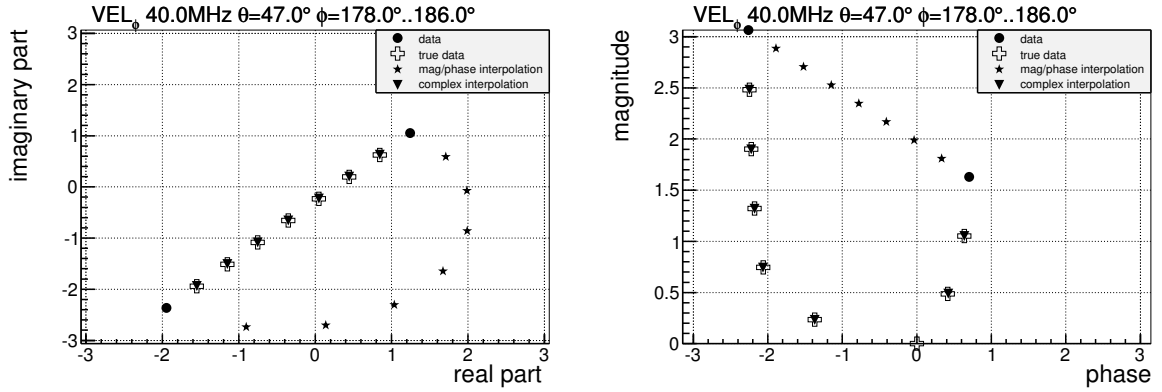
Figure 5.10: Difference between linear interpolation in Euler representation and complex interpolation.
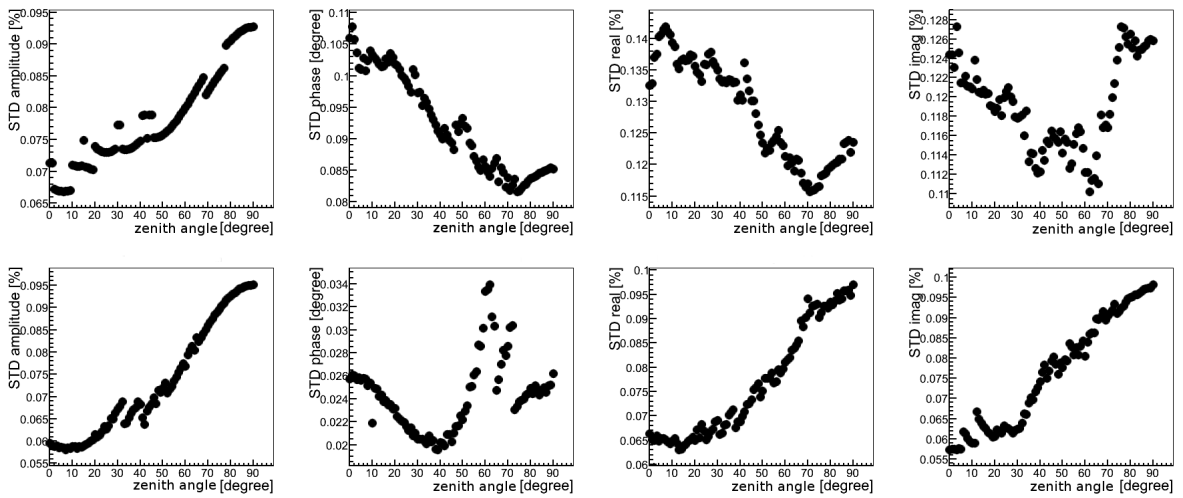
Figure 5.11: Interpolation error of the azimuth interpolation of the ϕ polarization of the VEL. The upper plots are for a linear interpolation in Euler representation and the lower plots are for a complex interpolation.

interpolation is well below 1% (1°). For the θ polarization of the VEL we obtain basically the same results. The results for all zenith angles and a frequency of 40 MHz for the ϕ polarization of the VEL are summarized in Fig. 5.11. For all zenith angles the interpolation error is well below 1%.

Zenith Angle and Frequency Interpolation   We use the same procedure as above to test the interpolation between different zenith angles and frequencies. We find that both methods work equally well as no physical phase jumps occur in these directions. The interpolation error is below 1% (or 1° respectively).

Hence, an interpolation of the *vector effective length* using the real and imaginary part leads to better or equally good results for all three dimensions (frequency, zenith and azimuth angle) and does not require the simulation of the VEL to be in a specific format. We have implemented the interpolation into the software framework $\overline{\text{Off}}\underline{\text{line}}$ using only C++ STL data containers which also turned out to be significantly faster than the old interpolation method which was based on ROOT.

5.5   Properties of cosmic-ray radio pulses

An example of a reconstructed electric-field trace of a cosmic-ray event is shown in Fig. 5.12. In principle, the radio pulse contains all information of the shower development as the radiation from all stages of the shower development is compressed in the electric-field pulse. In the following, we will present several observables that can be obtained from the cosmic-ray radio pulse and are used to reconstruct properties of the cosmic ray.

We compute the total Hilbert envelope which is the square-root of the quadratic sum of the Hilbert envelopes of the three components of the electric-field trace. The Hilbert envelope is the instantaneous amplitude and is especially useful to correctly determine the amplitude and position of the pulse maximum. As visible in Fig. 5.12, the electric-field pulse can cross zero at the position of the pulse maximum which is a result of the bandpass filtering (cf. Sec. 5.5.1). Hence, we define the pulse arrival time as the position of the maximum of the total Hilbert envelope. The uncertainty resulting from the finite time-binning of the trace can be overcome using upsampling. In most analysis, the trace is upsampled to a sampling interval of 1 ns resulting in a time uncertainty due to the finite binning of $1\,\text{ns}/\sqrt{12} = 0.3\,\text{ns}$ which is significantly smaller than other sources of time uncertainties such as the GPS clocks or the influence of noise.

The energy fluence f, i.e., the energy deposit per unit area, of the incoming electromagnetic radio pulse at each radio station is determined by calculating the time integral over the absolute value of the Poynting vector. This is achieved by squaring the magnitude of the electric-field trace and summing over a time window of 200 ns ($[t_1, t_2]$) around the pulse maximum which has been determined from the Hilbert envelope of the trace (cf. Fig. 5.12). The contribution of background noise (determined in the noise window $[t_3, t_4]$) is subtracted under the assumption that the main contribution is white noise. The energy fluence f is given by

$$f = \varepsilon_0 c \left(\Delta t \sum_{t_1}^{t_2} |\vec{E}(t_i)|^2 - \Delta t \frac{t_2 - t_1}{t_4 - t_3} \sum_{t_3}^{t_4} |\vec{E}(t_i)|^2 \right) , \qquad (5.8)$$

where ε_0 is the vacuum permittivity, c is the speed of light in vacuum and Δt is the size of one time bin. This quantity will be given in units of eV/m^2.

We also calculate the direction of the electric-field vector, i.e., the polarization direction of the signal. In the full width half maximum (FWHM) interval around the pulse maximum of the Hilbert envelope we observe that the reconstructed electric-field vectors are aligned approximately along the same direction for every time bin. To accurately determine the mean direction of the electric-field vector, we average over all vectors in the FWHM interval of the Hilbert envelope (cf. Fig. 5.12).
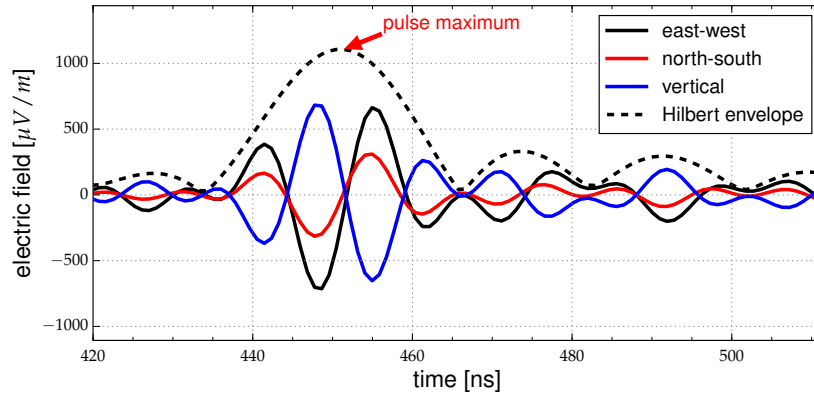
Figure 5.12: Reconstructed electric-field trace of one of the measured cosmic-ray radio events. An upsampling by a factor of five was applied. The shown Hilbert envelope (dashed line) is the square root of the quadratic sum of the Hilbert envelopes of the three polarization components. Figure and caption from [126].
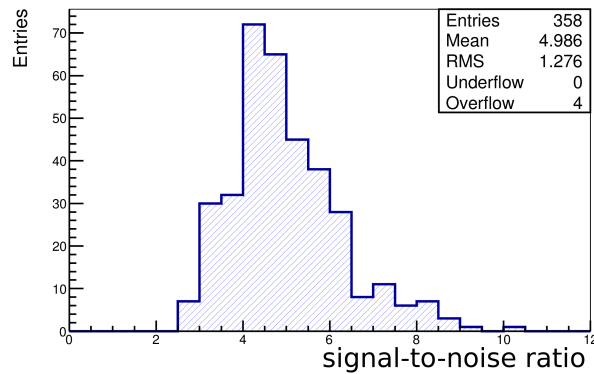
Figure 5.13: Signal-to-noise ratio of pure noise traces, i.e., traces that do not contain a signal. The asymmetry is due to the quadratic definition of the SNR.

5.5.1 Determination of uncertainties

The uncertainties of the observables of the radio pulse can be quantified using the signal-to-noise ratio (SNR). We define the SNR on the Hilbert envelope as the maximum squared divided by the noise RMS squared. This definition is not unique and several other definitions are possible and used throughout the literature. However, we showed in [254] that all common SNR definitions are strongly correlated and can be converted from one definition to the other. Therefore, the results obtained in the following are not only valid for our definition of the SNR but can be rescaled to other common definitions of the SNR using the findings of [254].

The measured SNR for pure noise traces is shown in Fig. 5.13. The expectation value of the SNR for the total component of a trace without signal is approximately five. The asymmetry towards higher values of the SNR is due to the quadratic definition of the SNR. From a technical point of view, a consistent SNR definition, i.e., a definition where the expectation value of pure noise is a SNR of unity [255], is irrelevant. Only if SNR values are interpreted the expectation for pure noise needs to be taken into account.

Simulation of electric-field traces

Analyzing simulations instead of real measurements has the huge advantage that the true air-shower properties are known. Thus, the full reconstruction pipeline can be tested and the impact of disturbing environmental influences (such as noise) can be estimated. For this purpose, a simple program was created to generate electric-field traces corresponding to specific air-shower properties. Furthermore, the $\overline{\text{Off}}\underline{\text{line}}$ software framework is extended by a module to read in these simulated electric-field traces. Hence, all modules dedicated to the reconstruction of electric-field properties can be easily tested.

We use a band-width limited delta pulse to describe the signal shape of the cosmic-ray radio signal, i.e., only one bin of the sampled electric-field trace is unequal zero. The frequency spectrum of a delta pulse is a uniform distribution of all frequencies. When the frequency spectrum is bandpass filtered from 30 to 80 MHz and transformed back to the time domain, the former delta pulse now oscillates as can be seen in Fig. 5.14 top. This small exercise already shows that the pulse shapes of the measured radio pulses originate mostly from the bandpass filtering. Therefore, most noise pulses look basically the same as cosmic-ray pulses in our detector.

We generate electric-field traces in the following way: First, the bandwidth limited delta pulse is generated for all three components of the electric field. The amplitudes of the three components of the electric field are adjusted following the geomagnetic emission model. This is

$$\vec{E} \propto \vec{v} \times \vec{B}, \tag{5.9}$$

where $\vec{B}$ is the geomagnetic field vector at the AERA site and $\vec{v}$ is the shower axis. The signal amplitude – which is defined as the maximum of the total component of the Hilbert envelope – is set to unity.

Second, measured noise is added to the signal in the time domain. This can be done in two different ways. On the one hand, the voltage traces of the periodic-triggered data can be used. However, this would require to first fold the simulated electric-field trace with the antenna response assuming a specific incoming direction of the signal pulse to obtain the voltage trace of the signal. Then the noise trace would be added to the signal trace. The resulting voltage trace would then be unfolded with the antenna response pattern to obtain the electric-field trace again. On the other hand, we can just use cosmic-ray events that are measured in coincidence with the surface detector where the electric-field trace has already been reconstructed using the directional information from the surface-detector reconstruction. Then, we use an interval of the trace after the cosmic-ray radio pulse as noise trace. Due to its simplicity and as it accurately resembles the actual situation in our measurement, we use the second approach in this study.

In this analysis, we use 152 different noise traces. For each simulated trace, we choose one of the 152 noise traces randomly. The noise trace is cut to the correct length and the start time of this interval is chosen randomly between 0 ns and 500 ns. The amplitude is set accordingly to the desired SNR. Noise for the three components of the electric field is taken from the corresponding components of the same noise trace. This is necessary because the different components are correlated. An example of such a trace can be seen in Fig. 5.14 bottom.

When the noise trace is added to the signal trace, the signal amplitude (and the position of the signal) is changed due to constructive and destructive interference. This means that also the signal-to-
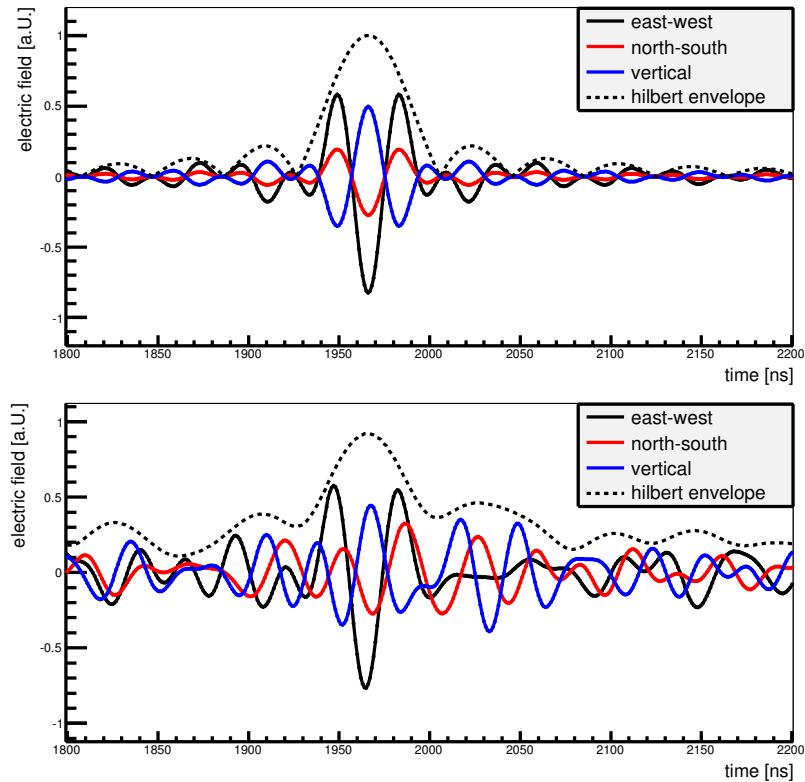
Figure 5.14: Example of a simulated electric-field trace. (top) Bandwidth limited delta pulse for all three components of the electric field. (bottom) Same as the upper plot but with noise.

noise ratio changes. To obtain the correct SNR, the signal amplitude of the signal trace is adjusted and the noise trace is added again. This is repeated several times in an iterative procedure until the SNR of the combined trace deviates less than 1% from the desired SNR. However, for small desired SNRs near the expectation value of pure noise traces (cf. Fig. 5.13) it can happen that the desired SNR can not be simulated within a precision of 1% because the pure noise trace itself has a SNR higher than the desired SNR.

Uncertainty of the electric-field vector

To study the influence of noise on the electric-field vector, more than 250,000 electric-field traces for different air-shower directions are generated and analyzed. All simulated traces are analyzed using $\overline{\text{Off}}\underline{\text{line}}$. The traces are read in with the module `RdMySimShowerReader` and the electric-field pulse properties are reconstructed using the modules `RdStationSignalReconstructor` and `RdEFieldVectorCalculator`. Hence, the same modules that are used in the reconstruction of cosmic-ray events are used and tested.

The reconstructed signal amplitudes for different signal-to-noise ratios are shown in Fig. 5.15. Each histogram contains the values of the maximum signal amplitude for one specific SNR. The standard deviation of the signal amplitude distribution is used as a measure of the uncertainty.

The result for all incoming directions and signal-to-noise ratios is shown in Fig. 5.16. In the left plot, the average signal amplitude (the mean of the histogram) is plotted versus the measured
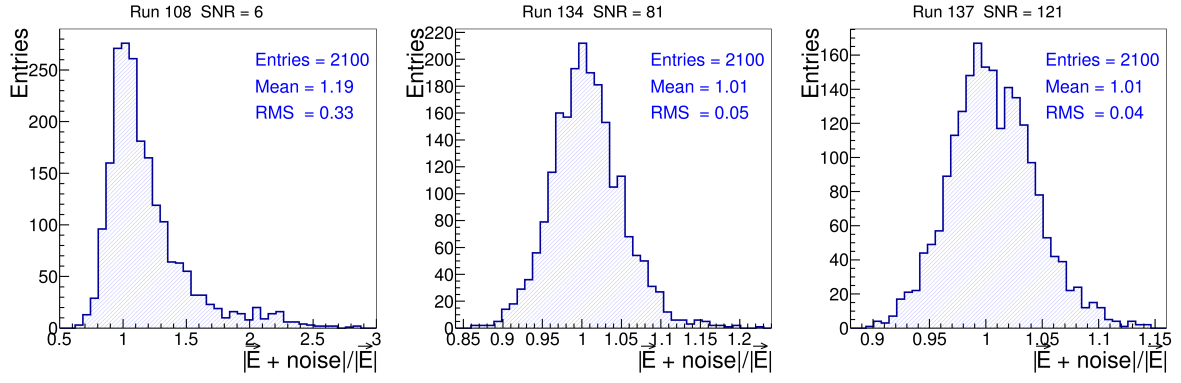
Figure 5.15: Variation of signal amplitude due to noise. The three histograms show the variation of the signal amplitude for simulations with different signal-to-noise ratios. Note that the x-axis ranges change.
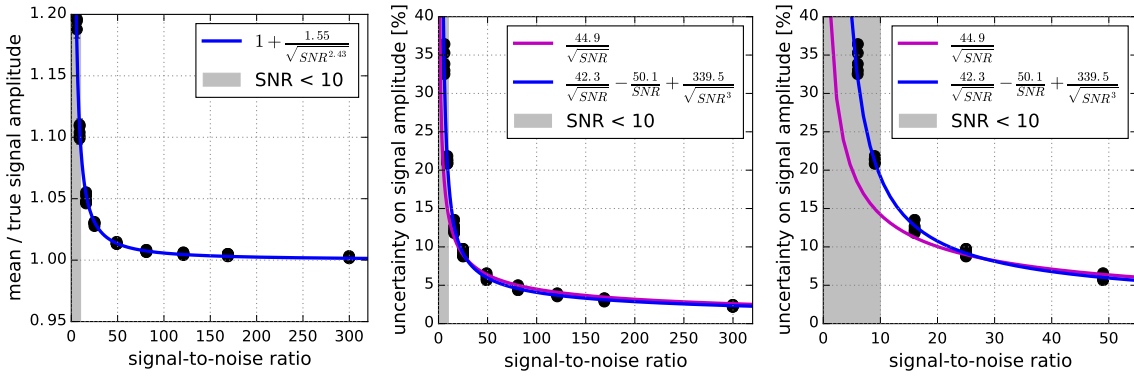
Figure 5.16: (left) Variation of the true signal amplitude as a function of the signal-to-noise ratio. Only at low SNR the signal amplitude is on average significantly increased. (center) The uncertainty on the signal amplitude as a function of the signal-to-noise ratio. Note that the average overestimation of the signal amplitude is compatible to the true amplitude amplitude within its uncertainties. Multiple data points for one SNR are the results for the different simulated arrival directions. (right) Zoom of center plot.

SNR. Only at very small SNRs the noise background has a significant influence on the average signal amplitude. The average change of signal amplitude can be described with the function

$$\frac{<|\vec{E}|>}{|\vec{E}_{true}|} = 1 + \frac{1.55 \pm 0.06}{\sqrt{SNR^{2.43 \pm 0.03}}} \ . \tag{5.10}$$

The dependence of the uncertainty of the signal amplitude on the SNR is shown in the center and right plot of Fig. 5.16. The uncertainty is in first-order anti-proportional to the square root of the SNR. This proportionality corresponds to the reasonable assumption that the uncertainty of the signal amplitude is proportional to the RMS of the noise trace as the following equation illustrates:

$$\frac{\sigma_{|\vec{E}|}}{|\vec{E}_{true}|} \propto \frac{1}{\sqrt{SNR}} \propto \frac{RMS}{|\vec{E}|} \ . \tag{5.11}$$

However, a closer inspection of the behavior at small signal-to-noise ratios (cf. right plot of Fig. 5.16) shows that such a simple parametrization is not sufficient to describe the signal uncertainty at small
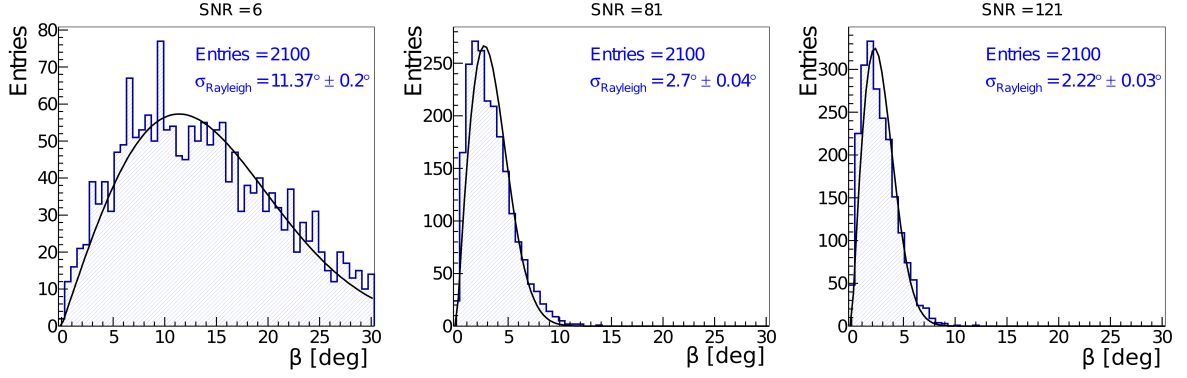
Figure 5.17: Variation of the angle β between Lorentz force and electric-field vector. The polarization of the electric-field vector was simulated accordingly to the geomagnetic emission process. Thus, the expectation of β is zero. The three histograms show the variation of β for simulations with different signal-to-noise ratios.

SNRs. Therefore, higher order correction terms are needed which results in the parametrization

$$\frac{\sigma_{|\vec{E}|}}{|\vec{E}_{true}|} = \frac{0.423 \pm 0.005}{\sqrt{SNR}} - \frac{0.501 \pm 0.062}{SNR} + \frac{3.395 \pm 0.175}{\sqrt{SNR}^3} . \tag{5.12}$$

This parametrization describes the true uncertainty with a precision of 5%.

Another quantity of interest is the polarization angle β of the electric-field pulse. In this study it is defined as the angle between the electric-field vector and the Lorentz force acting on the charged particles in the shower as we have simulated the polarization according to pure geomagnetic emission (cf. Eq. (5.9)). Hence, the expectation value of β is zero and any deviation from zero is due to noise. In general, one would define β as the deviation of measured polarization to the expectation from the geomagnetic and charge-excess emission. However, the findings obtained in this simplified simulation also apply to the more accurate definition of β.

The distribution of the reconstructed β angles for different SNRs is shown in Fig. 5.17. The distribution gets more narrow with higher SNRs and can be described with a Rayleigh function:

$$f(x) = \frac{x}{\sigma^2} \cdot \exp\left(-\frac{x^2}{2\sigma^2}\right) . \tag{5.13}$$

The position of the maximum of the Rayleigh function, which is the parameter σ of this function, is defined as the uncertainty on β. Fig. 5.18 shows that the uncertainty on the Lorentz angle is in first-order anti-proportional to the square-root of the SNR too. To describe the uncertainty at low SNR correctly, higher order correction terms are needed as well which results in the following parametrization:

$$\sigma_\beta = \frac{23.6 \pm 0.2}{\sqrt{SNR}} - \frac{4.3 \pm 2.9}{SNR} + \frac{41.8 \pm 7.2}{\sqrt{SNR}^3} \text{ deg}. \tag{5.14}$$

We use the same procedure as above to determine the uncertainty of the signal time that arises from interference of the signal pulse with noise. The dependence of the uncertainty of the signal time on the SNR is shown in Fig. 5.18 right. At the detection threshold of SNR = 10, the uncertainty is 2.3 ns and reduces quickly with increasing SNR. For an SNR greater than 32, the uncertainty is already
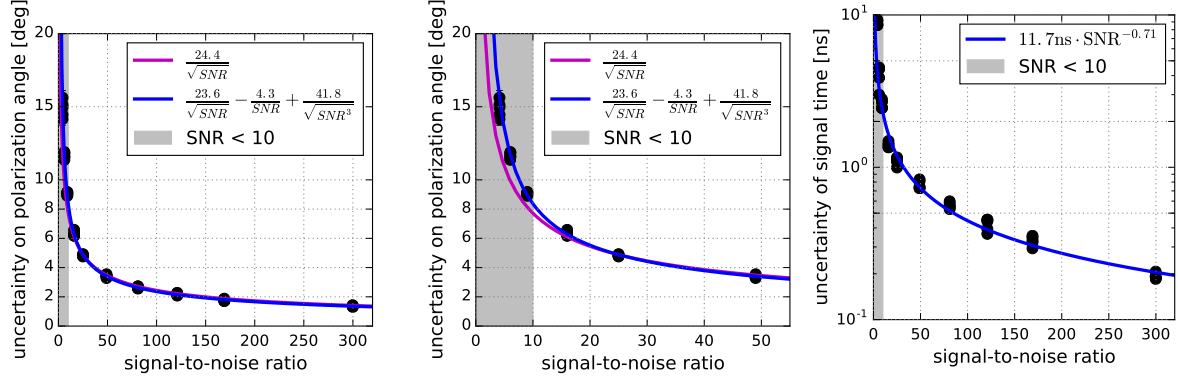
Figure 5.18: (left and center) Uncertainty of the Lorentz angle as a function of the signal-to-noise ratio. (right) Uncertainty on the signal time as a function of signal-to-noise ratio.

below 1 ns. The dependence can be described with

$$\sigma_{\text{signal time}} = 11.7 \, \text{ns} \, \text{SNR}^{-0.71} \, . \tag{5.15}$$

5.5.2 Uncertainty of the energy fluence

We estimate the uncertainty of the energy fluence by assuming that the measured electric-field amplitude $A(t)$ is the sum of the cosmic-ray radio pulse $S(t)$ and noise $e(t)$. Furthermore, we assume that the noise $e(t)$ is Gaussian distributed with mean $\mu = 0$ and standard deviation $\sigma = \sigma_e$. The energy fluence of A is then given by the equation

$$f(A) = \epsilon_0 c \Delta t \sum_{t_1}^{t_2} A(t_i)^2 = \epsilon_0 c \Delta t \sum_{t_1}^{t_2} [S(t_i) + e(t_i)]^2 = \epsilon_0 c \Delta t \sum_{t_1}^{t_2} \left[S(t_i)^2 + 2S(t_i)e(t_i) + e(t_i)^2 \right] \tag{5.16}$$

and the expectation value of $f(A)$ is

$$
\begin{aligned}
\langle f(A) \rangle =& \epsilon_0 c \Delta t \sum_{t_1}^{t_2} A(t_i)^2 = \epsilon_0 c \Delta t \sum_{t_1}^{t_2} \left[\langle S(t_i)^2 \rangle + 2\langle S(t_i)e(t_i) \rangle + \langle e(t_i)^2 \rangle \right] \\
=& \epsilon_0 c \Delta t \sum_{t_1}^{t_2} \left[\langle S(t_i) \rangle^2 + \underbrace{Var(S(t_i))}_{=0} + 2\langle S(t_i) \rangle \underbrace{\langle e(t_i) \rangle}_{=0} \right. \\
& \left. + 2\underbrace{Cov(S(t_i), e(t_i))}_{=0} + \underbrace{\langle e(t_i) \rangle^2}_{=0} + \underbrace{Var(e(t_i))}_{\sigma_e^2} \right] \\
=& \epsilon_0 c \Delta t \sum_{t_1}^{t_2} \left[\langle S(t_i) \rangle^2 + \sigma_e^2 \right] \, .
\end{aligned}
\tag{5.17}
$$

Hence, the best estimate of the energy fluence of the radio signal S is indeed

$$f(S) = \epsilon_0 c \Delta t \sum_{t_1}^{t_2} \left[A(t_i)^2 - \sigma_e^2 \right] \tag{5.18}$$

as defined in Eq. (5.8) where σ_e^2 is also calculated from the electric-field trace in a part where no signal is present. Following a similar calculation we can estimate the uncertainty of $f(S)$ by computing $\sigma_f^2 = Var(f) = \langle f^2 \rangle - \langle f \rangle^2$. After several lines of calculation it follows that

$$\sigma_f^2 = 4f\,\epsilon_0 c\,\Delta t\,\sigma_e^2 + 2\,(\epsilon_0 c)^2\,(t_2 - t_1)\,\Delta t\,\sigma_e^4. \tag{5.19}$$

5.6 Directional reconstruction

From the arrival times of the radio pulse measured in several radio detector stations, the incoming direction of the air shower can be reconstructed [220, 256, 257]. The simplest and most robust approach is to assume a plane wave as the shape of the wavefront of the radio pulse which corresponds to a source at infinite distance. Then, the expected pulse arrival times depend only on the zenith and azimuth angle of the incoming direction of the air shower and a combined measurement in three radio detector stations are sufficient to reconstruct the air-shower direction. However, as discussed in Sec. 3.1, the true signal front deviates from a plane wave and the reconstructed direction is therefore only accurate within one to two degrees.

The true radio wavefront can be described best with a hyperbolic wavefront, i.e., a combination of a conical wavefront with a spherical wavefront near the shower axis. Given the relatively large spacing of the radio detector stations, the correspondingly small average station multiplicity and the timing uncertainty, the hyperbolic wavefront can be approximated with a spherical or a conical wavefront without significant deterioration in accuracy. The expected arrival times for the different wavefront models can be calculated as

$$t_i^{planar}(\theta, \phi) \quad = -(\vec{n}(\theta, \phi) \cdot \vec{d_i})/c \tag{5.20}$$

$$t_i^{spherical}(R, \theta, \phi) \quad = |\vec{R}(R, \theta, \phi) - \vec{d_i}|/c \tag{5.21}$$

$$t_i^{conical}(\rho, \theta, \phi) \quad = (-\vec{n}(\theta, \phi) \cdot \vec{d_i} + |\vec{h}(\rho, \theta, \phi, \vec{d_i})|)/c, \tag{5.22}$$

where $\vec{n}$ is the incoming direction of the radio signal, $\vec{R}(R, \theta, \phi)$ is the source point of the spherical wave, $\vec{d_i}$ is the position of the radio detector station relative to the shower core position, ρ is the opening angle of the cone and $|\vec{h}|$ is the offset of the conical wavefront with respect to the plane wavefront as defined in Fig. 5.19 and can be calculated as $|\vec{h}| = |\vec{l}| \sin \rho$ with $|\vec{l}| = |(\vec{n} \cdot \vec{d_i})\vec{n} - \vec{d_i}|$. A detailed discussion of the spherical and the conical wave fit can be found in [256] and [257] respectively.

The shower direction is reconstructed using a χ^2 fit using the function

$$\chi^2 = \sum_{i=1}^{N} \left[\frac{(\tau_i - \langle \tau \rangle) - (t_i - \langle t \rangle)}{\sigma_i} \right]^2, \tag{5.23}$$

where τ_i is the measured time in station i, $\langle \tau \rangle$ ($\langle t \rangle$) is the mean of the measured (expected) times and σ_i is the time resolution in station i.

The spherical wavefront can be described with three parameters and an additional degree of freedom is lost as the absolute event time is set to the mean values $\langle \tau \rangle$ and $\langle t \rangle$. Hence, at least four stations with signal are required to reconstruct this wavefront. For nearly horizontal showers this wavefront
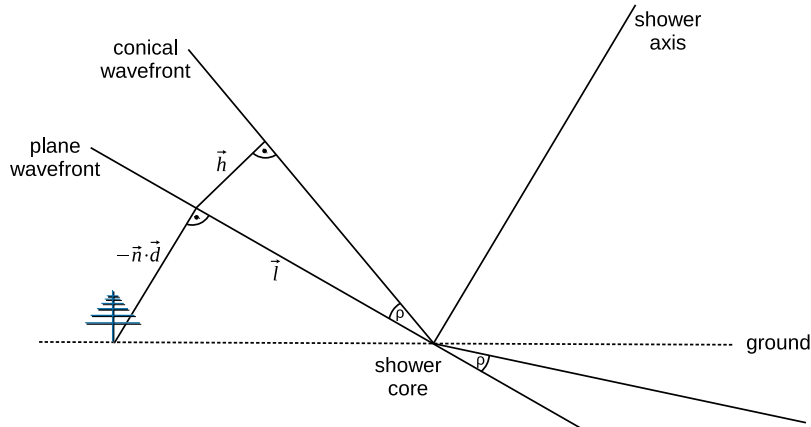
Figure 5.19: Sketch of a plane and conical wavefront.

model needs further adaption because the timing uncertainty can lead to unphysical time differences between two stations i and j. The maximum allowed time difference is $\Delta t_{i,j} = d_{i,j}/c$, where $d_{i,j}$ is the geometrical distance between the two stations which is obtained in the fit for purely horizontal showers ($\theta = 90°$). However, due to timing uncertainties the measured time difference can even exceed the maximum allowed time difference between two stations. To avoid a reconstruction bias towards $\theta = 90°$, we allow for a variation of the speed of light $c' = \gamma c$ and add the penalty term $(1 - \gamma)^2/\sigma_\gamma^2$ to the χ^2 function, where σ_γ is adjusted to the time resolution of the detector. To do so, we interpret the signal detection as a measurement of the speed of light and set $\sigma_\gamma = \sqrt{2}\,\sigma_t\,c/\Delta d$, where Δd is the average distance between two detector stations and σ_t is the average timing uncertainty. This functionality is used for zenith angles larger than $80°$ if more than four stations with signal are present.

The conical wavefront depends in addition to the direction (θ, ϕ) and the cone opening angle ρ also on the shower core position. In practice, this is a significant disadvantage as the core position obtained with other methods has a relatively large uncertainty. E.g., the shower core position reconstructed by the surface detector that can by used in a hybrid reconstruction has a typical uncertainty of $\mathcal{O}(50\,\mathrm{m})$. A combined fit of the shower direction, the cone opening angle ρ and the core position is relatively unstable and requires a large station multiplicity. Hence, although a conical wavefront in principle describes the true radio wavefront better than a spherical wavefront for most air showers, the fit of a spherical wavefront leads to a more stable and a more precise reconstructed air-shower direction in the actual measurement.

All wavefront models discussed above are implemented in the $\overline{\text{Off}}\underline{\text{line}}$ module `RdWaveFit`. The reconstruction is performed in several stages, starting with the plane wavefront and then fitting more parameters of the more complex wavefront models. If a more complex fit fails the solution of the simpler model is used. The reconstruction status is saved so that the user can apply quality cuts afterwards depending on the requirements of his analysis. However, many analyses use a hybrid reconstruction where the shower direction from the surface detector reconstruction can be used and the directional reconstruction from radio data is primarily used to confirm a cosmic-ray origin of the measured radio pulses. In these cases, a directional reconstruction using a plane wavefront is sufficient.
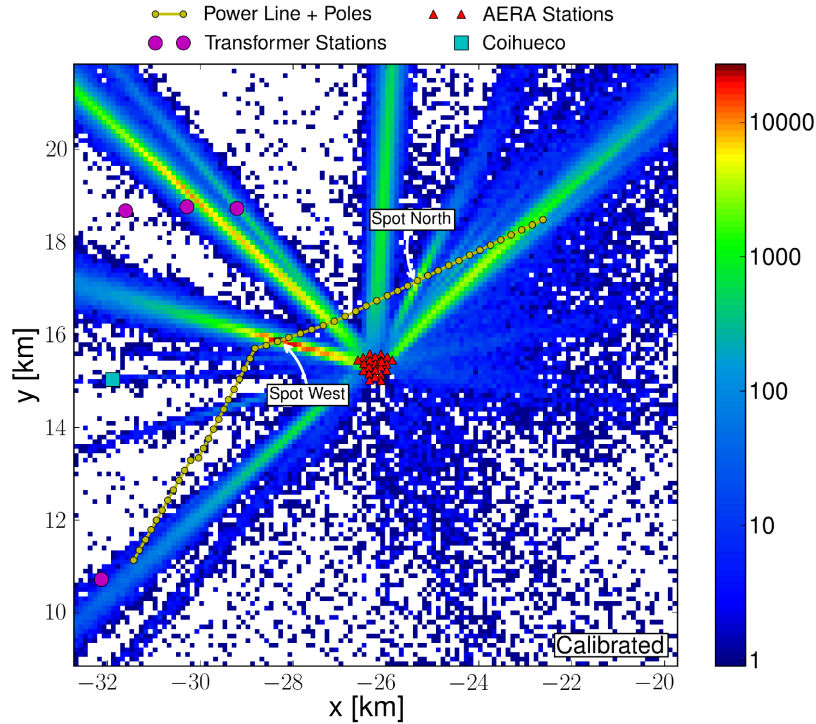
Figure 5.20: Map of the x and y position of the reconstructed source point of self-triggered data. The map is generated with a preliminary time calibration with a binning resolution of 100 x 100 m^2. At the 'Spot West' a single bin is filled with 27000 entries. Note the logarithmic color scale. Figure and captions adapted from [220].

5.6.1 Reconstruction of noise sources

Several noise sources that emit short radio pulses are present in the vicinity of the AERA detector. These are e.g. transformer stations or power-line poles [220, 258]. Their pulses look basically the same as cosmic-ray radio pulses in the AERA detector as the pulse shape is primarily determined by the limited frequency range of 30 - 80 MHz of the detector. Such noise events are recorded by the self-trigger and can be used for timing calibration purposes. The position of the noise source can be reconstructed using the spherical wavefront model. As the noise source has a constant position, we can determine the uncertainty of the fit by inspecting the scatter of the reconstructed noise source positions of several events. We can even determine the timing uncertainty of radio detector stations by inspecting the residuals of the spherical wave fit. Noise pulses are very frequent and more than 100,000 events have been recorded from the most prominent noise source in the west of the AERA array ("Spot West") in the first year of data taking. A map of reconstructed source points from the self-triggered data is shown in Fig. 5.20[2].

The GPS clocks of the radio detector stations have time offsets of several tens of nanoseconds that also drift in time. Without any time correction the residuals of the events from "Spot West" have a width of 13 ns which we use as an estimate of the timing uncertainty of the individual radio detector stations. In first order, we can calibrate the detector assuming constant time offsets between the GPS clocks of the radio detector stations that do not change in time. We determine the time offsets by minimizing the spread of the residuals for all events from "Spot West". Details of the procedure

---

[2]In the meanwhile the triggers have been improved to reduce triggers from noise sources significantly.

can be found in [220, 257]. In [257] four days of data from end of August 2012 have been used to determine the constant time offsets. With this calibration the width of the residuals of the events from "Spot West" could be reduced to 5.5 ns. However, due to the drifts of the time offsets this calibration is only valid for a certain time period. This problem can be overcome using the beacon system to correct the time offsets event-by-event (cf. Sec. 4.4.4). We find that the residuals of the events from "Spot West" reduce to 3 ns after beacon correction which is an independent confirmation of the beacon method.

5.7   Noise pulse probability

Parts of this chapter have been published in:

C. Welling, M. Erdmann, and C. Glaser
„Event Selection and Investigation of the Lateral Distribution and Polarization of Radio Signals from Cosmic Ray Induced Air Showers"
Internal note of the Pierre Auger Collaboration (2014), GAP 2014-079

C. Welling
„Investigation of the Lateral Distribution and Polarization of Radio Signals from Cosmic Ray Induced Air Showers at the Pierre Auger Observatory"
BA thesis (RWTH Aachen University, 2014)

Radio antennas with the high sensitivity necessary to detect radio emissions from cosmic rays also inevitably pick up signals from other sources. The 30 - 80 MHz frequency band is rather quiet but noise pulses still occur frequently which was already visible from the analysis of the precious section. We determine the noise-pulse rate by analyzing the periodic-triggered data between December 2013 and March 2014. In each recorded trace we search in a time window of 1000 ns, which is a typical size for the signal search window, for a pulse with a signal-to-noise ratio larger than 10. The frequency of noise pulses of the different radio detector stations is shown in Fig. 5.21 left.

Most air-showers are triggered in AERA by an external trigger from the Auger surface detector. AERA is triggered whenever the surface detector registers an event within a 5 km distance to the nearest radio detector station. Hence, the air shower is often too far away from the AERA detector to detect any radio pulses from the air shower. However, noise pulses coinciding with an SD event may occur and can be mistaken for a radio signal from the air shower. The first step to filter out these fake events is to compare the incoming directions of the radio and SD reconstructions and if the angular distance is greater than $20°$ the event is dismissed. Many false events are filtered out this way, but there is still a chance that both reconstructed arrival directions agree by mere coincidence. In the following we estimate the chance of such a fake coincidence in a toy Monte Carlo. First, we assume that all noise pulses are uncorrelated. Then a correlation of the noise pulses in neighboring stations is taken into consideration. And third, we investigate the situation of radio stations detecting an actual air shower in the presence of noise pulses.
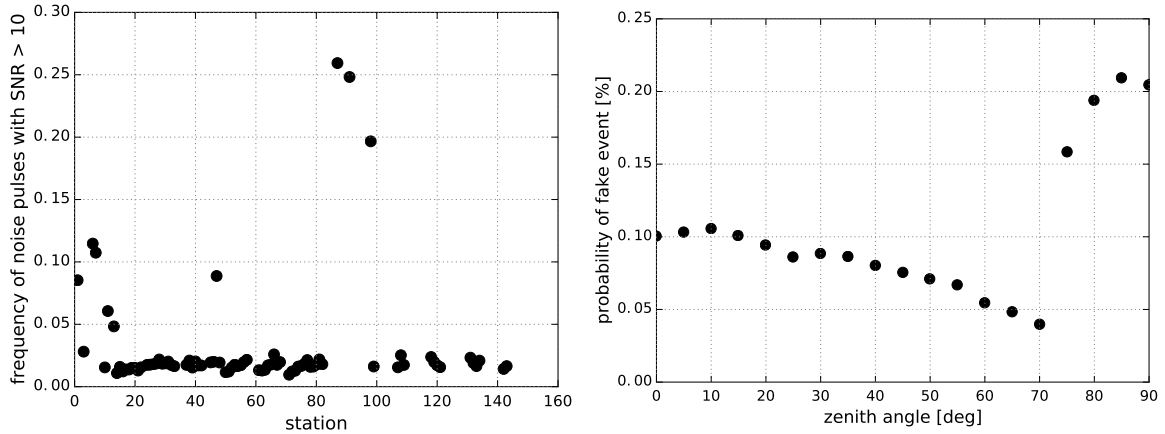
Figure 5.21: (left) Chance of finding a pulse with SNR > 10 within a 1000 ns noise trace. (right) Probability of uncorrelated noise pulses creating a fake event for different zenith angles for a signal search window of 1000 ns.

5.7.1 Uncorrelated noise pulses

We first consider that the occurrences of noise pulses are uncorrelated. Though some stations have a significantly higher noise pulse rate than the others (cf. Fig. 5.21 left), for simplicity we assume that for each station the chance of finding a noise pulse in any given 1000 ns interval is equal to the mean value extracted from Fig. 5.21 left which is $p_0 = 0.015$. Within the signal window, the signal time of a noise pulse is assumed to follow a uniform distribution.

We simulate the situation of an external trigger where no radio pulse originating from the air shower is visible in the AERA detector. The air-shower geometry is known from the SD reconstruction and the signal search window is set accordingly to the expected pulse arrival time t_{exp} that is calculated from the air-shower geometry. For each station of the AERA24 detector we randomly determine if the station has detected a pulse according to the probability of observing a noise pulse. For those stations we set the signal time to

$$t_{\mathrm{signal}} = t_{\mathrm{exp}} + t_{\mathrm{random}} \tag{5.24}$$

where t_{exp} is the expected signal time using a plane wavefront and t_{random} is a random number generated from a uniform distribution between 0 ns and the length of the signal search window. The time t_{exp} corresponds to the start position of the signal search window while t_{random} is the position of the event inside of the signal window.

If at least 3 stations have detected a signal, the incoming direction is reconstructed and compared to the incoming direction measured by the surface detector. If the angular distance is less than 20° the noise pulses would be interpreted as an actual signal from an air shower. By repeating this process multiple times and counting the instances in which the reconstructed direction from the noise pulses are in coincidence with the SD reconstruction, the probability of detecting a fake event can be determined. We find that this probability depends on the zenith angle of the air shower and present the zenith-angle dependent probabilities in Fig. 5.21 right. For each data point one million events were simulated. The azimuth angle was randomly chosen from a uniform distribution between 0° and 360° in each simulated event because the detector geometry might cause certain azimuth angles to be preferred in the reconstruction.
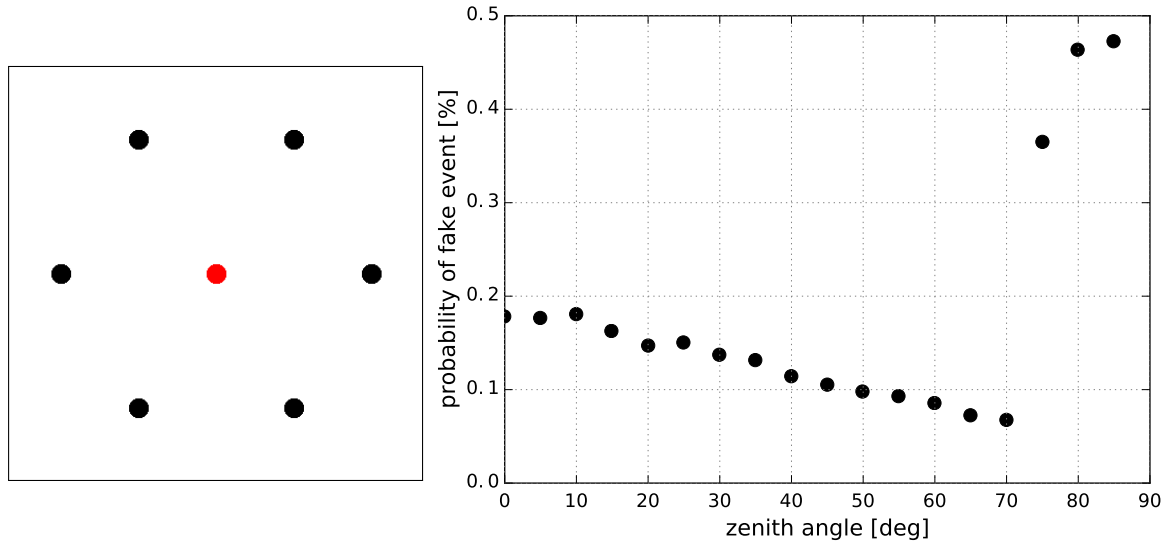
Figure 5.22: (left) Sketch of the geometry of the simulated radio detector stations. (right) Probability of correlated noise pulses creating a fake event as a function zenith angle for a signal search window of 1000 ns.

Table 5.1: Probability p_N of detecting noise pulses in N neighboring stations simultaneously in a 1000 ns signal window.

N	3	4	5	6	7
p_N	0.0102	0.0042	0.0029	0.0018	0.0007

The simulation shows that the probability of detecting fake events decreases with increasing zenith angles until $\theta = 70°$. The sudden increase for $\theta > 70°$ can be explained by the tendency of the simulation to reconstruct the zenith angle as $\theta = 90°$. This is because with a signal window of 1000 ns the signal time difference between two stations will often be larger than their geometrical distance divided by the speed of light. In that case, the best reconstruction results in a zenith angle of $90°$.

A probability of 0.1% or less may seem rather small, but since the number of SD events that are checked for a radio counterpart is large compared to the actual number of detectable air showers as no strict cut on the distance to AERA or on the cosmic-ray energy is applied, it is enough to produce a significant number of fake events.

5.7.2   Correlated noise pulses

A more realistic model for the occurrence of noise pulses is to account for correlations between noise pulses in neighboring stations. We simulate a cluster of seven stations with a distance of 125 m between neighboring stations which corresponds roughly to the geometry of AERA24. One station is in the middle while the other six are surrounding it, as illustrated in Fig. 5.22 left. We search for clusters where the central station and at least two of the surrounding stations have a signal. From the same periodic-triggered data set as used in the previous section the probability p_N of detecting noise pulses in N neighboring stations simultaneously was determined by checking each of the 1000 ns traces if it includes any of the clusters described above. The result is presented in Tab. 5.1.

In the toy Monte Carlo, the central station always has a signal while it is randomly determined

which of the neighboring stations have detected a radio pulse. The signal times were set in the same way as in the previous section and the reconstruction of the incoming direction was done in the same way. By determining the probability of the direction reconstructed from the noise pulses differing by less than $20°$ from the simulated direction and multiplying it with p_N, the probability of correlated noise pulses creating a fake event is calculated for each N. By adding the probabilities from all five cases ($N \geqslant 3$), the total probability of fake events from correlated noise pulses is calculated. We again show the result depending on the zenith angle of the air shower in Fig. 5.22 right. As in the case of uncorrelated noise pulses, the probability p of detecting a fake event first decreases with increasing zenith angle and then increases dramatically for $\theta > 70°$. The explanation for this phenomenon is the same as in the previous section. The probability p is significantly higher than in the case of uncorrelated noise pulses.

5.7.3   Contamination of cosmic-ray events by noise pulses

Noise pulses can also coincide with a cosmic-ray event, i.e., pulses have been detected in several radio detector stations but in some stations not the pulse originating from the air shower but a noise pulse has been identified. This situation has two effects. First, the noise pulse(s) can distort the reconstruction of the air-shower direction so that a cosmic-ray event is falsely rejected because the incoming direction reconstructed from radio and surface detector data differ by more than $20°$. Second, although in one or several radio detector stations a noise pulse have been detected, the air-shower direction is still reconstructed well enough to pass the $20°$ cut. Whereas the first case results in a lower efficiency the second case results in wrongly reconstructed air-shower properties such as the signal polarization or the radiation energy. Those events needs to be rejected before a high-level analysis.

To estimate the probability of any of those two cases happening, the following assumptions are made: In the toy Monte Carlo simulation, the shower core is located in the center of the AERA24 array. It is assumed that for each air shower all radio stations within a certain distance to the shower axis detect a pulse originating from the air shower. Noise pulses are assumed to be uncorrelated to one another and occur with the same probability as in Sec. 5.7.1. The signal from the air shower is assumed to be so strong compared to the noise pulses that only stations that have not detected a signal from the air shower are able to detect a noise pulse. When a noise pulse occurs far away from all other signal stations, this pulse is easy to distinguish from the air-shower pulses. Therefore, only noise pulses within a certain distance R_{noise} to the shower axis are considered.

In the first step, an air shower is simulated by defining its incoming direction (via the zenith and azimuth angle) and assigning a radio signal to all stations within a distance R_{signal} to the shower axis. Like in the previous sections, the azimuth angle is chosen randomly for each simulated event. The signal time at each station is set equal to

$$t_{\mathrm{signal}} = t_{\mathrm{exp}} + t_{\mathrm{Gauss}} \tag{5.25}$$

where t_{Gauss} is a random number drawn from a normal distribution with $\mu = 0\,\mathrm{ns}$ and $\sigma = 10\,\mathrm{ns}$ that is meant to simulate the statistical uncertainty of the signal time measurement.

In the next step, the stations within the distance R_{noise} from the shower axis that did not receive a signal from the air shower are randomly assigned a signal according to the probability of detecting a

(a) $R_{\mathrm{signal}} = 150\,\mathrm{m}$, $R_{\mathrm{noise}} = 250\,\mathrm{m}$

(b) $R_{\mathrm{signal}} = 150\,\mathrm{m}$, $R_{\mathrm{noise}} = 350\,\mathrm{m}$

(c) $R_{\mathrm{signal}} = 200\,\mathrm{m}$, $R_{\mathrm{noise}} = 400\,\mathrm{m}$

(d) $R_{\mathrm{signal}} = 300\,\mathrm{m}$, $R_{\mathrm{noise}} = 500\,\mathrm{m}$
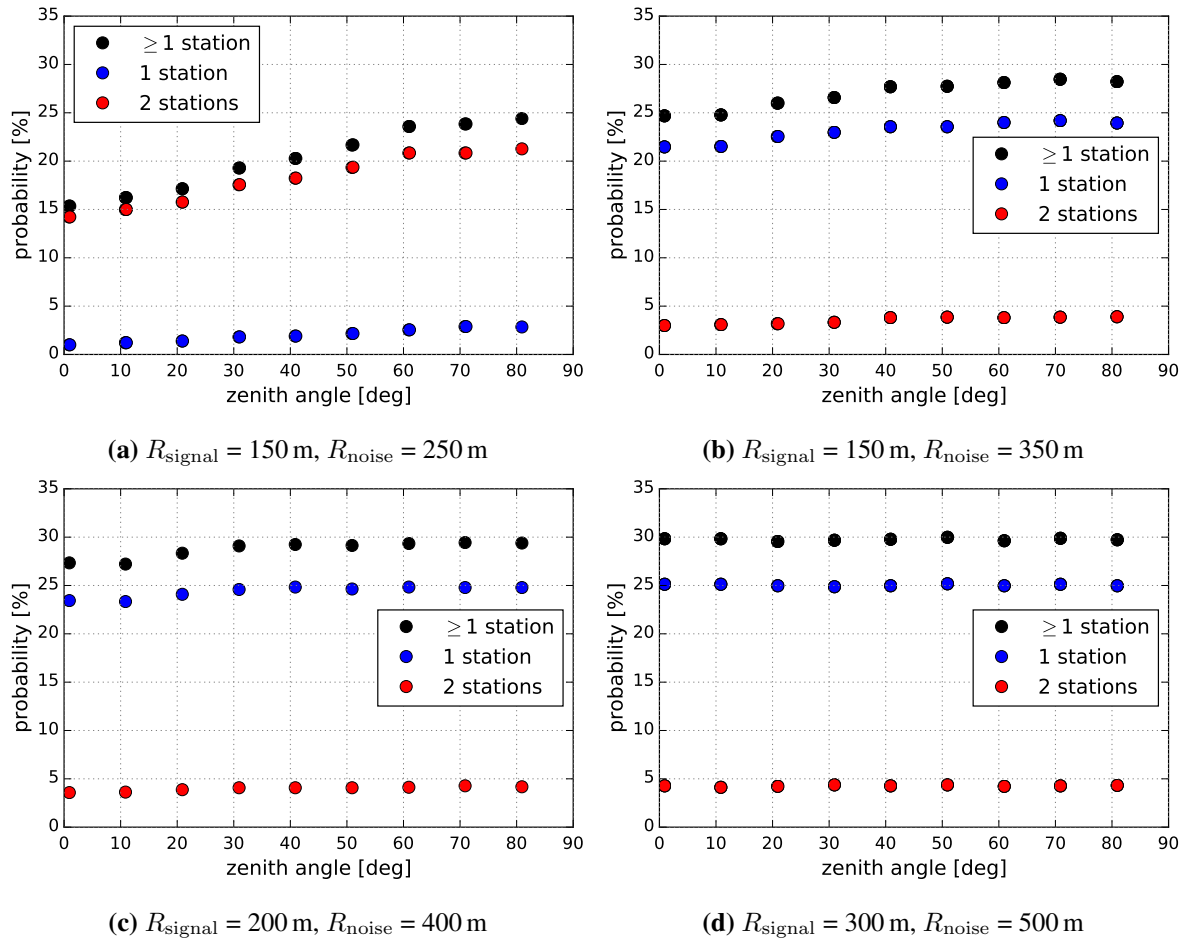
Figure 5.23: Probability that the signal from an air shower measured by the AERA24 array is contaminated by at least one (black), one (red) or two (blue) noise pulses.

noise pulse ($p = 1.5\%$, cf. Fig. 5.21). If a signal is assigned, the signal time is set randomly within the signal window of 1000 ns around the expected signal time. To estimate the probability of a cosmic-ray event being rejected based on the incoming direction, the incoming direction is reconstructed and the $20°$ cut is applied. For those events passing this cut, the number of noise pulses participating in the event are counted.

Since the radius in which the radio detector stations can detect air-shower signals vary with the incoming direction and energy of the cosmic ray, the simulation is done for shower radii of $R_{\mathrm{signal}} = 150\,\mathrm{m}$, $200\,\mathrm{m}$ and $300\,\mathrm{m}$ and different values for R_{noise}. The results are presented in Fig. 5.23. For each point 100,000 events have been simulated. For all settings of R_{signal} and R_{noise} the probability of a contamination by at least one noise pulse is found to vary between 15% and 30%, with contamination by a single noise pulse being by far the most likely case. The probability of a contamination by a noise pulse shows a dependency on the zenith angle only for small R_{signal}. To interpret this, one has to keep in mind that the simulation only considers the stations of the AERA24 array. Given a shower core in the center of the array, all stations are contained within a distance of about 600 m around the shower core. For this reason the number of stations within the radius R_{noise} increases with the zenith angle only for small values of R_{noise}. If all stations of the AERA array are taken into account, p depends on
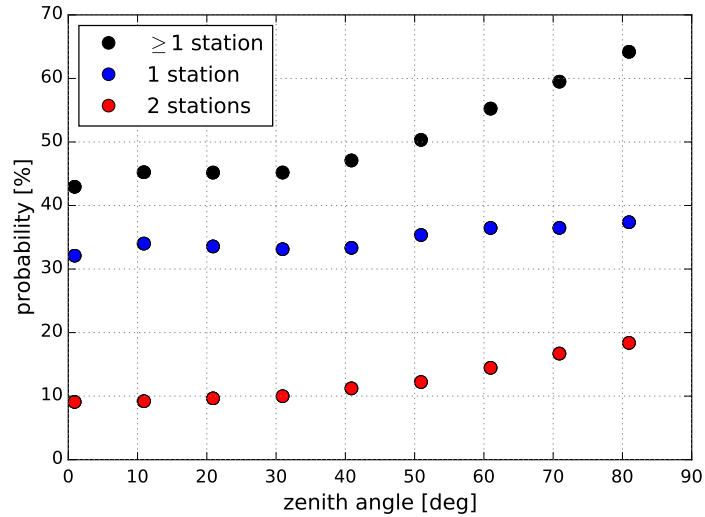
Figure 5.24: Probability that the signal from an air shower with R_{signal}= 300 m is contaminated by at least one (black), one (red) or two (blue) noise pulses within a radius of R_{noise} = 500 m from the shower axis if all AERA stations are considered.

the zenith angle for R_{signal} = 300 m as well as shown in Fig. 5.24.

For all simulated settings of R_{signal} the reconstructed incoming direction of the air shower agreed with the actual incoming direction within the $20°$ window. For the AERA24 array and a signal window of 1000 ns it is therefore unlikely that noise pulses cause an air shower to be falsely rejected based on the incoming direction. However, the simulations showed that the contamination of cosmic-ray events by noise pulses is not negligible and additional criteria need to be applied to reject individual stations from a cosmic-ray event.

5.8 Top down selection

One way to reject radio detector stations where a wrong pulse have been identified is the "top down selection". In this approach, the reconstruction of the air-shower direction is first performed only with the three stations with the smallest distance to the shower axis. At these stations the radio pulse originating from the air shower should be largest and therefore the probability of identifying a noise pulse instead of the air-shower pulse is smallest. The remaining stations with signal are sorted according to their distance to the shower axis. In an iterative procedure, one station after the other is added to the reconstruction of the air-shower direction, starting with the station with smallest distance to the shower axis. The last-added station is rejected if the directional reconstruction fails or if the fit quality is too low. This procedure is repeated until all stations with signal have been considered.

The fit quality is determined using the χ^2 probability. We require a value of at least 5% in the standard reconstruction. In the case of a plane wavefront model, the number of degrees of freedom is 1 for 4 stations participating in the fit. Thus, the χ^2 probability of 5% corresponds to a reduced χ^2 of ~ 4. In the case of six stations participating in the fit, the χ^2 probability of 5% corresponds to a reduced χ^2 of ~ 2.6. From this small example it is directly visible that the χ^2 probability is the preferred criterion of fit quality compared to, e.g., the reduced χ^2 of the fit as the probability of

exceeding a specific reduced χ^2 depends strongly on the degrees of freedom in the fit.

This functionality was implemented in the $\overline{\text{Off}}\underline{\text{line}}$ module `TopDownSelector` and is used in the standard AERA reconstruction. In [261] the performance of this module was evaluated and it was found that the inclusion of this module results in a significant increase of purity. In the reconstruction of data from the AERA124 array, the top down selector deselects at least one station in 15% of all cosmic-ray events. For those events, where at least one station is rejected, the average number of rejected stations is 3.6. In a more recent preliminary analysis [262] it was found that the top-down selector has a noise-pulse rejection efficiency of up to 90% depending on the zenith angle of the air shower while less than 1% of true signal pulses are falsely rejected.

5.9 Resampling of simulated extensive air showers including radio emission

---

Parts of this chapter have been published in:

M. Erdmann and C. Glaser

„A new Method for Resampling of Simulated Extensive Air Showers including Radio Emission"
Internal note of the Pierre Auger Collaboration (2013), GAP 2013-099

Monte-Carlo simulations of the radio emission from extensive air showers [130, 156] evolved so far that they can reproduce detailed measurements of the radio signal from extensive air showers [12, 14, 18] and became a useful and reliable tool to study radio emission from extensive air showers. However, a full Monte-Carlo simulation of an extensive air shower including radio emission is very time consuming. It takes roughly one CPU day for one air shower over the AERA24 array (e.g. an energy of 0.5 EeV and 24 observers). Please note that the radio signal has to be calculated for each observer individually. Therefore, computing resources are often the limiting factor for interesting analyses.

In this section we develop a method that uses our knowledge of radio emission to resample simulated air showers multiple times. We present a new method to transform the azimuth angle of the incoming direction of the air shower to arbitrary values. Thus, with one simulated air shower of one specific energy and zenith angle the whole azimuth-angle range can be covered. This reduces the necessary number of simulations by a factor of 10 - 100. In Sec. 5.10 this resampling method will be used to determine the efficiency of the AERA detector.

5.9.1 Method

The amplitude and polarization of the radio signal depends on first order on the angle between shower axis and magnetic field axis (geomagnetic emission) and on second order on the position of the observer relative to the shower axis (charge-excess emission) (cf. Sec. 3.1). Hence, the expected electric-field vector depends on the incoming direction of the air shower, the core position and the position of

(a) Observer at (-100 m, 0 m)   **(b)** Observer at (0 m, 0 m)   **(c)** Observer at (+100 m, 0 m)
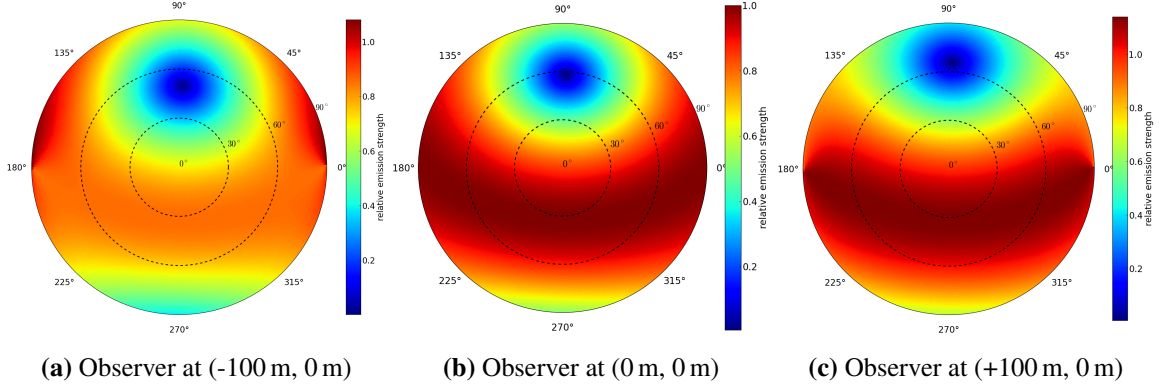
Figure 5.25: Skyplot of relative emission strength for different positions of the observer. The normalization is such that a maximum pure geomagnetic emission has an amplitude of one.

the observer and can be calculated as

$$\vec{E}_{\text{exp}} \propto \sin \alpha \cdot \vec{e}_{\text{geo}}(\theta, \phi) + a \cdot \vec{e}_{\text{CE}}(\theta, \phi, \vec{d}_i, \text{core}). \tag{5.26}$$

$\vec{e}_{\text{geo}}$ is the expected electric-field vector for geomagnetic emission which depends on the incoming direction of the air shower only (θ and ϕ are the zenith and azimuth angle) and can be calculated via $\vec{e}_{\text{geo}} = \vec{n}(\theta, \phi) \times \vec{B}$, where $\vec{n}$ is the shower axis and $\vec{B}$ the geomagnetic field of the Earth. The unit vector $\vec{e}_{CE}$ is the expected electric-field vector for charge-excess emission which depends in addition to the shower axis on the position of the radio station $\vec{d}_i$ and the position of the shower core. The angle α is the angle between shower axis and geomagnetic field and a is the charge-excess fraction which has been measured to be $\sim 14\%$ on average at AERA [12]. To get an impression of the formula, a skyplot of the relative emission strength for three different positions of the observer is shown in Fig. 5.25.

To resample a simulated air shower, we alter the azimuth angle of the geomagnetic field $\vec{B}$. This corresponds to a change of the azimuth angle of the incoming direction of the air shower but has the advantage that the distances between shower axis and observers do not change. (Actually, it corresponds to a change of the azimuth angle of the incoming direction of the air shower and a rotation of the detector around the shower core with the same change in azimuth angle. Due to the strong homogeneity of the AERA24 detector a rotation of the detector has only a minor to negligible influence on most analyses).

For each radio station the transformation matrix A which transforms the simulated electric-field vector onto the new electric-field vector for a different geomagnetic field is calculated by solving

$$\vec{E}_{\text{rot}}(\phi_1, ...) = A \cdot \vec{E}_{\text{sim}}(\phi_0, ...). \tag{5.27}$$

Then, the whole electric-field trace, i.e., the electric-field vector at each time bin of the trace, is multiplied with A to get the transformed trace.
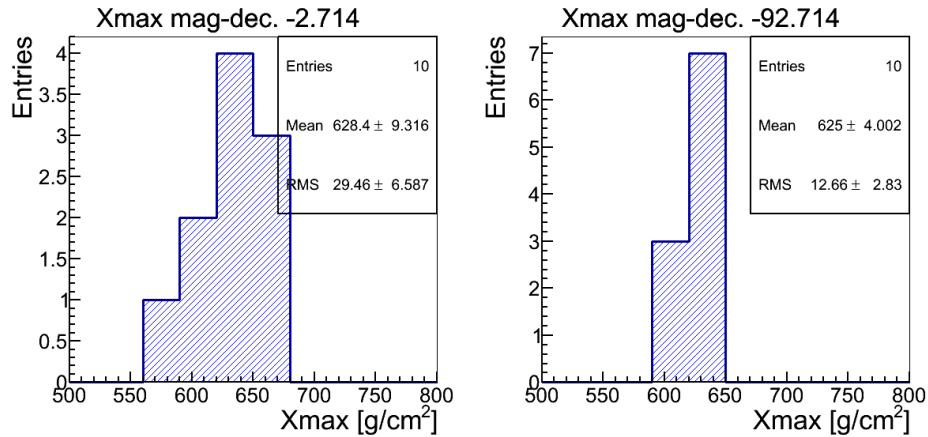
Figure 5.26: X_{max} distributions for the two sets of air showers with different magnetic-field declination.

5.9.2   Test of method

To check if this transformation of the electric-field trace to a new azimuth angle of the geomagnetic field leads to the same result as a full Monte-Carlo simulation with same cosmic-ray energy, zenith angle, core position and altered magnetic-field axis, the following test is performed.

We simulate multiple showers with the same shower parameters but different seeds using CoREAS. Thus, the difference in the radio signal is only due to shower-to-shower fluctuations. For all simulated showers we transform the electric-field traces to a magnetic field with different declination (azimuth angle). These transformed air showers are compared to new full Monte-Carlo simulations with the same shower parameters but different geomagnetic-field axis. Please note that the method can not be tested on a one-to-one bases because the shower developments of two showers with the same parameters including the seed but different geomagnetic-field axes will be different.

For the test, 10 iron-induced air showers with an energy of $1\,\mathrm{EeV}$, a zenith angle of $40°$, coming from the south, a shower core in the center of the AERA24 array and the geomagnetic field at AERA ($\vec{B}_1$) were simulated. Another 10 showers with the same parameters but a geomagnetic-field axis with the declination changed by $-90°$ ($\vec{B}_2$) were simulated. Air showers with iron primaries are simulated because iron-induced showers have less fluctuations. It is checked if by the transformation of the first 10 showers the result of the second 10 showers can be obtained.

The X_{max} distributions of the simulated air showers are shown in Fig. 5.26. The X_{max} distributions of both sets are not exactly the same, hence, we would expect small deviations between the transformed electric fields of the first set and the electric fields of the second set. The angular differences of the electric-field vectors of the two sets are shown in Fig. 5.27. In the left plot the electric fields of the first set were transformed whereas in the right plot no transformation was performed. A comparison of both distributions shows that the method works properly. An average agreement of better then two degrees is achieved. The distributions of the radio signal in station 14 normalized to an arbitrary reference signal is shown in Fig. 5.28. The signal distribution of the transformed air showers of set 1 (center) agrees well with the signal distribution of the simulated air showers of set 2 (right).

The signal distributions of all stations can be compared and checked for compatibility. To do so, we use the Student's-t distribution which is the correct test to check the means of two distributions
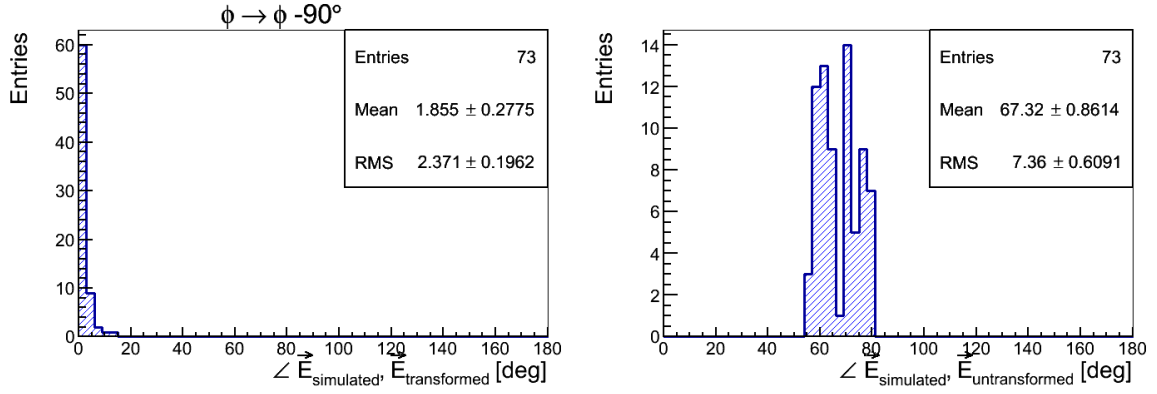
Figure 5.27: Angular difference between the directions of the electric-field vectors. (left) Comparison between a full Monte-Carlo simulation with geomagnetic field $\vec{B}_2$ and the transformed electric-field vectors from a Monte-Carlo simulation with geomagnetic field $\vec{B}_1$. (right) Comparison between the two simulation sets with different geomagnetic field.
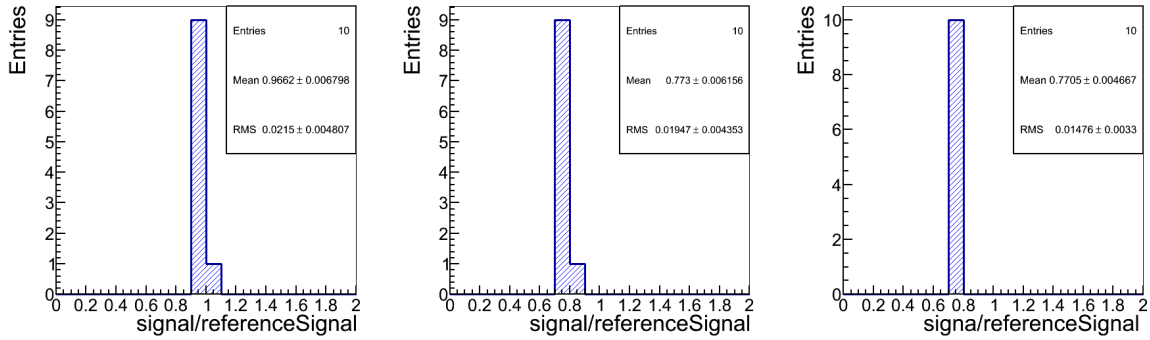
Figure 5.28: Signal distributions at station 14. (left) CoREAS simulation with $\vec{B}_1$. (center) Transformation of CoREAS simulation with $\vec{B}_1$ to $\vec{B}_2$. (right) CoREAS simulation with $\vec{B}_2$.

with unknown spread for compatibility [264]. The p-values of the t-tests for all 19 radio stations is presented in Fig. 5.29 left and a histogram of the test statistic and the t-pdf normalized to the same integral is shown in Fig. 5.29 right. To check if the distribution of the test statistic is compatible with the t-pdf a χ^2-test is performed and gives a compatibility of 69%. Hence, the mean of the transformed and the simulated signals are compatible.

5.9.3 Discussion

A variation in the azimuth angle of the incoming direction (or rather of the magnetic field axis) has the advantage that it has a very weak influence on the shower development. The primary particle type and energy remains the same and the shower will traverse exactly the same amount of atmosphere. Only the deflection of charged particles in the magnetic field is different. On the particle distribution this has only a non-negligible influence for very horizontal showers. On the radio side, only the emission strength of geomagnetic origin changes and, thereby, the polarization of the electric field changes as well due to the different ratio of geomagnetic and charge-excess emission. The relative change of emission strength and polarization is understood well and can be calculated analytically (cf. Eq. (5.26)).
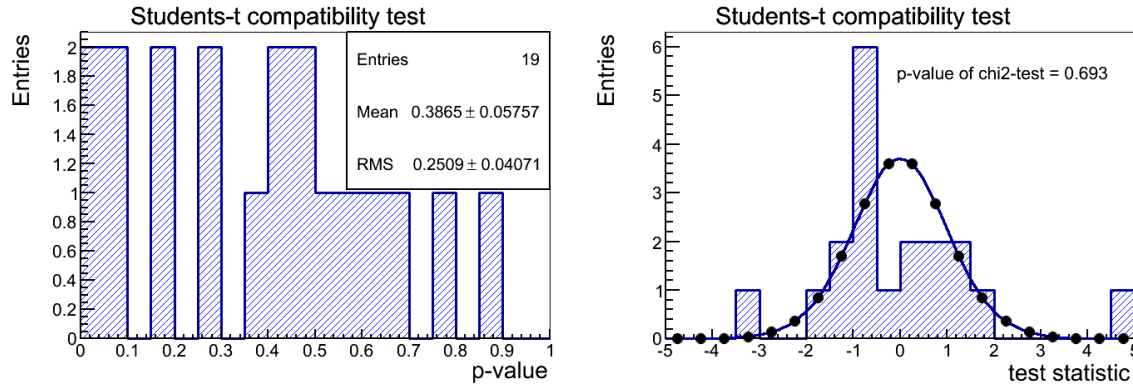
Figure 5.29: Compatibility of radio amplitude of transformed and simulated air showers using the Students-t statistic.

The method described above has been implemented into the Auger software framework $\overline{\text{Off}}\underline{\text{line}}$ and can be used easily by just adding a new module to the module sequence. An example of the corresponding module sequence can be found in B. The advantage of this resampling method is that the full electric-field trace remains available. This is in stark contrast to the approach developed in Sec. 3.3.1 where a generic simulation can be used to calculate the energy fluence at any position in the shower plane. However, for some analyses the full electric-field trace is required, e.g., to be able to perform a full detector simulation and to add measured noise traces to the simulated signal. For such analyses, the resampling method developed in this section reduces the computing costs by a factor of 10 - 100 and will be used in the next section to determine the efficiency of the AERA24 detector.

5.10 Cosmic-ray detection efficiency of the AERA24 detector

In this section, the detection efficiency of the AERA24 is determined using simulated air showers and a full detector simulation. We define the efficiency as the fraction of simulated events that can be successfully reconstructed after a full detector simulation has been performed that includes the adding of measured noise to the simulated signal.

2000 air showers are simulated with random incoming directions up to $60°$ zenith angle (uniformly distributed in the zenith and azimuth angle) and cosmic-ray energies between $10^{17}\,\text{eV}$ and $2 \times 10^{18}\,\text{eV}$ (uniformly distributed in the logarithm of the energy). The core position was chosen randomly such that the nearest AERA24 station is not further than $120\,\text{m}$ away. In other words, the core position is at any place within the AERA24 array or in a $120\,\text{m}$ margin around the array which corresponds roughly to the effective area of the detector. Using the resampling method presented in the previous section, 500 showers with different, randomly-chosen azimuth angles are generated for each fully simulated air shower.

The detector simulation includes the following steps. The antenna and detector response is applied to the simulated electric-field pulses yielding ADC traces. Then, randomly-chosen measured noise traces are added. (The periodically triggered data is used as noise traces.) The resulting ADC traces correspond to raw data of AERA except that the air-shower parameters are already known from the simulation. These traces are then fed into the standard reconstruction chain. The efficiency is
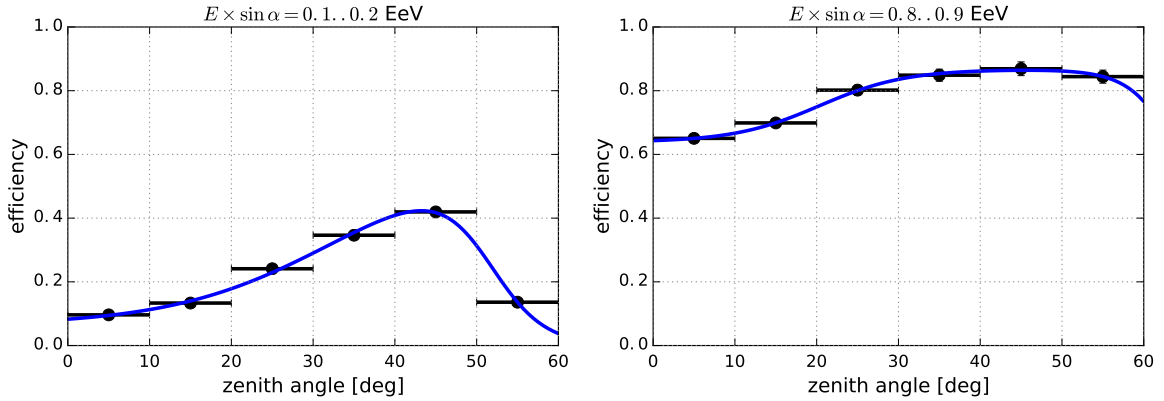
Figure 5.30: Cosmic-ray detection efficiency as a function of zenith angle for two bins of cosmic-ray energy times $\sin \alpha$. The efficiency curve is determined from a full detector simulation of simulated air showers and binned in $10°$ zenith angle bins. The blue curve shows a analytic function that is used to describe the data.

determined by counting the number of successfully reconstructed events that have a reconstructed air shower direction within $20°$ of the true air shower direction. This is the same cut as it is used for measured data in comparison to the SD reconstruction.

Not explicitly taken into account in this method is the trigger efficiency. Most of the cosmic-ray events are triggered externally by the SD. As the SD is fully efficient above an energy of $3 \times 10^{17} \, \text{eV}$, the AERA trigger is also fully efficient above this energy threshold. The efficiency of the self trigger is also implicitly taken into account as air showers that can be successfully reconstructed should also pass the self trigger as the signal-over-noise thresholds are typically set to lower levels as required in the reconstruction.

The efficiency of a radio detector depends on several air-shower parameters and is thus more complex than the efficiency of the surface detector which depends only on the cosmic-ray energy. The efficiency of a radio detector depends on the cosmic-ray energy, as an increased energy leads to more radiation energy and thereby also larger pulse amplitudes. As the radio emission is mainly due to the geomagnetic emission process, the pulse amplitudes also scale also with $\sin \alpha$ where α is the angle between shower axis and geomagnetic field. Both dependencies can be combined to an effective energy of

$$E' = E \times \sin \alpha \,. \tag{5.28}$$

In addition, the efficiency depends on the shower's zenith angle.

Hence, we analyze our simulation data set in different effective energy E' intervals and plot the efficiency versus the zenith angle. Two examples of the resulting efficiency curves are shown in Fig. 5.30. The general characteristic of all E' bins is that the efficiency first rises with increasing zenith angle until a certain value is reached and then decreases again. This is because the radio waves are not emitted isotropically but are forward beamed in a cone around the shower axis. For increasing zenith angles, the same radiation energy is distributed over a larger area. This is on the one hand due to a projection effect and on the other hand because the emission region is further away leading to a larger radius of the cone on the ground. If the illuminated area gets larger, the signal is detected in more stations and the efficiency rises. However, if the radiation energy is distributed over a larger

Table 5.2: Best-fit parameters of the efficiency curve defined by Eq. (5.29) for different bins of the effective energy $E' = E \times \sin \alpha$. For values of E' larger than $1\,\text{EeV}$ the efficiency is close to 1 over the complete zenith-angle range of $0° - 60°$.

$E'_{\min}$ [EeV]	$E'_{\max}$ [EeV]	p_0 [1/deg]	p_1 [deg]	p_2	p_3	p_4 [1/deg]	p_5 [deg]
0	0.1	0.13	20	0.033	0.0022	0.015	41
0.1	0.2	0.098	33	0.61	0.063	0.31	51
0.2	0.3	0.47	34	0.72	0.48	0.31	58
0.3	0.4	0.12	32	0.95	0.47	0.31	62
0.4	0.5	0.17	31	0.86	0.54	2.4	64
0.5	0.6	0.094	38	0.95	0.6	3.5	65
0.6	0.7	0.21	34	0.92	0.71	0.28	66
0.7	0.8	0.14	32	0.95	0.7	0.26	66
0.8	0.9	0.19	20	0.87	0.64	0.32	66
0.9	1	0.15	20	0.88	0.68	0.29	66

area, the signal in each individual station decreases. If the complete radiation energy is too small that all illuminated stations have sufficiently large signal-to-noise ratios, the efficiency decreases with increasing zenith angle. The zenith angle at which this turnover occurs depends on E' and moves to larger zenith angles with increasing E'.

We describe the efficiency curves with a combination of logistic functions

$$\varepsilon(\theta) = \left(\frac{p_2 - p_3}{1 + \exp(-p_0(\theta - p_1))} + p_3 \right) \times \frac{1}{1 + \exp(p_4(\theta - p_5))} \,, \tag{5.29}$$

where θ is the zenith angle and the parameters p_{0-5} are determined in a fit to the data. The parameter p_2 corresponds to the maximum achievable efficiency and p_3 to the minimum efficiency. The second term modulates the cutoff at high zenith angles and the parameter p_5 corresponds to the turnover point. The resulting parameters are presented in Tab. 5.2. For values of E' larger than $1\,\text{EeV}$ the efficiency is close to 1 over the complete zenith-angle range of $0° - 60°$. As this analysis was only performed up to zenith angles of $60°$, the fit values of the turnover points (p_5) must be interpreted with caution if its value is larger than $60°$. In particular, an extrapolation of the efficiency function to higher zenith angles will probably lead to incorrect results.

5.11   Analytic description of cosmic-ray radio pulses

In this section, a new approach to determine the properties of cosmic-ray radio pulses is presented that uses an analytic description of the signal pulse. The challenge in the determination of the pulse properties is that we do not directly measure the cosmic-ray radio pulse ("the signal") but an interference of the signal with the omnipresent noise. So far, the radio pulse is described by different observables that do not use all the information contained in the pulse. E.g., we integrate over the complete pulse to obtain the energy fluence, we just use the maximum of the pulse to determine the signal time or we determine the average polarization. These approaches might not lead to the best possible result as many information is neglected. In contrast, the general idea of this approach is to use all available information at once. This can be achieved by fitting an analytic model of the pulse form to the
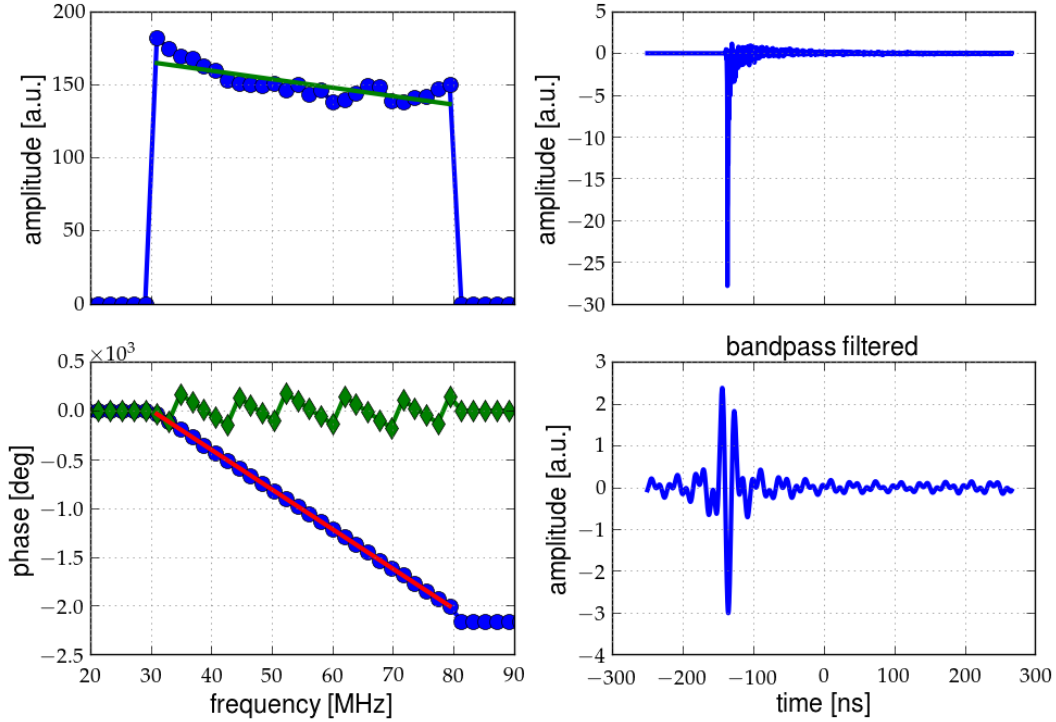
Figure 5.31: Time and frequency domain representation of a cosmic-ray radio pulse. (upper right) Simulation of a radio pulse using CoREAS. (lower right) Same pulse as above but bandpass filtered to 30 - 80 MHz. (upper left) Frequency spectrum of the bandpass limited pulse. (lower left) Phase spectrum of the bandpass limited pulse. The green diamonds show the phases in a wrapped form (limited to the interval of $[-\pi, +\pi]$) as they come out of the Fourier transform whereas the blue circles show the unwrapped phases.

complete trace. The idea behind is that the signal is highly correlated between succeeding time bins whereas the noise is expected to be less correlated. (The noise is not completely random as also the noise is restricted to the frequency bandwidth of the detector.) Hence, we would gain in sensitivity if we first fit an analytic description of the signal to the trace using all the available information and then compute the high-level quantities such as energy fluence, signal time, etc. from the fitted function.

As e.g. visible in Fig. 5.12, cosmic-ray radio pulses measured by AERA have a width of $\mathcal{O}(30\,\text{ns})$. The data is sampled every 5 ns or 5.5 ns and using the upsampling technique (cf. Sec. 5.2) the pulse amplitude at any time between the sampled points can be calculated as the frequency content is restricted to 30 - 80 MHz. Hence, per electric-field component, we have several data points on which we can fit the pulse model.

If the signal pulse is shown in the time domain it has a complicated form and it will be difficult to find a function that describes all the features. However, if the pulse is shown in the frequency domain, i.e., the amplitude and the phase as a function of frequency, the signal exhibits a simple form. As demonstrated in Fig. 5.31, the amplitude as well as the phase spectrum can be described by a straight line. Hence, only four parameters are required to describe the signal pulse.

A comparison between the radio pulse and our 4-parameter signal model, which is fitted to the signal, is shown in Fig. 5.32. The residuals show that the center of the pulse is described especially well and the general agreement is at a percent level compared to the maximum amplitude. The agreement
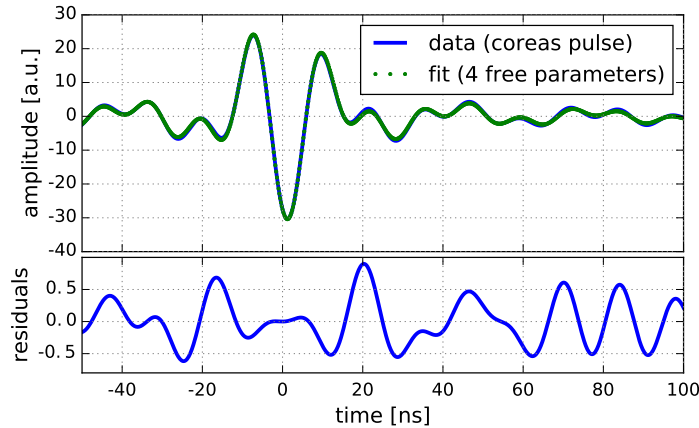
Figure 5.32: Bandpass-limited radio pulse as simulated by CoREAS (blue curve) compared with the four parameter fit (green dots). The green dots are plotted above the blue curve.
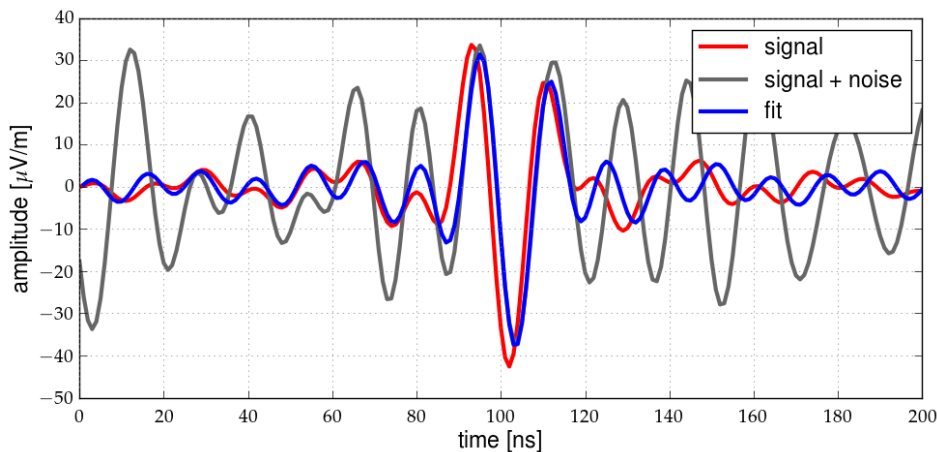
Figure 5.33: Time trace of a simulated cosmic-ray radio pulse after detector simulation. The red curve shows the simulated signal. The gray curve shows the electric-field trace after detector simulation and interference with a measured noise trace. The blue curve shows the result of the fit of the 4-parameter signal model.

could be further improved by using a more complex function to describe the amplitude frequency spectrum, e.g., by using an exponential function. However, as the signal is anyway disturbed by noise the simple 4-parameter model is sufficient to demonstrate the general feasibility of this method.

A time trace that results from the interference of the signal with noise is shown in Fig. 5.33. This trace was obtained using a full detector simulation, i.e., the detector response was applied to a simulated CoREAS radio pulse, then a measured noise trace was added to the signal and the detector response was unfolded to obtain back the electric-field trace. In this example, the signal is hardly visible in the noise and this measurement would not be usable with the traditional methods. However, with the fit of the 4-parameter signal model we can approximately recover the original signal pulse. Although this example looks promising, the fit might not work well at all circumstances and the uncertainties on the derived quantities (energy fluence, signal time, ...) still need to be quantified and compared to the traditional methods.

Another promising application of this approach is the reconstruction of the electric field of hori-
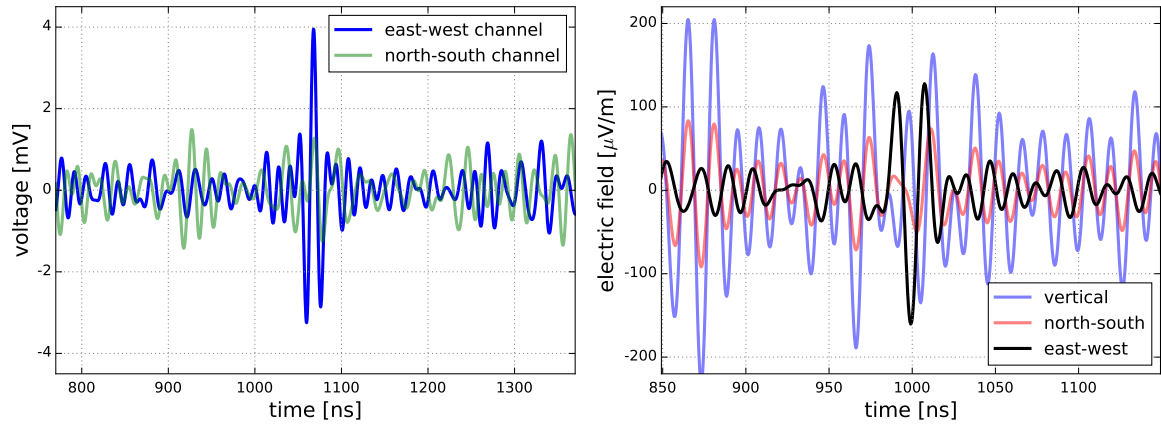
Figure 5.34: Example of a problematic electric-field reconstruction for an horizontal air shower arriving at a zenith angle of $68°$ and $17°$ east of south. (left) Voltage trace of a Butterfly antenna station. The signal pulse is clearly visible in the east-west channel. (right) Reconstructed three-dimensional electric-field trace. The signal is clearly visible in the east-west component of the electric field but the huge noise level in the vertical component makes the three-dimensional electric field unusable.

zontal air showers from the measured voltage traces. As AERA is instrumented only with an east-west and north-south polarized antenna, the vertical component of the electric field is not directly measured. For horizontal air showers this often leads to problems in the full three-dimensional electric-field reconstruction. If the radio pulse is polarized only in the east-west direction (as it is for showers coming from the south), the north-south channel contains only noise. In the electric-field reconstruction it is assumed that all measured signals (including the noise) originate from the direction of the air shower. Therefore, a certain signal in the north-south component can only be explained if the electric field also has a strong vertical component, because the electric-field vector needs to be polarized in the shower plane. This results in a z-component of the electric field that is overflooded by noise, as shown in Fig. 5.34. As a consequence, the energy fluence, the polarization and often also the signal time can not be determined although the signal is visible in the east-west component. This problem could be overcome by fitting the signal model directly to the measured voltage traces. Thereby the signal pulse can be separated from the noise. Then, the antenna response could be unfolded only from the signal pulse using the analytic description of the signal.

Another improvement relevant in this context can be made by the choice of coordinate system to represent the three-dimensional electric-field pulse. Due to historical reasons, the ground coordinate system is used to represent the electric field, i.e., the east-west (x), north-south (y) and vertical (z) component of the electric field is shown. However, a more convenient way would be to rotate the electric field into the shower plane. This has the advantage that the third component is always zero as an electromagnetic wave is polarized perpendicular to its direction of propagation. One could use a spherical coordinate system with its e_ϕ and e_θ components which is also the direct outcome of the electric-field reconstruction (cf. Eq. (5.6)). Alternatively, the axes in the shower plane can be aligned into the $\vec{v} \times \vec{B}$ and $\vec{v} \times (\vec{v} \times \vec{B})$ directions. An example of this coordinate transformation is presented in Fig. 5.35. With respect to the fit of the analytic signal model, the improvement is that the fit only needs to be performed in two electric-field components. Hence, only 8 instead of 12 free parameters need to be determined to describe the full signal pulse.
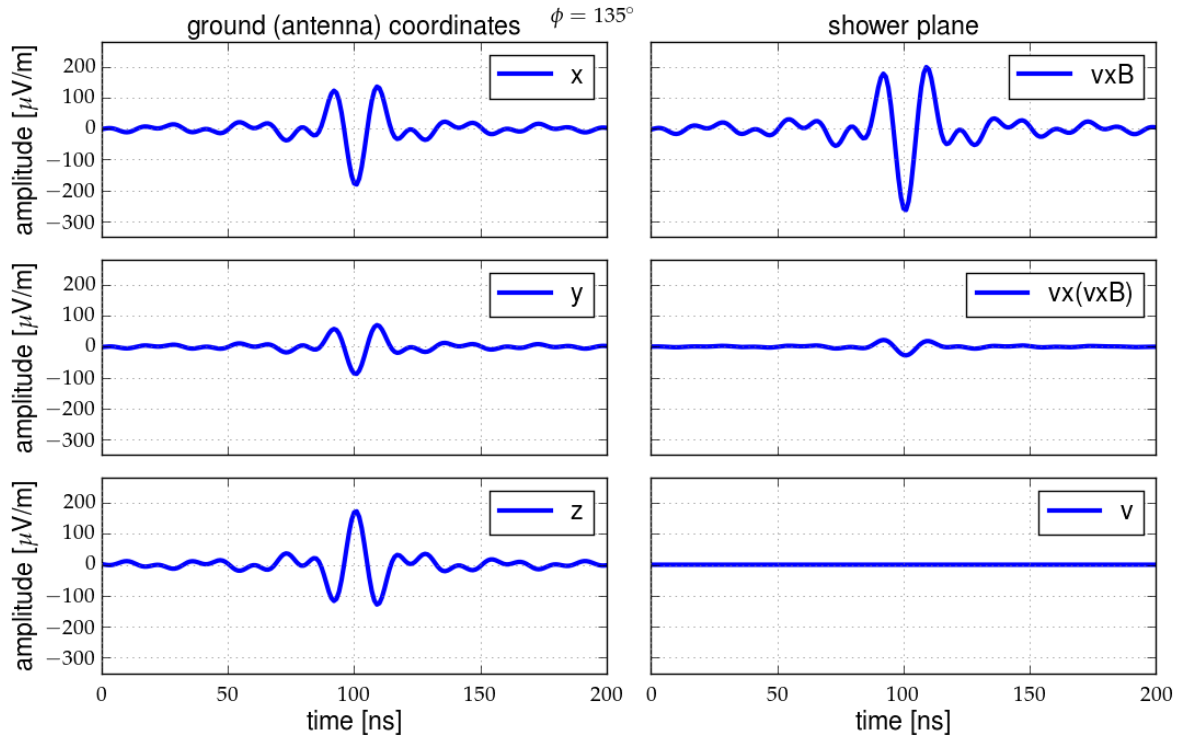
Figure 5.35: Three dimensional electric-field trace in ground coordinates (left) and in the shower plane (right).

An additional opportunity of this method is that the fit parameters are directly sensitive to air shower parameters or define new observables that have not been exploited so far. The slope of the amplitude frequency spectrum correlates with the position of the shower maximum [243]. During the evaluation of (CoREAS) air-shower simulations we found that the slope of the phase spectrum shows a correlation with the shower maximum as well. In addition, a new observable can be defined. The polarization of the signal pulse as a function of frequency can be computed from the frequency dependence of the amplitudes of the two electric-field components. As visible in Fig. 5.36, the polarization itself shows a correlation with the shower maximum as well as the change of the polarization with frequency.

Technical Details of the Implementation   To make use of the higher correlation between succeeding time bins of the signal pulse compared to the noise, the fit is performed in the time domain by minimizing the function

$$\chi^2 = \sum_i \frac{\left(u_{\mathrm{measured},i} - u_{\mathrm{model},i}\right)^2}{\sigma^2_{\mathrm{noise}}} , \tag{5.30}$$

where the index i indicates the time bin of the measured trace u_{measured} and the trace of our analytic model u_{model} and runs over a time window of typically ± 100 ns around the pulse maximum. In each minimization step the amplitude and phase frequency spectrum is calculated from the four fit parameters and transformed into the time domain using a fast Fourier transformation (FFT).

To get good initial values of the fit parameters we transform the measured trace into the Fourier domain and fit the amplitude and phase frequency spectra with straight lines. To be able to fit a straight line to the phase spectrum, the phases need to be unwrapped first. This imposes a principle problem
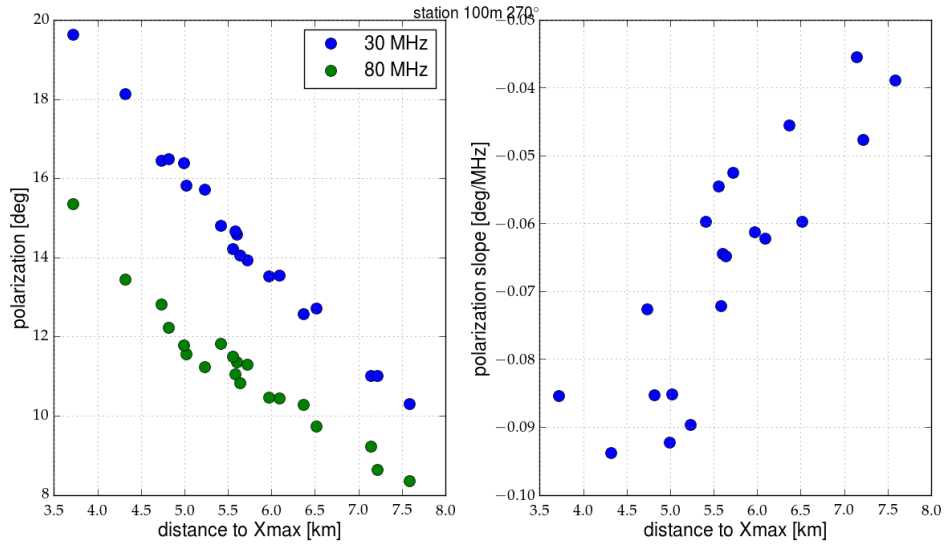
Figure 5.36: Sensitivity of the polarization to the shower maximum X_{max}. Each data point represents one air-shower simulation with an energy of 3.5×10^{17} eV, incident under a zenith angle of $46°$ and $7°$ south of east. We evaluate the signal at 100 m away from the shower axis into the negative $\vec{v} \times (\vec{v} \times \vec{B})$ direction. (left) Polarization as a function of distance from ground to the shower maximum. Shown is the polarization at 30 MHz (blue filled circles) and 80 MHz (green filled circles). (right) Rate of change of the polarization with frequency versus the distance to X_{max}.

as the frequency resolution is limited[3]. If the phase slope, i.e., the change of phase with frequency, is too steep and the difference between two frequency bins is larger than 2π, the unwrapping algorithm is ambiguous. However, we can overcome this problem by exploiting the following symmetry of the Fourier transformation. A change in the slope corresponds to a shift of the signal pulse in the time domain. If the position of the signal pulse is moved towards zero, the phase slope flattens. This is illustrated in Fig. 5.37. Hence, before the fitting process, we rotate the pulse maximum to bin zero, then we perform the fit and afterwards rotate the trace back to its original position.

This functionality was implemented into the software framework $\overline{\text{Off}}\underline{\text{line}}$ and is integrated in the standard reconstruction.

5.12 Python radio-tools package

During this thesis a tool package to simplify high-level data analyses of radio data has been developed. It is written in Python and available to the Pierre Auger Collaboration. It is a collection of all sorts of algorithms and interfaces often used by radio analyses. It is intended to assist analyses within the AERA group such that often used functionality does not need to be reinvented or rather reimplemented again. Instead one can build on a verified package and/or extend this package if a certain aspect is not yet covered. In the following, we present some of the functionality without any claim to completeness.

The tool package contains a collection of helper functions. All sorts of geometry operations are available such as the calculation of the expected electric-field polarization according to the geomag-

---

[3]The frequency resolution is determined by the length of the trace. For a typical length of 200 ns the frequency resolution is 5 MHz.
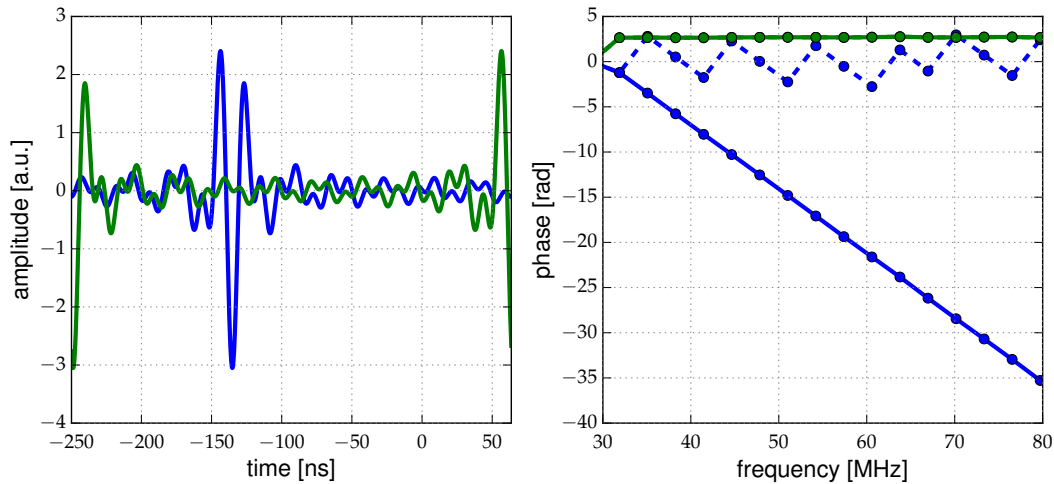
Figure 5.37: Illustration of the correspondence between pulse position and phase slope. (left) The original signal trace is shown in blue. The green line shows the same pulse but with the pulse position rotated to bin zero. (right) Corresponding phase frequency spectrum. The dashed blue line represents the phases in a wrapped form whereas the solid blue line shows the unwrapped phases. The green line represents the phases corresponding to the green curve in the left figure. Due to the shift in the pulse position the phases are almost flat and can be unwrapped correctly.

netic and charge-excess emission processes or the calculation of the distance from a point to the shower axis. We also provide the coordinate transformation to and from the $\vec{v} \times \vec{B}$ - $\vec{v} \times (\vec{v} \times \vec{B})$ coordinate system. All functions are implemented vectorized using *numpy* [265] routines such that computationally expensive calculations are actually performed in well-optimized implementations in C through *numpy*. Also AERA specific functionality such as the calculation of the uncertainty on the measured polarization from the signal-to-noise ratio is provided.

Furthermore, interfaces to environmental databases are available. An interface to access the weather monitoring information of the Pierre Auger Observatory such as temperature or atmospheric electric-field data is provided as well as further post processing such as the check for thunderstorm conditions at the time of a measured cosmic-ray event. We also provide an interface to GDAS (global data assimilation system) that provides altitude-dependent profiles of the main state variables of the atmosphere such as temperature, pressure, and humidity and give functions to calculate the quantities relevant for radio emission such as the air refractivity. In addition, we implemented atmospheric models such as the US standard atmosphere [132] and provide functions to, e.g., convert the position of the shower maximum measured in slant depth to the geometrical distance between observer and shower maximum (cf. Appendix D).

In addition, the functionality to create input files for the air-shower simulation programs CoREAS [156] and ZHAireS [130] is provided. If the simulated observer positions should be positioned on a star-shaped pattern in the shower plane, the corresponding ground coordinates are automatically calculated depending on the chosen zenith and azimuth angle of the air shower. Also the necessary lateral extend of the observer positions is adjusted automatically according to the estimated size of the footprint. In addition to the tools to generate the input of the simulations, also the functionality to parse the simulated air showers and their radio emission is provided. During the parsing the simulation

output is preprocessed. A Gaisser-Hillas function is fitted to the longitudinal shower profile and the electric field is filtered to a certain bandwidth and some derived quantities are already calculated such as the signal time or the radio energy fluence at each observer position. The output is saved as a Python object using the *pickle* functionality for simple read-in in later analyses. Next to the full output file, we also save a reduced output file that does not contain the full electric-field traces. This reduces the data volume by a factor of ~ 100 resulting in a file size of $\mathcal{O}(100\,\text{kB})$ per simulation. Hence, also several thousands of simulations can be downloaded and handled by local computing resources.

Measurement of radiation energy as a universal estimator of cosmic-ray energy

In this chapter, the measurement of the radiation energy in the radio signals of extensive air showers is presented and calibrated with data of the surface detector (SD) of the Pierre Auger Observatory. The surface detector itself was calibrated with the fluorescence detector. With the cross-calibration of AERA with SD we thus inherit the accurate energy scale of the Pierre Auger Observatory.

So far, all radio experiments have used experiment-specific quantities to reconstruct the cosmic-ray energy, such as the radio signal strength at a characteristic lateral distance from the shower axis [9, 20, 221, 266]. While this method has long been known to provide a good precision [267], it has the disadvantage that the corresponding energy estimators cannot be directly compared across different experiments. The main reason for this is that the shape of the lateral signal distribution changes significantly with observation altitude. The optimal characteristic distance varies with observation height and even at the same characteristic distance the radio signal strengths are significantly different (see [161] or the discussion in Sec. 6.4 for more details). Hence, a comparison between different experiments cannot be performed directly.

Here, we introduce a general approach with a direct physical interpretation. At each observer position we calculate the energy deposit per area of the cosmic-ray radio pulse and by integrating the two-dimensional lateral distribution function over the area we obtain the total amount of energy that is

transferred from the primary comic ray into radio emission during the air-shower development. This approach is independent of the shape of the signal distribution because energy, i.e., the integral over the signal distribution, is conserved.

We present the relation between the cosmic-ray energy and the total energy emitted by the air shower as a radio pulse, for primaries of energy in the EeV (= 10^{18} eV) range. To obtain this relation we use the LPDA radio stations of the Auger Engineering Radio Array located within the Pierre Auger Observatory in Argentina. The LPDA antennas have been thoroughly studied and calibrated ([225] and Sec. 4.4.4). We take advantage of the possibility to cross-calibrate these measurements with the well-understood data of the Observatory and with recent developments in understanding the radio-emission mechanisms, with their corresponding polarization patterns of the electric field and the particular lateral distribution of the total field strength [14, 156].

This chapter is structured as follows. We begin with the data selection and event reconstruction procedure. After that we describe the calibration that uses a likelihood procedure, and we discuss experimental uncertainties. Then, we present the energy measurement of the AERA radio detector, its resolution, the correlation of the radiation energy with the shower energy and we address the systematic uncertainty of the radiation energy as an energy estimator. Finally, we discuss the implications and new opportunities arising from this approach.

6.1 Data selection and event reconstruction

In this work we are using RD and SD data recorded between April 2011 and March 2013 when AERA was operating in its first commissioning phase. The data are stored as events, which refer to all relevant information that has been read out following a trigger. For this analysis, both self-triggered and externally triggered events are used.

6.1.1 Preselection of cosmic-ray candidates

In the case of the self-triggered events, a preselection is performed offline by searching for coincidences with the surface detector events. A radio event has to agree in time and location with an SD event to be considered as cosmic-ray candidate. The radio-trigger time and the time when the air shower core hits the ground have to agree within $\pm 20\,\mu$s. Such a conservative coincidence window also accounts for horizontal events, for which the time difference is expected to be larger.

For both trigger types, only events with a clear radio pulse in at least three stations are considered, to allow for a reconstruction of the incoming direction of the signal. For externally triggered events the requirement is a signal-to-noise ratio (SNR) greater than ten. Here the SNR is defined as the maximum of the Hilbert envelope-squared[1] divided by the noise variance. For self-triggered events the signal threshold is dynamically adjusted to the noise level to keep the trigger rate at a constant level of 100 Hz. We require that the reconstructed incoming directions from the radio and the surface detectors agree within $20°$ to be accepted as a cosmic-ray candidate. The $20°$ cut does not reflect the angular resolution of the SD nor that of the radio detector. This preselection cut retains the maximum

---

[1]The Hilbert envelope is the instantaneous amplitude.

number of cosmic-ray signals and significantly reduces the number of random (anthropogenic) noise pulses, which originate mainly from the horizon.

In addition, we apply quality cuts on the data of the surface detector [268]. The most important cuts are that the core position is closest to an active station and surrounded by a hexagon of active stations and that the zenith angle of the incoming direction be less than $55°$. A total of 181 cosmic-ray candidates with energies above 10^{17} eV remain.

As an engineering array, AERA was subject to several changes in software and hardware which significantly limited the uptime. In future, we expect a larger rate of cosmic rays due to the stabilized operation of the detector.

6.1.2 Reconstruction of radio data

We use the software framework $\overline{\text{Off}}\underline{\text{line}}$ [218] of the Pierre Auger Collaboration to process the measured raw data. First, the air shower is reconstructed using the surface detector information [175]. Second, the reconstruction using the radio detector data is performed [219]. Narrowband noise sources are filtered out using a radio-frequency interference suppression in the time domain. Sine waves with the frequency of noise sources are fitted to the measured voltage trace and subtracted.

We correct for the influence of the analog signal chain using the absolute calibration of the AERA station and reconstruct a three-dimensional electric field by using the direction of the shower and applying the simulated antenna response [225].

The energy fluence f, i.e., the energy deposit per unit area, of the incoming electromagnetic radio pulse at each radio station is determined by calculating the time integral over the absolute value of the Poynting vector. This is achieved by squaring the magnitude of the electric-field trace and summing over a time window of 200 ns ($[t_1, t_2]$) around the pulse maximum which has been determined from the Hilbert envelope of the trace (cf. Fig. 5.12). The contribution of background noise (determined in the noise window $[t_3, t_4]$) is subtracted under the assumption that the main contribution is white noise. The energy fluence f is given by

$$f = \varepsilon_0 c \left(\Delta t \sum_{t_1}^{t_2} |\vec{E}(t_i)|^2 - \Delta t \frac{t_2 - t_1}{t_4 - t_3} \sum_{t_3}^{t_4} |\vec{E}(t_i)|^2 \right) , \qquad (6.1)$$

where ε_0 is the vacuum permittivity, c is the speed of light in vacuum and Δt is the size of one time bin. This quantity is used throughout the whole analysis and will be given in units of eV/m^2. To approximate the uncertainty the noise level as described above is used. As the radio detector effects have been corrected for, the reconstructed energy fluence can be directly compared to air-shower simulations.

We also calculate the direction of the electric-field vector, i.e., the polarization direction of the signal. In the full width half maximum (FWHM) interval around the pulse maximum of the Hilbert envelope we observe that the reconstructed electric-field vectors are aligned approximately along the same direction for every time bin. To accurately determine the mean direction of the electric-field vector, we average over all vectors in the FWHM interval of the Hilbert envelope (cf. Fig. 5.12).

6.1.3   Selection of radio signals induced by cosmic rays

Given the amount of pulsed background noise at the AERA site, the preselected events are likely to contain non cosmic-ray signals that mimic cosmic-ray pulses. There are two scenarios possible: Signals in one or more stations are not caused by the air shower or an event contains only noise pulses that by chance led to a reconstructed incoming direction similar to that of the SD.

In order to reject background signals, we take advantage of the expected polarization of the radio signal. The polarization of the radio pulse is only used for this purpose and not considered for the energy estimation. In the frequency range of AERA (30 to 80 MHz) the dominant emission process is the geomagnetic emission [10, 12]. Here, a linear polarization of the electric field is expected to be in the direction of the Lorentz force (given by $\vec{e}_{\mathrm{geo}}$) that acts on the charged particles while they traverse the magnetic field of Earth. The polarization is altered by an additional emission which is linearly polarized radially towards the shower axis (given by $\vec{e}_{\mathrm{CE}}$), and is referred to as the charge-excess emission process [12, 120, 122, 269].

The expected direction of the electric-field vector is therefore calculated from the geomagnetic and the charge-excess contributions

$$\vec{E}_{\mathrm{exp}} \propto \sin \alpha \, \vec{e}_{\mathrm{geo}} + a \, \vec{e}_{\mathrm{CE}} \,, \tag{6.2}$$

where α is the angle between the shower axis and magnetic field of Earth, and a is the average relative charge-excess strength that has been measured to be 0.14 ± 0.02 at AERA [12]. In this approach, the direction of the geomagnetic contribution depends only on the incoming direction of the air shower whereas the charge-excess contribution depends in addition on the position of the radio station relative to the shower axis.

In Fig. 6.1, all stations with signal of a cosmic-ray candidate are shown, and the measured polarization is compared with the expectations of the two radio-emission mechanisms. The overall agreement between measured and expected field polarizations is quantified using the angular difference

$$\beta_i = \angle(\vec{E}_{\mathrm{meas},i}, \vec{E}_{\mathrm{exp},i}) \tag{6.3}$$

at each station i. For each event, the average deviation $\bar{\beta}$ of the individual deviations β_i of the stations with signal is calculated and will be used as criterion for a quality cut. Relevant uncertainties are taken into account as follows:

- The relative strength a of the charge excess can vary from event to event due to shower-to-shower fluctuations, and additional dependencies on the geometry of the air shower [125]. Therefore, for each possible values of a between 0 and 0.5 the average deviation $\bar{\beta}$ is calculated and only the smallest value of $\bar{\beta}$ is considered.
- The uncertainty of the SD shower core position is taken into account by variation of the core within its estimated uncertainties. In our data set the uncertainty varies between 10 m and 80 m depending on the energy and zenith angle. For each trial of the core position $\bar{\beta}$ is calculated. Again, only the smallest value of $\bar{\beta}$ is considered.
- Interference of the cosmic-ray radio signal with noise pulses can alter the polarization. Simulation studies showed that for a single radio station the uncertainty in β due to noise is below
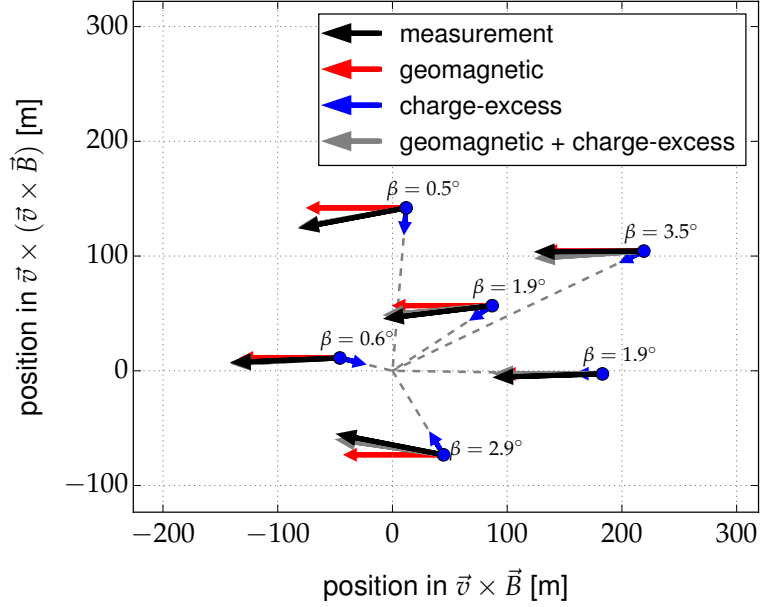
Figure 6.1: Polarization map of a single event. The axis coordinates are in the shower plane where the x-axis corresponds to the direction of the Lorentz force ($\vec{v} \times \vec{B}$) and the y-axis perpendicular to that and to the shower axis ($\vec{v} \times (\vec{v} \times \vec{B})$). The SD shower core is at the coordinate origin. The measured polarizations are shown as the black arrows. The gray arrows are the model expectations, and the red and blue arrows are the geomagnetic and the charge-excess components, respectively. The definition of β is described in the text. The air-shower properties of this event are: Energy of 0.9 EeV and arriving from a zenith angle of 36° and from 27° south of west. For the emission model of Eq. (6.2), the optimal value of the relative charge-excess strength is $a = 0.18$.

8° at detection threshold, and decreases to 1° at high signal-to-noise ratios. To obtain the average value of β for all radio stations in the event we compute a weighted mean with weights $w_i = 1/\sigma_{\beta_i}^2$ with σ_{β_i} being the expected uncertainty from the simulation.

We impose a limit on the average deviation $\bar{\beta}$ of the polarization direction. This maximum deviation is fixed at a value of 3°. This value is slightly above the combination of the following effects.

The incoming direction of an air shower reconstructed with the surface detector has an uncertainty between 1.3° and 0.7° depending on the cosmic-ray energy and the zenith angle [175]. Hence, the expected direction of the electric-field vector will have the same uncertainty. All antennas are aligned to the magnetic north (or perpendicularly to the magnetic north in case of the other polarization direction) with a precision of better than 1° [220]. All antennas are uniformly constructed and the two antennas of a radio station are identical. Asymmetries in the ground conditions have only negligible influence as the LPDA antenna is mostly insensitive towards the ground. A measurement at AERA has shown that the responses of all antennas differ by less than 0.3% [223].

A difference in the amplification of the signal chain of the north-south and east-west polarized antenna will influence the polarization measurement. From an individual measurement of the signal chain of all antennas the uncertainty is estimated to be 2.5% which results in a polarization uncertainty below 0.7°.

In addition, we neglect the dependence of the relative strength a of the charge excess on the distance between observer position and shower axis [125, 162]. For a single station this effect is

relevant. However, in our approach we only use the average deviation of all stations with signal also taking into account the uncertainty in the core position. Therefore the distance dependence will mostly average out. We estimate that the remaining additional scatter is $1.5°$.

We account for individual radio stations being contaminated with substantial noise signals by iterating through all configurations with only one and then more stations removed, down to the minimum of three stations. An event where the weighted average deviation $\bar{\beta}$ is greater than $3°$ for all station combinations is rejected. If $\bar{\beta}$ is less than $3°$ for any station combination and the fraction of selected stations is larger than 50% of the total number of stations with signal, the event candidate is considered a cosmic-ray event and only the stations from this particular combination are used. After this cut 136 events remain. The number of excluded single stations and complete events is compatible with the measured rate of noise pulses.

Most of the events recorded during thunderstorm conditions appear to be rejected by this selection procedure as the strong atmospheric electric fields of a thunderstorm influence the radio emission and alter the polarization of the radio signals [270, 271]. For two thirds of the events, a measurement of the atmospheric electric field is available. These events are checked for thunderstorm conditions using an algorithm described in [272]. Based on this check, two additional events were rejected. All cuts are summarized in Table 6.1.

Table 6.1: Overview of selection cuts and the number of events surviving these cuts. Preselection means: $E_{CR} \geqslant 0.1\,\text{EeV}$, standard SD quality cuts, $\geqslant 3$ radio stations with signal, SD and RD reconstructed incoming directions agree within $20°$. See text for details.

cut	number of events after cut
preselection (Sec. 6.1.1)	181
polarization cut ($\bar{\beta} < 3°$, Sec. 6.1.3)	136
no thunderstorm conditions (Sec. 6.1.3)	134
LDF fit converged ($\sigma < 300\,\text{m}$, Sec. 6.2)	126
$\geqslant 5$ stations with signal (only high-quality data set, Sec. 6.3)	47

6.1.4 Uncertainties on the energy fluence in a single radio station

In addition to the uncertainties on the amplification of the signal chain of 2.5% discussed above, no further uncertainties are expected that would result in a different response of stations within one event. To first order, the frequency content and the incoming direction of the radio pulse are similar at all observer positions. Therefore, an uncertainty of the antenna-response pattern has a negligible influence as it is evaluated for the same direction at all stations. Possible different ground conditions at different station positions that result in a different reflectivity of the soil are negligible due to the insensitivity of the antenna towards the ground. The 2.5% amplification uncertainty results in 5% uncertainty on the energy fluence f, as f scales quadratically with the electric-field amplitude. This uncertainty is added in quadrature to the signal uncertainty resulting from noise.
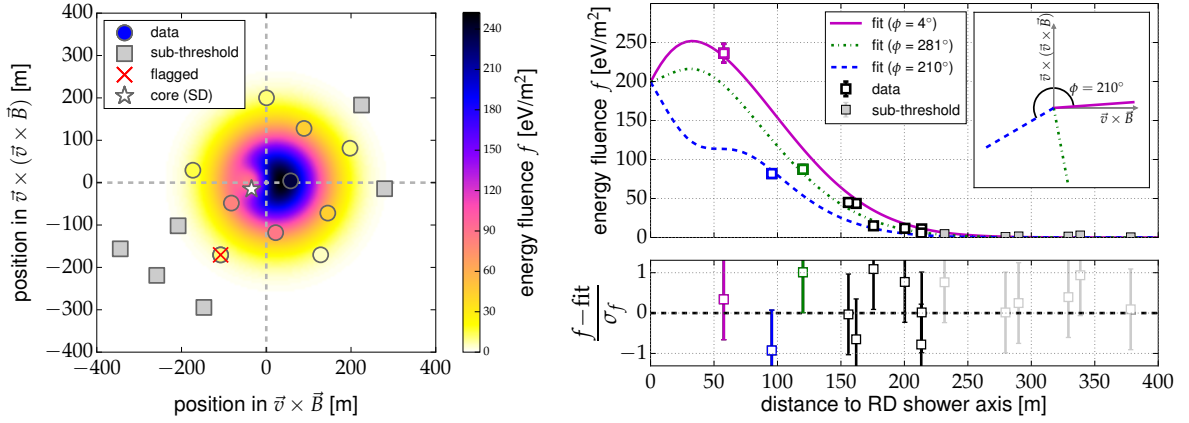
Figure 6.2: Lateral signal distribution of a single cosmic-ray event. The air-shower properties of this event are: Energy of 0.75 EeV and arriving at a zenith angle of 37° and from 44° west of south. Left: The energy fluence in the shower plane. The measurements are indicated as circles where the color shows the energy fluence. Gray squares are stations with signal below threshold and the red cross marks a station that is rejected due to a mismatch in the signal polarization. The background map shows the LDF parametrization. The coordinate origin is the reconstructed core position of the radio LDF fit. Note the lack of color contrast between the infill color of the data points and the background. This is indicative of the agreement between the data and the model. Right: Representation of the same data as a function of distance from the shower axis. The colored and black squares are the measured energy fluences and gray squares are the stations with signal below threshold. For the three data points with the highest energy fluence, the one-dimensional projection of the two-dimensional LDF onto lines connecting the radio-core position with the corresponding radio detector positions is illustrated with colored lines. This demonstrates the azimuthal asymmetry and complexity of the two-dimensional lateral distribution function. The inset figure shows the azimuthal direction of the three LDF projections. The distribution of the residuals (data versus fit) is shown as well.

6.2 Energy Estimator

To obtain an absolute energy estimator from the signals at the different distances to the shower axis (energy fluence f in units of eV/m^2) a LDF is used which takes into account the signal asymmetries due to constructive and destructive interference between the geomagnetic and charge-excess components, as well as Cherenkov time-compression effects [14]. This LDF describes the main features seen in simulated and measured cosmic-ray radio events. The LDF function is parametrized as

$$f(\vec{r}) = A\left[\exp\left(\frac{-(\vec{r} + C_1\,\vec{e}_{\vec{v}\times\vec{B}} - \vec{r}_{\text{core}})^2}{\sigma^2} \right) - C_0 \exp\left(\frac{-(\vec{r} + C_2\,\vec{e}_{\vec{v}\times\vec{B}} - \vec{r}_{\text{core}})^2}{(C_3 e^{C_4\,\sigma})^2} \right) \right]. \quad (6.4)$$

All coordinates are in the shower plane. $\vec{r}$ denotes the station position. The four fit parameters are the amplitude A, the slope parameter σ and the particle core position $\vec{r}_{\text{core}}$. In case of low station multiplicity, the particle core position is taken from the SD reconstruction, which enables us to also use events with only three or four stations with signal. C_0 - C_4 are constants that are estimated from CoREAS Monte Carlo simulations [156] and can be found in Appendix C.1. $C_0 - C_2$ are zenith-angle dependent. The LDF is fitted to the data using a chi-square minimization. An example of one air shower within our data set is shown in Fig. 6.2.

Some events do not contain sufficient information to fit the LDF, such as when only three stations
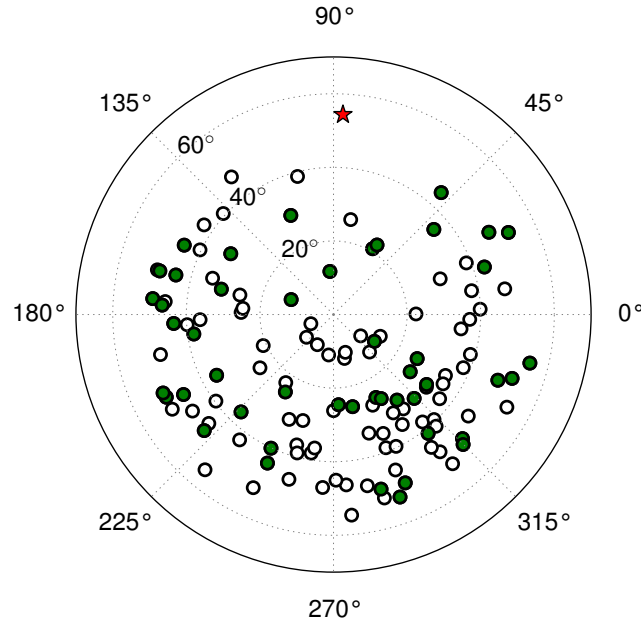
Figure 6.3: Skymap of the 126 selected events. Green filled circles denote air showers with at least five stations with signal and open circles denote air showers with less than five stations with signal. The red star denotes the direction of the magnetic-field axis at AERA. All measured events are at least $20°$ away from the magnetic-field axis. Therefore, the geomagnetic emission gives the dominant contribution to the radiation energy for all events.

with signal are present that have roughly the same signal strength. This results in an unphysically broad LDF. To reject these events we impose the quality cut $\sigma < 300$ m (Table 6.1). An analysis of air-shower simulations for the AERA geometry showed that the σ parameter of the LDF is never larger than 300 m.

In the following, only the 126 events that pass the quality cuts are considered and will be referred to as the full data set. To derive the accuracy of the energy estimation method, the data set will be further divided in a high-quality data set containing only events with at least five stations with signal, i.e., events where the core position can be reconstructed in the radio LDF fit.

6.2.1 Definition of the energy estimator

The spatial integral of the lateral distribution function gives the amount of energy that is transferred from the primary cosmic ray into radio emission in the AERA frequency band during the air-shower development, and will be given in units of eV. We define the energy estimator S_radio as this radiation energy divided by $\sin^2 \alpha$ to account for different emission strengths at different angles between shower axis and magnetic field, see Eq. (6.2),

$$S_\text{radio} = \frac{1}{\sin^2 \alpha} \int_{\mathbb{R}^2} f(\vec{r})\, \mathrm{d}^2\vec{r} = \frac{A\pi}{\sin^2 \alpha} \left(\sigma^2 - C_0 C_3^2\, e^{2C_4 \sigma} \right) , \tag{6.5}$$

where $\mathbb{R}^2$ denotes the shower plane. The positive σ^2 term dominates by far over the negative second term resulting in a positive value of S_radio. The $\sin^2 \alpha$ correction only holds if the geomagnetic emission is the dominant contribution which is the case for $\alpha > 10°$ at AERA. Due to the reduced

emission strength the number of detections for arrival directions within $10°$ of the geomagnetic field axis is suppressed. The angular distribution of the events is shown in Fig. 6.3.

6.2.2 Event-by-event uncertainties of the energy estimator

The following uncertainties are relevant for the energy estimator due to event-by-event fluctuations and summarized in Table 6.2:

- The gains of the low-noise amplifiers and filter amplifiers exhibit a temperature dependence. The effect has been measured and amounts to $-42\,\mathrm{mdB/K}$. Each air shower is measured under specific environmental conditions. In particular this implies that we have a random distribution of ambient temperatures which exhibit a Gaussian distribution with a standard deviation of $8.3°$ C. This corresponds to a fluctuation of the gain of 4%.
- An uncertainty of the simulated antenna response that depends on the incoming direction of the radio signal will lead to an event-by-event uncertainty as each event has a different incoming direction. The effect is determined to be 5% by comparison of the simulated antenna response with a measurement at AERA [225].
- The reconstructed direction of the air shower obtained with the SD has an uncertainty of less than $1.3°$. This has negligible influence on the antenna response pattern, since it can be considered uniform over such a small change of angle.

As the different uncertainties are independent, the total uncertainty of the electric-field amplitude is $\sqrt{4\%^2 + 5\%^2} \approx 6.4\%$ and therefore 12.8% on S_{radio}. The uncertainty of α can be neglected. The fit uncertainties of A and σ including their correlation are propagated into S_{radio} using Gaussian error propagation. In the case of events with less than five stations with signal, the core position of the surface detector reconstruction is used and its uncertainty is propagated into the fit uncertainty of S_{radio}. This fit uncertainty is added in quadrature to the statistical uncertainty of 12.8% of the energy estimator. The average fit uncertainty of S_{radio} is 46%. For events with at least five stations with signal the average uncertainty reduces to 24%.

6.2.3 Absolute scale uncertainties of the energy estimator

The dominant systematic uncertainties of the reconstructed electric-field amplitudes are the calibration of the analog signal chain and the antenna response pattern. The analog signal chain consists of the low-noise amplifier, the filter amplifier and all cables between the antenna and the analog-to-digital converter. The analog signal chain has been measured for each channel of each radio station separately in the field and differences are corrected for. The systematic uncertainty of the analog chain amounts to 6%.

The simulated antenna response pattern has been confirmed by measurements at an overall level of 4%. The systematic uncertainty of the measurement is 12.5% in the vector effective length [221]. Conservatively, the systematic uncertainty of the antenna-response pattern is therefore estimated as 12.5%.

Systematic uncertainties introduced by the usage of the two-dimensional signal distribution function of Eq. (6.4) are negligible. Detailed comparisons of the shape of the radio signal distribution measured with LOFAR with the predictions from CoREAS show no indication of any systematic

Table 6.2: Overview of uncertainties of the electric-field amplitude $\sigma_{|\vec{E}|}$ and the energy estimator S_{radio}. "$\oplus$" denotes a quadratic sum. The average fit uncertainty of S_{radio} is 46%, and 24% for the high-quality subset of events with at least five stations with signal.

source of uncertainty	$\boldsymbol{\sigma}_{|\vec{E}|}$	$\boldsymbol{\sigma} S_{\text{radio}}$
event-by-event		
temperature dependence	4%	8%
angular dependence of antenna response pattern	5%	10%
reconstructed direction	negligible	negligible
LDF fit uncertainty	-	error propagation of fit parameters
total event-by-event uncertainty	**6.4%**	**12.8% $\oplus$ fit uncertainty**
absolute scale		
absolute scale of antenna response pattern	12.5%	25%
analog signal chain	6%	12%
LDF model	<2.5%	<5%
total absolute scale uncertainty	**14%**	**28%**

discrepancy [18]. We determined the influence of the 2D-LDF model on the radiation energy in a representative CoREAS Monte Carlo data set for the AERA detector and found a systematic effect of less than 5%.

Combining all uncertainties in quadrature, the systematic uncertainty of the electric-field amplitude is 14%. The radio-energy fluence and the energy estimator scale with the amplitude squared. Therefore, the systematic uncertainty of the absolute scale of the radiation energy is 28%. We note that, as the cosmic-ray energy is proportional to the square root of the radiation energy (see next section), the systematic uncertainty of a radio cosmic-ray energy scale would remain at 14%.

6.3 Energy calibration

The radio-energy estimator S_{radio} is shown as a function of the cosmic-ray energy E_{CR} measured with the surface detector in Fig. 6.4 left. A clear correlation is observed. For the calibration function we follow the same method as used for the calibration of surface detector events with fluorescence detector events of the Pierre Auger Observatory [77, 205, 273]. The calibration function

$$S_{\text{radio}} = A \times 10^7 \, \text{eV} \, (E_{\text{CR}}/10^{18} \, \text{eV})^B \tag{6.6}$$

is obtained by maximizing a likelihood function that takes into account all measurement uncertainties, detector efficiencies and the steeply falling energy spectrum (the functional form and the derivation of the likelihood function can be found in Appendix C.2). The result of the calibration fit is $A = 1.58 \pm 0.07$ and $B = 1.98 \pm 0.04$. The correlation between A and B is 35%. The resulting slope is quite compatible with an exponent of $B = 2$ implying that the energy deposited in radio emission increases quadratically with the cosmic-ray energy. If B is fixed to 2 the fit result is $A = 1.59 \pm 0.06$. We can infer from Eq. (6.6) that, for a 1 EeV air shower perpendicular to the magnetic field axis, 15.8 MeV is deposited on average in radio emission in the frequency range of 30 to 80 MHz.

The upper right panel of Fig. 6.4 shows the scatter around the calibration curve for all air showers
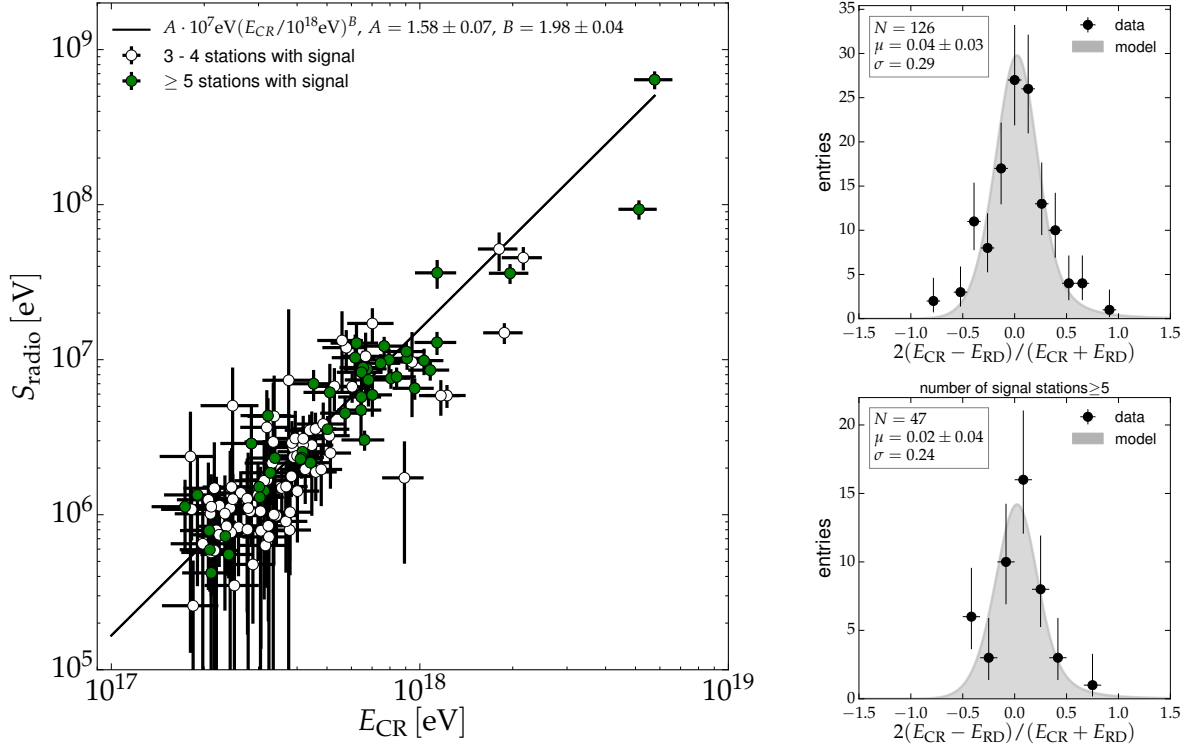
Figure 6.4: (left) The radio-energy estimator S_{radio} as a function of the cosmic-ray energy E_{CR} measured with the surface detector. A power law is fitted to the data using a likelihood approach which takes all uncertainties and detection efficiencies into account. Green filled circles denote air showers where the core position has been determined in the radio LDF fit, i.e., all air showers with at least five stations with signal. Open circles denote events with less than five stations with signal and use the SD core position. (right) Relative energy resolution: The energy of the radio detector is obtained using the fit in the left-hand figure. The upper histogram contains all air showers, and the lower histogram contains the air showers with at least five stations with signal (green filled circles). The expected distribution is shown as a gray shaded area which is computed from the fitted probability model that describes the fluctuations.

in our data set. This amounts to 29%. We also tested a high-quality data set containing only air showers with at least five stations with signal, where a determination of the core position in the radio LDF fit is possible. These air showers are marked by green filled circles in Fig. 6.4. The fit of the calibration curve gives a compatible result ($A = 1.60 \pm 0.08$, $B = 1.99 \pm 0.05$) and the scatter around the calibration curve reduces to 24% (lower right panel of Fig. 6.4).

To obtain a goodness-of-fit estimator, the measured distribution is compared to the expected distribution which is computed from the likelihood function, i.e., from the probability model that describes the fluctuations. The details of the derivation from the likelihood function is presented in Appendix C.3. The comparison yields a reduced chi-square value of $\chi^2/\text{ndf} = 13.8/12$ for the full data set and $\chi^2/\text{ndf} = 8.43/6$ for the high-quality data set. In particular, it shows that the estimated uncertainties of the energy estimator in Sec. 6.2.2 are compatible with the observed scatter around the calibration curve.

6.3.1 Uncertainties of the reconstructed cosmic-ray energy with the radio detector

To determine the energy resolution of the radio detector, the known resolution of the surface detector needs to be subtracted from the combined scatter. The average (statistical) SD energy resolution for all air showers in our data set is 18%. To obtain an estimate of the radio-energy resolution we use a Monte Carlo study which takes into account the energy and zenith angle dependence of the SD energy resolution. The combined scatter is simulated for different radio-energy resolutions, according to the number of air showers and the energy and zenith distribution of the data set. We find that the energy resolution of the radio detector is 22% for the full data set and 17% for the air showers where the core position could be determined in the radio LDF fit, when five or more radio stations have a significant signal. Details of this study can be found in Appendix C.4

In the above calculation we assumed that the energy estimates from the SD and radio reconstruction are uncorrelated for a fixed energy. However, an anti-correlation is expected as radio emission originates from the electromagnetic part of the air shower whereas the SD signal is mostly due to muons resulting from the hadronic shower component [274] and which are anti-correlated shower parameters for a fixed cosmic-ray energy. In case of an anti-correlation, the estimated radio-energy resolution would be even smaller making the above values conservative estimates.

Furthermore, we studied the effect of a possible bias in the SD reconstructed energy for different primaries where the detector is not fully efficient (0.1 EeV - 0.3 EeV) and has a slightly different efficiency curve for the two extreme scenarios of proton and iron primaries [175]. We found that the effect is negligible for our data set.

The uncertainty on the absolute scale of the energy estimator as discussed in Sec. 6.2.3 is calibrated out by correlating S_{radio} with E_{CR}. The method, however, inherits the uncertainties of the SD energy scale. This scale uncertainty is dominated by the FD scale uncertainty, which is used to calibrate the SD. It is 14% at energies $\geqslant 10^{18}$ eV [186] and increases to 16% at $10^{17.5}$ eV.

6.3.2 Precision and possible improvements of the energy reconstruction

We have found that the instrumental noise and the environmental influences are not the dominant contributions to our energy resolution. Applying the method described to a CoREAS Monte Carlo data set [140, 156], including a representative set of shower geometries as well as shower-to-shower fluctuations, but no instrumental or environmental uncertainties, a similar energy resolution is obtained for the same detector layout.

The intrinsic limitation in the energy resolution due to shower-to-shower fluctuations of the electromagnetic part of the shower is predicted to be smaller than 10% [9, 267] and we expect that the current energy resolution can be further improved. Under the condition that the LDF samples the relevant part of the signal distribution on the ground correctly for all geometries, the energy estimator should only be affected by the shower-to-shower fluctuations in the electromagnetic part of the shower. The only additional geometric dependence is due to the fact that the air shower might not be fully developed when reaching the ground, i.e., some part of the shower is clipped away. As the atmospheric depth increases with the secant of the zenith angle, clipping mostly affects high-energy vertical showers. Hence, we expect an additional dependence on the zenith angle. In the future, with larger statistics, this effect will be parametrized from data and will further improve the energy resolu-

tion. Also, a better understanding of the detector and the environmental effects, such as temperature dependencies, will help to improve the energy reconstruction.

Combined measurements, such as they are possible at the Pierre Auger Observatory, hold great potential for future improvements of the energy resolution due to the anti-correlation of the energy reconstructed with the radio and surface detectors.

6.3.3 The energy content of extensive air showers in the radio frequency range of 30 to 80 MHz

So far, the energy content of extensive air showers in the radio frequency range of 30 to 80 MHz has only been measured at the Pierre Auger Observatory in Argentina. However, our findings can be generalized by the following consideration.

To obtain a prediction that is independent of the location of the experiment, i.e., a universal formula to calculate the radiation energy from the cosmic-ray energy, the calibration function Eq. (6.6) can be normalized to the local magnetic field. We found that it is sufficient to correct only for the dominant geomagnetic part of the radio emission. This is because the increase of radiation energy due to the charge-excess emission is small, as constructive and destructive interference with the geomagnetic emission mostly cancel out in the integration of the energy densities over the shower plane, see Eq. (6.5). For the average relative charge-excess strength of 14% at AERA [12] the increase in radiation energy is only 2%. As most locations on Earth have a stronger magnetic field than the AERA site the effect of the charge-excess emission on the radiation energy will be even smaller. Within the statistical accuracy of the calibration function this effect can be neglected which leads to the universal prediction of the radiation energy

$$E_{30-80\,\mathrm{MHz}} = (15.8 \pm 0.7(\mathrm{stat}) \pm 6.7(\mathrm{sys}))\,\mathrm{MeV} \times \left(\sin\alpha \, \frac{E_{\mathrm{CR}}}{10^{18}\,\mathrm{eV}} \frac{B_{\mathrm{Earth}}}{0.24\,\mathrm{G}}\right)^2, \qquad (6.7)$$

where E_{CR} is the cosmic-ray energy, B_{Earth} denotes the local magnetic-field strength and $0.24\,\mathrm{G}$ is the magnetic-field strength at the AERA site. The systematic uncertainty quoted here is the combined uncertainty of S_{radio} (28%) and the SD energy scale (16% at $10^{17.5}$ eV). These two contributions amount to uncertainties of $5.1\,\mathrm{MeV}$ and $4.4\,\mathrm{MeV}$ in the measurement of the radiation energy at $1\,\mathrm{EeV}$, respectively. We note that the systematic uncertainty in the determination of the cosmic-ray energy from radio measurements is half of that of $E_{30-80\,\mathrm{MHz}}$, as the cosmic-ray energy scales with the square root of the radiation energy. This formula will become invalid for radio detectors at high altitudes because the amount of radiation energy decreases as – depending on the zenith angle – a significant part of the air shower is clipped away at the ground.

Please note that in practice the 30 to 80 MHz band is used by most experiments. Due to coherence effects, the cosmic-ray-induced radio emission is strongest below 100 MHz. Atmospheric noise and short-wave band transmitters make measurements below 30 MHz unfeasible. From 85 to 110 MHz the FM band interferes with measurements. Furthermore, radio emission at frequencies well beyond 100 MHz can be detected only in very specific geometries (observers at the Cherenkov angle) [127]. Hence, ground-based experiments exploit the frequency window from 30 to 80 MHz or measure in only slightly different frequency bands.

6.4   Cross-calibration of cosmic-ray observatories

The universal prediction of the radiation energy enables an accurate and model-independent way to cross-calibrate different cosmic-ray observatories which was not possible with previous approaches to reconstruct the cosmic-ray energy from radio data. Several analyses exploiting the calorimetric property of the radio emission for the determination of the energy of cosmic-ray particles have previously been published [7, 9, 20, 266]. All of these approaches used the radio-signal strength at a characteristic lateral distance from the shower axis as an estimator for the cosmic-ray energy. While this method has long been known to provide good precision [267], it has the marked disadvantage that the corresponding energy estimator cannot be directly compared across different experiments. Asymmetries arising from the charge-excess contribution [12, 122, 275] can be corrected for, and the air-shower zenith angle can be normalized out. The systematic influence of the observation altitude on the lateral signal distribution, however, poses a fundamental problem for such comparisons. In a simulation study, we have quantified the difference between radio amplitudes at the characteristic lateral distance measured for the same showers at sea level (altitude of LOFAR [13]) and at 1560 m above sea level (altitude of the radio detector array of the Pierre Auger Observatory [2]). We observe differences between -11% and +23% with an average deviation of 11%. These deviations in the measured amplitude arise from the fact that the lateral radio signal distribution flattens systematically with increasing distance of the radio antennas to the air-shower maximum. Furthermore, the optimal lateral distance at which to make the measurement also varies with observation altitude. This behavior is illustrated in Fig. 6.5. While absolute values for the amplitudes measured at a characteristic lateral distance as a function of cosmic-ray energy have been published by several experiments [9, 20, 221], no direct comparison between the energy scales of these cosmic-ray radio detectors has therefore been performed to date. (Most experiments obtain their energy scale based on surface detector arrays and thus incur uncertainties from hadronic interaction models.)

By using the radiation energy as an estimator of the cosmic-ray energy, we make an important conceptual step forward. Due to conservation of energy, and the absence of absorption in the atmosphere, the radiation energy measured at different observation altitudes is virtually identical. In the above-mentioned simulation study, the radiation energy was shown to vary less than 0.5% between an observation altitude of 1560 m above sea level and sea level itself. (This scatter arises from slight clipping effects of the air-shower evolution at an observation altitude of 1560 m above sea level and from statistical uncertainties in the determination of the radiation energy from the simulated radio-emission footprint.) The radiation energy directly reflects the calorimetric energy in the electromagnetic cascade of an extensive air shower, akin to an integral of the Gaisser-Hillas profile measured with fluorescence detectors. It constitutes a universal, well-defined quantity that can be measured with radio detectors worldwide and can thus be compared directly between different experiments.

Radiation Energy

$E_{30-80\,\mathrm{MHz}}$

$\propto \int A^2 \mathrm{d}^2 r$

The Radiation Energy reflects the calorimetric energy of the air shower. It is independent of observation altitude.

11.9 MeV

Auger altitude (1560 m a.s.l.)

11.9 MeV

LOFAR altitude (sea level)

Amplitude at optimal lateral distance

A

0.70 mV/m

0.56 mV/m

The optimal lateral distance and the amplitude measured there vary with observation altitude (even after charge-excess and zenith-angle correction).

One-dimensional lateral distributions
after ideal charge-excess asymmetry correction and for fixed zenith angle for a set of 22 air showers

Auger altitude (1560 m a.s.l.)

$0.70\,\mathrm{mV/m} \pm 7\%$ (at 140 m)

LOFAR altitude (sea level)

$0.56\,\mathrm{mV/m} \pm 7\%$ (at 190 m)

electric field amplitude A [mV/m]

distance to shower axis [m]

Measurements of the Radiation Energy for the same shower at 1560 m a.s.l. and at sea level vary by less than 0.5%.

radiation energy

N = 22
μ = − 0.16
σ = 0.45

entries

relative difference [%]

electric field at 140m

N = 22
μ = 11
σ = 8.2

entries

relative difference [%]

Measurements of A(140 m) for the same shower at 1560 m a.s.l. and at sea level vary very significantly. The same is true for A(190 m).
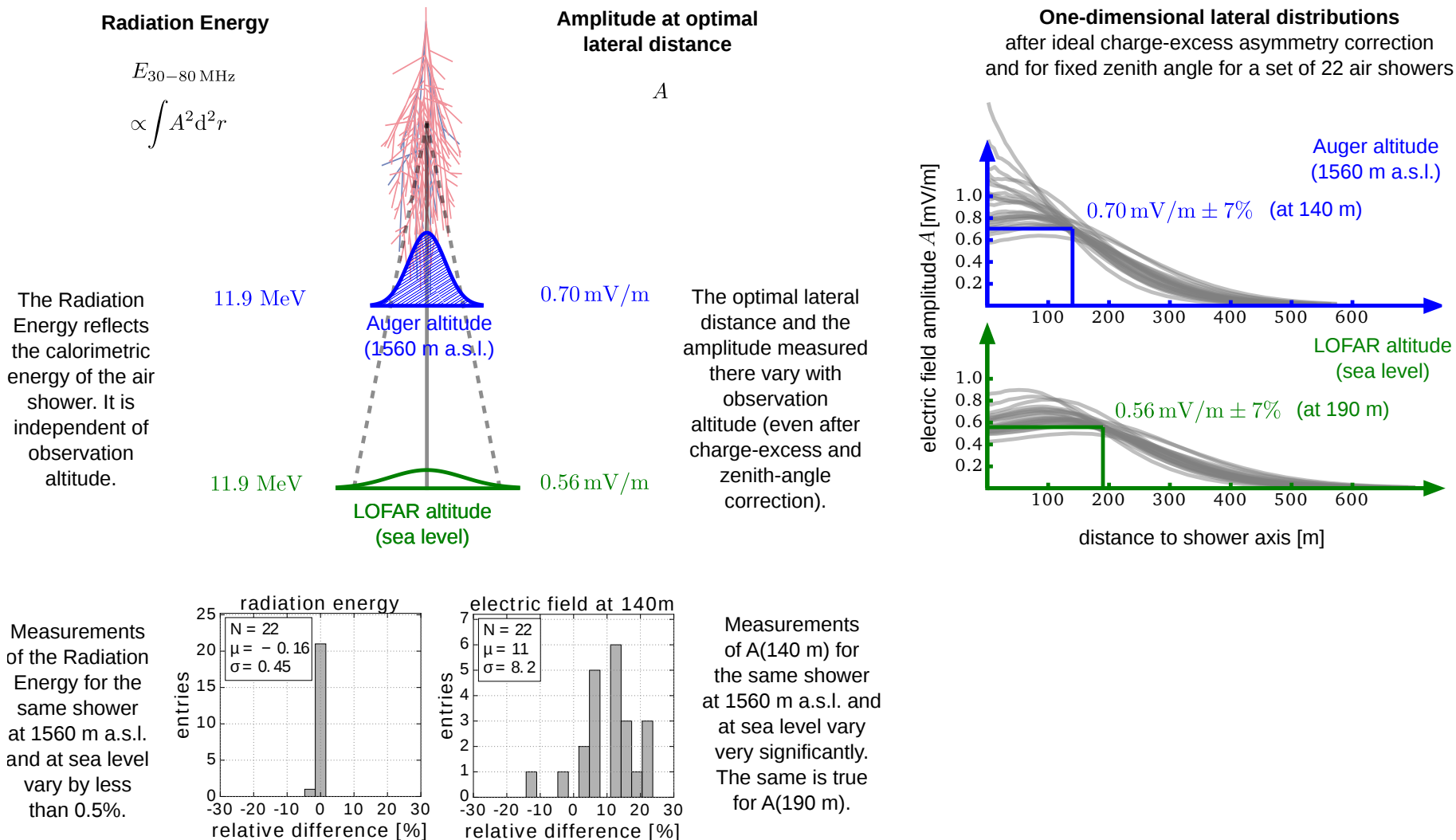
Figure 6.5: Illustration of the dependence of both the "radiation energy" and the "radio-amplitude measured at a characteristic lateral distance" on the altitude of observation. Sketch is from the supplemental material of [161].

The cosmic-ray energy scale
from first-principles calculations

In this chapter, we address one of the most important challenges in cosmic-ray physics: the accurate determination of the absolute energy scale of cosmic rays. An accurate energy scale is a crucial ingredient for most analyses of high-energy cosmic rays. Limited precision (i.e. energy resolution) can be overcome with increased statistics making the accuracy, i.e., the systematic uncertainty of the energy scale, even more important. By now, many results of the Pierre Auger Observatory are limited by systematic uncertainties (cf. the recent results presented in Chap. 2). In the following, we give a few examples where the accuracy in the energy scale is crucial for the interpretation of the data.

Accuracy is needed to determine the energies where the flux of cosmic rays exhibits distinct characteristics, e.g., the "ankle" at around 5 EeV, and the "cut-off" at above $\sim$25 EeV (cf. Fig. 2.2 and 2.3) which directly impacts the astrophysical understanding and parameters of astrophysical models [86, 276]. Furthermore, a small systematic uncertainty is crucial for the test of hadronic interactions at ultra-high energies, e.g., the deficit of muons in air-shower simulations could be mostly explained with a shift of the cosmic-ray energy by one standard deviation of the uncertainty towards higher energies (cf. [77] and Sec. 2.1).

So far, the Pierre Auger Observatory uses the fluorescence technique to determine the absolute energy scale. Telescopes measure the fluorescence light emitted by air showers which is proportional to the calorimetric shower energy and allows for an accurate determination of the energy of the primary particle [186]. However, fluorescence light detection is only possible at sites with good atmospheric conditions, and precise quantification of scattering and absorption of fluorescence light under changing atmospheric conditions requires extensive atmospheric monitoring efforts (cf. Sec. 4.3 and [168, 206, 207, 212]).

Here, an alternative option to determine the energy scale is presented. The measurement of radio signals from extensive air showers allows the determination of the cosmic-ray energy scale [161]. The measured radiation energy can be related to the electromagnetic shower energy using predictions from first-principles calculations. The full procedure to determine the energy scale with a radio detector is
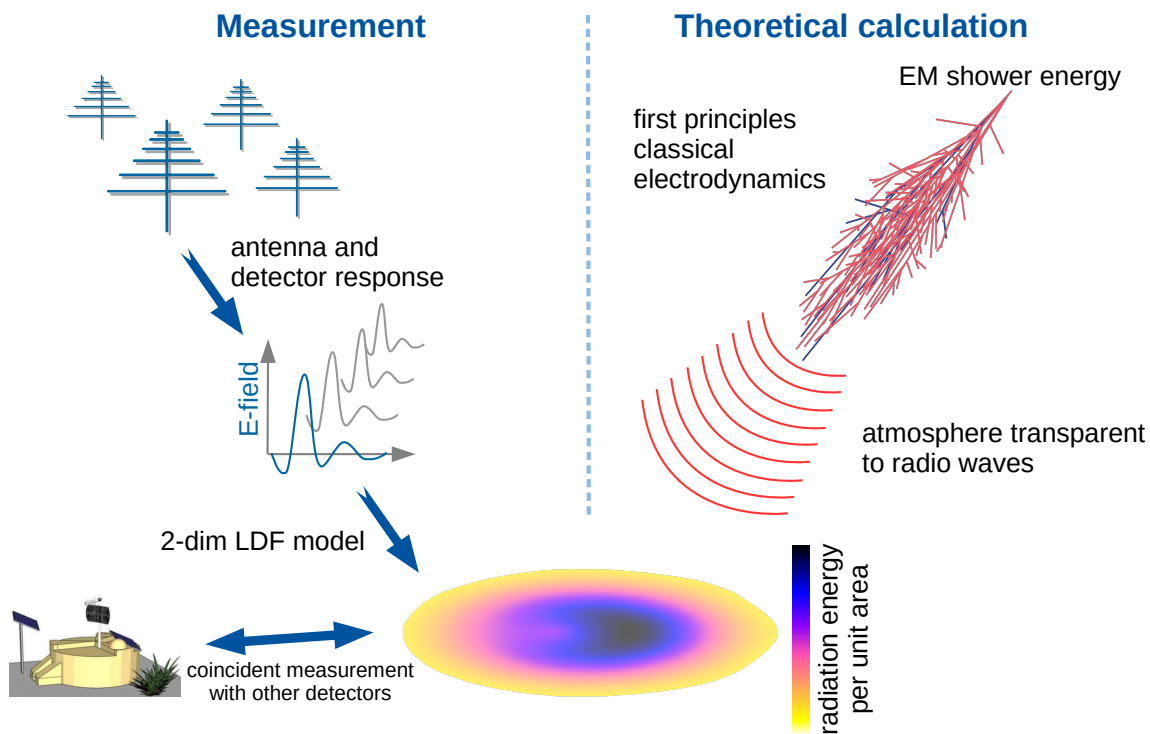
Figure 7.1: Illustration of the determination of the energy scale from first-principles calculations using the radio technique. The method is divided into an experimental part (the measurement of the radiation energy) and a theoretical part (the prediction of the radiation energy).

depicted in Fig. 7.1. The procedure can be subdivided into an experimental part, the measurement of the radiation energy, and a theoretical part, where the radiation energy is calculated from first principles. The measurement was already presented in Chap. 6: The electric-field pulses generated by air showers are obtained by unfolding the antenna and detector response from the measured voltage traces. Then, the energy fluence at each observer position is calculated and interpolated with a two-dimensional model of the signal distribution. The integral over the energy fluence then yields the total radiation energy. On the theoretical side which was presented in Sec. 3.3, the radiation energy is calculated via first principles from the electromagnetic air-shower component using classical electrodynamics. As the atmosphere is transparent to radio waves, the predicted radiation energy can be directly compared to the measurement. This radio energy scale is then propagated to other detectors via coincident measurements of air showers.

7.1   Comparison of RD and FD energy scales

In this section, we will combine the theoretical prediction of the radiation energy for a given electromagnetic shower energy of Sec. 3.3 with the measurement of the radiation energy in coincidence with the Auger surface detector (SD). Thereby, we can directly compare the radio energy scale with

Figure 7.2: Ratio of calorimetric to electromagnetic shower energy as a function of electromagnetic shower energy. The data was obtained from CORSIKA simulations with QGSJetII-04 (the same data set as used in Sec. 3.3). The small dots in the background show the value of each simulated air showers. The black filled circles denote the mean and spre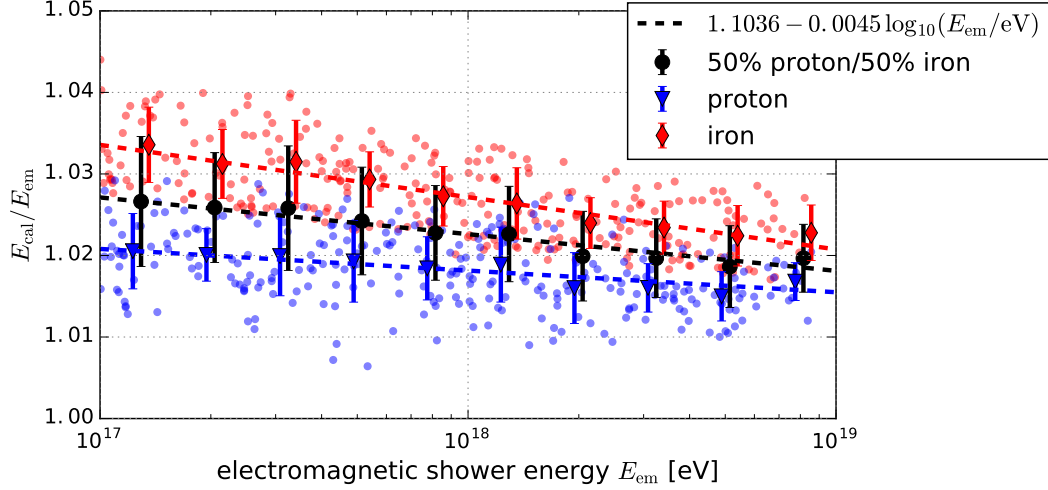ad of the ratio per energy bin. The blue triangles and red diamonds show the same for proton and iron induced air showers respectively. The dashed lines show a fit of a straight line to the full data (black), proton induced (blue) and iron induced air showers (red).

the energy scale set by the fluorescence detector (FD) as the SD was cross-calibrated with the FD. In Chap. 6, the measured radiation energy was cross-calibrated with the cosmic-ray energy as measured by the surface detector. For a comparison with the theoretical prediction of the radiation energy it is more convenient to correlate the radiation energy with the *calorimetric* energy. The calorimetric energy refers to the amount of energy that is directly measured with the fluorescence telescopes, i.e., the integral of the Gaisser-Hillas fit of the dE/dX longitudinal profile. This energy does not correspond exactly to the electromagnetic shower energy as also muons and to a smaller extend also hadrons deposit a small amount of their energy in the atmosphere and thereby contribute to the fluorescence light. The amount of the energy deposit of hadrons is ∼7% of the energy deposit of muons. The difference between calorimetric and electromagnetic shower energy is presented in Fig. 7.2. The difference varies between 1% and 4% and is on average 2.3% for an electromagnetic shower energy of $1\,\mathrm{EeV}$ in case of a mixed composition (50% protons/50% iron nuclei).

Hence, instead of cross-correlating the measured radiation energy with the cosmic-ray energy we directly use the calorimetric energy. This is possible because the SD was calibrated with the cosmic-ray energy that was reconstructed from FD data. The FD obtains the cosmic-ray energy from the measured calorimetric energy by applying an energy-dependent correction of the form

$$\frac{E_{\mathrm{inv}}}{1\,\mathrm{EeV}} = 0.174 \left(\frac{E_{\mathrm{cal}}}{1\,\mathrm{EeV}}\right)^{0.914}, \tag{7.1}$$

with $E_{\mathrm{inv}} = E_{\mathrm{cr}} - E_{\mathrm{cal}}$ and E_{cr} being the cosmic-ray energy. This correction was determined in a model independent way from measurements [117] and is referred to as *invisible energy correction*. To obtain the calorimetric energy from the cosmic-ray energy that was reconstructed by the surface detector, we remove the invisible energy correction.
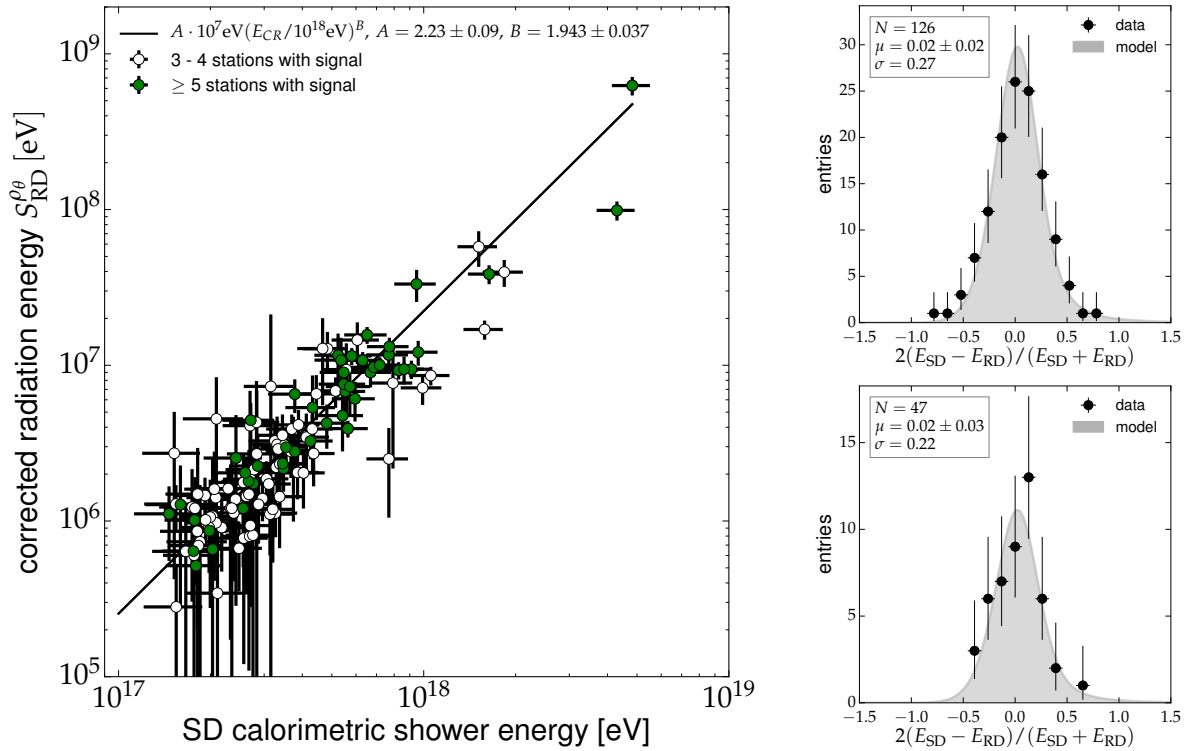
Figure 7.3: (left) The radio-energy estimator $S_{\mathrm{RD}}^{\rho\theta}$ of Eq. (3.28) including clipping correction according to the parametrization given in Tab. 3.3 as a function of the calorimetric shower energy measured with the surface detector. A power law is fitted to the data using a likelihood approach which takes all uncertainties and detection efficiencies into account. Green filled circles denote air showers where the core position has been determined in the radio LDF fit, i.e., all air showers with at least five stations with signal. Open circles denote events with less than five stations with signal and use the SD core position. (right) Relative energy resolution: The energy of the radio detector is obtained using the fit in the left-hand figure. The upper histogram contains all air showers while the lower histogram contains the air showers with at least five stations with signal (green filled circles). The expected distribution is shown as a gray shaded area which is computed from the fitted probability model that describes the fluctuations.

We also use an improved radio energy estimator. Instead of correcting only for the geometric dependence of the dominant geomagnetic emission process by dividing the radiation energy by $\sin^2\alpha$, we use the improved energy estimator developed in the simulation study of Sec. 3.3.4. The improved energy estimator also takes into account the dependence of the radiation energy on the air density at the emission region which was parametrized as a function of zenith angle. Furthermore, we apply the clipping correction, i.e., we correct for missing radiation energy of air showers that are not fully developed before reaching ground. We use the parametrization given in Tab. 3.3 for a mixed composition. The resulting correlation is presented in Fig. 7.3. A calibration function of the form $S_{\mathrm{RD}} = A \times E_{\mathrm{cal}}^{B}$ with free parameters A and B is fitted to the data using the same likelihood method as before in Sec. 6.3. The histograms on the right side of the figure show the scatter around the calibration curve for the full data set and for a high-quality data set containing only events with at least five stations with signal. The scatter reduces to 27% and 22% for the high-quality data set with respect to the previous cross-calibration of Chap. 6, indicating that the zenith angle and clipping correction developed in the simulation study are correctly described. Subtracting the SD energy resolution from the combined

scatter using the method presented in Appendix C.4 results in an energy resolution of AERA of less than 20% for the full and less than 14% for the high-quality data set.

The calibration constant A can then be compared to the prediction from first-principles calculations. The likelihood fit using the full data set yields $A = (22.3 \pm 0.9)\,\mathrm{MeV}$ and $B = 1.943 \pm 0.037$ corresponding to a radiation energy of $22.3\,\mathrm{MeV}$ for an air shower with a calorimetric energy of $1\,\mathrm{EeV}$ arriving perpendicularly to the geomagnetic field at a zenith angle of $45°$. The measured scaling with the calorimetric energy is compatible with the prediction from first-principles calculations of $B = 1.980 \pm 0.001$ (cf. Tab. 3.2). We performed several cross-checks to test the stability of the calibration constant A. The calibration constant obtained with the high-quality data set is $A = (22.8 \pm 1.0)\,\mathrm{MeV}$ and well compatible within the statistical uncertainty. If the slope of the calibration curve is fixed to $B = 1.98$ as predicted from the first-principles calculations, the parameter A takes a compatible value of $A = (22.7 \pm 0.9)\,\mathrm{MeV}$. As the clipping correction assumes a certain cosmic-ray composition, it could introduce a bias if the true cosmic-ray composition differs from the assumed mixed composition. Therefore, the analysis is repeated with a subset of events where the clipping correction is less than 2% of the radiation energy. A quantity of 68 events fulfills this condition and the resulting calibration constant is $A = (24.5 \pm 1.4)\,\mathrm{MeV}$ and thus also compatible within the statistical uncertainty.

Hence, from the comparison of air showers measured in coincidence by AERA and SD we obtain the following relation between corrected radiation energy and calorimetric energy with respect to the energy scale of FD of

$$S_{\mathrm{RD}}^{\rho_\theta} = (22.3 \pm 0.9)\,\mathrm{MeV} \left(\frac{E_{\mathrm{cal}}^{\mathrm{FD}}}{1\,\mathrm{EeV}} \right)^{1.943 \pm 0.037}, \tag{7.2}$$

which we correct for the difference between calorimetric and electromagnetic shower energy of 2.3% at $1\,\mathrm{EeV}$ according to Fig. 7.2 to obtain

$$S_{\mathrm{RD}}^{\rho_\theta} = (22.3 \pm 0.9)\,\mathrm{MeV} \left(1.023 \times \frac{E_{\mathrm{em}}^{\mathrm{FD}}}{1\,\mathrm{EeV}} \right)^{1.943 \pm 0.037} \tag{7.3}$$

$$= (23.3 \pm 0.9)\,\mathrm{MeV} \left(\frac{E_{\mathrm{em}}^{\mathrm{FD}}}{1\,\mathrm{EeV}} \right)^{1.943 \pm 0.037}. \tag{7.4}$$

This relation can be directly compared to the prediction from first-principles calculations (cf. Tab. 3.2). The calculations were performed for a refractivity at sea level of 2.92×10^{-4} which is slightly smaller than the refractivity at the site of the Pierre Auger Observatory of 3.12×10^{-4}. This increase in refractivity of $\sim7\%$ results in an increase of radiation energy by 2% (cf. Tab. 3.6). We correct this effect and obtain

$$S_{\mathrm{RD}}^{\rho_\theta} = (16.61 \pm 0.03)\,\mathrm{MeV} \left(\frac{E_{\mathrm{em}}^{\mathrm{theo}}}{1\,\mathrm{EeV}} \right)^{1.980 \pm 0.001}. \tag{7.5}$$

Using the energy scale based on the FD calibration, a radiation energy has been measured that is too large in comparison to the first-principles prediction. The two results can be brought into agree-

ment if the FD energy scale is increased by a factor of

$$\left(\frac{23.3 \,\mathrm{MeV}}{16.61 \,\mathrm{MeV}}\right)^{(1/1.98)} = 1.186 \approx +19\% \tag{7.6}$$

towards higher energies. Here, we used the slope parameter $B = 1.98$ from the simulation study as it has a much smaller uncertainty. We note that this offset is well compatible within the systematic uncertainties.

7.2 Systematic uncertainties of the radio energy scale

In this section we discuss the systematic uncertainties of the RD energy scale. All uncertainties presented here are given with respect to the cosmic-ray energy scale[1]. The uncertainties are summarized in Tab. 7.1. Next to the current uncertainties, we also present an estimate of improved uncertainties that should be achievable in the immediate and more distant future.

Experimental uncertainties   The uncertainties of the measurement of the radiation energy are discussed in detail in Sec. 6.2.3. They amount to 14% and are dominated by the uncertainty of the antenna response of 12.5% and the calibration of the signal chain of 6%. In the future, a significant improvement of this uncertainty is expected. A new calibration campaign has been already performed in March 2015 and yields an average uncertainty of 9% on the antenna response. A publication of this result is well advanced and the new calibration incorporated into the reconstruction of air showers [234]. The limiting factor of an antenna calibration measurement is the systematic uncertainty of the signal source. A reduction of this uncertainty to a 6% level seems realistic such that the antenna response pattern could be measured with an accuracy of ∼6% in a future calibration campaign. Also a new measurement of the signal chain is planned for the end of 2016 that will reduce the systematic uncertainty to 0.5%. Hence, in the immediate future a reduction of the experimental uncertainties to below 10% is expected and even a reduction to a 6% percent level seem realistic. Also the systematic uncertainty of the LDF model that currently contributes with an uncertainty of 2.5% is likely to be reduced to a negligible value with a refined LDF model or a different approach such as a template matching method.

   The experimental uncertainties currently contribute with 14% to the systematic uncertainty and are likely to be reduced down to 6% in the future.

Theoretical uncertainties   The calculation of the radio emission from the electromagnetic shower particles itself has no systematic uncertainties as the calculation is purely based on classical electrodynamics which does not have any free parameters. However, the modeling of the electromagnetic air-shower component is subject to uncertainties. Also approximations made in the simulation code to speed up the calculations result in additional uncertainties.

   The systematic uncertainty in modeling the air-shower development is estimated by using different (high- and low-energy) hadronic interaction models. Exchanging QGSJetII-04 with EPOS-LHC and

---

[1]As the radiation energy scales almost quadratically with the cosmic-ray energy, an uncertainty of $X\%$ on the radiation energy corresponds to an uncertainty of $(0.5 \times X)\%$ on the cosmic-ray energy scale.

Table 7.1: Summary of the systematic uncertainties of the radio energy scale.

source of uncertainty	current	immediate future	future
experimental uncertainties (Sec. 6.2.3)	**14.1%**	**9.4%**	**6.1%**
antenna response pattern	12.5%	9%	6%
analog signal chain	6%	0.5%	0.5%
LDF model	<2.5%	<2.5%	<1%
theoretical uncertainties	**2.5%**	**1.7%**	**1.7%**
air-shower modeling (Sec. 3.3.5)	0.13%	0.13%	0.13%
refractivity correction (Sec. 3.3.6)	1%	-	-
thinning (Sec. 3.3.5)	<0.15%	<0.15%	<0.15%
energy thresholds of shower particles (Sec. 3.3.5)	<0.5%	<0.5%	<0.1%
extraction of radiation energy (Sec. 3.3.2)	1.5%	<0.1%	<0.1%
CoREAS/ZHAireS difference (Sec. 3.3.7, [170])	1.7%	1.7%	1.7%
environmental uncertainties	**1.6%**	**1.6%**	**0.1%**
atmosphere (Sec. 3.3.6)	1.25%	1.25%	<0.1%
ground conditions ([234])	1%	1%	0.1%
invisible energy correction ([117])	**3.0%**	**3.0%**	**3.0%**
stat. uncertainty of cross-calibration with SD	**2.2%**	**<1%**	**<0.1%**
total absolute scale uncertainty	**14.8%**	**10.2%**	**7%**

FLUKA with UrQMD results in a difference in the predicted radiation energy of 0.18% each which is compatible within the statistical uncertainty of the comparison (cf. Sec. 3.3.5). The influence of hadronic interaction models is small because we correlate the radiation energy directly with the electromagnetic shower energy. We use the differences in radiation energy as an estimate of the systematic uncertainty. We add the two differences of the low- and high-energy hadronic interaction models in quadrature resulting in an uncertainty with respect to the cosmic-ray energy scale of below 0.13%.

The systematic uncertainties resulting from approximations in the air-shower simulation are estimated in the following way. Conservatively, we use the complete ad-hoc correction for a different air refractivity of +2% in radiation energy (+1% in cosmic-ray energy, cf. Sec. 3.3.6) as an estimate of the systematic uncertainty. Furthermore, the radiation energy is not determined from the full two-dimensional footprint but only from the energy fluence along one axis in the shower plane. This approximation leads to an average offset of 3% in radiation energy which is taken into account in the prediction (cf. Sec. 3.3.2). Again, we use the full offset as an estimate of the corresponding uncertainty. The impact of thinning and lower energy thresholds of the shower particles was studied and contributes with 0.15% and 0.5% to the systematic uncertainty (cf. Sec. 3.3.5). In the future with increased simulation time, all these approximations can be reduced to a negligible level.

An independent cross-check of a correct implementation of the underlying physics in the CoREAS simulation code was performed by a detailed comparison with the completely independent ZHAireS simulation code. The difference in the prediction of the radiation energy from the two codes is 3.3% and accordingly 1.7% with respect to the cosmic-ray energy (cf. Sec. 3.3.7 and [170]). We use this

difference as an additional contribution to the systematic uncertainty.

In total the theoretical uncertainties contribute with 2.5% to the systematic uncertainty and can be reduced to 1.7% in the future.

Environmental uncertainties   Changing atmospheric conditions, i.e., changing density profiles and varying refractivity, result in a scatter of 1.25% during the course of the year (cf. Sec. 3.3.6). We use this scatter as an estimate of the systematic uncertainty as we performed the calculations only for an average state of the atmosphere. To further reduce this uncertainty, separate simulations for monthly averages can be performed. Even separate simulations for each measured event are possible where the respective atmospheric conditions at the time of the event are obtained from GDAS data.

Changing ground conditions impact the reflectivity of the ground and thereby the antenna response. In case of the LPDAs, the antenna sensitivity towards the ground is small. A simulation of the antenna response pattern with realistic variations of ground parameters results in a change of the antenna response of ~1% [234, 235]. This uncertainty could be further reduced with a continuous monitoring of the ground conditions. A first prototype for such a continuous monitoring is already installed at the AERA site [277].

In summary, the environmental uncertainties contribute with 1.6% to the systematic uncertainty and can be reduced to 0.1% in the future.

Invisible energy correction   To obtain the cosmic-ray energy from the calorimetric energy, the invisible energy needs to be taken into account. This can be done using the parametrization presented in Eq. (7.1) that was obtained from a measurement and has a systematic uncertainty of 3% at 10^{18} eV [117]. In this measurement, only air showers with energies above 3×10^{18} eV have been used. However, it was checked with data from the $750\,\mathrm{m}$ spaced surface-detector array and the HEAT fluorescence telescopes which are already fully efficient at 3×10^{17} eV that the extrapolation towards lower energies is correct. If the RD and FD energy scales are compared, the uncertainty on the invisible energy correction is irrelevant as both detectors apply exactly the same correction.

Cross-calibration with SD/FD   To propagate the RD energy scale to the surface and fluorescence detectors of the Pierre Auger Observatory the corrected radiation energy is cross-correlated with the calorimetric energy measured by SD. Due to the limited statistics of 126 events, the parameter A of the calibration curve fitted to the data has a statistical uncertainty of 4%. Its contribution to the systematic uncertainty of the energy scale is thus 2%. By the time of writing, three and a half additional years of data are available such that the uncertainty could be reduced to below 1% with an update of the analysis. In the future with increasing statistics, this uncertainty will become negligible.

7.3   Comparison with the fluorescence technique

In this section we compare the fluorescence to the radio technique only in terms of achievable accuracy in the determination of the energy scale. Here, the radio technique has an advantage because several sources of uncertainties that have a significant influence in the fluorescence technique are negligible in case of radio measurements. Therefore, a systematic uncertainty of below 15% has been achieved

although this is the first time that the radio technique is used to determine the energy scale and the idea of such an analysis was proposed only recently [160, 161]. The achieved accuracy of 15% is already now well compatible with the fluorescence technique that has reached an uncertainty of 14% after years of optimizations [186]. Using the results of the new AERA antenna calibration campaign [234], the systematic uncertainty of the radio energy scale can be even reduced to ∼10% in the immediate future. With an improved antenna calibration setup, a further improvement down to a 7% level seems feasible.

The advantages of the radio technique are that the emission as well as the propagation of radio waves have only a small dependence on changing atmospheric conditions of ∼1.25%. In case of the fluorescence technique, scattering and absorption of fluorescence light depend strongly on the state of the atmosphere. Only extensive monitoring efforts (cf. Sec. 4.3) managed to reduce the corresponding systematic uncertainties to a level of 3.4% to 6.2% depending on the shower energy [186]. For radio, no atmospheric monitoring is needed except for a basic monitoring to reject periods of thunderstorms which additionally saves a significant amount of resources. Also the fluorescence yield, i.e., the conversion from deposited energy in the atmosphere to emitted fluorescence light, needs to be measured experimentally. Over the years the measurements have improved. The current best measurement has determined the fluorescence yield with an accuracy of 3.6% [186, 278]. In case of radio, the amount of radio emission can be calculated directly from the air-shower development via first-principles.

In addition, a laboratory measurement of the radio emission is possible. A first measurement of the radio emission in a laboratory experiment has already been performed [157]. However, its systematic uncertainty of ∼35% is too large to be used here. A more precise laboratory experiment, however, is doable in the future.

7.4 Extrapolation of the energy scale

So far, the cross-correlation of AERA with the SD has been performed in a limited energy range around $1\,\mathrm{EeV}$ (cf. Fig. 7.3). Hence, we can only definitely state that the RD and FD energy scales differ by 19% at cosmic-ray energies of around $1\,\mathrm{EeV}$. This offset might change at higher energies. The measurement shows no indication that the offset between the RD and FD energy scales changes with cosmic-ray energy but the number of events – especially at higher energies – is small such that no strong conclusion of the energy stability can be gained.

From the first-principles calculations of the radiation energy, no indication of an energy dependence of the scaling between corrected radiation energy and electromagnetic shower energy was found (cf. Fig. 3.18). However, the study was only performed up to energies of $10^{19}\,\mathrm{eV}$ and a different scaling at higher energies cannot be excluded. The systematic uncertainties of the measurement of the radiation energy are not expected to exhibit a significant energy dependence. The dominating uncertainty originates from the antenna response which is independent of the shower energy. However, this is different for the fluorescence technique, e.g., the correction for scattering and absorption in the atmosphere and the correction for the point spread function of the telescopes depend on shower energy.

In the future, a possible energy dependence can be investigated by comparing the RD and FD energy scales with larger statistics at higher energies. To obtain enough statistics at energies above
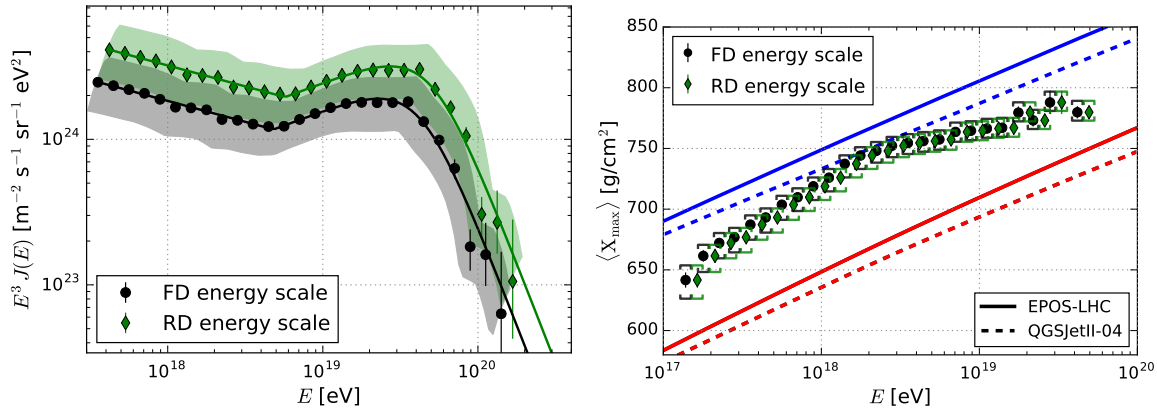
Figure 7.4: (left) Impact of the RD energy scale on the energy spectrum. The errorbars represent the statistical uncertainty (for most bins they are smaller than the marker size). The uncertainty bands denote the systematic uncertainty on the cosmic-ray energy of 14% in case of FD and 15% in case of RD. Data from [49]. (right) Impact of the RD energy scale on the measurement of the average X_{max}. The errorbars denote the statistical uncertainty and the square brackets denote the systematic uncertainty. The dashed (QGSJetII-04) and solid (EPOS-LHC) lines show the model prediction for proton (blue) and iron induced air showers (red). Data from [73].

10^{19} eV, data from all 153 AERA radio detector stations need to be used. As the efficiency increases with increasing zenith angle (as long as the cosmic-ray energy is large enough, cf. Sec. 5.10) the usage of inclined air shower becomes relevant. This requires a thorough calibration of the Butterfly antennas especially at high zenith angles. Furthermore, the Butterfly antenna is more sensitive to signals reflected from the ground which requires a continuous monitoring of the ground conditions to achieve small uncertainties in the antenna response. Also the reconstruction and analysis of inclined air showers require adaptions, e.g., the two-dimensional double-Gaussian LDF model needs to be modified as additional signal asymmetries from the projection on the ground are no longer negligible.

7.5   Implications of a shift in the energy scale

Under the assumption that the offset of 19% between the RD and FD energy scale does not change with increasing cosmic-ray energy, the impact of this energy shift on results of the Pierre Auger Observatory is investigated. The most obvious change exhibits the energy spectrum which is presented in Fig. 7.4 left. The position of the ankle moves to higher energies from 4.8×10^{18} eV to 5.7×10^{18} eV and the position of the cutoff $E_{1/2}$ increases from 4.2×10^{19} eV to 5×10^{19} eV. This increase certainly impacts the astrophysical interpretation of the spectrum [86, 276], although its exact impact has not been established yet.

The next result that is investigated is the interpretation of the X_{max} measurement which is an estimator of the cosmic-ray composition. The X_{max} values itself do not change but the energy at which the average X_{max} is compared to prediction of air-shower simulations differs. In the mean X_{max} vs. energy plot which is presented in Fig. 7.4 right, the data points shift to the right by 19% whereas the model predictions remain unchanged. Hence, the data points move from the proton lines towards the iron lines. A more quantitative picture can be gained by converting the mean X_{max} values to the aver-
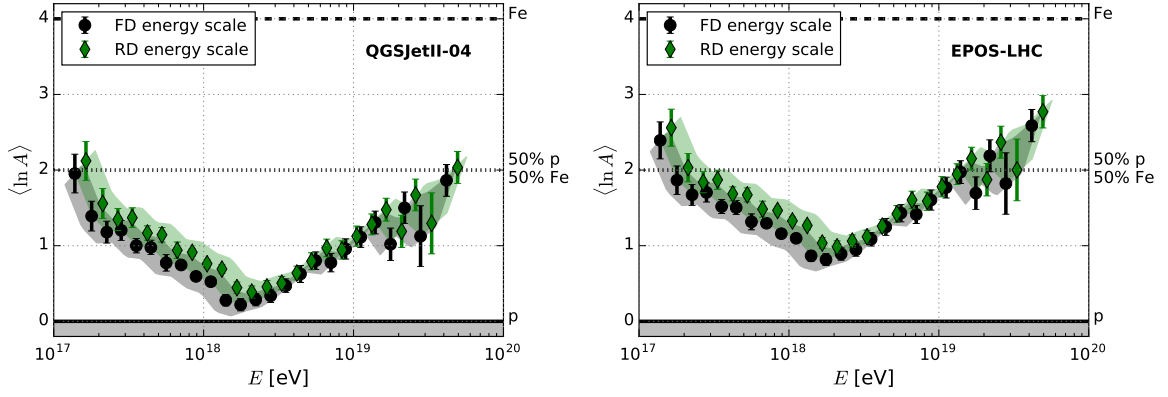
Figure 7.5: Impact of the RD energy scale on the interpretation of the average X_{max} in terms of average mass number A. $\langle \ln A \rangle$ was obtained from the average X_{max} using the parametrization presented in [70, 71] for the hadronic interaction model QGSJetII-04 (left) and EPOS-LHC (right). The uncertainty bands show the uncertainty resulting from the systematic uncertainty of the energy scale only. The systematic uncertainty from the X_{max} measurement itself is not shown for the sake of readability. Data from [73].

age logarithm of the mass number $\langle \ln A \rangle$ using the prediction of a certain hadronic interaction model (see Fig. 7.5). The average cosmic-ray composition gets slightly heavier with an average increase in $\langle \ln A \rangle$ of 0.17 for both EPOS-LHC and QGSJetII-04.

A stronger impact of an increase in measured cosmic-ray energy is visible in the measurement of $\langle R_\mu \rangle$ which is an estimator of the average relative number of muons (cf. Sec. 2.1 for an exact definition). The impact of the energy shift on the $\langle R_\mu \rangle$ measurement is presented in Fig. 7.6. The measured muon numbers are compared to predictions from hadronic interaction models for the two extremes of proton and iron induced air showers. Whereas the original measurement of $\langle R_\mu \rangle$ is significantly larger than the model prediction, the measurement that uses the RD energy scale is embraced by the model predictions for proton and iron induced air showers. Hence, the problem of a muon deficit in the simulations can be largely resolved by using the RD energy scale. In addition, by using the RD energy scale the discrepancy between the X_{max} and $\langle R_\mu \rangle$ measurements can be reduced.

7.6 Discussion

The measurement of air showers by their radio emission allows for an independent determination of the cosmic-ray energy scale. As the radio emission is less dependent on atmospheric conditions than the FD technique, an accuracy of 15% has been achieved without extensive monitoring and with a relatively small and inexpensive antenna array. Given that the radio technique was exploited here for the first time to determine the energy scale, a significant improvement in the future is expected. Using the results from the improved calibration of the antenna response, the systematic uncertainty will decrease to 10%. A further improvement in the future is expected.

Another general benefit is that the radio method is completely independent from the fluorescence technique. Hence, the radio method can be combined with the FD method to further reduce the systematic uncertainty of the energy scale. The RD energy scale presented here is compatible to the FD energy scale within the systematic uncertainties of 15% and 14% respectively. Hence, we calculate
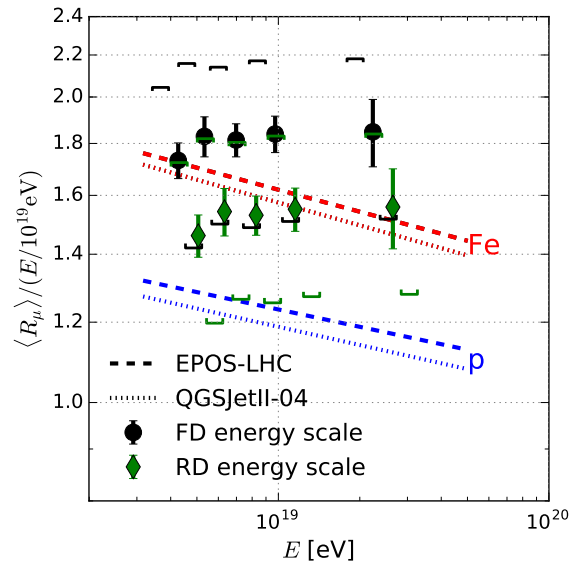
Figure 7.6: Impact of the RD energy scale on the measurement of the average relative number of muons on ground $\langle R_\mu \rangle$ as a function of cosmic-ray energy (black filled circles and green filled diamonds). The square brackets denote the systematic uncertainty which is dominated by the uncertainty of the energy scale. Also shown are the predictions from hadronic interaction models for proton and iron induced air showers. Data from [77].

the weighted mean of the two energy scales and obtain a shift of the FD energy scale of +7% with a reduced systematic uncertainty of 10%.

Conclusions

Ultra-high-energy cosmic rays can be measured by short radio pulses in the MHz regime emitted by extensive air showers. This radio technique is complementary to existing techniques such as surface detector arrays or fluorescence telescopes. It has a duty cycle of almost 100% and is sensitive to all main air-shower observables such as the cosmic-ray energy, mass, and arrival direction.

In this thesis, we developed a new method to determine the cosmic-ray energy. We showed that the radio technique is especially useful to determine the cosmic-ray energy with high accuracy and is superior to existing techniques in term of achievable accuracy. This is because the radio emission from air showers can be calculated from first principles, and radio waves are less influenced by environmental conditions compared to, e.g., fluorescence light. As an accurate energy scale is crucial for the interpretation of cosmic-ray measurements, the radio technique will thus be able to significantly advance this field of research.

We first studied the energy released in air showers in the form of MHz radiation in detail, using CoREAS air-shower simulations. Depending on the distance between the observer and the region in the atmosphere where the radiation is released, the shape of the signal distribution on the ground changes significantly. For small distances to the emission region, the signal distribution is narrow around the shower axis with large energies per unit area, whereas for large distances to the emission region the radiation energy is distributed over a larger area resulting in a broad signal distribution with a small amount of energy per unit area. As soon as the air shower has emitted all its radiation energy, the total radiation energy, i.e., the integral over the signal distribution on the ground, remains constant. In particular, it does not depend on the spacial signal distribution on the ground or on the observation altitude and is thus directly comparable between different experiments.

The simulated radiation energy – corrected for the dependence on the geomagnetic field – correlates best with the energy contained in the electromagnetic part of the air shower and exhibits quadratic scaling with the electromagnetic shower energy, as is expected for coherent emission. The electromagnetic shower energy can be converted to the primary cosmic-ray energy using predictions from hadronic interaction models or a direct measurement of the invisible energy fraction alternatively.

The simulated radiation energy has a second-order dependency on the air density of the emission region. After correcting this effect, the corrected radiation energy and the electromagnetic shower energy have a scatter of less than 3%. In addition, we presented a more practical parametrization of the dependence between radiation energy and electromagnetic shower energy using only the geometry of the air shower, i.e., without using X_{max} information, and obtained a resolution of 4%. This scatter of 4% is well below current experimental uncertainties, so that the radiation energy is well suited to estimate the cosmic-ray energy.

If the radiation energy is detected at a particular observation height, the air shower may not have released all its radiation energy. The strength of this clipping effect depends on the atmospheric depth between observation height and shower maximum. We presented a parametrization of this effect that

can be used in experiments to correctly determine the full radiation energy and thereby estimate the cosmic-ray energy. The radiation energy is influenced less by clipping than the electromagnetic part of the air shower as the radiation energy is released earlier in the shower development.

Then, we used data from the Auger Engineering Radio Array (AERA) which is the radio detector of the Pierre Auger Observatory. AERA is located within the low-energy extension of the Observatory where additional surface detector stations with a smaller spacing are present, which enables access to cosmic-ray energies down to 0.1 EeV. To most accurately determine the cosmic-ray energy, we only use the thoroughly calibrated 24 LPDA radio stations of the first stage of AERA deployment, with data collected between April 2011 and March 2013. At several observer positions, the energy deposit per area of the radio pulse of an extensive air shower is measured. Using recent progress in understanding the lateral signal distribution of the radio signals, this distribution is described by an empirical function. The spatial integral of the lateral distribution function gives the amount of energy that is transferred from the primary cosmic ray into radio emission in the 30 to 80 MHz frequency band of AERA during the air-shower development. We measured on average 15.8 MeV of radiation energy for a 1 EeV air shower arriving perpendicularly to a geomagnetic field of 0.24 G. The systematic uncertainty is 28% on the radiation energy and 16% on the cosmic-ray energy.

Using the results from the simulation study, the radiation energy is corrected for different emission strengths at different angles between shower axis and geomagnetic field, for changing emission strengths due to different air densities in the emission region as well as for missing radiation energy of air showers that are not fully developed before reaching the ground. This corrected radiation energy is compared with the calorimetric air-shower energy obtained from the the surface-detector reconstruction. Investigating the scatter around the calibration curve and subtracting the resolution of the surface detector we found that the energy resolution of the radio detector is 20% for the full data set, and 14% for the events with more than four stations with signal, where the core position could be determined in the radio LDF fit. Given the small shower-to-shower fluctuations of the electromagnetic component, we expect that with a deeper understanding of the detector and environmental effects, an even improved precision of the energy measurement can be achieved.

The first-principles calculations are compared to the measurement of the radiation energy with respect to the energy scale of the fluorescence detector (FD). We found that the first-principles calculations predict 19% larger cosmic-ray energies than given by the FD energy scale at energies around 1 EeV. The systematic uncertainty of the radio energy scale is 15% and is dominated by the detector calibration that contributes with 14%. Hence, the radio technique is well competitive to the fluorescence technique with its systematic uncertainty of 14% at energies above 10^{18} eV and 16% at energies of around 3×10^{17} eV. In particular, the difference in the energy scales is well compatible within the systematic uncertainties.

In the future, a significant improvement in the systematic uncertainty of the radio energy scale is expected. Using the results of a recently performed calibration campaign of the antenna response, the total systematic uncertainty can be reduced to 10%. With further improvements in the antenna calibration and more detailed first-principles calculations, a reduction of the uncertainty to 7% or below seems realistic. Hence, the radio technique together with the methods developed in this thesis can deliver unprecedented accuracy of the cosmic-ray energy scale. This will allow for a significant improvement in the interpretation of the results of the Pierre Auger Observatory.

Approximations in the calculation of the radiation energy

A.1 Approximation of the same phase between E_{geo} and E_{ce}

The validity of Eq. (3.11), which is based on the assumption that radio pulses originating from the geomagnetic and charge-excess components are in-phase, can be validated by inspecting simulated radio pulses at the $\phi = 45°$, $135°$, $225°$, $315°$ directions. At these positions the charge-excess signal splits up equally into the $E_{\vec{v}\times\vec{B}}$ and $E_{\vec{v}\times(\vec{v}\times\vec{B})}$ polarizations. Hence, we can determine $E_{ce}(t)$ from $E_{\vec{v}\times(\vec{v}\times\vec{B})}(t)$ and $E_{geo}(t)$ by subtracting $E_{ce}(t)$ from $E_{\vec{v}\times\vec{B}}(t)$:

$$E_{ce}(t) = \sin^{-1}\phi\, E_{\vec{v}\times(\vec{v}\times\vec{B})}(t) \tag{A.1}$$

$$E_{geo}(t) = E_{\vec{v}\times\vec{B}}(t) - \cos\phi\, E_{ce}(t) \overset{\phi=45°+n\cdot90°}{=} E_{\vec{v}\times\vec{B}}(t) - E_{\vec{v}\times(\vec{v}\times\vec{B})}(t)\,. \tag{A.2}$$

Then, we calculate $f_{\vec{v}\times\vec{B}}$ directly from $E_{\vec{v}\times\vec{B}}(t)$ and via Eq. (3.11) from $E_{geo}(t)$ and $E_{ce}(t)$. Fig. A.1 shows the difference for eight different simulated air showers (E = 0.5 EeV, zenith angle = 30°, 40°, 50°, 60°, azimuth angle = 180°, 270°). The distributions are centered around zero, the mean is slightly ($\sim$1%) shifted to negative differences, meaning that the approximation using Eq. (3.11) slightly overestimates the true energy density.

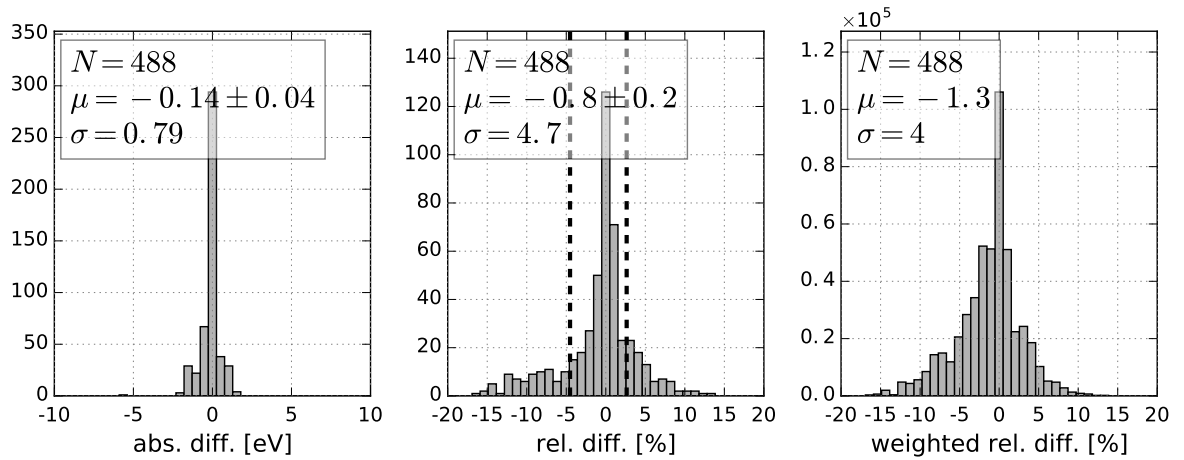**Figure A.1:** Difference between $f_{\vec{v}\times\vec{B}}$ calculated directly from $E_{\vec{v}\times\vec{B}}$ and $f_{\vec{v}\times\vec{B}}$ calculated via Eq. (3.11). The dashed lines show the 68% quantiles. The weight in the right histogram is $r \cdot f_{\vec{v}\times\vec{B}}$ with the distance r, i.e., it is weighted according to its influence on radiation energy.
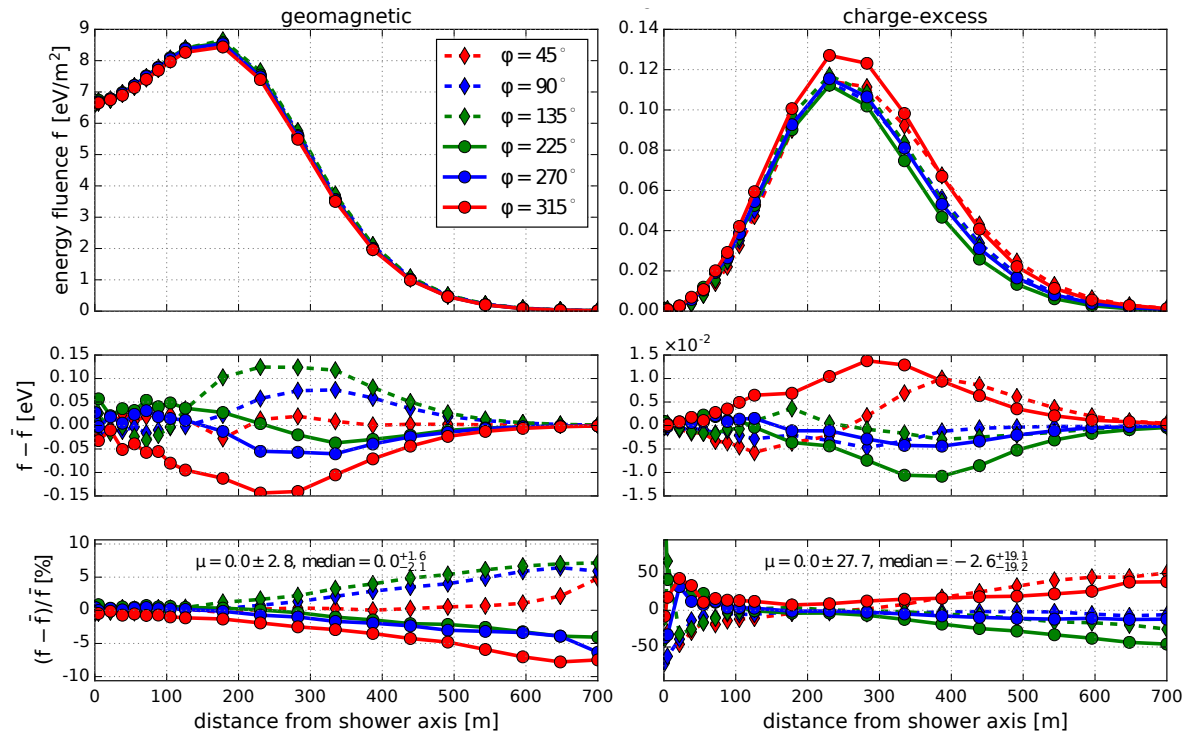
Figure A.2: Geomagnetic and charge-excess lateral signal distribution for six different azimuthal directions of an 0.5 EeV iron-induced air shower coming from the south with a zenith angle of $60°$. The lower plots show the absolute and relative deviation to the average LDF of the six azimuthal directions.

A.2 Approximation of radial symmetry of geomagnetic and charge-excess LDFs

The decomposition of the signal into the geomagnetic and charge-excess contribution of Eq. (A.2) can be used to check for the radial symmetry of the geomagnetic and charge-excess LDFs. Fig. A.2 shows the energy density versus the distance to the shower axis for the geomagnetic and charge-excess part for different azimuthal directions ϕ (cf. Fig. 3.11). The geomagnetic LDF exhibits only slight deviations from a radially symmetric LDF. The 68% quantile of the relative deviation is below 2%.

The relative deviations of the charge-excess LDF for different azimuthal directions are larger than for the geomagnetic LDF. The 68% quantiles vary between 12% and 20%. However, on an absolute scale the deviations are smaller than for the geomagnetic LDF. This could mean that the observed deviations, or at least a large part of them, are due to random fluctuations in the simulations. Even if there were a deviation from a radially symmetric charge-excess LDF it would have negligible influence on the total radiation energy. Only if the radiation energy of the charge-excess component is investigated on its own, could this introduce additional uncertainty.

B

Module sequence for resampling of air-shower simulations

Listing B.1: Example module sequence for the resampling of air shower simulations.

```
<loop numTimes="unbounded">
    <module>EventFileReaderOG</module>
    <!-- specify how often the shower should be resampled
    Note that in the first iteration  the event is not modified.
    numTimes=3 means the original event + 2 resampled events -->
    <loop numTimes="500" pushEventToStack="yes">
      <module>RdStationAssociator</module>

      <module>RdStationAzimuthResampler</module>

      <module>RdAntennaStationToChannelConverter</module>
      <module>RdChannelResponseIncorporator</module>
      <module>RdChannelResampler</module>
      <module>RdChannelTimeSeriesClipper</module>
      <module>RdChannelVoltageToADCConverter</module>

      <module>RdChannelNoiseASCIIImporter</module> <!-- import noise -->

      <module>RdEventInitializer</module>
      <module>RdChannelADCToVoltageConverter</module>
      <module>RdChannelSelector</module>
      <module>RdChannelPedestalRemover</module>
      <module>RdChannelResponseIncorporator</module>
      <module>RdChannelBandstopFilter</module>
      <module>RdChannelUpsampler</module>
      <module>RdPreWaveFitter</module>
      <loop numTimes="unbounded">
        <module>RdAntennaChannelToStationConverter</module>
        <module>RdStationSignalReconstructor</module>
          <module>RdDirectionConvergenceChecker</module>
        <module>RdWaveFit</module>
      </loop>
      <module> RdStationEFieldVectorCalculator</module>
      <module>RecDataWriterNG</module>
    </loop>
</loop>
```

Energy calibration

C.1 LDF parameters

Table C.1 gives the parameters used in the LDF function of Eq. (6.4).

Table C.1: Parameters C_0 - C_4 of Eq. (6.4). $C_3 = 16.25\,\mathrm{m}$ and $C_4 = 0.0079\,\mathrm{m}^{-1}$. The zenith-angle dependent values used to predict the emission pattern are given for zenith angle bins up to $60°$.

zenith angle	C_0	$C_1[\mathrm{m}]$	$C_2\,[\mathrm{m}]$
$0° - 10°$	0.41	-8.0 ± 0.3	21.2 ± 0.4
$10° - 20°$	0.41	-10.0 ± 0.4	23.1 ± 0.4
$20° - 30°$	0.41	-12.0 ± 0.3	25.5 ± 0.3
$30° - 40°$	0.41	-20.0 ± 0.4	32.0 ± 0.6
$40° - 50°$	0.46	-25.1 ± 0.9	34.5 ± 0.7
$50° - 60°$	0.71	-27.3 ± 1.0	9.8 ± 1.5

C.2 Likelihood function

In the following, the likelihood function used to determine the calibration function of Sec. 6.3 is derived.

If we had a perfect detector and there were no shower-to-shower fluctuations, the probability to measure an air shower with the energy E, incoming direction Θ, Φ and a radio signal S_{radio} would be given by

$$l_1(E, S, \Theta, \Phi) = \delta(S_{\mathrm{radio}} - S(E)) \cdot h(E, \Theta, \Phi), \tag{C.1}$$

where Θ and Φ is the zenith and azimuth angle, $h(E, \Theta, \Phi)$ is the event distribution, $S(E)$ is the calibration function and $\delta(...)$ the Dirac delta function.

As the detectors are not perfect and shower-to-shower fluctuations exist we need to convolve the PDF with the conditional PDFs $g_{Rd}(S_{\mathrm{radio}}|S, ...)$ and $g_{SD-sh}(E_{SD}|E, \Theta)$ which describe the probability to measure a radio signal S_{radio} or energy E_{SD} if the true radio signal and shower parameters are S, E and Θ. There is no analytic parametrization of the uncertainty of the radio energy estimator g_{Rd}. Therefore, for each event the uncertainty is determined in a Monte Carlo where all reconstructed parameters that influence the radio energy estimator are varied within their uncertainties. The uncertainty of the incoming direction is so small that it can be neglected.

The PDF l_1 needs to be folded with the conditional PDFs resulting in:

$$l_2(E_{SD}, S_{\text{radio}}, \Theta, \Phi) = \int\limits_0^\infty dE \int\limits_0^\infty dS\, g_{Rd}(S_{\text{radio}}|S, ...) \times g_{SD-sh}(E_{SD}|E, \Theta)$$
$$\times\, \delta(S - S(E)) \cdot h(E, \Theta, \Phi)\,. \tag{C.2}$$

Finally, the non 100% trigger and reconstruction efficiencies need to be taken into account by multiplying the PDF with the efficiency curves $\varepsilon_{SD}(E_{SD}, \Theta)$ and $\varepsilon_{Rd}(E_{SD}, \Theta, \Phi)$ resulting in

$$l_3(S_{\text{radio}}, E_{SD}, \Theta, \Phi) = \varepsilon_{SD}(E_{SD}, \Theta, \Phi) \times \varepsilon_{Rd}(E_{SD}, \Theta, \Phi)$$
$$\times \int\limits_0^\infty dE \int\limits_0^\infty dS\, g_{Rd}(S_{\text{radio}}|S, ...) \cdot g_{SD-sh}(E_{SD}|E, \Theta) \cdot \delta(S - S(E)) \cdot h(E, \Theta, \Phi)\,. \tag{C.3}$$

The event distribution can be determined directly from data using the bootstrap estimate

$$h(E, \Theta, \Phi) = \frac{1}{n} \sum_{i=1}^n \frac{\delta(E_{SD,i} - E) \cdot \delta(\Theta_i - \Theta) \cdot \delta(\Phi_i - \Phi)}{\varepsilon_{SD}(E_{SD,i}, \Theta_i, \Phi_i) \cdot \varepsilon_{Rd}(E_{SD,i}, \Theta_i, \Phi_i)}\,, \tag{C.4}$$

where the index i runs over all events n.

Inserting the event distribution in l_3 and adding an integral over Θ and Φ to remove the dependency on the incoming direction results in the likelihood function (for one pair of radio signal S_{radio} and SD cosmic-ray energy estimate E_{SD}) of

$$l(S_{\text{radio}}, E_{\text{SD}}) = \frac{1}{N} \sum_i \frac{\varepsilon_{\text{SD}}(E_{SD}, \Theta_i)\, \varepsilon_{\text{RD}}(E_{SD}, \Theta_i, \Phi_i)}{\varepsilon_{\text{SD}}(E_{SD,i}, \Theta_i)\, \varepsilon_{\text{RD}}(E_{SD,i}, \Theta_i, \Phi_i)}$$
$$\times\, g_{\text{RD}}(S_{\text{radio}}|S(E_{SD,i}), ...)$$
$$\times\, g_{\text{SD}-\text{sh}}(E_{\text{SD}}|E_{SD,i}, \Theta_i) \tag{C.5}$$

with

$$N = \int\limits_0^\infty dE_{SD} \int\limits_0^\infty dS_{\text{radio}}\, l(S_{\text{radio}}, E_{SD})\,. \tag{C.6}$$

The summation is performed over all events in the selected data set. $g_{\text{RD}}(S_{\text{radio}}|S, ...)$ and $g_{\text{SD}-\text{sh}}(E_{\text{SD}}|E, \Theta)$ are the conditional probability density functions, which describe the probability to measure a radio signal S_{radio} or energy E_{SD} if the true radio signal, energy and zenith angle are S, E and Θ. Φ denotes the azimuth angle. $g_{\text{RD}}(S_{\text{radio}})$ is obtained for each event in a Monte Carlo simulation where all reconstructed parameters that influence the radio-energy estimator are varied within their uncertainties. $\varepsilon_{\text{SD}}(E_{\text{SD}}, \Theta)$ and $\varepsilon_{\text{RD}}(E_{\text{SD}}, \Theta, \Phi)$ are the efficiencies of the surface and the radio detector. The radio efficiency has been determined with Monte Carlo air-shower simulations and a full-detector simulation and depends on the energy, the zenith and the azimuth angle. N is the normalization of the function to an integral of one.

C.3   Calculation of combined energy resolution from the likelihood probability model

The energy resolution histogram (cf. Fig. 6.4) can be predicted from the PDF $g(R)$ of the ratio

$$R = 2\frac{E_{\mathrm{SD}} - E_{\mathrm{RD}}(S_{\mathrm{radio}})}{E_{\mathrm{SD}} + E_{\mathrm{RD}}(S_{\mathrm{radio}})}\,. \tag{C.7}$$

The number of entries in one ΔR bin is given by

$$N = \int_{R_1}^{R_2} g(R)\mathrm{d}R\,. \tag{C.8}$$

To calculate $g(R)$ lets first consider the following theorem. Let X and Y be two random variables with a bijective function $u(x) = y$ that is continuously differentiable and has a continuously differentiable inverse function $u^{-1}(y)$. Then the probability density transforms as follows [264]:

$$f^Y(y) = f^X(u^{-1}(y))\left|\frac{du^{-1}(y)}{dy}\right|\,. \tag{C.9}$$

In our case, with $y \equiv R$, $x \equiv S_{\mathrm{radio}}$ and $u^{-1}(y) \equiv S_{\mathrm{radio}}(R)$, this means

$$g(R) = l(S_{\mathrm{radio}}(R))\left|\frac{dS_{\mathrm{radio}}(R)}{dR}\right|\,. \tag{C.10}$$

We start with Eq. (C.8) for an infinitesimal small bin dR. For a fixed SD energy we have:

$$dN = g(R)dR \tag{C.11}$$

$$= l(S_{\mathrm{radio}}(R))\left|\frac{dS_{\mathrm{radio}}(R)}{dR}\right|dR\,. \tag{C.12}$$

For a fixed SD energy, $l(S_{\mathrm{radio}})$ is known and corresponds to $l(S_{\mathrm{radio}}, E_{\mathrm{SD}})$ of Eq. (C.3). As the energy distribution of the measured events is encoded in $l(S_{\mathrm{radio}}, E_{\mathrm{SD}})$, it is taken into account by integrating over E_{SD}:

$$\Rightarrow dN = \int dE_{\mathrm{SD}}\, l(S_{\mathrm{radio}}(R), E_{\mathrm{SD}})\left|\frac{dS_{\mathrm{radio}}(R)}{dR}\right|dR\,. \tag{C.13}$$

Now lets calculate the differential $\left|\frac{dS_{\mathrm{radio}}(R)}{dR}\right|$. Solving Eq. (C.7) for E_{RD} yields

$$E_{\mathrm{RD}}(R) = E_{\mathrm{SD}}\frac{(2 - R)}{2 + R} \tag{C.14}$$

which is inserted into the calibration function

$$S_{\text{radio}} = A \times 10^7 \, \text{eV} \left(\frac{E_{\text{RD}}}{10^{18} \, \text{eV}} \right)^B \tag{C.15}$$

$$= A \times 10^7 \, \text{eV} \left(\frac{E_{\text{SD}}}{10^{18} \, \text{eV}} \frac{2 - R}{2 + R} \right)^B . \tag{C.16}$$

Its derivative is given by

$$\frac{dS_{\text{radio}}}{dR} = 4 \times 10^7 \, \text{eV} \left(\frac{E_{\text{SD}}}{10^{18} \, \text{eV}} \right)^B \left(\frac{2 - R}{2 + R} \right)^B \frac{AB}{R^2 - 4} . \tag{C.17}$$

Inserting Eq. (C.16) and (C.17) in Eq. (C.13), the expected PDF for the energy resolution histogram can be calculated.

C.4 Energy resolution of AERA

The combined energy resolution of SD and AERA (RD) can be determined from the scatter around the calibration curve (cf. Fig. 6.4). To obtain the RD energy resolution, the SD resolution needs to be subtracted from the combined scatter. How the two individual resolution add up to the combined scatter depends on the correlation between the reconstructed SD and RD cosmic-ray energies for the same true cosmic-ray energy which is investigated in this section.

As a first step, $10,000$ cosmic-ray energies were simulated uniformly distributed in the logarithm from $0.1 \, \text{EeV}$ to $10 \, \text{EeV}$. For SD a constant energy resolution of 18% was assumed which is the average uncertainty in our data set. The RD energy resolution was varied between 5% and 30%. To study the impact of different correlation coefficients ρ between the SD and RD reconstructed energies we vary ρ between 0 and -0.5. For each simulated energy, the corresponding SD and RD energies were smeared using a two-dimensional normal distribution according to the individual uncertainties and their correlation.

For each generated data pair $(E_{\text{SD}}, E_{\text{RD}})$ the relative difference

$$\frac{E_{\text{SD}} - E_{\text{RD}}}{0.5(E_{\text{SD}} + E_{\text{RD}})} \tag{C.18}$$

is filled into a histogram and the standard deviation of this histogram is the combined scatter σ_{tot}. The result is shown in Fig. C.1 as blue dots and lines. The red line shows the estimated combined uncertainty using the formula $\sigma_{\text{tot}}^2 = \sigma_{\text{SD}}^2 + \sigma_{\text{RD}}^2$. This shows that the combined scatter σ_{tot} is slightly underestimated with the quadratic sum of the individual uncertainties. Turning the argument around, for a combined scatter of, e.g., 29% the correct radio uncertainty (for $\sigma_{\text{SD}} = 0.18$ and $\rho = 0$) is 22% and not 23%.

The other thing that can be learned from this figure is that the radio energy resolution indeed decreases for increasing negative correlations between the reconstructed SD and RD energies for the same true cosmic-ray energy. For a negative correlation of $\rho = -0.5$, $\sigma_{\text{tot}} = 29\%$ and $\sigma_{\text{SD}} = 18\%$, the RD energy resolution would only be 15%.

In the following, this MC study is made more realistic by taking the same number of events and
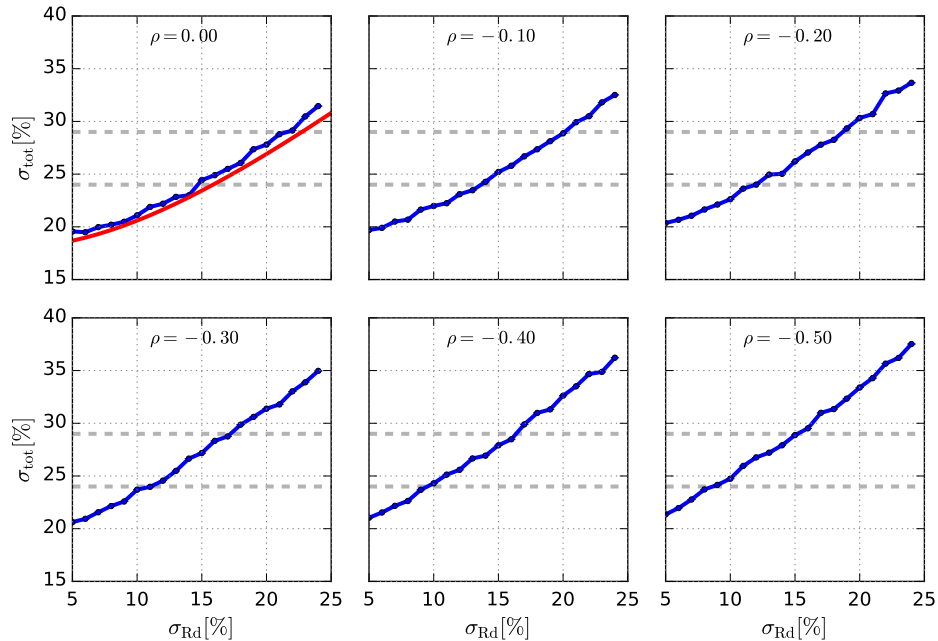
Figure C.1: The blue line shows the combined spread computed from Eq. (C.18) as a function of RD energy resolution for a fixed SD energy resolution of 18% and different correlation coefficients ρ. The red line shows an estimate of the combined spread if the energy resolutions of SD and RD are added in quadrature.

energy distribution as in the AERA24 data set used in the energy calibration of Sec. 6.3. In addition, the SD energy resolution is not constant but depends on the energy itself and on the zenith angle which we take into account in the following. One MC realization of the 126 events can be seen in Fig. C.2. To determine the significance of the estimated RD energy resolution, the analysis is repeated 50 times. The result is shown in Fig. C.3. Assuming zero correlation between both reconstructed energies, one reads off a RD energy resolution of 22% (for the full data set with $\sigma_{\text{tot}} = 0.29$). From the size of the errorbars, also the statistical significance of the RD energy resolution can be extracted. With a probability of 68%, the RD energy resolution is between 20% - 24%. If a correlation of $\rho = -0.3$ is assumed the RD uncertainty would only be 18%.

The analysis is repeated for the high quality data set containing only 47 events. Due to the smaller statistics the spread of different MC realizations get larger. To get a good estimate of the mean and spread, 200 MC realizations are generated. The result shown in Fig. C.4. For the high quality data set with $\sigma_{\text{tot}} = 24\%$, the corresponding RD resolution is 17% and can vary between 13% and 21%. For a correlation of $\rho = -0.3$ the RD resolution would decrease to below 13%.
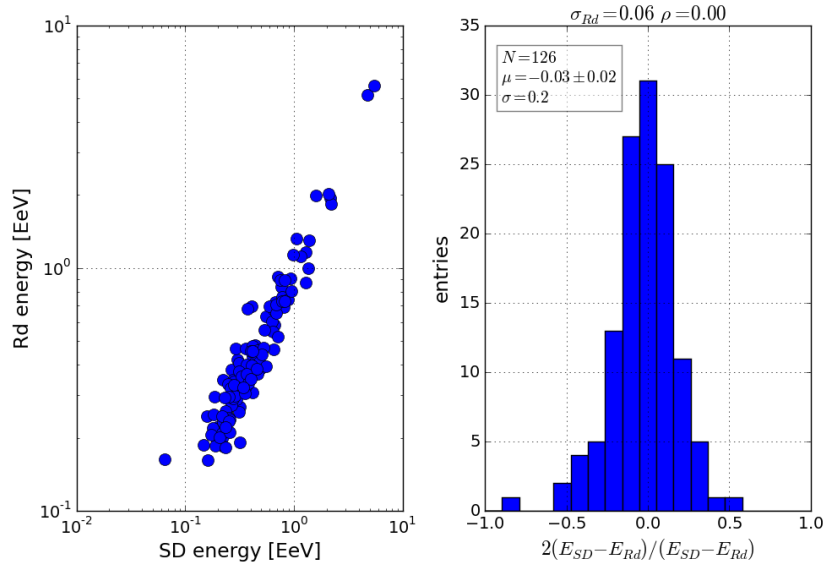
Figure C.2: Example of a MC realization for a fixed RD energy resolution of 6% and a correlation of $\rho = 0$. The SD energy uncertainty is calculated from the energy and zenith dependent parametrization.
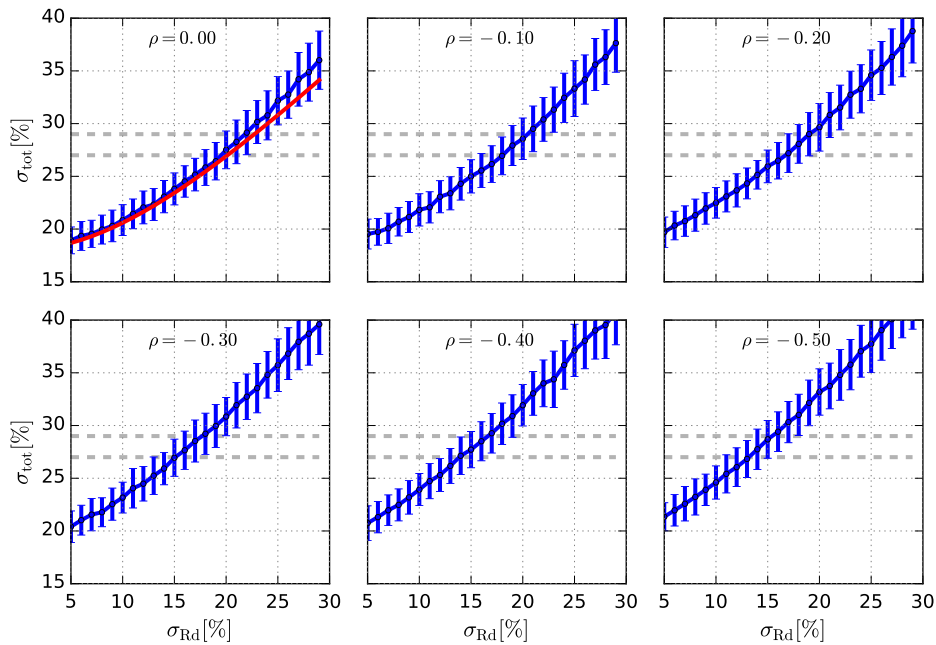
Figure C.3: MC for the 126 events of the AERA24 data set. The combined spread is plotted versus the RD energy resolution for different correlations. Blue markers are the mean of 50 MC realizations and the errorbar shows the spread (standard deviation) around the mean.

Figure C.4: MC for the 47 high-quality events of the AERA24 data set. The combined spread is plotted versus the RD energy resolution for different correlations. Blue markers are the mean of 200 MC realizations and the errorbar shows the spread (standard deviation) around the mean.

Modeling of atmospheric density profiles

The density profile of the Earth's atmosphere, i.e., the density as a function of height above sea level $\rho(h)$, is typically mo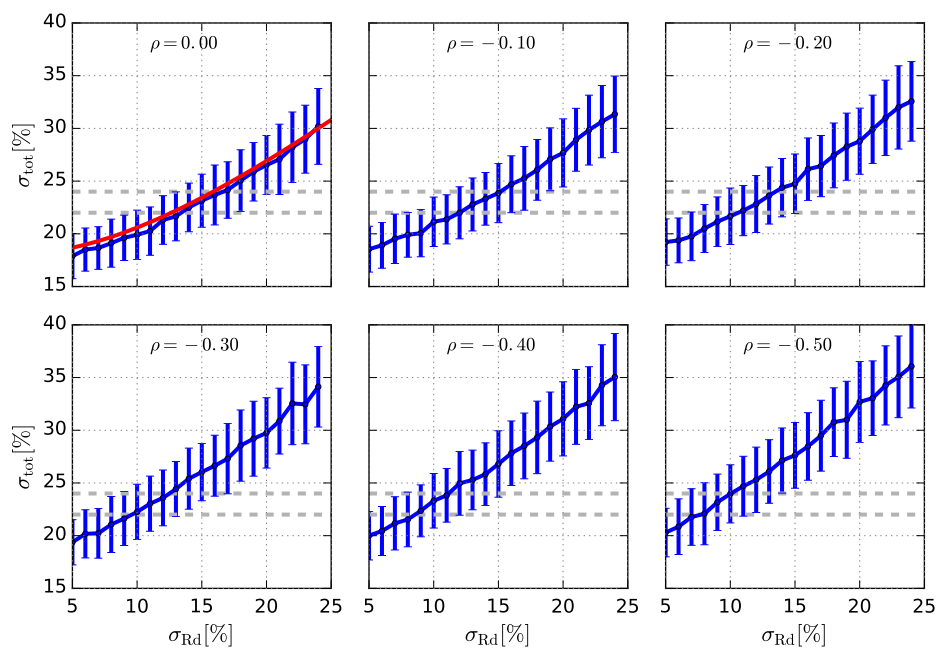deled by splitting up the atmosphere in different layers where the density profile of each layer is described by an exponential function except of the last (highest) layer which is modeled with a constant density. Above a typical height of $112.8\,\text{km}$ the atmosphere vanishes and the density is zero. The density profile is parametrized as

$$\rho(h) = \begin{cases} b_i/c_i e^{-h/c_i} & i \in [0,3] \\ b_4/c_4 & i = 4 \end{cases}, \tag{D.1}$$

where b_i and c_i are constants and h is the perpendicular height above sea level.

Different models of the atmosphere differ by the boundaries of the layers and the constants of the exponential function. Such a description of the atmosphere is available for different geographic locations. A common standard is the model of the US standard atmosphere [132] which is defined by the following parameters.

layer boundaries [km]	b in [g/cm^2]	c in [cm]
0 - 4	1222.66	994186.38
4 - 10	1144.91	878153.55
10 - 40	1305.59	636143.04
40 - 100	540.18	772170.16
100 - 112.8	1.	10^9

For the location of the Pierre Auger Observatory, monthly averaged profiles have been determined using data from weather balloon flights and GDAS [133, 167–169]. All these models are implemented in the air-shower simulation software CORSIKA and the definitions are given in the manual of the software [140].

For the analysis of air showers one is typically not interested in the density at a specific height but in the amount of atmosphere above a certain height. Also air showers have different incoming direction so that the quantity of interest is the amount of atmosphere along the path of the air shower. Expressed in mathematical formulas we are interested in the following relations:

- The amount of atmosphere above a certain height h along a shower path of zenith angle θ: $\mathbf{T}(\boldsymbol{\theta}, \mathbf{h})$
- The height that corresponds to a certain amount of atmosphere X along a shower path with zenith angle θ: $\mathbf{h}(\boldsymbol{\theta}, \mathbf{X})$

- The density at the position defined by the amount of atmosphere X along a shower path with zenith angle θ: $\boldsymbol{\rho}(\boldsymbol{\theta}, \mathbf{X}) = \boldsymbol{\rho}(\mathbf{h}(\boldsymbol{\theta}, \mathbf{X}))$
- The amount of atmosphere between ground ($h = h_0$) and the position of the shower maximum $X_{\max}$ (for a shower with zenith angle θ): $\mathbf{D}_{\mathbf{X}_{\max}}(\boldsymbol{\theta}, \mathbf{X}_{\max}) = \mathbf{T}(\boldsymbol{\theta}, \mathbf{h_0}) - \mathbf{X}_{\max}$
- The geometrical distance along the shower path (with zenith angle θ) between ground and the position of the shower maximum $X_{\max}$: $\mathbf{D}_{\mathbf{X}_{\max}}^{\mathrm{geo}}(\boldsymbol{\theta}, \mathbf{X}_{\max}) = \mathbf{l}(\mathbf{h}(\boldsymbol{\theta}, \mathbf{X}), \boldsymbol{\theta})$, where $l(h, \theta)$ converts the (vertical) height above ground to a distance along the shower path with zenith angle θ.

If the incoming direction of the air shower is not too horizontal, i.e., for zenith angles below $\sim 60°$, the curvature of the Earth can be neglected and the vertical height above ground h transforms to a distance along the shower path l as

$$l = h/\cos\theta, \tag{D.2}$$

where θ is the zenith angle of the air shower. Then $T(\theta, h)$ is given by

$$T(\theta, h) = \frac{1}{\cos\theta} T(h) = \frac{1}{\cos\theta} \int\limits_h^\infty \rho(h')\mathrm{d}h'. \tag{D.3}$$

The function $T(h)$ can be solved analytically and yields

$$T(h) = \int\limits_h^\infty \rho(h')\mathrm{d}h' = a_i + b_i \cdot e^{-h/c_i} \quad i = 0, ..., 3 \tag{D.4}$$

for the first four layers and

$$T(h) = \int\limits_h^\infty \rho(h')\mathrm{d}h' = a_4 + b_4 \cdot h/c_4 \tag{D.5}$$

for the last layer with constant density.

For horizontal air showers the curvature of the Earth (and the Earth's atmosphere) can no longer be neglected which is illustrated in the sketch shown in Fig. D.1. The relation between perpendicular height above ground h and distance along the shower path l takes the following form

$$h(l) = \sqrt{l^2 \sin^2\theta + (l\cos\theta + r_E)^2} - r_E \tag{D.6}$$

and

$$l(h) = \sqrt{r_E^2 \cos^2\theta + h^2 + 2rh} - r_E \cos\theta, \tag{D.7}$$

where r_E is the radius of the Earth.

The amount of atmosphere along a path l starting at l_1 is given by

$$T(\theta, h) = T(l) = \int\limits_{l_1}^\infty \rho(l)\mathrm{d}l = \int\limits_{h_1}^\infty \rho(h)\left|\frac{\mathrm{d}l}{\mathrm{d}h}\right|\mathrm{d}h, \tag{D.8}$$
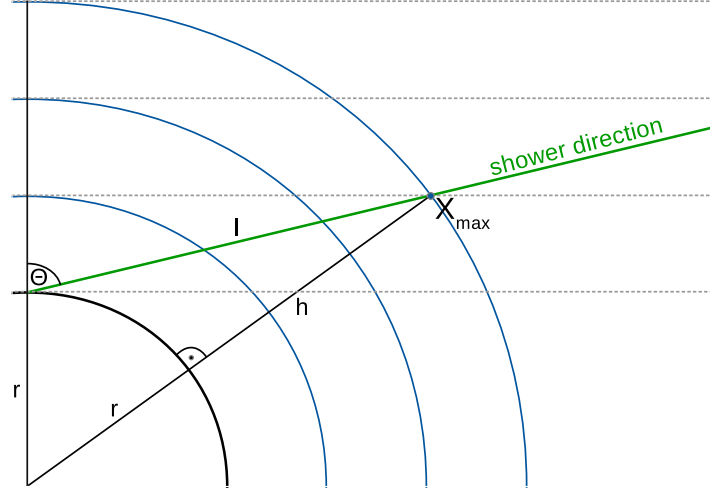
Figure D.1: Exaggerated sketch of a curved atmosphere. The blue lines indicate heights of same density. The dashed lines mark heights of same density for the approximation of a flat atmosphere.

where the Jacobian determinant $\left|\frac{\mathrm{d}l}{\mathrm{d}h}\right|$ for a curved atmosphere is given by

$$\frac{\mathrm{d}l(h)}{\mathrm{d}h} = \frac{h + r_E}{\sqrt{r_E^2 \cos^2 \theta + h^2 + 2hr_E}} \,. \tag{D.9}$$

Due to the complexity of this Jacobian determinant, no analytic solution for the integral of Eq. (D.8) exists. The integral can be solved numerically, however, with the downside slow performance. In particular the determination of the geometric distance to X_{max} is computationally expensive as the distance l is obtained via finding the root of the equation

$$\int_l^\infty \rho(l')\mathrm{d}l' - X_{\mathrm{max}} = 0 \,, \tag{D.10}$$

where in each iteration to find the root, the integral over the density needs to be solved numerically.

A practical solution to overcome this problem is to approximate the integral of Eq. (D.8) analytically. Therefore, we use a Taylor expansion of $\left|\frac{\mathrm{d}l}{\mathrm{d}h}\right|$ around the solution for a flat atmosphere, i.e., we substitute with $x = \frac{h}{r_E}$, which is zero in the limit of a flat atmosphere ($r_E \to \infty$)

$$\frac{\mathrm{d}l(h)}{\mathrm{d}h} = \frac{x + 1}{\sqrt{\cos^2 \theta + x^2 + x}} \,. \tag{D.11}$$

and expand around $x = 0$

$$\frac{\mathrm{d}l(h)}{\mathrm{d}h} = \frac{1}{\cos \theta} - \frac{\sin^2 \theta}{\cos^3 \theta} x + \frac{3}{2} \frac{\sin^2 \theta}{\cos^5 \theta} x^2 + \frac{1}{2} \frac{\sin^2 \theta (\cos^2 \theta - 5)}{\cos^7 \theta} x^3 + \mathcal{O}(x^4) \,. \tag{D.12}$$
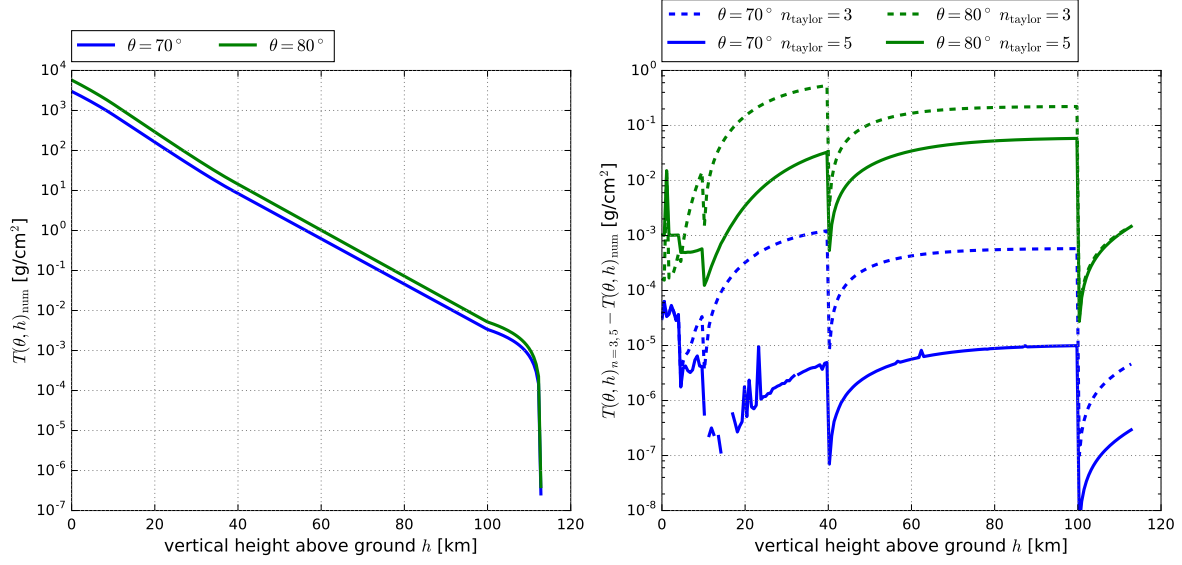
Figure D.2: (left) The amount of atmosphere above a certain height along the path of the air shower for two different zenith angles. (right) Comparison between the (exact) numerical result and the analytic approximation using a Taylor expansion until 5th order. The different colors represent different zenith angles. If a part of the line is not visible, the difference is below 10^{-8} g/cm^2.

Then, Eq. (D.8) can be solved analytically and gives

$$T(\theta, h) = \int \rho(l') \mathrm{d}l' = \int \rho(h') \left| \frac{\mathrm{d}l'}{\mathrm{d}h'} \right| \mathrm{d}h' \tag{D.13}$$

$$= a_i + b_i e^{-h_1/c_i} \left[\frac{1}{\cos\theta} - \frac{\sin^2\theta}{\cos^3\theta} \frac{c_i + h_1}{r_E} + \frac{3}{2} \frac{(2c^2 + 2ch + h^2)\sin^2\theta}{r_e^2 \cos^5\theta} + \mathcal{O}\left(\left(\frac{h}{r_e}\right)^3 \right) \right],$$

for heights within the first four layers and

$$T(\theta, h) = \int \rho(l') \mathrm{d}l' = \int \rho(h') \left| \frac{\mathrm{d}l'}{\mathrm{d}h'} \right| \mathrm{d}h' \tag{D.14}$$

$$= a_i - b_i \cdot h/c_i \left[\frac{1}{\cos\theta} - \frac{\sin^2\theta}{2\cos^3\theta} \frac{h}{r_E} + \frac{\sin^2\theta h^2}{2\cos^5\theta r_E^2} + \frac{\sin^2\theta(\cos^2\theta - 5)h^3}{8\cos^7\theta r_E^3} + \mathcal{O}\left(\left(\frac{h}{r_e}\right)^4 \right) \right],$$

for heights within the last layer.

The constants a_i need to be calculated once for each layer boundary and zenith angle via numerical integration. To achieve a good precision and to simultaneously reduce the number of zenith angles for which the constants a_i are calculated, we calculate the constants for 100 zenith angles equally spaced in $\cos\theta$ and interpolate between the zenith angles using cubic splines.

The precision of the approximation using a Taylor expansion until 5th order is presented in Fig. D.2. Even for large zenith angles of $80°$ the uncertainty in the analytic approximation of $T(\theta, h)$ is less than 0.1 g/cm^2.

To obtain the function $h(\theta, X)$ we solve

$$T(\theta, h)_{n=5} = X \tag{D.15}$$
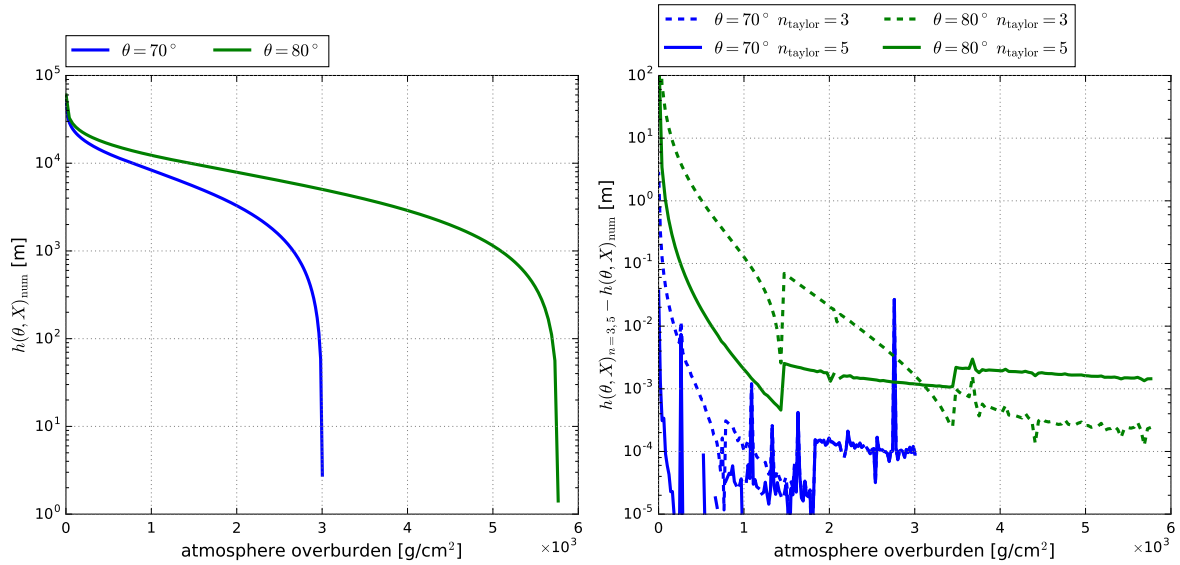
Figure D.3: (left) The height that corresponds to a certain amount of atmosphere above along the path of the air shower. (right) Comparison between the (exact) numerical result and the analytic approximation using a Taylor expansion until 5$^{\text{th}}$ order. The different colors represent different zenith angles. If a part of the line is not visible, the difference is below 10^{-6} m.

numerically for h, where $T(\theta, h)_{n=5}$ denotes the analytic approximation of $T(\theta, h)$ using a Taylor expansion until 5$^{\text{th}}$ order. The precision of this approximation is shown in Fig. D.3.

Using the formulas derived here, the atmosphere can be modeled mostly analytically and with high precision. Thereby, the curvature of the atmosphere is taken into account and the formulas also apply for horizontal air showers. These formulas are used in the analysis of Sec. 3.3.

Bibliography

[1] L. Evans and P. Bryant, „LHC Machine", J. Inst. **3**, 8001 (2008).

[2] A. Aab et al. (Pierre Auger Collaboration), „The Pierre Auger Cosmic Ray Observatory", Nucl. Instrum. Meth. A **798**, 172–213 (2015).

[3] V. Hess, „Über Beobachtungen der durchdringenden Strahlung bei sieben Freiballonfahrten", Phys. Zeitschriften **XIII**, 1084–1091 (1912).

[4] H. Kawai et al. (Telescope Array Collaboration), „Telescope Array Experiment", Nucl. Phys. B, Proc. Suppl. **175-176**, 221–226 (2008).

[5] V. Prosin et al., „Tunka-133: results of 3 year operation", Nucl. Instrum. Meth. A **756**, 94–101 (2014).

[6] H. R. Allan, „Radio Emission From Extensive Air Showers", Prog. Elem. Part. Cosm. Ray Phys. **10**, edited by J. G. Wilson and S. A. Wouthuysen, 171–302 (1971).

[7] H. Falcke et al. (LOPES Collaboration), „Detection and imaging of atmospheric radio flashes from cosmic ray air showers", Nature **435**, 313–316 (2005).

[8] D. Ardouin et al. (Codalema Collaboration), „Radioelectric field features of extensive air showers observed with CODALEMA", Astropart. Phys. **26**, 341–350 (2006).

[9] W. Apel et al. (LOPES Collaboration), „Reconstruction of the energy and depth of maximum of cosmic-ray air showers from LOPES radio measurements", Phys. Rev. D **90**, 062001 (2014).

[10] D. Ardouin et al. (Codalema Collaboration), „Geomagnetic origin of the radio emission from cosmic ray induced air showers observed by CODALEMA", Astropart. Phys. **31**, 192–200 (2009).

[11] C. Glaser for the Pierre Auger Collaboration, „Results and perspectives of the Auger Engineering Radio Array", Proc. of ARENA 2016, Groningen, The Netherlands (2016), arXiv:1609.01513.

[12] A. Aab et al. (Pierre Auger Collaboration), „Probing the radio emission from air showers with polarization measurements", Phys. Rev. D **89**, 052002 (2014).

[13] M. P. van Haarlem et al., „LOFAR: The LOw-Frequency ARray", A&A **556**, A2 (2013).

[14] A. Nelles et al., „A parameterization for the radio emission of air showers as predicted by CoREAS simulations and applied to LOFAR measurements", Astropart. Phys. **60**, 13–24 (2015).

[15] A. Corstanje et al., „The shape of the radio wavefront of extensive air showers as measured with LOFAR", Astropart. Phys. **61**, 22–31 (2015).

[16] F. Gaté for the Pierre Auger Collaboration, „X_{max} reconstruction from amplitude information with aera", Proc. of ARENA 2016, Groningen, The Netherlands (2016), arXiv:1609.06510.

[17] S. Buitink et al., „Method for high precision reconstruction of air shower Xmax using two-dimensional radio intensity profiles", Phys. Rev. D **90**, 082003 (2014).

[18] S. Buitink et al., „A large light-mass component of cosmic rays at $10^{17} - 10^{17.5}$ electronvolts from radio observations", Nature **531**, 70–73 (2016).

[19] A. Nelles et al., „The radio emission pattern of air showers as measured with LOFAR – a tool for the reconstruction of the energy and the shower maximum", J. Cosmol. Astropart. Phys. 05(2015)018 .

[20] P. A. Bezyazeekov et al. (Tunka-Rex Collaboration), „Measurement of cosmic-ray air showers with the Tunka radio extension (Tunka-Rex)", Nucl. Instrum. Meth. A **802**, 89–96 (2015).

[21] D. Kostunin et al., „Reconstruction of air-shower parameters for large-scale radio detectors using the lateral distribution", Astropart. Phys. **74**, 79–86 (2016).

[22] T. Huege, „Radio detection of cosmic ray air showers in the digital era", Physics Reports **620**, 1–52 (2016).

[23] F. G. Schröder, „Radio detection of cosmic-ray air showers and high-energy neutrinos", to be published in Prog. Part. Nucl. Phys. (2016), arXiv:1607.08781.

[24] M. Motoki et al., „Precise measurements of atmospheric muon fluxes with the BESS spectrometer", Astropart. Phys. **19**, 113–126 (2003).

[25] M. Ave et al., „The TRACER instrument: a balloon-borne cosmic-ray detector", Nucl. Instrum. Meth. A **654**, 140–156 (2011).

[26] E. Seo et al. (CREAM Collaboration), „Cosmic-ray energetics and mass (CREAM) balloon project", Adv. Space Res. **33**, 1777–1785 (2004).

[27] W. R. Binns et al., „The SuperTIGER instrument: measurement of elemental abundances of ultra-heavy galactic cosmic rays", ApJ **788**, 18 (2014).

[28] M. Casolino and P. Picozza (PAMELA Collaboration), „The PAMELA experiment: A space-borne observatory for heliospheric phenomena", Adv. Sp. Res. **41**, 2043–2049 (2008).

[29] A. A. Abdo et al., „Measurement of the cosmic ray $e^+ + e^-$ spectrum from 20 GeV to 1 TeV with the Fermi Large Area Telescope", Phys. Rev. Lett. **102**, 181101 (2009).

[30] M. Aguilar et al., „First result from the alpha magnetic spectrometer on the international space station: precision measurement of the positron fraction in primary cosmic rays of 0.5–350 GeV", Phys. Rev. Lett. **110**, 141102 (2013).

[31] E. Seo et al., „Cosmic ray energetics and mass for the international space station (ISS-CREAM)", Adv. Space Res. **53**, 1451–1455 (2014).

[32] K. Olive et al. (Particle Data Group), „Review of particle physics", Chinese Phys. C **38**, and 2015 update, 090001 (2014).

[33] J. J. Engelmann, P. Ferrando, A. Soutoul, P. Goret, and E. Juliusson, „Charge composition and energy spectra of cosmic-ray nuclei for elements from Be to NI - Results from HEAO-3-C2", A&A **233**, 96–111 (1990).

[34] D. Mueller, S. P. Swordy, P. Meyer, J. L'Heureux, and J. M. Grunsfeld, „Energy spectra and composition of primary cosmic rays", ApJ **374**, 356 (1991).

[35] K. Asakimori et al. (JACEE Collaboration), „Cosmic-ray proton and helium spectra: results from the JACEE experiment", ApJ **502**, 278–283 (1998).

[36] J. Alcaraz et al. (AMS Collaboration), „Cosmic protons", Phys. Lett. B **490**, 27–35 (2000).

[37] J. Alcaraz et al., „Helium in near earth orbit", Phys. Lett. B **494**, 193–202 (2000).

[38] T. Sanuki et al., „Precise measurement of cosmic-ray proton and helium spectra with the BESS spectrometer", ApJ **545**, 1135–1142 (2000).

[39] M. Boezio et al., „The cosmic-ray proton and helium spectra measured with the CAPRICE98 Balloon experiment", Astropart. Phys. **19**, 583–604 (2003).

[40] S. Haino et al., „Measurements of primary and atmospheric cosmic-ray spectra with the BESS-TeV spectrometer", Phys. Lett. B **594**, 35–46 (2004).

[41] V. A. Derbina et al., „Cosmic-ray spectra and composition in the energy range of 10-1000 TeV per particle obtained by the RUNJOB experiment", ApJ **628**, L41–L44 (2005).

[42] F. Aharonian et al. (HESS Collaboration), „First ground-based measurement of atmospheric cherenkov light from cosmic rays", Phys. Rev. D **75**, 042004 (2007).

[43] A. D. Panov et al., „Elemental energy spectra of cosmic rays from the data of the ATIC-2 experiment", Bulletin of the Russian Academy of Sciences: Physics **71**, 494–497 (2007).

[44] M. Ave et al., „Composition of primary cosmic-ray nuclei at high energies", ApJ **678**, 262–273 (2008).

[45] H. S. Ahn et al., „Energy spectra of cosmic-ray nuclei at high energies", ApJ **707**, 593–603 (2009).

[46] T. Antoni et al. (KASCADE Collaboration), „The cosmic-ray experiment KASCADE“, Nucl. Instrum. Meth. A **513**, 490–510 (2003).

[47] G. Navarra et al., „KASCADE-grande: a large acceptance, high-resolution cosmic-ray detector up to 10^{18} eV“, Nucl. Instrum. Meth. A **518**, 207–209 (2004).

[48] T. Antoni et al. (KASCADE Collaboration), „KASCADE measurements of energy spectra for elemental groups of cosmic rays: Results and open problems“, Astropart. Phys. **24**, 1–25 (2005).

[49] I. Valiño et al. (Pierre Auger Collaboration), „The flux of ultra-high energy cosmic rays after ten years of operation of the Pierre Auger Observatory“, Proceedings of Science, 34th ICRC, The Hague, The Netherlands (2015).

[50] W. D. Apel et al. (KASCADE-Grande Collaboration), „Kneelike structure in the spectrum of the heavy component of cosmic rays observed with KASCADE-Grande“, Phys. Rev. Lett. **107**, 171104 (2011).

[51] N. Grigorov et al., Sov. J. Nucl. Phys. **11**, 588–94 (1970).

[52] N. Grigorov et al., Proc. Int. Conf. on Cosmic Rays, Hobart **1**, 1746–51 (1971).

[53] N. Grigorov et al., Proc. Int. Conf. on Cosmic Rays, Hobart **1**, 1752–9 (1971).

[54] T. V. Danilova et al., „The Energy Spectrum of the Primary Cosmic Rays in the Range 10^{13} - 10^{16} eV“, International Cosmic Ray Conference **8**, 129 (1977).

[55] M. Nagano et al., „Energy spectrum of primary cosmic rays between $10^{14.5}$ and 10^{18} eV“, J. Phys. G: Nucl. Phys. **10**, 1295–1310 (1984).

[56] K. Asakimori and JACEE Collaboration, „Energy spectra and composition of cosmic rays above 1 TeV per nucleon.“, International Cosmic Ray Conference **2**, 57–60 (1991).

[57] K. Asakimori and JACEE Collaboration, „Energy spectra of protons and helium nuclei above 5 TeV/nucleon.“, International Cosmic Ray Conference **2**, 97–100 (1991).

[58] Y. A. Fomin et al., „Energy spectrum of cosmic rays at energies of 5 x 10^{15} - 5 x 10^{17} ev“, International Cosmic Ray Conference **2**, 85 (1991).

[59] M. Amenomori et al. (Tibet ASγ Collaboration), „The cosmic-ray energy spectrum between $10^{14.5}$ and $10^{16.3}$ eV covering the "knee" region“, ApJ **461**, 408 (1996).

[60] M. Glasmacher et al., „The cosmic ray composition between 10^{14} and 10^{16} eV“, Astropart. Phys. **12**, 1–17 (1999).

[61] F. Arqueros et al. (HEGRA Collaboration), „Energy spectrum and chemical composition of cosmic rays between 0.3 and 10 PeV determined from the cherenkov-light and charged-particle distributions in air showers“, A&A **359**, 682–694 (2000), arXiv:`astro-ph/9908202`.

[62] M. Amenomori et al. (Tibet ASγ Collaboration), „The all-particle spectrum of primary cosmic rays in the wide energy range from 10^{14} to 10^{17} eV observed with the tibet-III air-shower array“, ApJ **678**, 1165–1179 (2008).

[63] R. U. Abbasi et al. (HiRes Collaboration), „First observation of the Greisen-Zatsepin-Kuzmin suppression“, Phys. Rev. Lett. **100**, 101101 (2008).

[64] J. Abraham et al. (Pierre Auger Collaboration), „Observation of the suppression of the flux of cosmic rays above 4 x 10^{19} eV“, Phys. Rev. Lett. **101**, 061101 (2008).

[65] M. G. Aartsen et al. (IceCube Collaboration), „Measurement of the cosmic ray energy spectrum with IceTop-73“, Phys. Rev. D **88**, 042004 (2013).

[66] D. Ivanov et al. (Telescope Array Collaboration), „TA spectrum summary“, Proceedings of Science, 34th ICRC, The Hague, The Netherlands (2015).

[67] V. Verzi, „Cosmic rays: air showers from low to high energies“, Proceedings of Science, 34th ICRC, The Hague, The Netherlands (2015).

[68] V. Berezinsky, A. Gazizov, and S. Grigorieva, „On astrophysical solution to ultrahigh energy cosmic rays“, Phys. Rev. D **74**, 043005 (2006).

[69] M. Unger et al. (Telescope Array and Pierre Auger Collaboration), „Report of the working group on the composition of ultra-high energy cosmic rays", Proceedings of Science, 34th ICRC, The Hague, The Netherlands (2015).

[70] P. Abreu et al. (Pierre Auger Collaboration), „Interpretation of the depths of maximum of extensive air showers measured by the Pierre Auger Observatory", J. Cosmol. Astropart. Phys. 02(2013)026 .

[71] A.-J. Aahn for the Pierre Auger Collaboration, „Inferences about the mass composition of cosmic rays from data on the depth of maximum at the Auger Observatory", Proc. 33rd ICRC, Rio de Janeiro, Brazil (2013).

[72] A. Aab et al. (Pierre Auger Collaboration), „Depth of maximum of air-shower profiles at the Pierre Auger Observatory. I. measurements at energies above $10^{17.8}$ eV", Phys. Rev. D 90, 122005 (2014).

[73] A. Porcelli et al. (Pierre Auger Collaboration), „Measurements of X_{max} above 10^{17} eV with the fluorescence detector of the Pierre Auger Observatory", Proceedings of Science, 34th ICRC, The Hague, The Netherlands (2015).

[74] A. Aab et al. (Pierre Auger Collaboration), „Depth of maximum of air-shower profiles at the Pierre Auger Observatory. II. composition implications", Phys. Rev. D 90, 122006 (2014).

[75] J. Belz et al. (Telescope Array Collaboration), „Summary of UHECR composition measurements by the Telescope Array experiment", Proceedings of Science, 34th ICRC, The Hague, The Netherlands (2015).

[76] T. Pierog, I. Karpenko, J. M. Katzy, E. Yatsenko, and K. Werner, „EPOS LHC: test of collective hadronization with data measured at the CERN large hadron collider", Phys. Rev. C 92, 034906 (2015).

[77] A. Aab et al. (Pierre Auger Collaboration), „Muons in air showers at the Pierre Auger Observatory: mean number in highly inclined events", Phys. Rev. D 91, 032003 (2015).

[78] S. Ostapchenko, „QGSJET-II: towards reliable description of very high energy hadronic interactions", Nucl. Phys. B Proc. Suppl. 151, 143–146 (2006).

[79] S. A. Colgate, „Acceleration in astrophysics", Phys. Scr. T52, 96–105 (1994).

[80] E. Fermi, „On the Origin of the Cosmic Radiation", Phys. Rev. 75, 1169–1174 (1949).

[81] F. M. Rieger, V. Bosch-Ramon, and P. Duffy, „Fermi acceleration in astrophysical jets", Ap&SS 309, 119–125 (2007).

[82] T. Winchen, „The principal axes of the directional energy distribution of cosmic rays measured with the Pierre Auger Observatory", PhD thesis (RWTH Aachen University, 2013).

[83] A. M. Hillas, „The Origin of Ultra-High-Energy Cosmic Rays", Annu. Rev. Astron. Astrophys. 22, 425–444 (1984).

[84] K. Kotera and A. V. Olinto, „The astrophysics of ultrahigh-energy cosmic rays", ARA&A 49, 119–153 (2011).

[85] R. Durrer and A. Neronov, „Cosmological magnetic fields: their generation, evolution and observation", Astron. Astrophys. Rev. 21, 62 (2013).

[86] D. Walz, „Constraining models of the extragalactic cosmic-ray origin with the pierre auger observatory", PhD thesis (RWTH Aachen University, 2016).

[87] S. Hackstein, F. Vazza, M. Brüggen, G. Sigl, and A. Dundovic, „Propagation of ultrahigh energy cosmic rays in extragalactic magnetic fields: a view from cosmological simulations", Mon. Not. R. Astron. Soc. 462, 3660–3671 (2016).

[88] R. Beck and R. Wielebinski, „Magnetic fields in galaxies", 641–723 (2013).

[89] R. Jansson and G. R. Farrar, „A new model of the galactic magnetic field", ApJ 757, 14 (2012).

[90] R. Jansson and G. R. Farrar, „The galactic magnetic field", ApJ 761, L11 (2012).

[91] M. C. Beck et al., „New constraints on modelling the random magnetic field of the MW", J. Cosmol. Astropart. Phys. 05(2016)056 .

[92] M. Erdmann, G. Müller, M. Urban, and M. Wirtz, „The nuclear window to the extragalactic universe", Astropart. Phys. (2016) 10.1016/j.astropartphys.2016.10.002.

[93] J. W. Cronin, „Cosmic rays: the most energetic particles in the universe", Rev. Mod. Phys. **71**, 165–172 (1999).

[94] R. Adam et al. (Planck Collaboration), „Planck intermediate results. XLII. large-scale galactic magnetic fields", A&A (2016) 10.1051/0004-6361/201528033.

[95] K. Greisen, „End to the cosmic ray spectrum?", Phys. Rev. Lett. **16**, 748–750 (1966).

[96] G. Zatsepin and V. Kuzmin, „Upper Limit of the Spectrum of Cosmic Rays", JETP Lett. **4**, 78–80 (1966).

[97] P. Abreu et al. (Pierre Auger Collaboration), „Anisotropy and chemical composition of ultra-high energy cosmic rays using arrival directions measured by the Pierre Auger Observatory", J. Cosmol. Astropart. Phys. 06(2011)022 .

[98] R. U. Abbasi et al. (Telescope Array Collaboration), „Indications of intermediate-scale anisotropy of cosmic rays with energy greater than 57 EeV in the northern sky measured with the surface detector of the Telescope Array experiment", ApJ **790**, L21 (2014).

[99] K. Kawata for the Telescope Array Collaboration, „Ultra-high-energy cosmic-ray hotspot observed with the Telescope Array surface detectors", Proceedings of Science, 34th ICRC, The Hague, The Netherlands (2015).

[100] J. Aublin for the Pierre Auger Collaboration, „Arrival directions of the highest-energy cosmic rays detected with the Pierre Auger Observatory", Proceedings of Science, 34th ICRC, The Hague, The Netherlands (2015).

[101] M.-P. Véron-Cetty and P. Véron, „A catalogue of quasars and active nuclei: 12th edition", A&A **455**, 773–777 (2006).

[102] J. Abraham et al. (Pierre Auger Collaboration), „Correlation of the highest-energy cosmic rays with nearby extragalactic objects", Science **318**, 938–943 (2007).

[103] P. L. Ghia et al. (Pierre Auger Collaboration), „Highlights from the Pierre Auger Observatory", Proceedings of Science, 34th ICRC, The Hague, The Netherlands (2015).

[104] A. Aab et al. (Pierre Auger Collaboration), „Large scale distribution of ultra high energy cosmic rays detected at the Pierre Auger Observatory with zenith angles up to 80°", ApJ **802**, 111.

[105] I. Al Samarai for the Pierre Auger Collaboration, „Indications of anisotropy at large angular scales in the arrival directions of cosmic rays detected at the Pierre Auger Observatory", Proceedings of Science, 34th ICRC, The Hague, The Netherlands (2015).

[106] A. Aab et al. (Pierre Auger and Telescope Array Collaborations), „Searches for large-scale anisotropy in the arrival directions of cosmic rays detected above energy of 10^{19} eV at the Pierre Auger Observatory and the Telescope Array", ApJ **794**, 172 (2014).

[107] O. Deligny for the Pierre Auger and Telescope Array Collaborations, „Large-scale distribution of arrival directions of cosmic rays detected at the Pierre Auger Observatory and the Telescope Array", Proceedings of Science, 34th ICRC, The Hague, The Netherlands (2015).

[108] C. Glaser, M. Erdmann, J. R. Hörandel, T. Huege, and J. Schulz, „Simulation of radiation energy release in air showers", J. Cosmol. Astropart. Phys. 09(2016)024 .

[109] C. Glaser, M. Erdmann, J. R. Hörandel, T. Huege, and J. Schulz, „Simulation of the radiation energy release in air showers", Proc. of ARENA 2016, Groningen, The Netherlands (2016), arXiv:1609.05743.

[110] R. Engel, D. Heck, and T. Pierog, „Extensive air showers and hadronic interactions at high energy", Ann. Rev. Nucl. Part. S. **61**, 467–489 (2011).

[111] P. K. F. Grieder, *Extensive Air Showers - High Energy Phenomena and Astrophysical Aspects*, Vol. 1 (Springer, 2010).

[112] J. Matthews, „A Heitler model of extensive air showers", Astropart. Phys. **22**, 387–397 (2005).

[113] W. Heitler, *Quantum theory of radiation*, 2nd edition (Oxford Univ. Press., 1944).

[114] J. F. Carlson and J. R. Oppenheimer, „On multiplicative showers", Phys. Rev. **51**, 220–231 (1937).

[115] J. Schulz, „Cosmic radiation - reconstruction of cosmic-ray properties from radio emission of extensive air showers", PhD thesis (Radboud University Nijmegen, 2016).

[116] T. K. Gaisser, *Cosmic rays and particle physics* (Cambridge University Press, 1990).

[117] M. Tueros for the Pierre Auger Collaboration, „Estimate of the non-calorimetric energy of showers observed with the fluorescence and surface detectors of the Pierre Auger Observatory", Proc. 33rd ICRC, Rio de Janeiro, Brazil (2013), arXiv:1307.5059.

[118] J. Schulz for the Pierre Auger Collaboration, „Status and prospects of the Auger Engineering Radio Array", Proceedings of Science, 34th ICRC, The Hague, The Netherlands (2015).

[119] J. Hörandel, „Radio detection of cosmic rays with LOFAR", Proceedings of Science, 34th ICRC, The Hague, The Netherlands (2015).

[120] F. D. Kahn and I. Lerche, „Radiation of cosmic ray air showers", Proc. R. Soc. Lon. Ser. A **289**, 206 (1966).

[121] P. Abreu et al. (Pierre Auger Collaboration), „Results of a self-triggered prototype system for radio-detection of extensive air showers at the Pierre Auger Observatory", J. Inst. **7**, P11023 (2012).

[122] G. A. Askaryan, „Excess negative charge of an electron-photon shower", Sov. Phys. JETP **14**, 441 (1962).

[123] J. H. Hough and J. R. Prescott, „Mechanisms for radio signals associated with extensive air showers", in Proceedings of the VI. interamerican seminar on cosmic rays, Vol. 2 (Universidad Mayor de San Andres, La Paz, Bolivia, 1970), p. 527.

[124] J. R. Prescott, J. H. Hough, and J. K. Pidcock, „Mechanism of radio emission from extensive air showers", Nature (London) Phys. Sci. **223**, 109–110 (1971).

[125] P. Schellart et al., „Polarized radio emission from extensive air showers measured with LOFAR", J. Cosmol. Astropart. Phys. 10(2014)014 .

[126] A. Aab et al. (Pierre Auger Collaboration), „Energy estimation of cosmic rays with the Engineering Radio Array of the Pierre Auger Observatory", Phys. Rev. D **93**, 122005 (2016).

[127] A. Nelles et al., „Measuring a cherenkov ring in the radio emission from air showers at 110-190MHz with LOFAR", Astropart. Phys. **65**, 11 (2015).

[128] K. Werner and O. Scholten, „Macroscopic treatment of radio emission from cosmic ray air showers based on shower simulations", Astropart. Phys. **29**, 393–411 (2008).

[129] M. Ludwig and T. Huege, „REAS3: Monte Carlo simulations of radio emission from cosmic ray air showers using an end-point formalism", Astropart. Phys. **34**, 438–446 (2011).

[130] J. Alvarez-Muñiz, W. R. Carvalho, and E. Zas, „Monte Carlo simulations of radio pulses in atmospheric showers using ZHAireS", Astropart. Phys. **35**, 325–341 (2012).

[131] W. Apel et al. (LOPES Collaboration), „The wavefront of the radio signal emitted by cosmic ray air showers", J. Cosmol. Astropart. Phys. 09(2014)025 .

[132] National Aeronautics and Space Administration (NASA), „US standard atmosphere 1976", NASA-TM-X-74335 (1976).

[133] P. Abreu et al. (Pierre Auger Collaboration), „Description of atmospheric conditions at the Pierre Auger Observatory using the Global Data Assimilation System (GDAS)", Astropart. Phys. **35**, 591–607 (2012).

[134] W. R. Nelson, Y. Namito, and D. W. O. Rogers, Report SLAC 265, Stanford Linear Accelerator Center (1985).

[135] T. Pierog, „Modelling hadronic interactions in cosmic ray Monte Carlo generators", EPJ Web of Conferences 99, edited by D. Berge, A. de Roeck, M. Mangano, and B. Pattison, 09002 (2015).

[136] S. Ostapchenko, „Monte Carlo treatment of hadronic interactions in enhanced pomeron scheme: QGSJET-II model", Phys. Rev. D 83, 014018 (2011).

[137] F. Riehn, R. Engel, A. Fedynitch, T. K. Gaisser, and T. Stanev, „A new version of the event generator Sibyll", Proceedings of Science, 34th ICRC, The Hague, The Netherlands (2015).

[138] G. Battistoni et al., „The FLUKA code: description and benchmarking", AIP Conf. Proc. 896, 31–49 (2007).

[139] M. Bleicher et al., „Relativistic hadron-hadron collisions in the ultra-relativistic quantum molecular dynamics model", J. Phys. G: Nucl. Part. Phys. 25, 1859–1896 (1999).

[140] D. Heck, G. Schatz, T. Thouw, J. Knapp, and J. Capdevielle, „CORSIKA: A Monte Carlo code to simulate extensive air showers", Report FZKA 6019 (1998).

[141] S. J. Sciutto, *AIRES, a system for air shower simulation and analysis*, (2002) http://www2.fisica.unlp.edu.ar/aires.

[142] A. Hillas, „Shower simulation: lessons from MOCCA", Nucl. Phys. B Proc. Suppl. 52, 29–42 (1997).

[143] M. Kobal et al. (Pierre Auger Collaboration), „A thinning method using weight limitation for air-shower simulations", Astropart. Phys. 15, 259–273 (2001).

[144] O. Scholten, K. Werner, and F. Rusydi, „A macroscopic description of coherent geo-magnetic radiation from cosmic-ray air showers", Astropart. Phys. 29, 94–103 (2008).

[145] K. D. de Vries, A. M. van den Berg, O. Scholten, and K. Werner, „Coherent cherenkov radiation from cosmic-ray-induced air showers", Phys. Rev. Lett. 107, 061101 (2011).

[146] K. D. de Vries, O. Scholten, and K. Werner, „The air shower maximum probed by cherenkov effects from radio emission", Astropart. Phys. 45, 23–27 (2013).

[147] K. D. de Vries, O. Scholten, and K. Werner, „The EVA code, macroscopic modeling of radio emission from air showers based on full MC simulations including a realistic index of refraction", AIP Conf. Proc. 1535, Proc. of ARENA 2012, Erlangen, Germany, 133 (2013).

[148] K. Werner, K. D. de Vries, and O. Scholten, „A realistic treatment of geomagnetic cherenkov radiation from cosmic ray air showers", Astropart. Phys. 37, 5–16 (2012).

[149] J. D. Jackson, *Classical electrodynamics*, edited by 2nd (John Wiley & Sons, 1975).

[150] C. W. James, H. Falcke, T. Huege, and M. Ludwig, „General description of electromagnetic radiation processes based on instantaneous charge acceleration in endpoints", Phys. Rev. E 84, 056602 (2011).

[151] E. Zas, F. Halzen, and T. Stanev, „Electromagnetic pulses from high-energy showers: implications for neutrino detection", Phys. Rev. D 45, 362–376 (1992).

[152] J. Alvarez-Muñiz, A. Romero-Wolf, and E. Zas, „Cerenkov radio pulses from electromagnetic showers in the time domain", Phys. Rev. D 81, 123009 (2010).

[153] N. N. Kalmykov, A. A. Konstantinov, and R. Engel, „Radio emission from extensive air showers as a method for cosmic-ray detection", Physics of Atomic Nuclei 73, 1191–1202 (2010).

[154] K. Belov, „Radio emission from air showers. comparison of theoretical approaches", AIP Conf. Proc. 1535, Proc. of ARENA 2012, Erlangen, Germany, 157–161 (2013).

[155] J. Alvarez-Muñiz, W. R. Carvalho, M. Tueros, and E. Zas, „Coherent cherenkov radio pulses from hadronic showers up to EeV energies", Astropart. Phys. 35, 287–299 (2012).

[156] T. Huege, M. Ludwig, and C. W. James, „Simulating radio emission from air showers with CoREAS", AIP Conf. Proc. 1535, Proc. of ARENA 2012, Erlangen, Germany, 128–132 (2013).

[157]   K. Belov et al., „Accelerator measurements of magnetically induced radio emission from parti-
        cle cascades with applications to cosmic-ray air showers", Phys. Rev. Lett. **116**, 141103 (2016).

[158]   P. Gorham et al., „The Antarctic Impulsive Transient Antenna ultra-high energy neutrino de-
        tector: design, performance, and sensitivity for the 2006-2007 balloon flight", Astropart. Phys.
        32, 10–41 (2009).

[159]   M. Risse and D. Heck, „Energy release in air showers", Astropart. Phys. **20**, 661 (2004).

[160]   C. Glaser for the Pierre Auger Collaboration, „The energy content of extensive air showers in
        the radio frequency range of 30-80 MHz", Proceedings of Science, 34th ICRC, The Hague,
        The Netherlands (2015).

[161]   A. Aab et al. (Pierre Auger Collaboration), „Measurement of the radiation energy in the radio
        signal of extensive air showers as a universal estimator of cosmic-ray energy", Phys. Rev. Lett.
        116, 241101 (2016).

[162]   K. D. de Vries, A. M. van den Berg, O. Scholten, and K. Werner, „The lateral distribution
        function of coherent radio emission from extensive air showers determining the chemical com-
        position of cosmic rays", Astropart. Phys. **34**, 267–273 (2010).

[163]   J. Alvarez-Muñiz, W. R. Carvalho, H. Schoorlemmer, and E. Zas, „Radio pulses from ultra-
        high energy atmospheric showers as the superposition of Askaryan and geomagnetic mecha-
        nisms", Astropart. Phys. **59**, 29–38 (2014).

[164]   T. K. Gaisser and A. M. Hillas, „Reliability of the method of constant intensity cuts for recon-
        structing the average development of vertical showers", Proc. of 15th Int. Cosmic Ray Conf.
        in Plovdiv, Bulgaria **8**, 353 (1977).

[165]   M. de Domenico, M. Settimo, S. Riggi, and E. Bertin, „Reinterpreting the development of ex-
        tensive air showers initiated by nuclei and photons", J. Cosmol. Astropart. Phys. 07(2013)050
        .

[166]   T. N. G. Trinh et al., „Influence of atmospheric electric fields on the radio emission from
        extensive air showers", Phys. Rev. D **93**, 023003 (2016).

[167]   B. Keilhauer, M. Will, et al. (Pierre Auger Collaboration), „Description of atmospheric condi-
        tions at the Pierre Auger Observatory using meteorological measurements and models", Eur.
        Phys. J. Plus **127**, 96 (2012).

[168]   P. Abreu et al. (Pierre Auger Collaboration), „The Rapid Atmospheric Monitoring System of
        the Pierre Auger Observatory", J. Inst. **7**, P09001 (2012).

[169]   M. Will, D. Heck, and B. Keilhauer, „Monthly average profiles for CORSIKA and offline
        based on data from the global data assimilation system (GDAS)", Internal note of the Pierre
        Auger Collaboration, GAP 2011-133, 2011.

[170]   M. Gottowik, „Systematic studies on radio emission of extensive air showers with coreas and
        zhaires simulations", MA thesis (Bergische Universität Wuppertal, 2016).

[171]   E.-J. Ahn, R. Engel, T. K. Gaisser, P. Lipari, and T. Stanev, „Cosmic ray interaction event
        generator SIBYLL 2.1", Phys. Rev. D **80**, 094003 (2009).

[172]   P. Abreu et al. (Pierre Auger Collaboration), „The exposure of the hybrid detector of the Pierre
        Auger Observatory", Astropart. Phys. **34**, 368–381 (2011).

[173]   H.-J. Mathes for the Pierre Auger Collaboration, „The HEAT telescopes of the Pierre Auger
        Observatory status and first data", Proc. 32nd ICRC, Beijing, China **3**, 761 (2011).

[174]   J. Abraham et al. (Pierre Auger Collaboration), „Trigger and aperture of the surface detector
        array of the Pierre Auger Observatory", Nucl. Instrum. Meth. A **613**, 29–39 (2010).

[175]   I. Mariş for the Pierre Auger Collaboration, „The AMiga infill detector of the Pierre Auger
        Observatory: performance and first data", Proc. 32nd ICRC, Beijing, China **1**, 267 (2011).

[176]   B. Wundheiler for the Pierre Auger Collaboration, „The AMIGA muon counters of the Pierre
        Auger Observatory: performance and studies of the lateral distribution function", Proceedings
        of Science, 34th ICRC, The Hague, The Netherlands (2015).

[177] R. Gaior for the Pierre Auger Collaboration, „Detection of cosmic rays using microwave radiation at the Pierre Auger Observatory", Proc. 33rd ICRC, Rio de Janeiro, Brazil (2013).

[178] P. Gorham et al., „Observations of microwave continuum emission from air shower plasmas", Phys. Rev. D **78**, 032007 (2008).

[179] E. Conti, G. Collazuol, and G. Sartori, „Experimental study of the microwave emission from electrons in air", Phys. Rev. D **90**, 071102 (2014).

[180] R. Šmída et al., „First experimental characterization of microwave emission from cosmic ray air showers", Phys. Rev. Lett. **113**, 221101 (2014).

[181] I. A. Samarai et al., „Molecular bremsstrahlung radiation at GHz frequencies in air", Phys. Rev. D **93**, 052004 (2016).

[182] J. Abraham et al. (Pierre Auger Collaboration), „Properties and performance of the prototype instrument for the Pierre Auger Observatory", Nucl. Instrum. Meth. A **523**, 50–95 (2004).

[183] M. de Oliveira, V. de Souza, H. Reis, and R. Sato, „Manufacturing the Schmidt corrector lens for the Pierre Auger Observatory", Nucl. Instrum. Meth. A **522**, 360–370 (2004).

[184] J. Abraham et al. (Pierre Auger Collaboration), „The fluorescence detector of the Pierre Auger Observatory", Nucl. Instrum. Meth. A **620**, 227–251 (2010).

[185] J. T. Brack et al., „Absolute calibration of a large-diameter light source", J. Inst. **8**, P05014 (2013).

[186] V. Verzi for the Pierre Auger Collaboration, „The energy scale of the Pierre Auger Observatory", Proc. 33rd ICRC, Rio de Janeiro, Brazil, 928 (2013).

[187] L. Tomankova, „Optical properties and calibration of the pierre auger fluorescence detector", PhD thesis (Karlsruhe Institute of Technology (KIT), 2016).

[188] F. Arqueros, J. R. Hörandel, and B. Keilhauer, „Air fluorescence relevant for cosmic-ray detection—summary of the 5th fluorescence workshop, El Escorial 2007", Nucl. Instrum. Meth. A **597**, 1–22 (2008).

[189] M. Giller, G. Wieczorek, A. Kacperczyk, H. Stojek, and W. Tkaczyk, „Energy spectra of electrons in the extensive air showers of ultra-high energy", J. Phys. G: Nucl. Part. Phys. **30**, 97–105 (2004).

[190] F. Nerling, J. Blümer, R. Engel, and M. Risse, „Universality of electron distributions in high-energy air showers—description of cherenkov light production", Astropart. Phys. **24**, 421–437 (2006).

[191] M. D. Roberts, „The role of atmospheric multiple scattering in the transmission of fluorescence light from extensive air showers", J. Phys. G: Nucl. Part. Phys. **31**, 1291–1301 (2005).

[192] J. Pekala, P. Homola, B. Wilczyńska, and H. Wilczyński, „Atmospheric multiple scattering of fluorescence and cherenkov light emitted by extensive air showers", Nucl. Instrum. Meth. A **605**, 388–398 (2009).

[193] M. Giller and A. Śmiałkowski, „An analytical approach to the multiply scattered light in the optical images of the extensive air showers of ultra-high energies", Astropart. Phys. **36**, 166–182 (2012).

[194] M. Ave et al. (Airfly Collaboration), „Spectrally resolved pressure dependence measurements of air fluorescence emission with AIRFLY", Nucl. Instrum. Meth. A **597**, 41–45 (2008).

[195] M. Ave et al. (Airfly Collaboration), „Precise measurement of the absolute fluorescence yield of the 337nm band in atmospheric gases", Astropart. Phys. **42**, 90–102 (2013).

[196] J. Rosado, F. Blanco, and F. Arqueros, „On the absolute value of the air-fluorescence yield", Astropart. Phys. **55**, 51–62 (2014).

[197] A. Aab et al. (Pierre Auger Collaboration), „Reconstruction of inclined air showers detected with the Pierre Auger Observatory", J. Cosmol. Astropart. Phys. 08(2014)019 .

[198]   J. Abraham et al. (Pierre Auger Collaboration), „Measurement of the energy spectrum of cosmic rays above 10^{18} eV using the Pierre Auger Observatory", Phys. Lett. B **685**, 239–246 (2010).

[199]   C. Bonifazi for the Pierre Auger Collaboration, „The angular resolution of the Pierre Auger Observatory", Nucl. Phys. B, Proc. Suppl. **190**, 20–25 (2009).

[200]   K. Kamata and J. Nishimura, „The lateral and the angular structure functions of electron showers", Prog. Theor. Phys. Supp. **6**, 93–155 (1958).

[201]   K. Greisen, „The extensive air showers", Progress in Cosmic Ray Physics **3**, 1 (1956).

[202]   D. Newton, J. Knapp, and A. Watson, „The optimum distance at which to determine the size of a giant air shower", Astropart. Phys. **26**, 414–419 (2007).

[203]   J. Hersil, I. Escobar, D. Scott, G. Clark, and S. Olbert, „Observations of extensive air showers near the maximum of their longitudinal development", Phys. Rev. Lett. **6**, 22–23 (1961).

[204]   A. Schulz, „Measurement of the energy spectrum and mass composition of ultra-high energy cosmic rays", PhD thesis (Karlsruher Institut für Technologie (KIT), 2016).

[205]   H. P. Dembinski, B. Kégl, I. C. Mariş, M. Roth, and D. Veberič, „A likelihood method to cross-calibrate air-shower detectors", Astropart. Phys. **73**, 44–51 (2016).

[206]   J. Abraham et al. (Pierre Auger Collaboration), „A study of the effect of molecular and aerosol conditions in the atmosphere on air fluorescence measurements at the Pierre Auger Observatory", Astropart. Phys. **33**, 108–129 (2010).

[207]   J. Abraham et al. (Pierre Auger Collaboration), „Atmospheric effects on extensive air showers observed with the Surface Detector of the Pierre Auger Observatory", Astropart. Phys. **32**, 89–99 (2009).

[208]   B. Keilhauer, J. Blümer, R. Engel, and H. Klages, „Altitude dependence of fluorescence light emission by extensive air showers", Nucl. Instrum. Meth. A **597**, 99–104 (2008).

[209]   M. Monasor, J. Vázquez, D. Garcıa-Pinto, and F. Arqueros, „The impact of the air-fluorescence yield on the reconstructed shower parameters of ultra-high energy cosmic rays", Astropart. Phys. **34**, 467–475 (2011).

[210]   B. Keilhauer et al., „Nitrogen fluorescence in air for observing extensive air showers", EPJ Web of Conferences **53**, 01010 (2013).

[211]   B. Fick et al., „The central laser facility at the Pierre Auger Observatory", J. Inst. **1**, P11003 (2006).

[212]   P. Abreu et al. (Pierre Auger Collaboration), „Techniques for measuring aerosol attenuation using the central laser facility at the Pierre Auger Observatory", J. Inst. **8**, P04009 (2013).

[213]   S. BenZvi et al., „Measurement of the aerosol phase function at the Pierre Auger Observatory", Astropart. Phys. **28**, 312–320 (2007).

[214]   J. Chirinos for the Pierre Auger Collaboration, „Cloud monitoring at the Pierre Auger Observatory", Proc. 33rd ICRC, Rio de Janeiro, Brazil (2013).

[215]   P. Abreu et al. (Pierre Auger Collaboration), „Identifying clouds over the Pierre Auger Observatory using infrared satellite data", Astropart. Phys. **50-52**, 92–101 (2013).

[216]   S. BenZvi et al., „The Lidar system of the Pierre Auger Observatory", Nucl. Instrum. Meth. A **574**, 171–184 (2007).

[217]   V. Rizi, A. Tonachini, M. Iarlori, and G. Visconti (Pierre Auger Collaboration), „Atmospheric monitoring with LIDARs at the Pierre Auger Observatory", Eur. Phys. J. Plus **127**, 92 (2012).

[218]   S. Argirò et al., „The Offline software framework of the Pierre Auger Observatory", Nucl. Instrum. Meth. A **580**, 1485–1496 (2007).

[219]   P. Abreu et al. (Pierre Auger Collaboration), „Advanced functionality for radio analysis in the Offline software framework of the Pierre Auger Observatory", Nucl. Instrum. Meth. A **635**, 92–102 (2011).

[220] S. Fliescher, „Antenna Devices and Measurement of Radio Emission from Cosmic Ray in-
duced Air Showers at the Pierre Auger Observatory", PhD thesis (RWTH Aachen University,
2011).

[221] K. Weidenhaupt, „Antenna calibration and energy measurement of ultra-high energy cosmic
rays with the Auger Engineering Radio Array", PhD thesis (RWTH Aachen University, 2014).

[222] K. Weidenhaupt, „LPDA-Antennas for Large Scale Radio Detection of Cosmic Rays at the
Pierre-Auger-Observatory", Diploma Thesis (2009).

[223] M. Stephan for the Pierre Auger Collaboration, „Antennas, Filters and Preamplifiers designed
for the Radio Detection of Ultra-High-Energy Cosmic Rays", Proc. Asia-Pacific Microw.
Conf. **TH3G-49** (2010).

[224] D. Charrier, „Antenna development for astroparticle and radioastronomy experiments", Nucl.
Instrum. Meth. A **662**, S142–S145 (2012).

[225] P. Abreu et al. (Pierre Auger Collaboration), „Antennas for the detection of radio emission
pulses from cosmic-ray induced air showers at the Pierre Auger Observatory", J. Inst. **7**,
P10011 (2012).

[226] J. Kelley for the Pierre Auger Collaboration, „Data acquisition, triggering, and filtering at the
Auger Engineering Radio Array", Nucl. Instrum. Meth. A **725**, Proc. Very Large Vol. Neutrino
Telesc. Work. 2011, Erlangen, Germany, 133–136 (2013).

[227] C. Rühle, „Entwicklung eines schnellen eingebetteten Systems zur Radiodetektion kosmischer
Strahlung", PhD thesis (Karlsruher Instituts für Technologie (KIT), 2014).

[228] C. Timmermans et al., „Description of the scintillator triggered AERA-II stations", GAP 2013-
074, Internal note of the Pierre Auger Observatory, 2013.

[229] A. M. van den Berg, D. M. Varnav, and G. Zarza, „Fiber communication system for the Auger
Engineering Radio Array at the Southern Auger Observatory", GAP-2011-035, Internal note
of the Pierre Auger Observatory, 2011.

[230] R. Krause for the Pierre Auger Collaboration, „Detection of ultrahigh-energy cosmic rays with
the Auger Engineering Radio Array", Nucl. Instrum. Meth. A, Proc. 14th, Vienna Conference
on Instrumentation (VCI), Vienna, Austria (2016) 10.1016/j.nima.2016.06.048.

[231] F. Briechle for the Pierre Auger Collaboration, „In-situ absolute calibration of electric-field
amplitude measurements with the radio detector stations of the Pierre Auger Observatory",
Proc. of ARENA 2016, Groningen, The Netherlands (2016), arXiv:1609.01511.

[232] „RSG1000 signal generator", www.teseq.de/produkte/RSG-1000.php.

[233] F. Briechle, „Octocopter position reconstruction for calibrating the Auger Engineering Radio
Array", MA thesis (RWTH Aachen University, 2015).

[234] A. Aab et al. (Pierre Auger Collaboration), „Calibration of the LPDA radio stations at the
Pierre Auger Observatory using an octocopter", in preparation.

[235] R. Krause, PhD thesis (in preparation, RWTH Aachen University, 2017).

[236] A. Aab et al. (Pierre Auger Collaboration), „Nanosecond-level time synchronization of au-
tonomous radio detector stations for extensive air showers", J. Inst. **11**, P01018 (2016).

[237] J. Kelley and C. Timmermans, „Trigger and Filter Settings for Cosmic Ray Self-Triggering in
AERA", Internal note of the Pierre Auger Collaboration, 2011.

[238] Benoît Revenu for the AERA Central DAQ group, „AERA central trigger", Internal note of
the Pierre Auger Collaboration, GAP 2012-115, 2012.

[239] M. Erdmann, S. Fliescher, L. Mohrmann, and K. Weidenhaupt, „A novel method of selecting
cosmic ray candidates", Internal note of the Pierre Auger Collaboration, GAP 2011-108, 2011.

[240] M. Zöcklein, „Calibration of the Auger Engineering Radio Array using the Galactic Radio
Background", BA thesis (RWTH Aachen University, 2016).

[241] T. Karskens, „An absolute calibration of the antennas at LOFAR", MA thesis (Radboud University Nijmegen, 2015).

[242] A. Nelles et al., „Calibrating the absolute amplitude scale for air showers measured at LOFAR", J. Inst. **10**, P11005–P11005 (2015).

[243] S. Jansen, „Radio for the masses - cosmic ray mass composition masurements in the radio frequency domain", PhD thesis (Radboud University Nijmegen, 2016).

[244] Federal Aviation Administration, „Automatic dependent surveillance-broadcast (ADS-B) out performance requirements to support air traffic control (ATC) service", Federal Register **75**, 103 (2010).

[245] O. Kambeitz for the Pierre Auger Collaboration, „Measurement of horizontal air showers with the Auger Engineering Radio Array", Proc. of ARENA 2016, Groningen, The Netherlands (2016), arXiv:1609.05456.

[246] C. Glaser, „Energy measurement and strategy for a trigger of ultra high energy cosmic rays measured with radio technique at the Pierre Auger Observatory", MA thesis (RWTH Aachen Universisty, 2012).

[247] E. Thébault et al., „International geomagnetic reference field: the 12th generation", Earth, Planets and Space **67**, 79 (2015).

[248] S. Grebe, S. Jansen, and C. Timmermans, „Suppression of self-introduced narrowband RFI in the time domain", Internal note of the Pierre Auger Collaboration, GAP 2013-012, 2013.

[249] H. Nyquist, „Certain topics in telegraph transmission theory", Trans. AIEE **47**, 617–644 (1928).

[250] C. E. Shannon, „Communication in the presence of noise", Proc. Institute of Radio Engineers **37**, 10–21 (1949).

[251] A. V. Oppenheim and R. W. Schafer, *Discrete-Time Signal Processing*, edited by T. Robbings, 2nd edition (Prentice Hall, 1999).

[252] M. Erdmann, C. Glaser, and K. Weidenhaupt, „A new method of the interpolation of the antenna response pattern", Internal note of the Pierre Auger Collaboration, GAP 2013-090, 2013.

[253] G. Burke and A. Poggio, *Numerical Electromagnetics Code (NEC) method of moments, parts I,II,III*, tech. rep. (Lawrence Livermore National Laboratory, 1983).

[254] M. Erdmann, C. Glaser, and K. Weidenhaupt, „Error estimation of cosmic ray radio signals", Internal note of the Pierre Auger Collaboration, GAP 2013-059, 2013.

[255] F. G. Schroeder et al., „On noise treatment in radio measurements of cosmic ray air showers", Nucl. Instrum. Meth. A **662, Suppl**, S238–S241 (2012).

[256] L. Mohrmann, „Measurement of radio emission from cosmic ray induced air showers at the Pierre Auger Observatory with a spherical wave reconstruction", MA thesis (RWTH Aachen, 2011).

[257] A. Leurs, „Measurement of cosmic ray induced air showers using a conical wave form reconstruction of radio emission signals at the Pierre Auger Observatory", MA thesis (RWTH Aachen University, 2013).

[258] A. van den Berg, W. Docters, E. Fraenkel, K. de Vries, and K. Weidenhaupt, „Locating transient noise sources at radio detection sites", Internal note of the Pierre Auger Collaboration, GAP 2011-083, 2011.

[259] C. Welling, M. Erdmann, and C. Glaser, „Event selection and investigation of the lateral distribution and polarization of radio signals from cosmic ray induced air showers", Internal note of the Pierre Auger Collaboration, GAP 2014-079, 2014.

[260] C. Welling, „Investigation of the lateral distribution and polarization of radio signals from cosmic ray induced air showers at the Pierre Auger Observatory", BA thesis (RWTH Aachen University, 2014).

[261] J. Neuser, „Cosmic rays and the atmospheric electric field", PhD thesis (Bergische Universität Wuppertal, 2015).

[262] C. Welling, MA thesis (in preparation, RWTH Aachen University, 2017).

[263] M. Erdmann and C. Glaser, „A new method for resampling of simulated extensive air showers including radio emission", Internal note of the Pierre Auger Collaboration, GAP 2013-099, 2013.

[264] E. Cramer and U. Kamps, *Statistik griffbereit*, 5th ed. (Institut für Statistik und Wirtschaftsmathematik, RWTH Aachen University, 2013).

[265] „Numerical Python (NumPy)", http://www.numpy.org/.

[266] C. Glaser for the Pierre Auger Collaboration, „Energy estimation for cosmic rays measured with the Auger Engineering Radio Array", AIP Conf. Proc. **1535**, Proc. of ARENA 2012, Erlangen, Germany, 68–72 (2013).

[267] T. Huege, R. Ulrich, and R. Engel, „Dependence of geosynchrotron radio emission on the energy and depth of maximum of cosmic ray showers", Astropart. Phys. **30**, 96–104 (2008).

[268] A. Schulz for the Pierre Auger Collaboration, „The measurement of the energy spectrum of cosmic rays above 3×10^{17} eV with the Pierre Auger Observatory", Proc. 33rd ICRC, Rio de Janeiro, Brazil (2013).

[269] O. Scholten, K. D. de Vries, and K. Werner, „Coherent radiation from extensive air showers", Nucl. Instrum. Meth. A **662**, S80 (2012).

[270] M. Ender et al., „Radio emission of extensive air showers during thunderstorms", Proc. 31st ICRC, Lodz, Poland **1**, 219 (2009).

[271] P. Schellart et al., „Probing atmospheric electric fields in thunderstorms through radio emission from cosmic-ray-induced air showers", Phys. Rev. Lett. **114**, 165001 (2015).

[272] S. Nehls, „Calibrated measurements of the radio emission of cosmic ray air showers", PhD thesis (Institut für Kernphysik, Universität Karlsruhe, 2008).

[273] I. Mariş for the Pierre Auger Collaboration, „Measurement of the energy spectrum of cosmic rays above 3×10^{17} eV at the Pierre Auger Observatory", Proc. of Science **EPS-HEP2013**, 405 (2013).

[274] G. Farrar for the Pierre Auger Collaboration, „The muon content of hybrid events recorded at the Pierre Auger Observatory", Proc. 33rd ICRC, Rio de Janeiro, Brazil, 1108 (2013).

[275] V. Marin for the Codalema Collaboration, „Charge excess signature in the Codalema data. interpretation with SELFAS2", Proc. 32nd ICRC, Beijing, China **1**, 291 (2011).

[276] R. A. Batista et al., „CRPropa 3—a public astrophysical simulation framework for propagating extraterrestrial ultra-high energy particles", J. Cosmol. Astropart. Phys. 05(2016)038 .

[277] M. Kasten, „Aufbau einer Mess-Station zur kontinuierlichen Bestimmung der Bodeneigenschaften beim Auger Engineering Radio Array", MA thesis (Bergische Universität Wuppertal, 2015).

[278] M. Ave et al. (AIRFLY Collaboration), „Precise measurement of the absolute fluorescence yield of the 337 nm band in atmospheric gases", Astropart. Phys. **42**, 90–102 (2013).

[279] M. Erdmann, R. Fischer, C. Glaser, D. Klingebiel, R. Krause, et al., „A field study of data analysis exercises in a bachelor physics course using the internet platform VISPA", Eur. J. Phys. **35**, 35018 (2014).

[280] Christian Glaser for the VISPA group, „Vispa: direct access and execution of data analyses for collaborations", J. Phys. Conf. Ser. **608**, 16th Int. Workshop on Advanced Computing and Analysis Techniques in physics research (ACAT), Prague, Czech Republic, Sep 2014, 012027 (2015).

[281] F. Briechle, M. Erdmann, C. Glaser, and R. Krause, „Octocopter position reconstruction for calibrating the Auger Engineering Radio Array", Internal note of the Pierre Auger Collaboration, GAP 2015-081, 2015.

Zusammenfassung

Ultra hochenergetische Cosmic-Rays (UHECRs) können über kurze Radiopulse im MHz Bereich gemessen werden, die von ausgedehnten Luftschauern abgestrahlt werden. Diese Methode ist komplementär zu bisherigen Techniken zur Messung von UHECRs z.B. über die Messung der Schauerteilchen am Boden oder die Beobachtung von Fluoreszenzlicht mit Teleskopen. Die Radiomessung ist sensitiv auf die wichtigsten Luftschauerparameter wie die Energie, die Masse und die Ankunftsrichtung des Cosmic-Rays.

In dieser Arbeit wurde eine neue Methode zur Messung der Cosmic-Ray Energie entwickelt, die zeigt, dass die Messung von UHECRs über Radiopulse besonders gut und besser als bisherige Methoden für eine genaue Messung der Energie geeignet ist. Dies liegt primär daran, dass die Radioemission der Luftschauer direkt mit Hilfe der klassischen Elektrodynamik berechnet werden kann und dass Radiowellen deutlich weniger stark von veränderten Umweltbedingungen beeinflusst werden als z.B. das Fluoreszenzlicht. Da eine genaue Bestimmung der Energieskala entscheidend für die Interpretation von Cosmic-Ray Messungen ist, wird die Radiomethode ermöglichen, dieses Forschungsfeld maßgeblich voranzubringen.

Dazu wurde im ersten Teil der Arbeit die Energie, die in Luftschauern in Form von MHz-Strahlung freigesetzt wird, mit Hilfe von Luftschauersimulationen berechnet, die wir im Folgenden als Strahlungsenergie bezeichnen. Während sich die Signalverteilung auf dem Boden stark mit unterschiedlicher Geometrie des Schauers ändert, bleibt die Strahlungsenergie konstant sobald sich der Luftschauer voll entwickelt hat. Insbesondere ist die Strahlungsenergie unabhängig von der Beobachtungshöhe und lässt sich dadurch zum direkten Vergleich verschiedener Experimente nutzen. Nach einer Korrektur der berechneten Strahlungsenergie auf die Abhängigkeit vom Erdmagnetfeld sowie der Dichte der Atmosphäre in der Emissionsregion, korreliert die korrigierte Strahlungsenergie mit der elektromagnetischen Schauerenergie und zeigt eine Streuung von weniger als 3%.

Im zweiten Teil der Arbeit wird die Strahlungsenergie der Luftschauer am Auger Engineering Radio Array (AERA) gemessen, einem Array von mehr als 150 autonom arbeitenden Radiostationen verteilt auf einer Fläche von $17\,\mathrm{km}^2$. AERA ist der Radiodetektor des Pierre Auger Observatoriums welches das weltweit größte Observatorium für kosmische Strahlung ist und eine Fläche von mehr als $3000\,\mathrm{km}^2$ im Westen von Argentinien mit einem Array von über 1600 Teilchendetektoren und 27 Fluoreszenzteleskopen instrumentiert. Durch einen Vergleich mit der Messung der Cosmic-Ray Energie durch die Teilchendetektoren, die wiederum über die kalorimetrische Energiemessung der Fluoreszenzteleskope kalibriert wurden, wurde eine Strahlungsenergie von 15.8 MeV im Frequenzbereich von 30-80 MHz für einen Luftschauer mit einer Energie von 1 EeV gemessen, der eine Ankunftsrichtung parallel zum Erdmagnetfeld hat. Die Energieauflösung des Radiodetektors beträgt 14% für Luftschauer, die in mindestens fünf Radiostationen gemessen wurden, und ist damit konkurrenzfähig in der Präzision der Energiemessung zu der Messung über Teilchendetektoren.

Im finalen Teil der Arbeit wird die theoretische Berechnung mit der Messung der Strahlungsenergie verglichen, die auf der Energieskala der Fluoreszenzteleskope basiert. Die Berechnungen aus klassischer Elektrodynamik liefern 19% größere Cosmic-Ray Energien. Die systematische Unsicher-

heit der Radioenergieskala ist dabei 15% und damit bereits jetzt konkurrenzfähig zu der Energieskala der Fluoreszenzteleskope mit ihrer systematischen Unsicherheit von 14%.

Durch eine Verbesserung der Detektorkalibration ist in Zukunft eine deutliche Verbesserung in der systematischen Unsicherheit der Radioenergieskala zu erwarten. Durch die Verwendung einer bereits neu durchgeführten Kalibration, kann die systematische Unsicherheit der Energieskala auf 10% reduziert werden. Mit weiteren Verbesserungen ist eine Reduzierung der Unsicherheit auf 7% möglich. Zusammenfassend lässt sich sagen, dass die Radiotechnologie zusammen mit den Methoden, die in dieser Arbeit entwickelt wurden, die Bestimmung der Energieskala mit nie dagewesener Genauigkeit erlaubt und dadurch die Interpretation der Daten des Pierre Auger Observatoriums deutlich verbessern wird.

List of publications

Published articles with significant personal contribution

C. Glaser, M. Erdmann, J. R. Hörandel, T. Huege, and J. Schulz
„Simulation of Radiation Energy Release in Air Showers"
J. Cosmol. Astropart. Phys. 09(2016)024
The work presented in this publication was primarily performed by the author of this thesis. The text of the publication has been written by the author of this thesis and was revised and copy-edited by the co-authors of the publication.

A. Aab et al. (Pierre Auger Collaboration)
„Energy Estimation of Cosmic Rays with the Engineering Radio Array of the Pierre Auger Observatory"
Phys. Rev. D **93**, 122005 (2016)
The work presented in this publication was primarily performed by the author of this thesis. The text of the publication has been written by the author of this thesis and was revised and copy-edited by the co-authors of the publication.

A. Aab et al. (Pierre Auger Collaboration)
„Measurement of the Radiation Energy in the Radio Signal of Extensive Air Showers as a Universal Estimator of Cosmic-Ray Energy"
Phys. Rev. Lett. **116**, 241101 (2016)
The work presented in this publication was primarily performed by the author of this thesis. The text of the publication has been revised and copy-edited by the author of this thesis.

A. Aab et al. (Pierre Auger Collaboration)
„Calibration of the LPDA Radio Stations at the Pierre Auger Observatory using an Octocopter"
in preparation
The author of this thesis has contributed to the parts of the analysis where the impact of the new calibration on cosmic-ray radio pulses is investigated and where the uncertainty of the electric-field amplitude is determined. The text of the publications has been revised and copy-edited by the author of this thesis.

M. Erdmann, R. Fischer, C. Glaser, D. Klingebiel, R. Krause, et al.
„A field study of data analysis exercises in a bachelor physics course using the internet platform VISPA"
Eur. J. Phys. **35**, 35018 (2014)
The author of this thesis has participated in the field study and contributed to the development of the VISPA platform. The text of the publications has been revised and copy-edited by the author of this thesis.

Conference proceedings

C. Glaser, M. Erdmann, J. R. Hörandel, T. Huege, and J. Schulz

„Simulation of the Radiation Energy Release in Air Showers"

Proc. of ARENA 2016, Groningen, The Netherlands (2016), arXiv:1609.05743

The work presented in this publication was primarily performed by the author of this thesis. The text of the publication has been written by the author of this thesis and was revised and copy-edited by the co-authors of the publication.

C. Glaser for the Pierre Auger Collaboration

„Results and Perspectives of the Auger Engineering Radio Array"

Proc. of ARENA 2016, Groningen, The Netherlands (2016), arXiv:1609.01513

The work presented in this publication was primarily performed by the author of this thesis. The text of the publication has been written by the author of this thesis and was revised and copy-edited by the co-authors of the publication.

C. Glaser for the Pierre Auger Collaboration

„The Energy Content of Extensive Air Showers in the Radio Frequency Range of 30-80 MHz"

Proceedings of Science (2015), 34th ICRC, The Hague, The Netherlands

The work presented in this publication was primarily performed by the author of this thesis. The text of the publication has been written by the author of this thesis and was revised and copy-edited by the co-authors of the publication.

Christian Glaser for the VISPA group

„VISPA: Direct Access and Execution of Data Analyses for Collaborations"

J. Phys. Conf. Ser. **608**, 012027 (2015), 16th Int. Workshop on Advanced Computing and Analysis Techniques in physics research (ACAT), Prague, Czech Republic, Sep 2014

The author of this thesis contributed to the development of VISPA and implemented the graphical steering of the Pierre Auger analysis framework. The text of the publication has been written by the author of this thesis and was revised and copy-edited by the co-authors of the publication.

Internal publications

M. Erdmann, C. Glaser, and K. Weidenhaupt
„Error Estimation of Cosmic Ray Radio Signals"
Internal note of the Pierre Auger Collaboration (2013), GAP 2013-059
The work presented in this publication was primarily performed by the author of this thesis. The text of the publication has been written by the author of this thesis and was revised and copy-edited by the co-authors of the publication.

M. Erdmann, C. Glaser, and K. Weidenhaupt
„A new method of the interpolation of the antenna response pattern"
Internal note of the Pierre Auger Collaboration (2013), GAP 2013-090
The work presented in this publication was primarily performed by the author of this thesis. The text of the publication has been written by the author of this thesis and was revised and copy-edited by the co-authors of the publication.

M. Erdmann and C. Glaser
„A new Method for Resampling of Simulated Extensive Air Showers including Radio Emission"
Internal note of the Pierre Auger Collaboration (2013), GAP 2013-099
The work presented in this publication was primarily performed by the author of this thesis. The text of the publication has been written by the author of this thesis and was revised and copy-edited by the co-authors of the publication.

C. Welling, M. Erdmann, and C. Glaser
„Event Selection and Investigation of the Lateral Distribution and Polarization of Radio Signals from Cosmic Ray Induced Air Showers"
Internal note of the Pierre Auger Collaboration (2014), GAP 2014-079
The work presented in this publication is based on the Bachelor thesis of C. Welling which was supervises by the author of this thesis. The text of the publication has been revised and copy-edited by the author of this thesis.

F. Briechle, M. Erdmann, C. Glaser, and R. Krause
„Octocopter Position Reconstruction for Calibrating the Auger Engineering Radio Array"
Internal note of the Pierre Auger Collaboration (2015), GAP 2015-081
The text of the publication has been revised and copy-edited by the author of this thesis.